DEPOSITION AND PROTECTION MECHANISMS OF ZIRCONIUM CONVERSION COATINGS ON ALUMINIUM ALLOY, STEEL AND ZINC SUBSTRATES

Ana Kraš

Doctoral Dissertation
Jožef Stefan International Postgraduate School
Ljubljana, Slovenia

Supervisor: Prof. Ingrid Milošev, Jožef Stefan International Postgraduate School and Jožef Stefan Institute, Ljubljana, Slovenia

Evaluation Board:
Assoc. Prof. Miha Čekada, Chair, Jožef Stefan International Postgraduate School and Jožef Stefan Institute, Ljubljana, Slovenia
Prof. Miran Gaberšček, Member, National Institute of Chemistry and Faculty of Chemistry and Chemical Technology, University of Ljubljana, Slovenia
Dr. Sviatlana V. Lamaka, Member, Institute of Surface Science, Helmholtz-Zentrum Hereon, Germany

MEDNARODNA PODIPLOMSKA ŠOLA JOŽEFA STEFANA
JOŽEF STEFAN INTERNATIONAL POSTGRADUATE SCHOOL

Ana Kraš

DEPOSITION AND PROTECTION MECHANISMS OF ZIRCONIUM CONVERSION COATINGS ON ALUMINIUM ALLOY, STEEL AND ZINC SUBSTRATES

Doctoral Dissertation

MEHANIZMI DEPOZICIJE IN ZAŠČITE CIRKONIJEVIH KONVERZIJSKIH PREVLEK NA PODLAGAH IZ ALUMINIJEVE ZLITINE, JEKLA IN CINKA

Doktorska disertacija

Supervisor: Prof. Ingrid Milošev

Ljubljana, Slovenia, May 2024

To my mother and father

Acknowledgments

If I may summarize the main point of this journey, it would be to embrace challenges as opportunities to grow, with this thesis marking a significant milestone in that process, all thanks to the invaluable guidance and support I have received.

My greatest appreciation goes to Prof. Ingrid Milošev for her unwavering support, guidance, assistance with time management and constant reminders on the importance of perseverance.

I would also like to thank Dimitrij Us, MSc, and Dr. Sabina Ovčjak for generously sharing SurTec chemical pretreatment solutions and providing extensive industry insights on conversion coatings. A big thank you also goes to Domagoj Jadanić, MSc., for kind reccomendations in preparing the metallographic samples using Struers equipment. Dr. Neil Spinner's enlightening webinars on electrochemical impedance spectroscopy, which provided a solid guide for further exploration in the field, are highly appreciated.

My gratitude also extends to Dr. Ignasi Puigdomènech for valuable discussions and selfless expert advice on constructing diagrams using Spana. Special thanks to Prof. Davorin Kramar for invaluable advice on the use of response surface methodology. Many thanks also go to Dr. Iosif Fromondi from Methrom Autolab for his continuous accessibility and expert support in utilizing Autolab products and NOVA software.

I am deeply thankful for the enriching experience at Helmholtz-Zentrum Hereon through the ERASMUS+ program, particularly to Dr. Sviatlana Lamaka and the Electrochemistry and Big Data Department for their warm welcome, generosity, selfless sharing of ideas, and expert guidance. Many thanks to Yulong Wu, MSc., for kindly assisting with the scanning micro-probe technique measurements.

I extend my gratitude to Prof. Philippe Marcus and Dr. Antoine Seyeux for their invaluable assistance with the ToF-SIMS measurements and data interpretation.

I also like to thank my current colleagues at the Department of Physical and Organic Chemistry, especially Dr. Rodič for experimental support and discussions, Barbara Kapun, BSc., for SEM/EDS analyses, and all my other colleagues for their support and camaraderie, making me feel at home, especially Dr. Matjaž Dlouhy.

Nevertheless, I am truly grateful to Prof. Sanja Martinez and Prof. Zoran Mandić for sparking my love for electrochemistry.

Additionally, I wish to express my gratitude for the funding provided by the Slovenian Research and Innovation Agency, which made this research possible through grants P2–0393 and PR–09806.

Amidst the multitude who have contributed to my academic and personal growth, it is those who challenged me negatively that have shaped me the most, hopefully serving as a reminder of who I strive not to become.

Finally, my deepest gratitude goes to my parents, Davor and Ljerka, for their unwavering love and support throughout this journey, and to my long-time friends, Nikolina, Nina, Jan, Marija, and those made along the way, for their unwavering encouragement and the memories we have shared, which have made this journey all the more meaningful.

Abstract

This thesis focuses on the development and optimisation of zirconium conversion coatings (ZrCCs) on cold-rolled steel (CRS), zinc (Zn), and aluminium alloy AA5754 substrates through a multidimensional approach.

The utilization of statistical tools, specifically response surface methodology (RSM), enabled the assessment of the individual and mutual effects of various parameters in the zirconium conversion bath (H_2ZrF_6 concentration, pH, and conversion time) on corrosion resistance responses of ZrCCs obtained by different evaluation techniques. Specifically, CRS and Zn favoured mid to higher concentrations (825–1226 ppm), longer conversion times (430–480 s), and mid to higher pH levels (4.0–4.6), while AA5754 favoured significantly lower concentrations (150 ppm), shorter immersion times (230 s), and a higher pH (4.6). This is attributed to the preferential, thicker zirconium conversion coating deposition on intermetallic particles, accompanied by cracking. RSM models derived from Electrochemical Impedance Spectroscopy were the most effective for characterising and optimising ZrCCs on all substrates, suggesting it as the most universal ZrCC evaluation technique.

Updating equilibrium predominance diagrams for Zr–OH and Zr–F aqueous speciation implied the tetramer $Zr_4(OH)_8^{8+}$ as a fundamental building block in the solid phase of ZrCCs. This also suggested that the ZrCC process is of a sol-gel nature and not only an electrochemical one. Time-of-Flight Secondary Ion Mass Spectrometry further confirmed the presence of polymerized tetrameric structures in ZrCCs on CRS formed under conditions previously shown to be vital for adequate coating formation (pH = 4.0).

The proposed sol-gel chemistry of ZrCCs was further examined using SiO_2 and ZrO_2 colloidal pretreatments. SiO_2 pretreatment significantly improved the uniformity and reduced the cracking of ZrCCs on AA5754, unlike ZrO_2, which showed a limited impact on coating morphology and corrosion protection, implying the need to form a Si–Zr network to enhance corrosion resistance.

Additionally, the electrochemical behaviour of F^- and Cl^- in NH_4HCO_3 buffer at different concentrations was examined to assess their suitability as additives in the H_2ZrF_6 bath. It was revealed that F^- induced significant complex formation on CRS and AA5754, narrowing the passive region of aluminium, while Cl^- mainly led to pitting on AA5754 at higher concentrations. In contrast, equilibrium calculations further revealed the hat corrosion of zinc was mainly influenced by the overall ionic strength and further complexation with the buffering agent at higher pH levels and not with halide ions.

This dissertation lays the groundwork for future research aiming to refine the methodologies applied and extend the findings to industrial applications.

Povzetek

Disertacija obravnava razvoj in optimizacijo cirkonijevih konverzijskih prevlek (ZrCCs) na podlagah iz hladno valjanega jekla (CRS), cinka (Zn) in aluminijeve zlitine AA5754 z uporabo večdimenzionalnega pristopa. Uporabili smo statistična orodja, zlasti metodo odzivne površine (RSM), za oceno posameznih in skupnih učinkov različnih parametrov v cirkonijevi konverzijski kopeli, kot so koncentracija H_2ZrF_6, pH in čas konverzije na korozijsko upornost ZrCC. Posebej sta CRS in Zn ugodno reagirala na srednje do visoke koncentracije (825−1226 ppm), daljše čase konverzije (430−480 s) in srednje do visoke pH vrednosti (4,0−4,6), medtem ko se AA5754 bolje odziva na bistveno nižje koncentracije (150 ppm), krajše čase potopitve (230 sekund) in višji pH (4,6). Slednji rezultat izhaja iz večje elektrokemijske raznolikosti površine AA5754, ki pelje do preferenčne tvorbe debelejše plasti cirkonijeve konverzijske prevleke na intermetalnih delcih (angl. Intermetallic particles, IMPs), kar vodi do razpok.
Modeli RSM, ki smo jih izpeljali iz elektrokemijske impedančne spektroskopije (EIS), so se izkazali za najučinkovitejše pri karakterizaciji in optimizaciji ZrCC na vseh podlagah.

S posodobljanjem ravnotežnih porazdelitvenih diagramov za Zr−OH in vodne zvrsti Zr−F smo nakazali, da je tetramer $Zr4(OH)_8^{8+}$ osnovni gradnik v trdni fazi ZrCC. To prav tako potrjuje, da je proces tvorbe ZrCC tudi sol-gel narave, ne zgolj elektrokemične. Z analizo sekundarne ionske masne spektrometrije z analizatorjem na čas preleta (ToF-SIMS) smo nadalje potrdili prisotnost tetramernih struktur v ZrCC na CRS, ustvarjenih pod pogoji, ključnimi za ustrezno oblikovanje prevleke in pridobivanje želenih zaščitnih lastnosti (pH 4,0).

Predlagano sol-gel kemijo ZrCC smo dodatno preučili z uporabo predobdelav s koloidnim SiO_2 in ZrO_2. Predobdelava s SiO_2 je bistveno izboljšala enakomernost in zmanjšala razpoke ZrCC na AA5754, za razliko od ZrO_2, ki je imel omejen vpliv na morfologijo prevleke in zaščito pred korozijo, kar nakazuje na potrebo po oblikovanju mreže Si−Zr za izboljšanje odpornosti proti koroziji.

Poleg tega smo preučili elektrokemijsko obnašanje ionov F^- in Cl^- v pufru NH_4HCO_3 pri različnih koncentracijah, da bi ocenili njihovo primernost kot dodatke v kopeli H_2ZrF_6. Rezultati kažejo, da F^- inducira pomembno kompleksacijo na CRS in AA5754, kar zoži pasivno območje aluminija, medtem ko Cl^- predvsem vodi do jamičaste korozije na AA5754 pri višjih koncentracijah. Nasprotno so ravnotežni izračuni dodatno razkrili, da je korozija cinka predvsem odvisna od skupne ionske moči in dodatne kompleksacije s pufrom v alkalnem območju in ne s halogenidnimi ioni.

Na ta način smo postavili temelje za prihodnje raziskave, ki ciljajo na izboljšanje uporabljenih metodologij in razširitev ugotovitev na industrijske aplikacije.

Contents

List of Figures

List of Tables

Abbreviations

AA	...	aluminium alloy
AA5754	...	aluminium alloy 5754
ATR-FTIR	...	attenuated total reflectance Fourier transform infrared spectroscopy
CCD	...	central composite design
CC	...	conversion coating
CCC	...	chromate conversion coating
CPE	...	constant phase element
CRS	...	cold-rolled steel
DoE	...	design of experiments
DFT	...	density functional theory
DO	...	dissolved oxygen
EDS	...	energy dispersive x-ray spectroscopy
EEC	...	equivalent electrical circuit
EIS	...	electrochemical impedance spectroscopy
EQCM	...	electrochemical quartz crystal microbalance
FIB	...	focused ion beam
HER	...	hydrogen evolution reaction
HSAB	...	hard and soft acids and bases
IMP	...	intermetallic particle
OCP	...	open circuit potential
ORR	...	oxygen reduction reaction
PPC	...	potentiodynamic polarisation curve
PPC	...	phosphate conversion coating
RSM	...	response surface methodology
SEM	...	scanning electron microscopy
SIT	...	specific ion interaction theory
TEM	...	transmission electron microscopy
ToF-SIMS	...	time-of-flight secondary ion mass spectrometry
XPS	...	x-ray photoelectron spectroscopy
Zn	...	zinc
ZrCC	...	zirconium conversion coating

Chapter 1

Introduction

1.1 Corrosion

The extent of the influence of corrosion on human activity ranges from rusted fences and patinated statues to rare, but more dramatic, oil spills or even aeroplane crashes. Simply put, corrosion is the gradual deterioration of a material, preferably metal, due to its interaction with the surrounding environment. Above all, one must understand that corrosion is driven by the **redox potential difference in the microenvironment of the metal surface**, as it is foremost an electrochemical process. Thereupon, locations with more positive potential are regarded as cathodic and more negative as anodic, respectively [1]. Active corrosion is characterised by anodic reactions resulting in an electrolyte-soluble product. Dissolved metal ions can form sparingly soluble deposits of oxide and hydroxide, a state known as passivity. However, passive layers provide a different degree of corrosion protection, with properties greatly dependent on the substrate [1]. As a refined metal aims at only one thing: to return to the thermodynamically stable state of its ore at the earliest opportunity, the main corrosion products are compounds naturally found in ores, particularly oxides and hydroxides, occasionally accompanied by chlorides, sulphates and carbonates [2]. With the main anodic reaction being metal oxidation, countered with the main cathodic reaction of oxygen and/or hydrogen reduction, and, given that the corroding metal acts as an electrical conductor along with the electrolyte as an ionic conductor, a corrosion cell can be considered equal to a short-circuited galvanic cell. Consequently, successful electrochemical corrosion demands the existence of **anode-cathode pairs, an electrical conductor** and **an ionic conductor**, as illustrated in Figure 1.1[3].

The aforementioned potential difference resulting in corrosion is a **combination of metallurgical properties**, such as impurities, grain boundaries, inclusions, intermetallic particles or second phases originating from metal processing [3], and **environmental properties**, such as pH value, temperature, pressure, viscosity, chemical composition, constituent concentration (i.e. different availability of electroactive species at the surface), electrical or thermal conductivity, to name but a few [4, 5]. Since the environment is ever-changing with many parameters in complex interactions, potential differences will always somehow occur. Consequently, corrosion stands as an inevitable fate of every metal [1]. However, metals remain the leading manufacture and construction materials to date, owing to their matchless performance. Consequently, it has been practical to develop a wide range of corrosion protection methods tailored to address the most influential corrosion factor in each specific case. The establishment of proper corrosion management can significantly minimize the damage, the main motivation being cost savings between 15 % and 35 %, as corrosion expenses annually reach up to 3.4 % of global GDP [6].

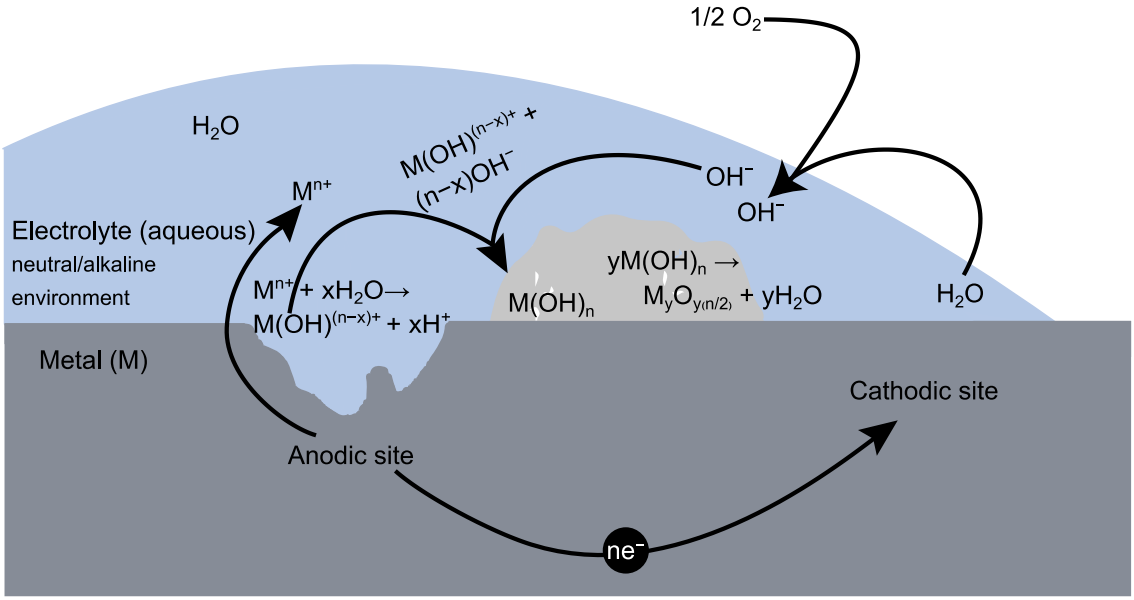

Figure 1.1: A schematic of the corrosion process.

1.2 Conversion Coatings: Old vs. New Generation

Corrosion protection methods aim to modify the metal (its metallurgical or surface parameters), the environment (e.g., the addition of inhibitors to electrolytes), or both [4, 5]. For metals of industrial importance, more precisely, aluminium (and its alloys), steel, and galvanised steel, surface modifications have become extensively employed for resisting corrosion [7], owing to their cost-effectiveness and practicability [5]. One particular method of surface modification that has been successfully employed in the aerospace and automotive industry are conversion coatings (CC). In a conversion coating, as the name implies, a metal surface is converted into an adherent layer of improved corrosion protection properties through a chemical or electrochemical reaction. In general, during conversion, anodic areas of the metal surface matrix undergo oxidation, accompanied by hydrogen and oxygen reduction at cathodic areas (such as intermetallic particles (IMPs) and grain boundaries), leading to alkalisation and precipitation of various inorganic phases from the conversion bath [8, 9]. These phases, whether amorphous or crystalline, act as barriers against corrosive agents from the electrolyte, providing only limited protection to the underlying substrate. Instead, the primary function of CCs is to serve as a pretreatment layer that enhances the adhesion of subsequent layers in a multi-coating system. However, if the conversion coating fails, the top coat experiences rapid degradation. Therefore, in the final step before application, it is essential to study conversion coatings both independently and in conjunction with the top coat.

For over a century, conversion coatings based on chromate (CCC) for aluminium/light metals and phosphate (PCC) for ferrous substrates have been successfully employed. However, The Environmental Protection Agency (EPA) has categorized Cr(VI) as a human carcinogen by the inhalation route of exposure [10]. As such, some Cr(VI) compounds are currently under authorisation as substances of very high concern (Annex XIV to REACH) [11] while others have further been restricted (Annex XVII to REACH) [12] under Registration, Evaluation, Authorisation and Restriction of Chemicals (REACH) [13] regulation in the European Union (EU) and the European Economic Area (EEA). Regarding Cr(III), a current alternative for Cr(VI), EPA has also raised concerns about

possible reoxidation to Cr(VI), along with potential carcinogenicity of Cr(III) itself [14, 15], which will lead to a complete ban of all Cr-based compounds soon. Nevertheless, the limit of Cr resources is nearing [16], which is the final justification for finding viable alternatives soon. Similarly, REACH restrictions have been posed on PCCs as well [17], leading to a growing interest in finding alternatives that will match or exceed their performance. Whether for price, availability, environmental or health impact, possible alternatives for existing technologies are often shortlisted to only a few. In the light of new conversion coatings, the search has stalled on Cr close neighbours in the periodic table of elements, more precisely, Zr and Ti [18].

1.2.1 Zirconium conversion coatings

Owing to Zr commercial availability and lower cost, ZrCCs have predominantly matured to commercial applications. In general, ZrCCs offer cost reductions of up to 30 % due to faster conversion times, operating at room temperature, fewer process stages (no conditioning stage needed), smaller tanks, and virtually no sludge generated, which makes maintenance easier due to decreased need for tank (immersion application) and spray nozzle (spray application) cleaning as well as heat exchanger blocking. Also, ZrCCs work well with most substrates, including steel, galvanized steel, aluminium, and its alloys. ZrCCs can be integrated into existing equipment, making facility switches straightforward [19, 20, 21, 22]. At the moment, ZrCCs have met the performance of standard PCCs only on aluminium surfaces, the performance on steel and galvanized steel surfaces is yet to be reached [23]. On the other hand, Cr has reached substitution in the automotive industry but remains the top choice in the aerospace industry [15], owing to more stringent requirements that CCCs can meet due to their higher corrosion resistance with added self-healing ability, as CCCs always contain some amount of the soluble Cr(VI) originating from the process that can migrate to the defect and undergo reduction to the insoluble Cr(III), thus sealing the defect. With constant improvements experienced through generations beyond, there are reviews summarizing numerous studies on conversion coatings belonging to each generation [5, 8, 9]. It is thus clear that understanding the chemistries of all conversion agents is crucial for a successful replacement [24].

The ZrCC process typically involves five steps: cleaning, rinsing, coating, rinsing, and drying, with the possibility of modifications. Before cleaning, surface grinding and polishing can be performed [9]. Each step has a distinct impact on the final coating performance. Like their predecessors, ZrCCs obey the above-described mechanism of surface alkalisation, i.e., pH-driven precipitation, most commonly from baths containing hexafluorozirconic acid (H_2ZrF_6) as the Zr-bearing component. Besides, current commercial baths include film-forming agent salts, activators, accelerators, pH adjusters, and other additives for performance enhancement. However, the influence of each additive in the conversion bath and their interactions on the subsequent performance are still not fully understood [25, 26].

While the mechanism of Zr/TiCC deposition may seem substrate-independent, its performance is generally inferior to CCC. The unique chemistry of Cr contributes to the ability of CCCs to provide both barrier and active corrosion protection. This is achieved through the self-healing ability provided by redox reactions involving Cr(VI) species, which allows for forming a protective layer after mechanical or chemical damage in a wide range of environmental conditions [27]. This property has not been replicated in alternative options due to the aforementioned lack of active corrosion protection.

Nevertheless, although not the least soluble type of film, ZrCCs offer a passivation range across a significantly wider pH range (Figure 1.2) compared to previous technologies, making them a promising candidate for the gradual replacement of CCCs and PPCs. Solubility calculations were conducted in Spana software using its default database at 25°C.

This involved using aqueous and solid species as input parameters and setting their log activity to 0. The main CC solid species selected were: $Zr(OH)_4$ (am) as a representative of ZrCCs, $Cr(OH)_3$ (am) as a representative of CrCCs, and $Zn_3(PO_4)_2{\times}4H_2O$ (cr) for PPC, along with native (hydro)oxides of steel ($Fe(OH)_3$ (am)), aluminium (AlOOH (s)), and zinc (ZnO (cr)). The decision to employ amorphous or crystalline phases was based on available literature data on species formed during conversion, as it significantly affects solubility, with the former being much more soluble than the latter. More details on performing thermodynamic equilibrium calculations will be provided in *Chapters 3* and *4*.

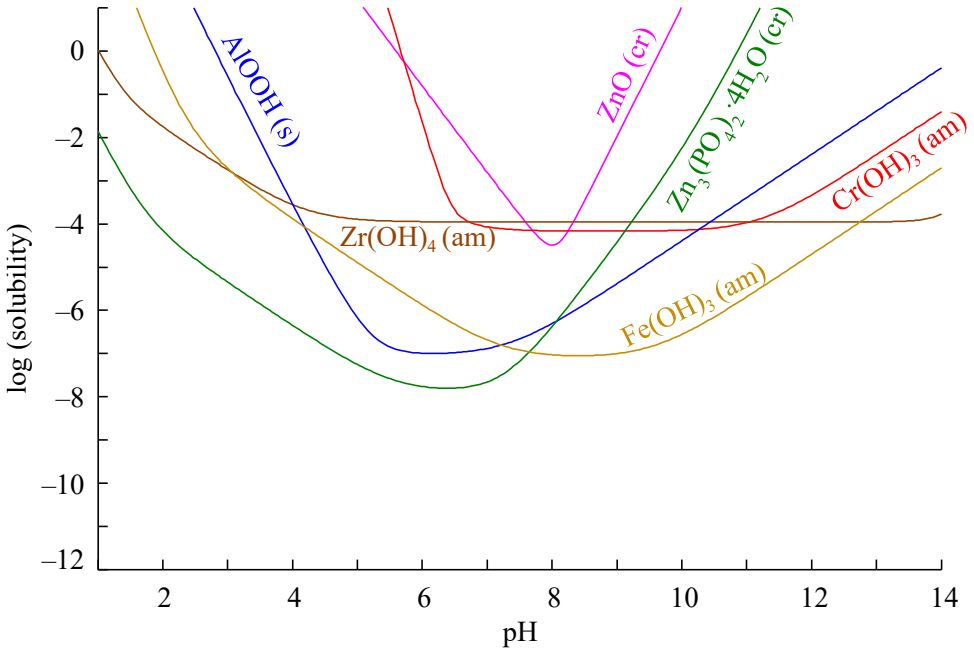

Figure 1.2: Comparison of solubilities of different CCCs components and native (hydro)oxides.

1.2.2 Problems associated with zirconium conversion coatings

The scientific literature presents significant variations in the results obtained from the same substrates and under similar conditions, ranging from poor performance to surpassing their predecessors [9]. Furthermore, it seems like the comprehensive knowledge of ZrCCs is exclusively documented in industrial reports and patents, which, despite database availability, can be hindered by paywalls and complex language and often lack essential information required for a fundamental understanding of its mechanism, thus impeding the finding of pathways for improvement. Additionally, most scientific papers in the field of ZrCCs primarily focus on evaluating and reporting the performance of ZrCCs compared to previous literature findings. Moreover, most of them use commercial ZrCCs having undisclosed compositions while paying little to no attention to the chemistry of Zr or other ZrCC bath additives. Therefore, to mitigate potential issues arising from undisclosed ZrCC bath compositions, this PhD thesis conducted studies using H_2ZrF_6 acid only as the source of Zr with the current emphasis on corrosion protection rather than adhesion promotion. The research focused on three widely used substrates in the automotive industry: cold-rolled steel (CRS), pure zinc (to represent galvanised surfaces), and aluminium alloys (AAs) [28], from which AA5754 was arbitrarily chosen in this thesis [29].

While the problems associated with ZrCCs are evident in many literature studies, only a few have addressed these issues [26, 30, 31, 32, 33, 34]. Based on an extensive review of the literature, including both the available patents as well as scientific papers, we have identified several significant issues related to ZrCC, including the following:

1. Commercial recommendations offer a broad range of operating conditions, which must be tested and refined to determine the optimal conditions for ZrCC baths. The ultimate goal would be to find optimal conditions on various substrates and enable the development of a multi-metal coating.
2. Enhanced cathodic activity at IMPs on aluminium alloys causes the preferential deposition of ZrCCs thereat. This non-uniform deposition leads to inconsistent ZrCC thickness. Generally, the thickness of ZrCCs on all substrates typically falls within the range of 10 to 80 nm, which is considerably lower compared to previous technologies and could present a disadvantage [9]. This also limits the range of techniques that can be effectively employed to measure such thin coatings.
3. The high irreproducibility of formed ZrCCs can be attributed to strong propensity of Zr for hydrolysis, sensitivity to solution composition, and high affinity for coordination and geometry exchange. These characteristics make it challenging to produce Zr compounds with consistent properties [35].
4. The combination of the second and third problems raises a new problem: identifying an appropriate evaluation technique for assessing the performance of such thin and inhomogeneous coatings, particularly in electrochemical applications.
5. There is a lack of knowledge regarding the in-situ formation of Zr coatings and the localised effects during the process. Understanding these aspects is crucial for advancing the understanding and control of ZrCC properties.

In a rapidly evolving technological landscape [19], the key towards top-notch products lies in understanding how to manipulate various process parameters. Therefore, to achieve comparable or even better performance than CCCs, it is imperative to broaden the scope of ZrCC studies equally across different substrates (not only on Al and its alloys) and by employing diverse bath conditions. The latter includes considering factors such as bath composition, pH, immersion time, temperature, stirring, etc. Design of Experiment (DoE), a family of statistical methodologies used to systematically plan, conduct, analyse, and interpret experiments, otherwise widely adopted in the industry, could be of immense help [36]. Inside DoE, one of the most popular statistical tools used is response surface methodology (RSM), which offers several advantages, the main being the efficient exploration of a wide range of parameter combinations through a relatively small number of experiments. By focusing on building mathematical models that describe the relationship between the response variable and the input factors, RSM enables the identification of optimal process conditions that yield the desired response [37].

The existing literature primarily emphasized the electrochemical properties of the substrate/coating system when studying the precipitation of Zr oxide in ZrCCs. This process involves hydroxylation triggered by cathodic reactions, leading to a pH increase [9]. Therefore, research on conversion coating processes should address the electrochemical aspects, particularly those that enable the control of pH increase during conversion. Electrochemistry is a powerful tool for obtaining important information about the substrate in a selected electrolyte. In corrosion studies, selecting a solution with the appropriate level of corrosiveness is crucial. If the solution is excessively aggressive, such as the commonly used 3.5 wt.% NaCl specified by well-established corrosion standards like ASTM G31−72

[38], it can result in excessive corrosion across all samples, with a particular impact on thin films like ZrCCs. On the other hand, if the solution lacks sufficient aggressiveness, it may fail to differentiate between samples with varying levels of corrosion susceptibility. Additionally, when dealing with thin films, electrochemical results often show a similar magnitude, resulting in statistically unreliable data. Thus, by selecting the proper solution, a wider range of electrochemical techniques can be applied, which, when combined with a proper testing technique, allows for a more comprehensive and accurate analysis.

Another issue not sufficiently approached in the literature are both pre- and posttreatments concerning conversion coatings. Within this context, the sealing process, a customary industrial procedure, encompasses the application of a sealant layer, often composed of a polymer or an alternative conversion coating, onto the surface previously subjected to conversion. Notably, certain literature studies have demonstrated that the posttreatment of a Ti-based conversion coating with $NiSO_4$ significantly enhances the corrosion resistance of coated CRS [39]. Nonetheless, other sealing methods, such as sodium silicate (Na_2SiO_3) solution posttreatment [40], simple boiling water sealing or air-drying, also prove effective [41]. Parallelly, our research group's investigations highlighted the substantial impact of air drying or sodium chloride immersion on the electrochemical behaviour of ZrCCs, underscoring the necessity of studying posttreatments for ZrCC [42, 43]. On the other hand, the literature has paid even less attention to pretreatments. Assuming the sol-gel characteristic inherent in the ZrCC process leads to the introduction of a pretreatment surface conditioning using nanoparticulate oxide. Nanoparticulate oxide resolves challenges stemming from prolonged Jernstedt's salts use [44], offering an extended pH stability range and improved temperature resistance. Candidates for these oxides encompass ZrO_2 and SiO_2. These anionically charged particles disperse, impartially adhering to metal surfaces, forming nuclei that function as subsequent microcathodes, ensuring uniform deposition of the conversion coating [45].

Besides conversion coatings, Zr has many uses, including nuclear reactors (Zircaloy 1), artificial gemstones, ceramics, and cosmetics, to name a few [46]. Thus, understanding the aqueous chemistry of Zr is not only of fundamental but also practical importance. Despite the extensive research on the chemistries of CCCs and PCCs over the past century [5, 8], the aqueous chemistry of Zr has not received sufficient attention. The coexistence of diverse Zr mononuclear and polynuclear species in the solution, resulting from the gradual and slow attainment of an equilibrium state during spontaneous hydrolysis and condensation, has contributed to a lack of consensus among literature sources regarding the Zr-species and their corresponding stability constants [47, 48, 49]. While literature reports on the structure of ZrCCs commonly rely on XPS (X-ray photoelectron spectroscopy), indicating a mixture of amorphous zirconia (ZrO_2) along with smaller quantities of ZrF_4, oxyhydroxides, and/or oxyfluorides [42, 50], the lack of knowledge regarding the proper forms of Zr in the solution as well as the solid form renders the exact structure of ZrCCs remains not fully elucidated. Another technique which enables to study the building species of thin films is time-of-flight secondary ions mass spectrometry (ToF-SIMS) utilised in our previous studies as well [34, 42]. Further, it has not been considered in the conversion coating community that the formation and thickening of the coating are fundamentally based on sol-gel chemistry [51].

Using *in-situ* techniques that enable real-time tracking of conversion coating formation would be helpful. Although they were more frequently employed on conversion coatings in general [52, 53, 54, 55, 56, 57, 58, 59, 60], they were very scarce in the field of ZrCCs [31, 32, 61, 62]. Among the potential techniques, scanning micro-probe techniques [63, 64] would be particularly useful for ZrCC studies. scanning micro-probe techniques offer unique capabilities for investigating localised corrosion phenomena. Corrosion processes often occur heterogeneously, with variations in pH and dissolved oxygen concentration at

different locations on the surface of a material [65]. By scanning a microelectrode across the sample surface and monitoring local electrochemical activity, scanning micro-probe techniques can map variations such as pH and dissolved oxygen concentration, providing spatially resolved information about corrosion activity. This information can aid in understanding the mechanisms of corrosion initiation and propagation. Regarding ZrCCs, scanning micro-probe techniques can assist in unravelling the exact ZrCC mechanism by being sensitive to localised changes on different substrates, which may not be detectable using macro methods.

All of the problems above captured our attention and have been investigated to varying extents in this dissertation. Given the lack of comprehensive understanding of ZrCC behaviour, particularly at a fundamental level, these investigations constitute a significant novelty in the field.

1.3 Purpose of the Dissertation

The dissertation aims to tackle various issues concerning zirconium conversion coatings and enhance our understanding of their deposition and protection mechanisms. This aim was accomplished by expanding the range of ZrCC studies to encompass different substrates and bath conditions while also delving into the intricacies of the coating formation process through both empirical and theoretical methods. The systematic characterisation and evaluation of ZrCCs, including their aqueous chemistry, structural composition, corrosion resistance, electrochemical behaviour, thickness evaluation, and local conversion mechanism, contribute to the development of enhanced ZrCC formulations and provide insights into the fundamental understanding of their formation and performance on different substrates. The ultimate aim is to improve the performance and expand the applications of ZrCCs as an environmentally friendly alternative.

1.4 Goals of the Dissertation

Utilise RSM to:

- Explore the design space to identify optimal operating ranges and evaluate factor interactions in the H_2ZrF_6-based ZrCC bath on CRS, Zn, and aluminium alloy AA5754 substrates.
- Compare non-electrochemical methods (drop test) and electrochemical techniques (potentiodynamic polarisation curves (PPC) and electrochemical impedance spectroscopy (EIS)) to assess the suitability of specific techniques for deriving corrosion resistance parameters for ZrCC evaluation.

- Conduct measurements in less aggressive media (dilute Harrison's solution, simulated acid rain) to enhance the accuracy of evaluating corrosion parameters and understanding the corrosion behaviour.
- Revisit the aqueous chemistry of Zr, specifically focusing on its hydrolysis behaviour in Zr−OH and Zr−F systems.
- Demonstrate the proposed structure of ZrCCs using ToF-SIMS and confirm the presence of zirconium oxide in a tetrameric form, particularly $Zr_4(OH)_8^{8+}$.
- Compare the influence of F^- and Cl^- on corrosion resistance of different substrates (CRS, Zn, and AA5754) using electrochemical methods of open circuit potential (OCP) and PPCs.

- Conduct and evaluate a colloidal pretreatment before ZrCC application to enhance corrosion resistance.

Employ local electrochemical measurements of pH and dissolved oxygen concentration to gain insights into the localized conditions at interface metal/electrolyte during ZrCC formation.

1.5 Hypotheses

- Utilising RSM explores ZrCC design space on CRS, Zn, and AA5754, identifying optimal condition ranges and factor interactions to enhance corrosion resistance.
- Conducting electrochemical measurements in less aggressive media (e.g., dilute Harrison's solution and simulated acid rain) yields precise corrosion parameter evaluations and a deeper understanding of the ZrCC corrosion behaviour.
- Aqueous chemistry in Zr−OH and Zr−F systems illuminates the importance of considering sol-gel chemistry in ZrCC formation beyond electrochemical aspects.
- Zirconia in ZrCCs exhibits a tetrameric form, confirmable with ToF-SIMS.
- The influence of F^- and Cl^- is different on CRS, Zn and AA5754, which is reflected in the ZrCC process.
- Non-preferential adsorption of colloidal particles on the metal surface ensures their uniform distribution, acting as nucleation sites for ZrCC precipitation, resulting in a uniform ZrCC coating on AA5754. Thus, applying colloidal SiO_2 or ZrO_2 pretreatment enhances the corrosion resistance of the formed ZrCCs.
- Local pH and dissolved oxygen concentration measurements using scanning micro-probe techniques assist in deciphering the complete ZrCC mechanism on various substrates, based on the premise that different substrates yield different results even under similar ZrCC conversion bath parameters.

1.6 Methodology

The methodology encompasses a diverse set of methods and instruments, categorised as follows:

- Statistical tools for experimental design: response surface methodology (RSM).
- Surface characterisation methods: attenuated total reflectance Fourier transform infrared spectroscopy (ATR-FTIR), scanning electron microscopy combined with energy-dispersive X-ray spectroscopy (SEM-EDS), focused ion beam scanning electron microscopy (FIB-SEM), ellipsometry and time-of-flight secondary mass spectrometry (ToF-SIMS).
- Conventional electrochemical methods used to evaluate corrosion performance: open circuit potential (OCP), electrochemical impedance spectroscopy (EIS), and potentiodynamic polarisation curves (PPC).
- Non-electrochemical test of coating porosity: drop test.
- *In-situ* local electrochemical scanning micro-probe techniques, employing pH sensitive potentiometric and O_2 sensitive amperometric micro-probes

Chapter 2

Deposition Mechanisms of ZrCCs and Corrosion Protection of AA5754, CRS and Zn

"All models are wrong, but some are useful."

George Box, 1976 [66].

2.1 Literature Review

As mentioned in *Chapter 1*, investigating CCs for corrosion resistance, both alone and with subsequent coatings, is critical as their corrosion failure can rapidly compromise the entire multi-coating system. The scientific literature displays considerable variability in results for similar conditions. However, comprehensive knowledge of ZrCCs is predominantly found in industrial reports and patents. While the former is less accessible, the latter often presents information in a complex and specialized manner, limiting their practical implementation for improvement. Additionally, most scientific particles on ZrCCs concentrate solely on performance assessment, neglecting vital chemistry details and utilizing undisclosed commercial compositions [9].

Thus, broadening the scope of ZrCC studies across diverse substrates is imperative, moving beyond the current focus on aluminium and its alloys. Understanding the influence and possible interactions between ZrCCs and various bath conditions is crucial for achieving comparable or even superior performance to conventional conversion coatings. Consequently, this *Chapter* emphasizes a comprehensive investigation into the three widely used substrates in the automotive industry: CRS, Zn and AA5754. While Zn and CRS are expected to demonstrate comparable corrosion behaviour in ZrCCs, aluminium alloys introduce an added complexity by containing various intermetallic particles often acting as cathodic sites [9]. This contributes to the development of notably thicker ZrCCs on these particles, yielding an inhomogeneous coating further susceptible to electrolyte leaching. Most studies on ZrCC were conducted on AAs of series 2xxx and 6xxx, while comparative studies on series 5xxx are relatively scarce [9, 34]. Our previous study showed that ZrCC deposited in the conversion bath of 200 ppm H_2ZrF_6 for 10 min provided good corrosion protection for AA5754 in 0.5 M NaCl with impedance values at the frequency of 3 mHz in the range of MΩ cm^2 after 3 days of immersion. The corrosion protection is favored on AA3005 over AA5754, although both alloys contain the same IMPs: $(MnFe)Al_6$ or α-$(MnFe)_3SiAl_{12}$; however, AA5754 contains mainly $(MnFe)Al_6$ with a much higher ratio of Fe/Mn = 7.8 than AA3005 which has a Fe/Mn ratio of 0.8. Both of these IMPs are noble relative to the alloy matrix and act as local cathodes [34]. Consequently, it is expected that AA5754 will be even more sensitive to changes in conversion bath parameters than CRS and Zn due to

different deposition mechanisms, with coatings being much thicker above IMPs than on the alloy matrix [9, 33, 34, 43].

When several factors influence a particular process characteristic, the Design of Experiment (DoE), a family of statistical methodologies, could be beneficial [37]. Using DoE, one can learn about the investigated process, differentiate between significant and insignificant factors, determine interactions between factors, construct predictive mathematical models, and optimise the response(s) [37]. Despite being widely adopted in industrial research after its inception over a century ago, the application of DoE in scientific research remains relatively limited. One of the primary merits of DoE lies in its ability to efficiently explore the combined effects of several input factors in a smaller number of experiments. This starkly contrasts the traditional One Factor at a Time (OFAT) approach, which examines only one factor while keeping others constant, risking the exploration of only a partial experimental space and overlooking potential interactions between factors [36, 67].

In DoE, when dealing with various influencing factors, the usual approach is to use a screening design to identify the most influential ones. However, one can also perform this initial screening based on experience and a thorough review of scientific literature and patents. We focused on investigating the conversion step using H_2ZrF_6 as a Zr-bearing component without incorporating common additives found in commercial ZrCC baths [68]. However, commercial cleaners, as per the manufacturer's recommendations, were utilized to comply with industrial applications.

Our assessment of pure H_2ZrF_6 conversion revealed that pH, concentration, and conversion time are the three most influential factors in the ZrCC process. Moreover, our experience suggests that the three factors contribute to the response independently and interact at specific levels [33, 34, 42, 43]. From the industrial point of view, continued and replenished bath lines are desired, which could be achieved with lower concentrations and lower immersion times that will not leave the bath depleted, both of which are successfully resolved in ZrCC baths [32, 69]. Following numerous commercial ZrCC bath recommendations, ZrCC baths typically operate at room temperature with a pH range of 3–5. This aspect was further elaborated upon in our previous publication [51], featured in *Chapter 3*, on the aqueous chemistry of Zr species, focusing on the distribution of Zr species with respect to pH. The conversion time varies based on the application method (spraying with shorter immersion, immersion with longer times) and goal (adhesion improvement with short immersion, corrosion resistance with extended times/higher concentrations). Thicker coatings inherently provide enhanced corrosion protection; however, excessive thickness can accelerate the delamination of the topcoat [70, 71]. However, both scientific and industrial literature lacks a consensus regarding the specific levels at which these factors should be used. Having three known influential factors with a wide range of values naturally leads to employing RSM as a DoE method. RSM models relationships between multiple factors and the response of interest, identifying factor interactions and determining if the relationship is linear, quadratic, or more complex. What sets RSM apart from other experimental designs is its particular advantage of modelling quadratic effects, which is reflected as a curvature (non-linearity) in the relationship between input factors and the response [37, 67]. To the best of our knowledge, very few studies have applied DoE in conversion coatings [72, 73, 74, 75, 76, 77, 78], and even fewer have utilised RSM [76, 77, 78]. Only one study has specifically applied RSM to investigate ZrCC. However, this study primarily focused on optimising ZrCC on a magnesium alloy before electrocoating [76].

The importance of selecting an appropriate response for any experiment cannot be overstated. In this case, it is the corrosion protection of ZrCCs. However, the thin nature of ZrCCs poses challenges when determining the optimal drying state for ZrCC, subsequent to which an evaluation is conducted. Typically, air drying stands out as the most straightforward posttreatment method for water-based coatings. Choosing the most appropriate corrosion protection assessment technique and selecting an electrolyte for electrochemically based studies

also add complexity to the process. Taking these factors into account is essential for a thorough and precise analysis, a consideration that was central to this study.

The use of an excessively aggressive solution, like the commonly employed 3.5 wt.% NaCl specified in well-established corrosion standards, such as ASTM G31−72 [38], can lead to excessive corrosion across all samples, particularly noticeable in thin films. Conversely, if the solution lacks sufficient aggressiveness, it may not effectively distinguish between samples with different corrosion susceptibilities [42, 79, 80, 81]. In our opinion, using a dilute Harrison's solution (DHS) can be more convenient for assessing the aggressiveness of typical corrosion test electrolytes while still allowing for observing corrosion behaviour changes in thin coatings. DHS is a modification of the original Harrison's solution, presumably made by Timminis [82]. Using $(NH_4)_2SO_4$ together with a reduced amount of NaCl compared to a common 3.5 wt.% solution has demonstrated more reliable results in predicting atmospheric corrosion. It has become a common choice for prohesion testing of primers (the first, adhesion promotion layers in direct contact with the metal surface) [83, 84, 85] and has also been occasionally utilized, albeit rarely, in electrochemical testing of primers [86].

Despite its infrequent implementation in the existing literature, electrochemical techniques are complementary, and more should be employed simultaneously [87]. References such as [88, 89] comprehensively tackled this problem. Among these techniques, destructive ones, such as PPCs, directly examine the coating integrity. However, they can alter or destroy the sample during testing, thus limiting sample variability and obscuring significant influences. On the other hand, non-destructive techniques, such as EIS, maintain the sample integrity and offer higher sensitivity, enabling the detection of subtle variations and small differences between samples, thus exhibiting decreased reproducibility [90]. It would be highly advantageous to compare the credibility of these techniques in ranking the relative corrosion protection of different ZrCCs. Additionally, for comparison, an independent method for corrosion assessment should be employed, and one such simple and convenient option is a so-called “drop test.” Combining destructive and non-destructive techniques can provide a more comprehensive understanding of the ZrCC behaviour, performance, and potential degradation mechanisms [84, 91, 92, 93].

In fact, we addressed all the problems as mentioned above after encountering them in our initial RSM study. By expanding the experimental scope through RSM to address data reliability issues in thin film analysis, to enhance result credibility, we believe we can offer valuable insights into ZrCC. This sets the groundwork for future research on various substrates and additives.

2.2 Experimental

2.2.1 2.1.1 Materials

Low-carbon CRS was used as a 1 mm thick panel (ACT Test Panels LLC, Hillsdale, Michigan, USA) with the chemical composition obtained by X-ray fluorescence spectroscopy: C 0.04 wt.%, Mn 0.2 wt.%, S 0.01 wt.%, Fe remainder. Zinc was supplied as a 1 mm thick foil (Goodfellow Cambridge Ltd., UK) with a manufacturer-specified chemical composition: 98.8 % Zn. Aluminium alloy EN AW-5754 (denoted as AA5754) in the form of a 1.5 mm thick panel was supplied by Impol 2000 d.d., Slovenska Bistrica, Slovenia. The following chemical composition was specified by the manufacturer: Mg 2.6–3.6 wt.%, Mn 0–0.5 wt.%, Si 0–0.4 wt.%, Fe 0–0.4 wt.%, Cr 0–0.3 wt.%, Zn 0–0.2 wt.%, Ti 0–0.15 wt.%, Cu 0–0.1 wt.%, Al reminder. Original panels were cut into smaller 2.5 cm × 3.5 cm square sheet specimens with 3 mm diameter holes punched for easier immersion into H_2ZrF_6 conversion baths. For SEM, samples were cut out to dimensions of up to 1 cm^2.

2.2.2 Chemicals

Solutions used in this work were prepared from as-received analytical reagent grade chemicals: absolute ethanol (EtOH, Merck KGaA, Darmstadt, Germany), acetone (Carlo Erba, Val de Reuil Cedex, France), NaCl (Fisher Scientific, Leicestershire, UK), $(NH_4)2SO_4$ (Acros Organics Geel, Belgium), NH4HCO3 (Sigma-Aldrich, Steinheim, Germany), H_2ZrF_6 (50 wt. % in water, Sigma-Aldrich, Saint Louis, USA), $CuSO_4{\times}5H_2O$ (Sigma-Aldrich, Saint Louis, USA), HCl (37 %, VWR International S.A.S, Fontenay-sous-Bois, France) $Pb(CH_3COO)_2 \times 3H_2O$ (Sigma-Aldrich, Saint Louis, USA). For chemical pretreatments, chemical products from SurTec® (SurTec International GmbH, Bensheim, Germany), supplied by SurTec Adria, d.o.o. (Ljubljana, Slovenia) were used: SurTec® 089, SurTec® 132, SurTec® 141 and SurTec® 496. SurTec® 089 is a detergent booster concentrated liquid product containing non-ionic surfactant alcohols in ethoxylated forms of amines, alkyls and fatty alcohols. SurTec® 132 is a slightly alkaline builder, free of silicates and surfactants, containing tetrapotassium pyrophosphate. SurTec® 141 is an alkaline builder, free of surfactants, containing phosphates, sodium tetraborate and silicates. SurTec® 496 is a high-end desmutting concentrated liquid product containing sulfuric acid, iron(III) salts, nitric acid and hydrofluoric acid.

Solutions were made using Milli-Q Direct water (Millipore, Billerica, Massachusetts, USA) with a resistivity of 18.2 MΩ cm at 25 °C and the total organic carbon (TOC) value below 5 ppb was used for rinsing samples and solution preparation.

2.2.3 Sample and solution preparation

2.2.3.1 Grinding

The first step in sample preparation was manual wet-grinding with SiC papers up to P4000 grit on a LaboPol-5 grinding/polishing machine at 300 rpm (Struers, Ballerup, Denmark). Grinding to a P4000 grit was considered sufficient to ensure appropriate roughness ($R_a \approx 20{-}30$ nm) for applying nanometric ZrCC coatings, as the created roughness is known to be in the nanometric range. After grinding, samples were cleaned by 5-minute ultrasonication in absolute ethanol using a 37 kHz, 100 % power Elmasonic P ultrasonic bath. Finally, samples were rinsed with absolute ethanol and Milli-Q water and dried with compressed N_2.

2.2.3.2 Chemical pretreatment

Glass beakers (V=500 ml) were used for rinsing baths. Chemical pretreatment before conversion was performed via alkaline cleaning and an additional step of desmutting for AA5754 by immersion in respected SurTec® solutions on a C-MAG HS 7 magnetic hotplate stirrer (IKA®-Werke GmbH & Co. KG, Staufen, Germany) under stirring rate of 150 rpm and temperature of 60°C (except for the desmutting step, which was performed at room temperature), according to lab-modified recommendations from SurTec for each substrate:

- For CRS: a 5 min alkaline cleaning in 5 vol.% (50 mL/L) SurTec® 132 + 0.6 vol.% (6 mL/L) SurTec® 089, pH=7.3
- For Zn: a 5 min alkaline cleaning in a mixture of 2 vol.% (20 mL/L) SurTec® 141 + 0.5 vol.% (5 mL/L) SurTec® 089, pH=12.8
- For AA5754: a 10 min alkaline cleaning in 3 vol.% (30 mL/L) SurTec® 132 + 0.5 vol.% (5 mL/L) SurTec® 089, pH=7.4, followed by a 3 min acid desmutting in 20 vol.% (200 mL/L) SurTec® 496, pH=0.3

Each alkaline cleaning/desmutting step was followed by a double rinse with Milli-Q Direct water: (i) ca. 30 s rigorous circular rinse with a wash bottle on both sample sides, and (ii) a 1-minute dip in a clean Milli-Q Direct water bath. Since ZrCCs are extremely sensitive to alkaline

contamination, at least two rinses are required between the cleaner and coating stages [94]. The aim of the chemical pretreatment step was, besides impurity removal, to ensure a hydrophilic surface for successful zirconium conversion [26]. A simple "water-break test", when rinse water evenly coated the entire sample surface after cleaning, was used as an indicator for efficient surface cleaning [71, 95].

2.2.3.3 Conversion treatment

Immediately after the chemical pretreatment, samples (with the entire surface still wet) were immersed in H_2ZrF_6 conversion baths with different combinations of factor settings predetermined by the employed RSM design, as described in the following section. Since zirconia precipitation from H_2ZrF_6 occurs at a rather low pH (3–5) [9, 51], H_2ZrF_6 solutions were prepared by diluting 50 wt.% H_2ZrF_6 solution firstly in a small volume of water and filled up to the final volume, while the pH was set under vigorous stirring using a diluted (15 wt.%) NH_4HCO_3 solution that also serves as a buffer, prolonging the lifetime of prepared baths [71]. pH was measured using a pH meter 827 pH-lab connected to a Solitrode HF combined pH electrode suitable for measurements in HF and F^- containing solutions (Metrohm AG, Herisau, Switzerland). Teflon beakers (V = 250 ml) were used for conversion baths. Samples were immersed in conversion baths and hung onto a plastic stick. Prepared H_2ZrF_6 solutions were stored in polyethylene bottles due to HF release with pH increase [51].

The conversion bath was not stirred, as it was preliminarily observed that stirring with our set-up leads to less uniform coating formation. Consequently, samples were occasionally lightly moved back and forth through the conversion bath to allow fresh solution access to the surface, a practice occasionally observed in industrial settings with manual immersion.

After conversion, samples were dried with the stream of compressed N_2 in the bottom-up direction and dried for 10 min on a C-MAG HP 4 (IKA®-Werke GmbH & Co. KG, Staufen, Germany) hotplate at 80 °C, according to common industrial practice. One series of samples for drop tests and electrochemical measurements on AA5754 and Zn were performed after leaving them to air-dry to assess the influence of drying.

2.2.1 Response surface methodology

After an extensive review of the available literature, we explored a range of H_2ZrF_6 concentrations from 150 to 1500 ppm, pH levels from 3 to 5, and conversion times from 60 to 900 s.

Investigating such a range using a central composite design (CCD) of RSM (Figure A.3) resulted in the variation of all factors at 5 levels: concentration was varied at 150, 424, 825, 1226 and 1500 ppm, pH was varied at 3.0, 3.4, 4.0, 4.6 and 5.0 and conversion time was varied at 60, 230, 480, 730 and 900 s, as presented in Table 2.1. These factor-setting combinations are somewhat counterintuitive from the traditional point of view of planning the experiments, yet these make design models with high predictive power, enabling process insights from fewer measurements. It must be noted that such a wide parameter range, spanning an order of magnitude, is commonly employed in screening experiments. This approach is initially used to identify the most influential factors, followed by a more detailed design for a better understanding and optimisation of the process. However, it is important to consider that if the model successfully explains variability within the chosen parameter range, validated through statistical analysis, regression models, and assessments of goodness of fit, it confirms the suitability of the selected range. Hence, only the centre point (825 ppm/480 s/pH 4.0) was sextuplicated, according to the postulation of RSM.

In contrast to CRS and Zn, where such a broad range model resulted in the assessment of optimal range, in the case of AA5754, the design required two augmentations with additional runs (Table 2.2) in the part of the experimental space indicating optimal performance, namely,

concentration variations at 150, 656 and 825 ppm, pH at 3.4, 4.0 and 4.3 and conversion time at 355, 418 and 480 s thus resulting in a D-optimal design.

Table 2.1: Summary of the initial central composite design applied on CRS, Zn and AA5754.

Factor	A	B	C
Name	pH	t	c
Units		s	ppm
Type	Numeric	Numeric	Numeric
SubType	Continuous	Continuous	Continuous
Min.	3.00	60.00	150.00
Max.	5.00	900.00	1500.00
Coded Low	−1 ↕ 3.41	−1 ↕ 230.27	−1 ↕ 423.64
Coded High	+1 ↕ 4.59	+1 ↕ 729.73	+1 ↕ 1226.36
Mean	4.00	480.00	825.00
Std. Dev.	0.5041	211.73	340.27

Table 2.2: Summary of the central composite design after the second augmentation for AA5754.

Factor	2.5	B	C
Name	pH	t	c
Units		s	ppm
Type	Numeric	Numeric	Numeric
SubType	Continuous	Continuous	Continuous
Min.	3.41	230.27	150.00
Max.	4.59	480.00	825.00
Coded Low	−1 ↕ 4.00	−1 ↕ 230.27	−1 ↕ 150.00
Coded High	+1 ↕ 4.59	+1 ↕ 480.00	+1 ↕ 825.00
Mean	4.08	439.03	693.16
Std. Dev.	0.4582	194.78	377.00

Thus, the main text of this thesis includes only the RSM plots after the last augmentation focused on the concentration region 150–825 ppm, pH 4.0–4.6 and conversion time between

230–480 s. Tabular RSM results, along with all additional information necessary for understanding the execution of RSM in this work, including augmentations for AA5754, ANOVA (analysis of variance) test results, and model adjustments for each RSM response are provided in Appendix A, A.4. A concise theoretical background on DoE and RSM is provided in Appendix A, A.3.

RSM was performed via Design-Expert software version 13 (Stat-ease, Inc., Minneapolis, MN, USA). Corrosion resistances obtained by different non-electrochemical and electrochemical methods were chosen as RSM responses for 3 different metal substrates to compare their sensitivity and feasibility for observing the effects of conversion bath factors. For an easier follow-through, the sample preparation, measurements and important factors considered are given in the form of a flowchart in Figure A.1.

2.2.2 Measurements of corrosion resistance

2.2.2.1 Non-electrochemical measurements

First, a straightforward and non-electrochemical approach known as the drop test was used. The method is based on measuring the time in s needed for the coating to fully dissolve, indicated by a change in colour signifying that the reagent cations reached the bare metal surface, enabling their reduction (Cu or Pb herein). For CRS and AA5754, "Akimov's reagent" [93] was used (82 g/L $CuSO_4 \times 5H_2O$, 33 g/L NaCl, and 13 mL/L of 0.1 N HCl, pH=3.6), while $Pb(CH_3COO)_2$ (50 g/L, pH=5.6) was used for Zn. It was preliminarily shown, the use of Akimov's reagent was too aggressive, leading to the instant dissolution of ZrCC-Zn samples, presumably due to an excessively acidic pH for Zn (*vide infra*). The response obtained from this method is referred to as the "protective ability" (PA). PA measurements were conducted following a 10-minute conversion and drying period at 80 °C for all substrates. Additionally, for AA5754 and Zn, measurements were taken after 24 h of air drying.

2.2.2.2 Electrochemical measurements

Electrochemical experiments were carried out with a Multi Autolab/M204 (Metrohm Autolab, Utrecht, Netherlands) potentiostat/galvanostat controlled by NOVA 2.1. software. Measurements were conducted in homemade modified "clamp-on" electrochemical cells (250 mL), which are suitable for flat, thin-coated samples and less susceptible to crevice corrosion [79]. Respective cell parts were custom-made and assembled by bonding with a strong 1-component solvent adhesive ACRIFIX® 1S 0116 (Evonik Performance Materials GmbH, Darmstadt, Germany). Electrochemical measurements were performed in a three-compartment set-up: the sample as a working electrode (WE) was attached to the bottom by pressing it against an o-ring, which allowed for the easier escape of gas bubbles formed by cathodic reactions, presumably reducing the risk of crevice corrosion. A carbon rod was used as the counter electrode (CE), and a saturated Ag/AgCl (3 M) electrode was used as the reference electrode (RE); E=0.297 V vs. standard hydrogen electrode, set near the WE, to minimize the uncompensated iR drop. All potentials herein are referred to the Ag/AgCl (3 M) scale. The area of the working electrode was 0.785 cm^2. All measurements were performed at ambient conditions.

Before electrochemical measurements, samples were allowed to rest at the OCP and monitored for a conditional time until reaching a quasi-stable state. The rest period was followed by electrochemical impedance and potentiodynamic measurements. This decision was made because there was no risk of electrode alteration due to an excessively high chosen amplitude used in EIS in this particular case. The additional experimental improvement would include separate measurements of cathodic and anodic polarisation curves due to possible changes during the cathodic scan. Due to many experiments, however, PPCs were not measured separately.

To lower the effect of electrolyte aggressiveness inducing corrosion already at the rest potential, the time for OCP measurement was modified for each substrate: for AA5754, samples were left to stabilize for 1 h, while samples of CRS, as they started to corrode already at OCP, were left to approach Kelly's recommendation of quasi-stationary state approximation when 5 mV does not change over a 10 min period, which was in most cases established in 20–30 min [104]. Zn samples, the only ones indicating metastable pitting during OCP, were arbitrarily left to stabilize for 300 s.

Electrochemical impedance spectra (EIS) were recorded at the OCP with a perturbation potential amplitude of ± 10 mV (root mean square). A range of 51 logarithmically spaced frequencies were applied across 7 decades, from 100 kHz to 10 mHz. The EIS data was fitted using the NOVA 2.1 software, which employs a nonlinear least-squares regression approach to fit the experimental data to the equivalent circuit model using the Levenberg-Marquardt optimisation algorithm. The iR drop compensation was not considered, as all samples exhibited an iR drop of less than 1 mV at low frequencies.

Potentiodynamic polarisation curve (PPC) measurements were conducted in the potential region starting from −150 mV vs. OCP to 1 V vs. reference electrode in the anodic direction until the current reached 1 mA or 1 V. The scan rate was 1 mV s^{-1}. Tafel extrapolation method to extract corrosion factors (corrosion potential, E_{corr}, and corrosion current density, j_{corr}) from PPCs was performed using NOVA 2.1 software, from which polarisation resistance, R_p was calculated according to the standard ASTM G59–97 [97].

The electrolyte in the study was a dilute Harrison's solution (3.5 g/L $(NH_4)_2SO_4$ and 0.5 g/L NaCl, pH=5.2) usually used for the simulation of atmospheric conditions and a trade-off between corrosivity of the solution and ability to rank corrosion properties between different ZrCCs.

Different electrochemical responses were used in RSM: For CRS, R_p was determined only from EIS. In the case of AA5754, R_p was evaluated using both EIS and PPC. In the case of Zn, the impedance modulus ($|Z|$) measured with EIS at a frequency of 0.25119 Hz was used along with R_p from PPC (*vide infra*). In addition, for both AA5754 and Zn, the j_{corr} was derived from PPCs. The criteria for selecting optimal preparation conditions were based on maximal R_p or $|Z|$ and minimal j_{corr}.

2.2.2.2.1 EIS experimental details

Making an unambiguous assignment of certain time constants is facilitated by performing EIS measurements under various conditions. These conditions exert different influences on specific time constants, for example, by altering the electrolyte properties (pH, concentration) [98], utilizing time-resolved measurements, modifying the perturbation potential, or repeating measurements at specific perturbation potentials [99, 100]. Additionally, advanced surface analysis techniques are desired to study the exact layer structure. Rather than that, in this work, the power of analysing EIS spectra obtained from a larger set of samples is leveraged to unravel the different time constants. In addition, the selection of EECs was based on prior knowledge of both the substrate and ZrCC behaviour in NaCl-containing solutions, comparing the presence/absence of specific time constants compared to the bare substrates.

After EIS measurements, samples were checked to comply with EIS conditions for stability, causality and linearity by analysing raw AC potential and current data, either through the Kramer-Kroning's test, Lissajous and AC/potential resolution plot [100]. Raw EIS data analysis tools are readily available and, as such, were used in NOVA 2.1. software.

Following Occam's razor principle [100], the proposed equivalent electrical circuits (EECs) for fitting EIS spectra consist of the minimum number of elements required for the physical interpretation of the data. Emphasis was given to obtaining the best predicting and not fitting model that captures major electrochemical processes. Therefore, the proposed models are only tentative but have proved helpful in interpreting the effects of conversion bath factors. The number of time constants relied solely on visual inspection of Nyquist and Bode plots, i.e.,

symmetry in phase angle peaks and capacitive arcs and the analysis of fit residual errors. Periodicity in residual error analysis indicates that not all time constants have been considered [101]. In particular, in the case of AA5754, while the symmetry of phase angle in Bode plots for ZrCC-free samples and the analysis of residual errors suggest the inclusion of additional time constants, likely corresponding to aluminium oxide and charge transfer at the electrolyte/metal interface, we employed a single time constant to fit all EIS spectra of AA5574 incorporated into a simple Randles circuit ([R(RCPE)]). This choice still maintained the significantly improved polarisation resistance values in ZrCC-free samples. Connections of Voigt elements incorporating CPE were used to describe different electrochemical phenomena. CPE instead of C was employed to compensate for the distribution of relaxation times caused by surface inhomogeneities [102].

In all cases involving multiple time constants, a "ladder" R−CPE circuit [102] was utilized ([R([R(RCPE)]CPE)] further justified by the porous nature of the obtained ZrCC and substrate oxides, where both the substrate and coating are exposed to the electrolyte. In the case of a ladder circuit, a resistance is connected in series to a parallel combination of another RCPE couple. A ladder circuit instead of a serial connection of Voigt elements also resulted in lower fit residual errors.

Unfortunately, as a reference shunt has not been used herein [103, 104], the high-frequency inductance (above 10^5 Hz) was affected by the RE impedance, making it difficult to determine small capacitive loop impedances at high frequencies accurately. However, this influence was limited to the high-frequency region and did not affect the mid- and low-frequency regions, which are of greater interest for coating evaluation.

If diffusion or induction effects were observed at low frequencies but within a very narrow range, they were disregarded since they did not dominate corrosion behaviour. Instead, the effects that exhibited a more capacitive behaviour, as determined by the fitted value of n, were used for coating evaluation.

2.2.3 Surface analysis

After grinding up to 4000 grit, samples for SEM imaging were further polished using a 1 µM diamond suspension Dia-Duo 2 on an MD-Nap polishing cloth (Struers, Ballerup, Denmark). Cleaning and conversion steps were performed in Petri dishes in non-stirred solutions due to the smaller sample size than those used for non-electrochemical and electrochemical measurements. Zn and AA5754 samples for SEM were allowed to air-dry for 24 h.

SEM analyses were performed using a field emission SEM JSM 7600 F, JEOL, Japan, equipped with energy dispersive X-ray spectroscopy (Inca Oxford 350 EDS SDD). SEM images were recorded in secondary electron (SE) and back-scattered modes using a concentric backscatter (CBS) detector. Beam voltages of 5 kV and 15 kV were used, the latter owing to its higher penetration depth for AA5754, only to enable detection of intermetallic particles (*vide infra*). Before analysis, samples were coated with a thin carbon layer to reduce the charging effect.

2.3 Results and Discussion

2.3.1 Electrochemical results

The main thesis text contains only discussion-relevant electrochemical results for ZrCC-substrates prepared based on the parameters set by RSM. All the other results are given in Appendix A, A.2.

2.3.1.1 Potentiodynamic polarisation curves

PPCs on CRS on one of the best- (825 ppm/480 s/pH 4.0) and one of the least-performing ZrCC-coated samples (424 ppm/230 s/pH 3.4) along with ZrCC-free samples are presented in Figure 2.1a and Table A.1. PPC curves for ZrCC-free samples (bare and alkaline-cleaned) are similar, with a slight improvement in the latter. Among the ZrCC-coated samples, which show only slightly decreased j_{corr} values compared to ZrCC-free ones, another distinction lies in a slight anodic shift and inconclusive current density values; intriguingly, the sample with poorer performance displays almost the same and slightly improved current density values compared to the supposedly better one. Assuming porosity formation in CRS-ZrCC during electrolyte exposure, these pores might serve as anodic sites, potentially leading to ZrCCs displaying worse PPC results than ZrCC-free samples, as shown in [105]. Essentially, the tiniest defect within such a thin coating suffices to trigger corrosion during the anodic potentiodynamic scan. This is further demonstrated as no significant difference was observed between the two represented ZrCC samples in PPC curves, justifying the decision to forego further PPC analysis on CRS samples.

Concerning Zn (Figure 2.1b–d) and Table A.2, PPCs reveal no consistent alterations in corrosion potential or passivation region. However, there is a marginal reduction in corrosion current densities compared to ZrCC-free samples, although within a similar order of magnitude. As a result, further confirmation through ANOVA is necessary to ascertain statistically significant differences (Appendix A, A.4.2), as will be explained below.

The decision to restrict PPC response in RSM methodology *(vide infra)* solely to Zn substrates while excluding CRS samples was based on observations of a general improvement of ZrCC treatment on the former (Table A.2), as opposed to an anodic shift in E_{corr} values and significant corrosion resulting from the destructive nature of PPC on CRS (Table A.1).

A consistent cathodic shift is generally observed across all AA5754-ZrCC-treated samples (Figure 2.2a-c and Table A.3), except for the sample ZrCC deposited at 480 ppm/60 s/pH 4.0. This shift is accompanied by an extension of the passive region within the ZrCCs, especially for samples 150 ppm/230 s/pH 4.6 and 150 ppm/480 s/pH 4.6, the latter showing a slightly more extended prolongation as compared to ZrCC-free samples. Conversely, for the alkaline-cleaned and alkaline-cleaned and desmutted samples, an anodic shift is noticeable, alongside a reduction in j_{corr}. However, for the alkaline-cleaned and desmutted sample, a pitting onset occurred at a significantly more negative potential compared to the alkaline-cleaned sample. The j_{corr} of ZrCC-treated samples exhibit minimal divergence. Nevertheless, it is worth noting that the samples 825 ppm/480 s/pH 3.0 and 825 ppm/480 s/pH 4.0 stand out, suggesting a potential adverse impact of lower pH and higher concentrations, for the latter, particularly within the middle to higher pH range. Thus, these findings permit the implementation of electrochemical parameters deduced for PPCs as responses for RSM. However, it is necessary to employ ANOVA in RSM to identify significant differences (Appendix A, A.4.3). Based on F-values, which indicate the significance of model terms, obtained after the second augmentation (Appendix A, A.3)), we discerned that the two most significant factors for j_{corr} and R_p from Tafel extrapolation are concentration and the interaction between conversion time and concentration. Notably, higher F-values indicate stronger influences of model terms on the response. Moreover, it is observed that concentration positively impacts j_{corr}, while the interaction between conversion time and concentration has a negative effect on R_p from Tafel extrapolation.

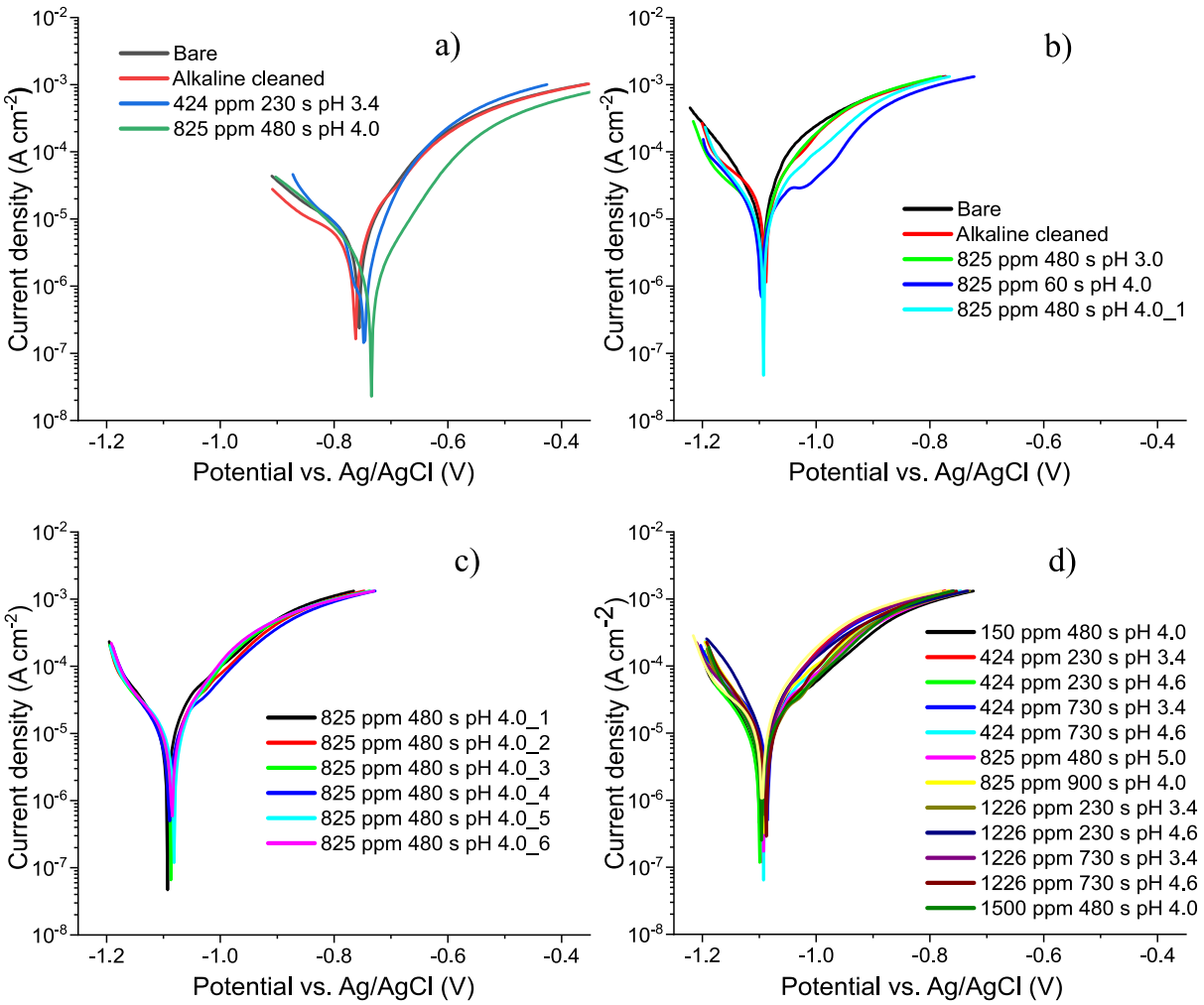

Figure 2.1: Potentiodynamic polarisation curves in dilute Harrison's solution recorded for: (a) CRS, (b-d) Zn; (b) chosen Zn results for discussion, (c) Zn results of central point repetitions, d) results obtained under the remaining conditions. $\mathrm{d}E/\mathrm{d}t = 1$ mVs^{-1}. Rest periods at OCP were (a) 20–30 min, and (b-d) 300 s.

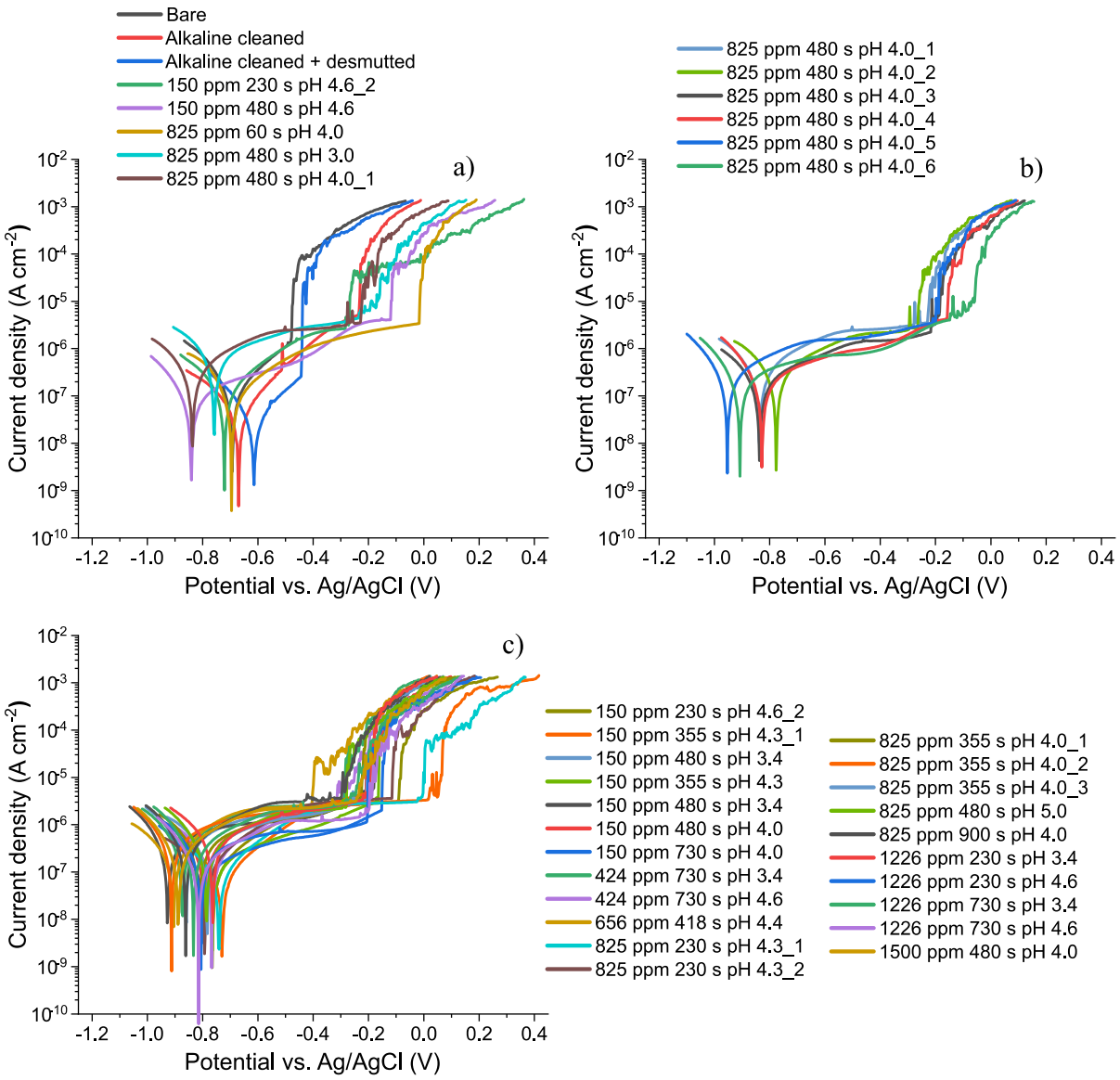

Figure 2.2: Potentiodynamic polarisation curves in dilute Harrison's solution recorded for AA5574: (a) chosen results for discussion, (b) results of central point repetitions, and (c) results obtained under the remaining conditions. $\mathrm{d}E/\mathrm{d}t = 1$ mVs^{-1}. Rest periods at OCP were 1 h.

2.3.1.2 Electrochemical impedance spectroscopy data

CRS samples (Figure 2.3a-c) exhibited either one (Figure 2.3d) or three time constants, which directly correlate with the amount of ZrCC coating present and the formation of iron corrosion products (*vide infra*). By theory, the first time constant is ascribed to the coating, while the second to the corrosion process [99]. However, the porous nature of ZrCC and iron corrosion products implies that EIS spectra can show features related to both geometric and kinetic phenomena [106].

The first unresolved high-frequency time constant (Figure 2.3a-c) with a small capacitive loop (up to 100 Ω, which was not fitted as its value is negligible and due to high-frequency effects induced by reference electrode) can be ascribed either to electrolyte resistance inside pores at the passive film/electrolyte interface, with an interfacial capacitance of the pore wall or to the dielectric properties of the barrier surface film [102]. Thus, for cases displaying three time constants, the EEC, including only two time constants, was used (Figure 2.3e). This is another confirmation of the inadequacy of using PPC for ZrCCs corrosion evaluation on CRS. Most

probably, interconnected pores developed in the coating during exposure to electrolyte result in the shape of the obtained PPC being similar to the bare substrate [107].

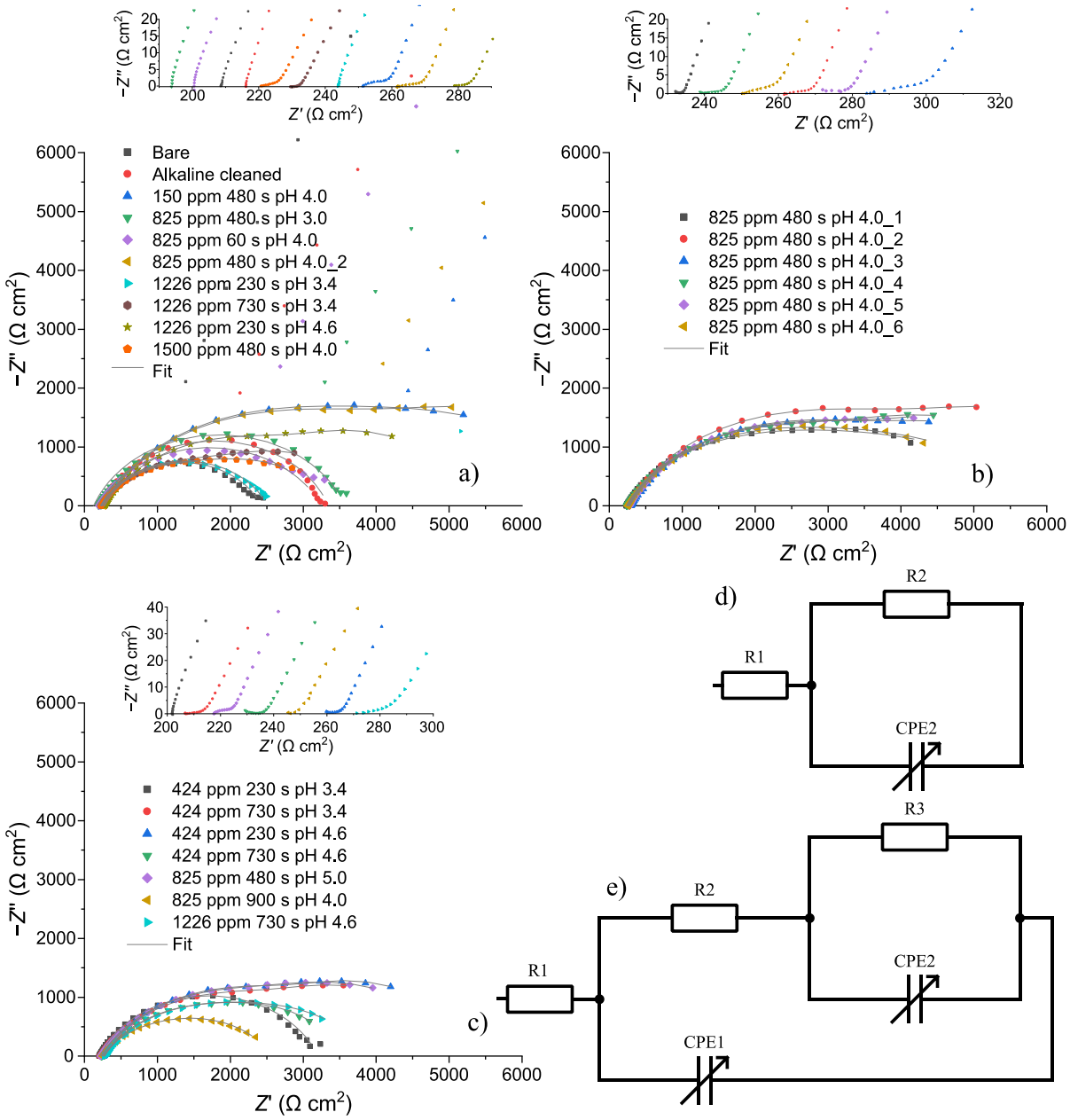

Figure 2.3: EIS results for CRS in dilute Harrison's solution with insets at high frequencies: (a) chosen results for discussion, (b) results of central point repetitions, (c) results obtained under the remaining conditions. EECs used for EIS fitting: (d) Bare CRS, CRS-ZrCC treated at pH $<$ 4.0, with conversion time $>$ 60 s, (e) CRS-ZrCC samples treated at pH $\geq$ 4.0 and conversion time $\geq$ 230 s. Rest periods at OCP were 20 min.

The second, middle-frequency time constant (R2–CPE1) can be ascribed to the charge transfer resistance of faradaic reactions inside defects and CPE 1 to a double layer capacitance, i.e., the capacitance at which those reactions occur [108]. On the other hand, the third time constant in the low-frequency range (R3–CPE2), although not fully resolved due to limited low-frequency measurements, can be linked, based on n values, to capacitive behaviour associated with the capacitive response of corrosion products. The R3 value can be attributed to the relaxation of the corrosion products on the electrode surface [108, 109, 110, 111, 112, 113].

Further confirmation was provided after a 24-h exposure to dilute Harrison's solution, which resulted in a change in only the third time constant. This change was observed as an increase in capacitance and a decrease in R3, attributable to rust layer growth. Notably, no alterations were observed in the other time constants, indicating that the ZrCC remained intact and that the developed rust layer was non-protective, not affecting the charge transfer resistance, as shown in Figure A.2 and Table A.4 in Appendix A, A.2.

FTIR analysis also revealed the formation of lepidocrocite (γ–FeOOH) during exposure to dilute Harrison's solution, as indicated in Figure A.9 in Appendix A, A.6.2, aligned with previous reports of lepidocrocite formation in low-aggressive corrosion environments [114]. Pilling-Bedworth ratio indicates the development of non-protective oxides for iron (and its alloys) due to the larger volume of the oxide compared to its metal elementary cell, leading to rupture and enabling further corrosion through the rust layer [115]. Taking into account all these results and the fact that lepidocrocite exhibits high porosity, a layer of rust can be assumed to grow on top of ZrCC [109, 114].

Nevertheless, all CRS-ZrCC samples that exhibited three time constants show improvement in R_{ct} values, owing to ZrCC (Table A.4). On the other hand, the sample prepared at 825 ppm, 60 s and pH 4.0 and samples prepared at pH < 4.0, except for those prepared at longer conversion time (730 s), all show only one time constant, comparable to ZrCC-free samples, as a result of a merge of other time constants into a single R-value, probably dominated by R_{ct}, as no ZrCC has formed. In addition, all samples treated at pH ≥ 4.0 and 730 s exhibited smaller values of R3, likely due to increased porosity caused by greater thickness (Table A.4). Nevertheless, due to the overlap of time constants and the thin nature of formed films, for the overall evaluation of the CRS-ZrCC system with RSM, the polarisation resistance, R_p, expressed as the sum of the main two resistances obtained by EIS was used [116] (Table A.4). Although sharing the same order of magnitude, R_{ct} can be approximated by R_p measurements from DC methods [116] such as LPR (linear polarisation resistance) [117] or PPC, however, due to the inherent capability of EIS to capture multiple processes and non-destructiveness, the latter is preferred (*vide infra*).

Zn samples exhibited a very small unresolved high-frequency time constant that can be attributed either to a barrier layer of ZnO (arising from alkaline cleaning or etching with H_2ZrF_6) (Figure 2.4a-c and Table A.5), or porosity effects, the latter being more probable, as most samples exhibited a more or less prominent, distorted, high-frequency tail typical for porous electrodes [126], [127]. However, all Zn samples exhibited significant diffusional effects, as shown by a large second time constant in low concentrations and short conversion times, and distorted semicircles in the rest of the cases with n values between 0.1–0.3. This is similar to cases in [128], [129], [130]. Diffusion effects probably arise from the diffusion of species from the bulk or formation of corrosion products. Thus, the width of capacitive arcs in Nyquist spectra can be referred to as diffusion resistance. In the latter case, Lissajous plots and Kramers-Kronig tests indicated that these fluctuations signify instability during measurements. This instability is likely due to inconsistent conversion layer formation, resulting in the accumulation of corrosion products and their related diffusion [122]. Therefore, fitting was not conducted. Instead, an absolute impedance value at a chosen frequency of 0.25119 Hz was employed as a corrosion resistance response (Table A.5). This decision was based on the most significant deviation between high and low diffusion resistances observed at that frequency. Moreover, this frequency aligns with the conclusion of the middle time constant when visual distinction is feasible – likely indicating charge transfer resistance. Afterwards, it was observed that this very frequency also confers more weight to well-performing samples in drop tests and less weight to poorly performing ones. Hence, it can serve as a convenient corrosion evaluation parameter for ZrCCs on Zn, effectively accommodating RSM results and providing a more comprehensive grasp of ZrCC process behaviour.

However, it is important to note that the samples displaying high diffusion resistance during EIS measurements also displayed stability during measurement and passed Lissajous and

Kramers-Kronig test analysis. These samples were indeed eligible for fitting (EEC from Figure 2.3e), indicating a finite length transmissive boundary case modelled by an O-element (open boundary finite length diffusion) [102]. In this case, a fixed diffusion layer with a fixed thickness can be considered as being contained in the solid film, both ZrCC and corrosion products.

However, it has been observed that the O-element cannot efficiently model that behaviour, as n values of CPE are very close but not exactly 0.5 when employing a Voigt element to fit the diffusion constant, suggesting deviation from typical diffusion behaviour.

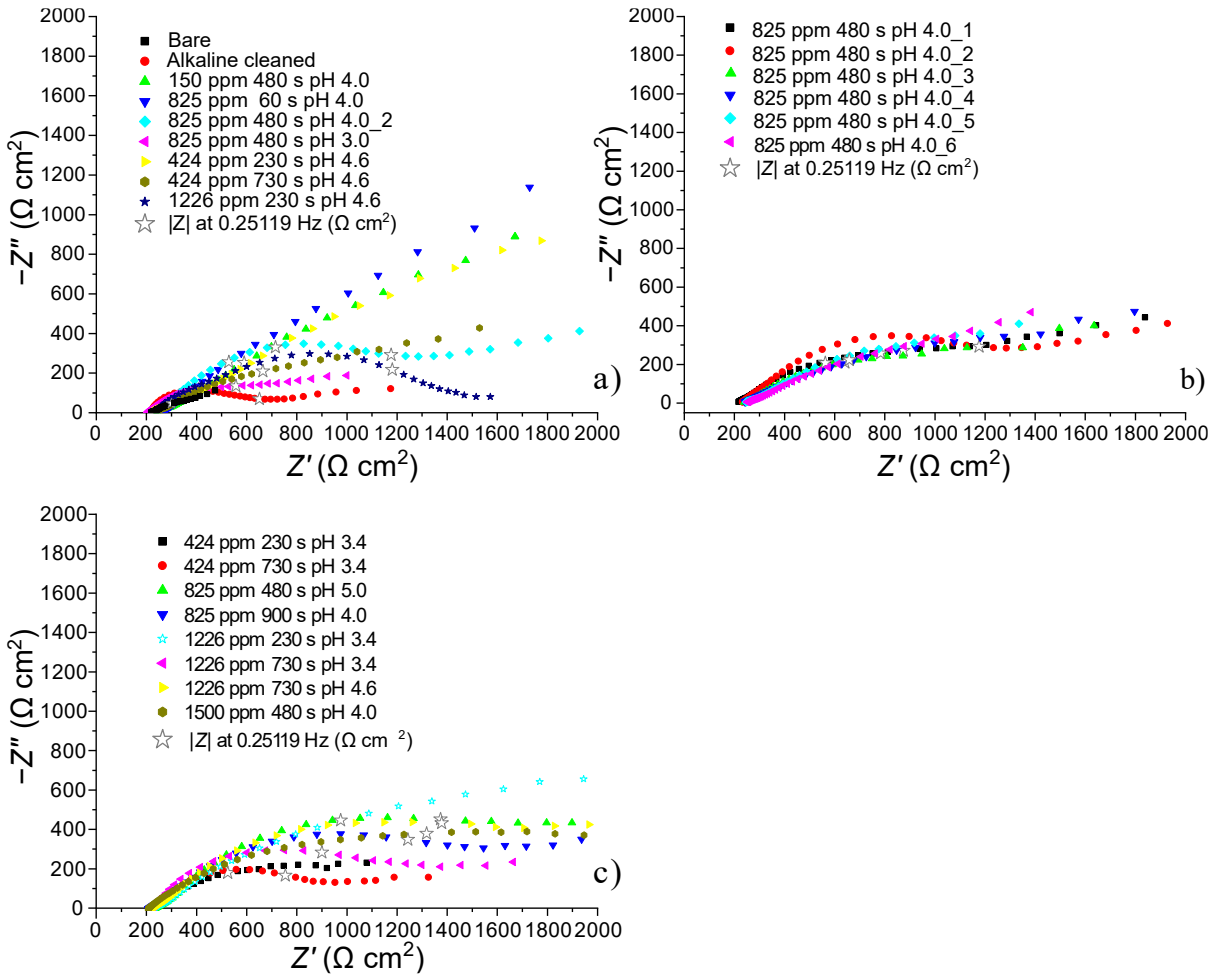

Figure 2.4: EIS results for Zn in dilute Harrison's solution: (a) chosen results for discussion, (b) results of central point repetitions, (c) results obtained under the remaining conditions. Rest periods at OCP were 300 s.

Using an RCPE element to represent diffusional effects is justified because putting a resistor in parallel to capacitance always describes a process involving energy dissipation (resistor) co-occurring with energy storage (capacitor) [100, 102]. As a matter of fact, it has been shown that using RCPE can be more accurate in describing an O-element [123, 124, 125, 126] and has already been employed in conversion coating studies [108, 127]. In that case, R accounts for diffusion resistance, i.e., growth of the diffusion layer, while accompanying admittance of CPE represents diffusion of charge carriers. The increase in diffusion resistance can be attributed to the thickening of the diffusion path, possibly due to forming a more compact corrosion product layer. On the other hand, the increase in admittance values is associated with forming a less dense film, whether it is the ZrCC or Zn corrosion products layer, similar to the EIS investigation on CCCs on Alclad 2024–T3 by Campestrini et al. [108]. This would also explain that the corrosion process has reached a steady state due to reduced corrosion resistance on samples with

lower ZrCC thickness. Finally, in the case of the bare Zn sample (Figure 2.4a), a very high diffusion resistance value is observed, reaching infinity and resembling the behaviour of a pure W-element [100, 102], which is most likely a result of the growth of a thick and porous Zn corrosion products layer (*vide infra*).

It is noteworthy that any deviation from perfect, semi-infinite linear behaviour should result in disturbance of the diffusion process, most likely by more influences at the same time. "Perfect" semi-infinite linear diffusion, i.e., diffusion occurring in one dimension bound by the planar electrode side, can be described by a Warburg element only when the phase angle is 45° in the low-frequency region. In other cases, when a low-frequency tail shows deviation from a 45° angle, a CPE with n different but close to 0.5 is usually employed [102].

The overall EIS data indicate that the corrosion behaviour of Zn-ZrCC is predominantly influenced by diffusion rather than charge transfer. The inherent instability of Zn, observed by fluctuations already during OCP measurements followed by low-frequency fluctuations during EIS measurements, introduces further errors in subsequent PPC measurements, compounded by their destructive nature. Thus, as summarised later in Table 2.3, Zn-ZrCC behaviour, influenced by mass-transport control, is more accurately delineated through EIS than PPC, as Tafel extrapolation is inherently apt for describing activation processes [65]. Additionally, the absence of diffusion control in ORR regions of subsequent PPCs of Zn could imply the diffusion of corrosion products, rather than oxygen or hydrogen, from the bulk electrolyte.

Transmission electron microscopy (TEM) analysis of Šekularac et al. [33], confronted with the barrier layer theory of MacDonald [128], showed a tri-layer (the bottom and middle that cannot be easily distinguished and a distinguished top layer) structure of ZrCC on an AA3003 alloy which preserved overall thickness during a 5-day immersion in 0.5 M NaCl. However, the bottom layer thickened due to the incorporation of substrate and substrate alloying element corrosion products. The top (outer) layer preserved the Zr content by exchanging F^- with Cl^- ions from the solution. However, the middle layer, consisting mainly of ZrO_2, experienced the least alteration. This contrasts CCCs, which contain chromate corrosion products and a porous CCC layer separated from the substrate by a dense barrier layer [128]. Zr in ZrCC does not change its valency state, unlike Cr, meaning that the corrosion products formed only pertain to the underlying substrate.

One time constant is observed in all Nyquist plots for AA5754-ZrCC (Figure 2.5 and Table A.6). However, in all cases, significantly smaller capacitive arcs in the Nyquist plot obtained for ZrCC-coated samples than ZrCC-free samples do not favour the higher corrosion protection offered by ZrCCs, as would be concluded based on PPC results (Figure 2.2 and Table A.3). The reason for this will be explained in the section below on SEM micrographs (Figures 2.14-2.15), which show cracking of remarkably thicker ZrCCs on Al—Fe intermetallic particles (IMPs). According to the results, the best-performing samples are at low concentration (150 ppm), low to middle conversion time (230–480 s) and higher pH (4.6) that approached the corrosion resistance of the bare sample. In addition, corrosion resistivity among ZrCC-free samples follows the sequence alkaline-cleaned + desmutted > alkaline-cleaned > bare.

Owing to the same low-frequency limit applied in measurements (0.01 Hz), the EEC employed herein is similar to one used by Buchheit et al. [129] with only one time constant (R2—CPE1), i.e., inserted EEC from Figure 2.5. It should be noted that the inductive behaviour at low frequencies observed in the Nyquist spectra (Figure 2.5a-c) was without any discernible pattern. Moreover, this inductive behaviour was not associated with pitting, as confirmed by visual analysis. Instead, it appears to be caused by surface roughness, adsorption effects, or ion exchange from the solution [120, 130] (potentially involving Cl^- and F^-, as shown by the XPS study by Šekularac et al. [43]). In this case, R presents a response of defects formed during exposure and CPE interfacial capacitance on which those reactions occur. Presumably, possible contributions of pore impedance and charge transfer resistance are all summed up in the polarisation resistance R_p.

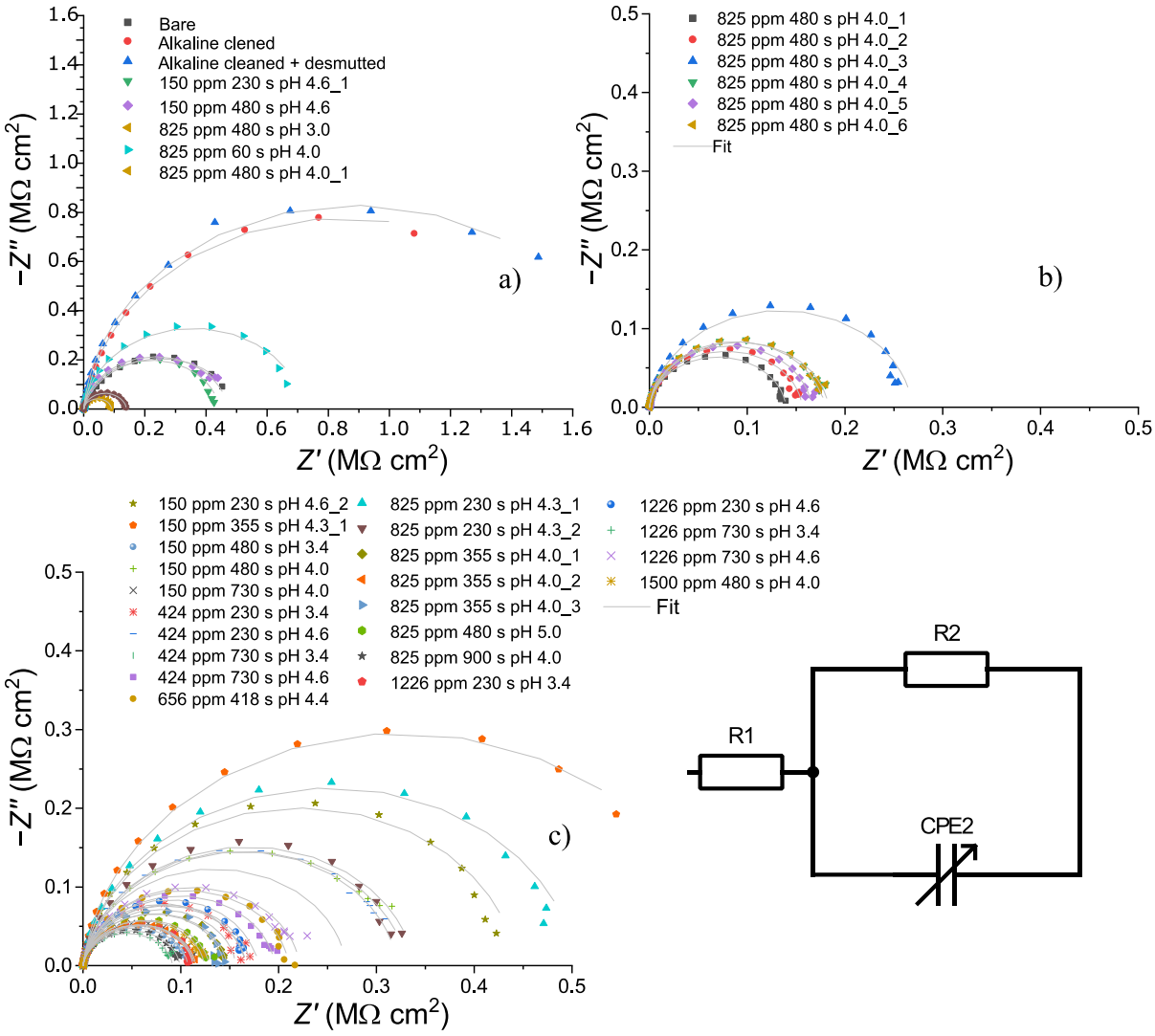

Figure 2.5: EIS results (Nyquist plots) in dilute Harrison's solution for AA5574: (a) chosen results for discussion with inserted EEC used for EIS fitting of all samples (upper left), (b) results of central point repetitions, (c) results obtained under the remaining conditions. Rest periods at OCP were 1 h.

2.3.2 RSM results

Results obtained for thin films are often within the same order of magnitude, i.e., a comparable range of mean values, leading to statistically unreliable data. In such cases, a larger sample size becomes necessary when the effect size is insufficient to achieve statistical significance. By employing a larger sample size, such as in RSM, the power of the statistical test can be increased, making it easier to detect statistically significant differences [36, 37, 67, 131], effectively employed for this specific purpose in this study. Above-design points refer to measured values that exceed the predicted surface, whereas below-design points indicate values falling beneath them, representing a disparity between predicted and actual observations. The extent of results is represented on colour scales above the graphs.

Respected ZrCC results are compared to bare and chemically pretreated samples, both referred to as "ZrCC-free" samples.

To reiterate, the PA of all substrates was assessed after exposure to 80°C and, additionally, after 24 h of air-drying at room temperature on Zn and AA5754. R_p obtained from EIS was used for CRS as the only electrochemical response. In contrast, |Z| at 0. 25119 Hz for Zn and R_p for

AA5754 from EIS, along with j_{corr} and R_p obtained from Tafel extrapolation, were used as responses for Zn and AA5754 after 24 h of air drying (see Table 2.3).

2.3.2.1 RSM for the protective ability

Based on RSM plots in Figure 2.6a,b and Table A.7 for CRS, the optimal performance of ZrCC based on drop test is in the middle to higher concentrations (825–1226 ppm) as well as middle to higher pH values (4.0–4.6), suggesting that the optimum has already been reached in the central point (825 ppm, pH 4.0 and 480 s). A threshold for a good PA value for each substrate was estimated to be higher than the last applied ZrCC pretreatment (*vide infra*).

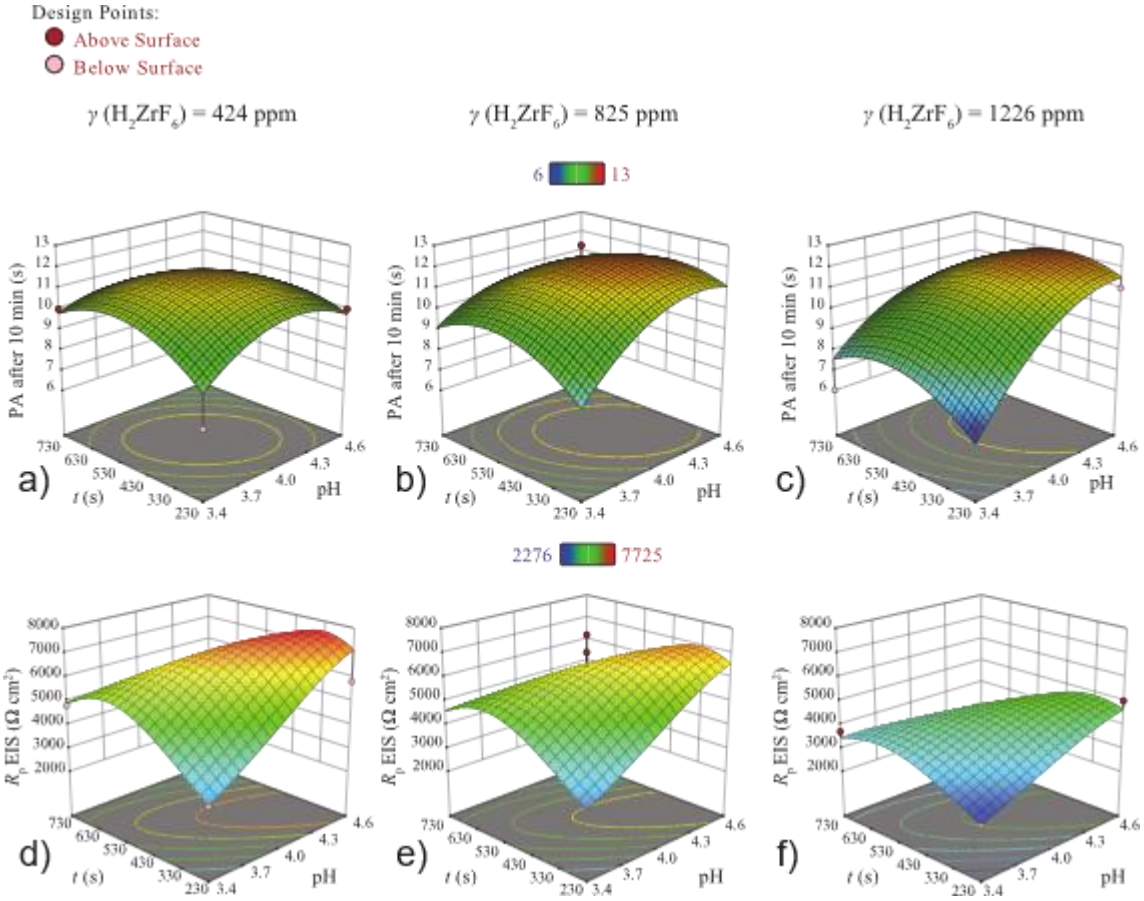

Figure 2.6: RSM plots for CRS for different responses: (a-c) PA after 10 min and (d-f) R_p EIS for concentrations $\gamma(H_2ZrF_6)$ of 424, 825 and 1226 ppm.

Comparing all CRS-ZrCC samples to the ZrCC-free ones, it is evident that the bare sample demonstrates the highest protective ability value (19 s) (Table A.7). In contrast, the alkaline-cleaned sample exhibits a comparable value of 11 s. However, the noteworthy resistance of the bare sample can be attributed to its hydrophobic nature (deduced only visually by the water droplet shape), which is significantly diminished following alkaline cleaning, subsequently facilitating the deposition of ZrCC (Table A.7). Furthermore, the alkaline-cleaned sample shows values comparable to those of ZrCC-treated samples due to higher hydrophilicity in both cases, which is presumably undesirable for corrosion resistance. However, this property is counterbalanced in ZrCCs to enhance the adhesion of subsequent organic coatings (*vide infra, Chapter 5*). In contrast to other samples (*vide infra*) the observed colour variations in the formed coatings on CRS (ranging from gold to purple with an increase in conversion time, indicating increased thickness) and the resulting hue of red during copper reduction additionally hint at

the existence of certain corrosion protection benefits offered by ZrCC-treated samples. This becomes especially apparent when considering cases where the hue of the drop colour appeared more pink than red on well-performing ZrCC samples, in contrast to the reddish hue observed in poorly performing and ZrCC-free samples. However, both the ZrCC colour and the drop colour were not chosen as RSM responses because they involve categorical factors necessitating a higher number of descriptors, which, unfortunately, remains unaddressed here, given the limited range of possibilities (pink or red, purple or gold). Due to the nature of this method, the exact determination of the point at which the colour changes may be relatively subjective and would, among other requirements, necessitate the test to be run by several persons independently.

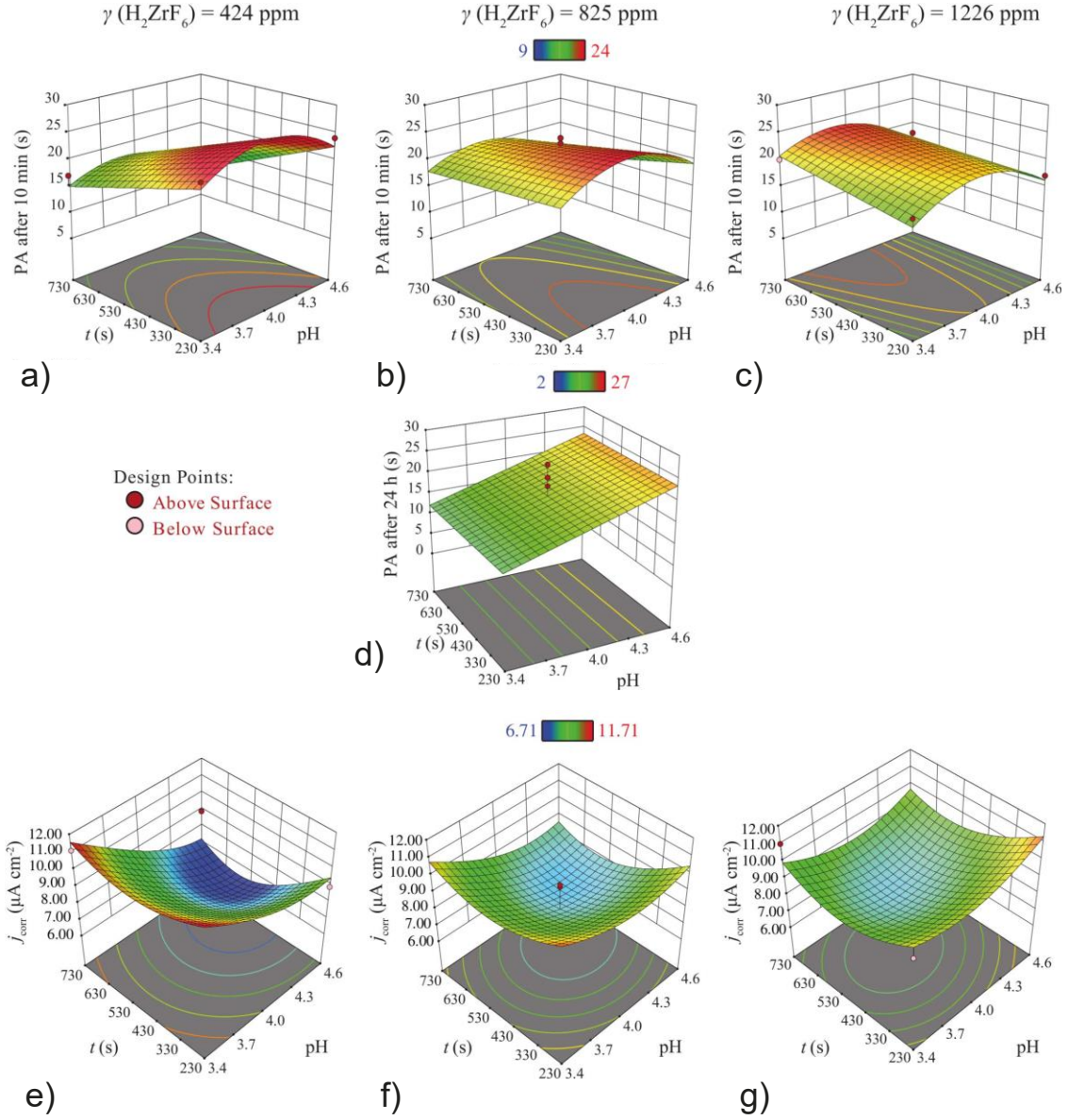

Figure 2.7: RSM plots for Zn for different responses: (a-c) PA after 10 min, (d) PA after 24 h and (e-g) j_{corr} from PPCs.

The RSM plots for Zn, with optimal conditions for PA after 10 min of curing at 80 ºC, show an intriguing trend (Figure 2.7a-c and Table A.8). Optimum moves from lower concentrations and lower conversion times toward higher concentrations and higher conversion times with a slight curvature at the middle pH value (4.0). However, this response plot resolves after 24 h (Figure

2.7d), although guiding the experimental space only to higher pH values for the concentration of 825 ppm. This is a direct result of a considerable decrease in PA for samples with pH < 4.0, in contrast to the improvement seen in samples with a pH 4.0, most probably due to the formation of ZnO filling in the pores.

Furthermore, the growth of native (hydro)oxide within presumed pores developed in ZrCCs during electrolyte exposure could enhance the overall corrosion resistance of ZrCCs. This approach is supported by the long-established Pilling-Bedworth ratio [115], which indicates the development of protective oxides for zinc but not for iron. In fact, leaving ZrCCs on CRS in the air leads to rusting [132], while a significant improvement of ZrCCs has been observed before on aluminium alloy substrates and Zn, either by allowing for native (hydro)oxides development on air or by leaving in the electrolyte for 24 h [33, 34, 133, 134].

In other words, some samples that initially seemed to exhibit better corrosion protection failed after 24 h (compare Table A.8 and Figure 2.7a-c with Figure 2.7d), emphasising the importance of assessing the conversion coating as a mixture of ZrCC and native (hydro)oxide and another confirmation of the hypothesis of taking into account the Pilling-Bedworth ratio when considering native (hydro)oxide growth inside thin films on different substrates. While appearing essential to boost the corrosion resistance of the primer, it is noteworthy that the resulting oxide film might exhibit distinct adhesion properties from the primer [143]. As drop test results of ZrCC-free samples for Zn did not show any protective ability, as indicated by 0 s in Table A.8 after 10 min (*vide infra*).

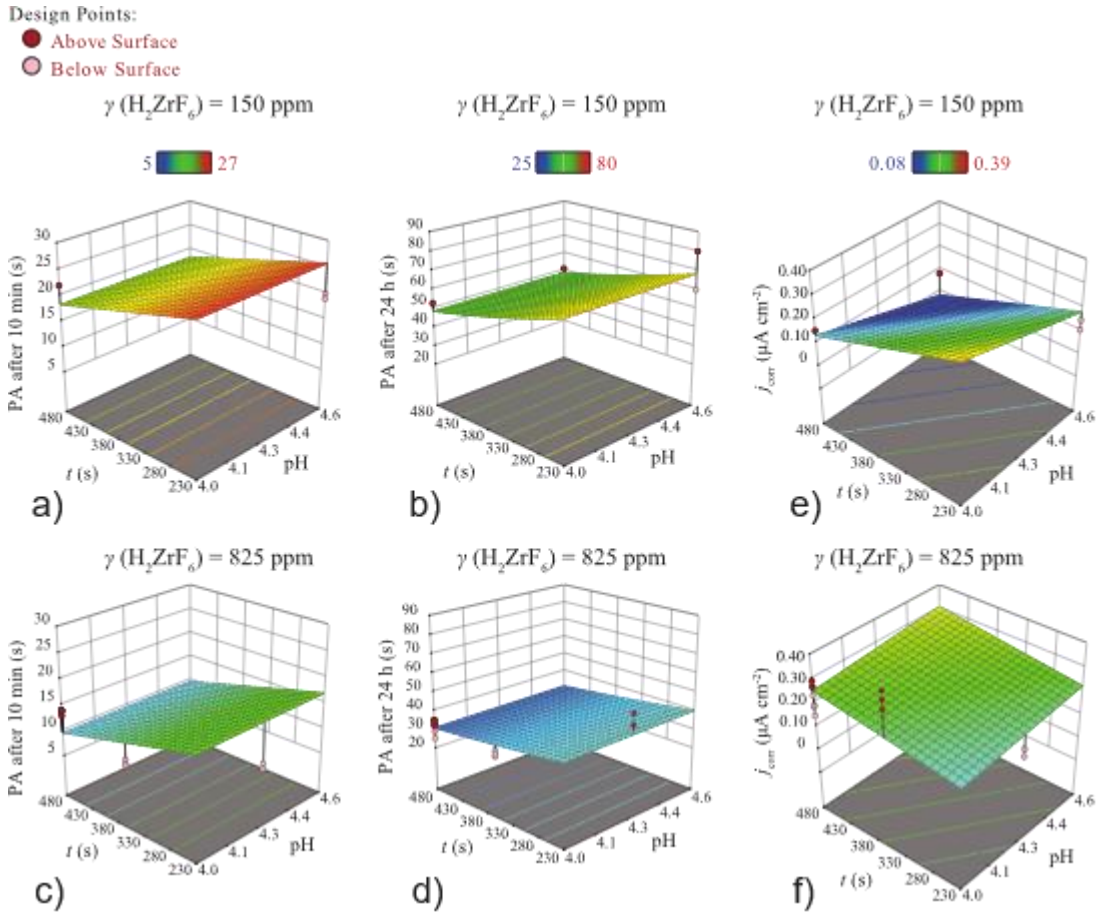

Figure 2.8: RSM plots for AA5754 (after the second augmentation) for different responses: (a,c) PA after 10 min, (b,d) PA after 24 h and (e-f) j_{corr} from PPCs.

From Figure 2.8a–d and Table A.9, it can be observed that PA values for AA5754 are higher at lower concentrations of 150 ppm than at 825 ppm. Moreover, there is a marked enhancement after 24 h (Figure 2.8b,d) for all samples, although with reduced predictive variability at higher concentrations compared to the 10-minute timeframe (Figure 2.8a,c). This phenomenon is likely due to the development of a more densely packed film formed upon exposure to air, potentially involving the growth of a native alumina film within the pores. Drop test results of ZrCC-free samples also follow that trend, with alkaline-cleaned + desmutted sample showing the highest PA value (52 s), as shown in Table A.9.

However, pH does not emerge as an influential factor in determining PA within both timeframes, evidenced by a lack of curvature. Moreover, while the RSM plots do not attain an optimal point, they serve as valuable guides for narrowing the experimental space down to lower concentrations and shorter conversion times.

In summary, for CRS, optimal PA values are near the central point of middle to higher concentrations, conversion time and pH. AA5754 shows better results with prolonged drying at lower concentrations and shorter conversion times, with pH not a significant influencing factor. For Zn, PA after 24 h only serves as a more consistent factor for exploring the experimental space toward higher pH values, at the very least.

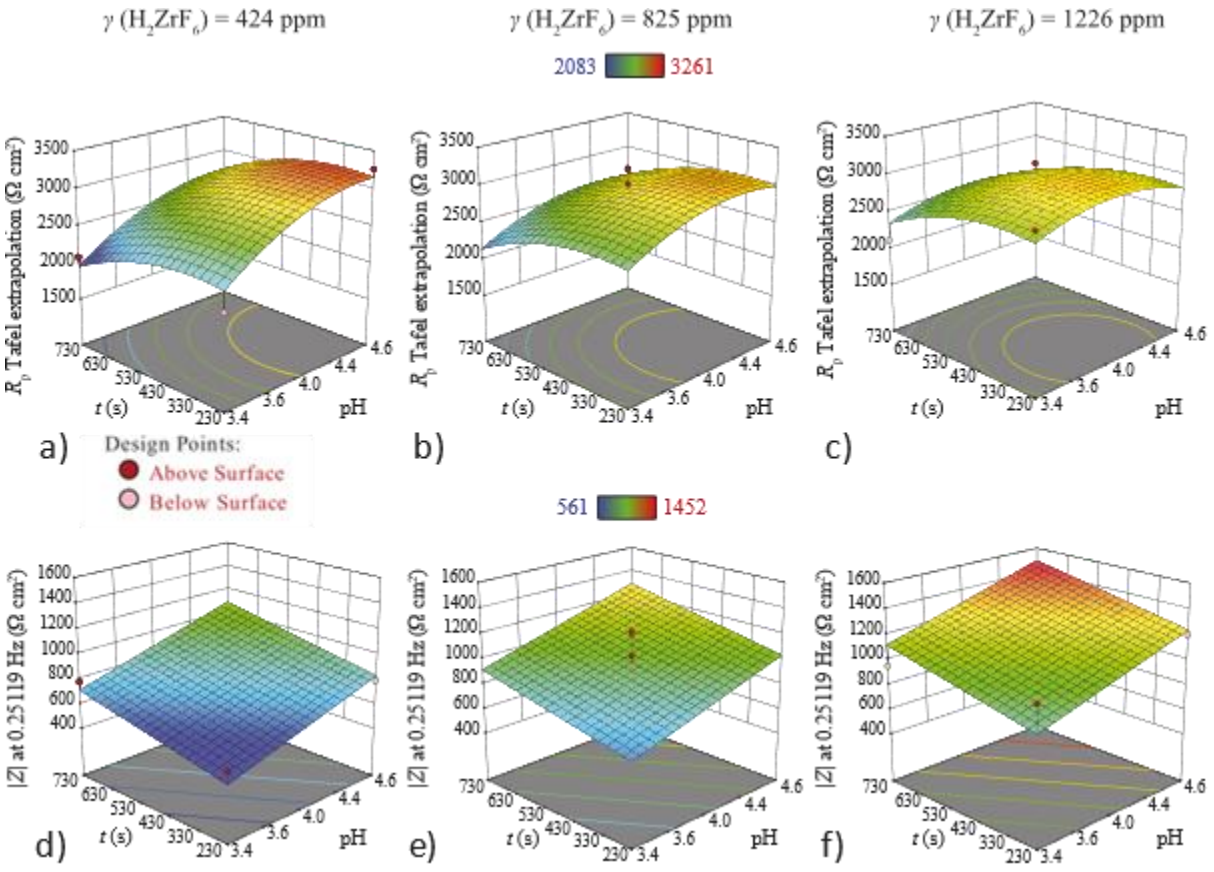

Figure 2.9: RSM plots for Zn for different responses: (a-c) R_p Tafel and (d-f) $|Z|$ at 0.25119 Hz for concentrations $\gamma(H_2ZrF_6)$ of 424, 825 and 1226 ppm.

2.3.2.2 RSM for corrosion current density

From Figure 2.7e–g and Table A.8, the lowest value for Zn is obtained at lower concentrations (424 ppm), middle conversion times, and higher pH levels (4.6). However, this minimum value increases as the concentration rises towards lower pH values, resulting in a somewhat

inconclusive trend. A higher variability between the experimental and predicted values also accompanies this observation.

These results imply that j_{corr} might not be the most appropriate parameter for evaluating Zn-ZrCC performance, even though it accurately presents the obtained data.
The RSM plots for AA5754 (Figure 2.8e,f and Table A.9) indicate that the minimum j_{corr} corresponds to lower concentrations (150 ppm), middle to higher conversion times, and elevated pH levels (4.6). However, this minimum shifts towards shorter conversion times and a middle pH range at higher concentrations (825 ppm), accompanied by a significant discrepancy between predicted and measured data. These results imply that j_{corr} might not be the most appropriate parameter for evaluating ZrCC performance, even though it accurately presents the obtained data.

2.3.2.3 RSM for polarisation resistance from Tafel extrapolation

In RSM plots for Zn (Figure 2.9e–g and Table A.8), the predicted optimum for R_p is at lower concentrations (424 ppm) coupled with higher pH (4.6) and shorter conversion times (230 s). There is a noticeable decline in the response with an increase in concentration (825 ppm), yet the trend concerning pH and conversion time is maintained, distinguishing it slightly from the results obtained for j_{corr}.

In Figure 2.10a,b and Table A.9, the optimum for R_p obtained through Tafel extrapolation of PPCs on AA5754 is predicted at higher pH levels (4.3–4.6), with a low concentration (150 ppm) and a conversion time (480 s). This starkly contrasts with higher concentrations (825 ppm), where a marginal increase in R_p is observed at shorter conversion times (230 s) and lower pH values (4.0).

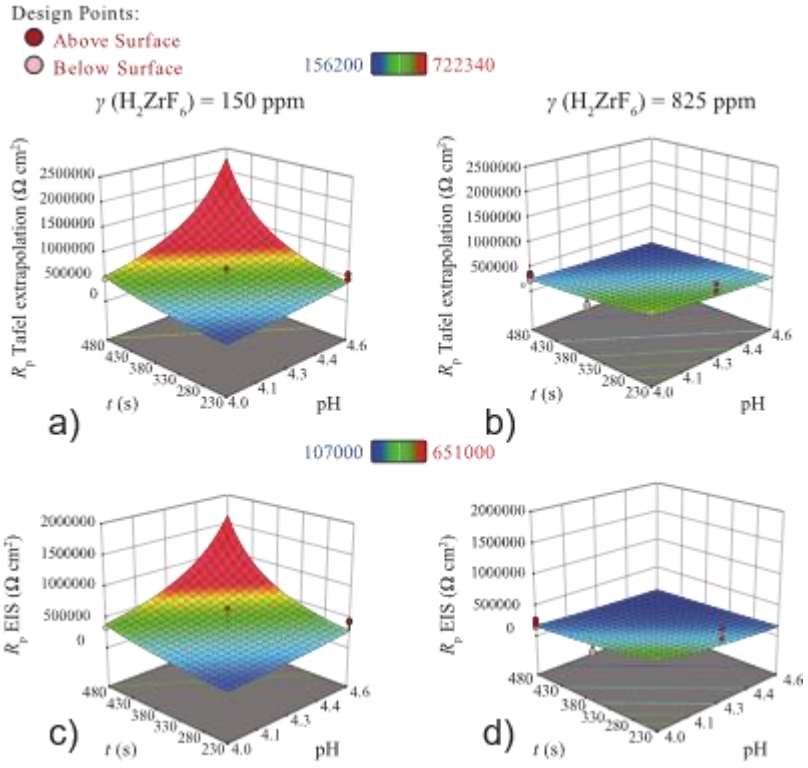

Figure 2.10: RSM plots for AA5754 (after the second augmentation) for different responses: (a-b) R_p Tafel and (c-d) R_p EIS for concentrations $\gamma(H_2ZrF_6)$ of 150 and 825 ppm.

2.3.2.4 RSM for EIS results

RSM plots for R_p on CRS (Figure 2.6d–f and Table A.7) suggest a trend towards lower concentrations and higher pH levels, even though the measured values in that range were not as high as at the central point, i.e., 825 ppm/480 s/pH 4.0 (Table A.7). However, it can be inferred that the optimum has already been reached at the central point after accounting for the impact of its variability estimated from ANOVA and shown by the contrast between predicted and repeated measured central points. EIS seems to exhibit a higher sensitivity to the concentration effect than the drop test and, in fact, to all other factors and their interactions. This is evidenced by the accompanying F-values for specific model terms in Appendix A, A.4.1.

In the context of Zn (Figure 2.9d–f and Table A.8), the derived RSM surface expressed as $|Z|$ at 0.25119 Hz diverges from its previously discussed responses, indicating an optimum at higher concentrations (1226 ppm), longer conversion times (730 s), pH (4.6), suggesting its sensitivity to reflect ZrCC resistance as increased thickness due to the effect of longer conversion time.

The obtained RSM surface for R_p from EIS (Figure 2.10c,d and Table A.9) for AA5754 closely resembles the R_p from Tafel extrapolation (Figure 2.10a,b), indicating a strong correlation. Specifically, the optimum conditions are once again projected at higher pH levels (4.3–4.6), accompanied by a low concentration (150 ppm) and a medium conversion time (480 s).

2.3.2.5 Comments on the overall feasibility of RSM models

The statistical analysis of RSM models, as detailed in Appendix A, A.4, suggests that all models are capable of navigating the experimental space for characterisation, evidenced by the adequate precision values that measure the signal-to-noise ratio. This indicates that the obtained 3D plots can indeed highlight paths toward optimal regions, as described in previous sections. However, not all models are equally suited for both characterisation and optimisation (Table 2.3), the latter being marked by satisfying the difference between the predicted and adjusted R^2 values (refer to Appendix A, A.3 for more RSM terminological explanations). This explains why different optimal regions are obtained for different corrosion resistance responses on the same substrate (Table 2.4). Specifically, for CRS, the PA after 10 min model seems suitable for characterisation, whereas the R_p from the EIS model is effective for both characterisation and optimisation. In the case of Zn, considering both adequate precision and the difference between the adjusted and predicted R^2, the PA after 10 min and R_p from Tafel extrapolation models are the least suitable for characterisation and entirely unsuitable for optimisation. In contrast, the j_{corr} model is more apt for characterisation.

However, the PA after 24 h and $|Z|$ at 0.25119 Hz models are effective for both characterisation and optimisation, making the optimal regions thus identified more convenient than those of Tafel extrapolation responses. Nonetheless, R_p from EIS is superior in identifying more significant factors, thereby making it the best overall response for evaluation. Lastly, for AA5754, the PA after 10 min can be used for both optimisation and characterisation; however, it makes less physical sense compared to using the PA after 24 h, which is more convenient for characterisation. The j_{corr} model is the least suitable, while the R_p from Tafel extrapolation is better for characterisation. Once again, R_p from EIS is the most suitable for both characterisation and potential optimisation, as it shows the lowest discrepancy in criteria for the difference between predicted and adjusted R^2 compared to other electrochemical responses. The fact that the feasibility of certain responses varies with the substrate complicates the optimisation. Nevertheless, EIS arises as a mutual evaluation technique suitable for both characterisation and optimisation of all substrates and care must be taken in choosing the type of resistance as a response, as it differs between the substrates.

Table 2.3: Comparison of the feasibility of each technique and its responses for evaluating ZrCCs based on RSM model analysis.

Technique		Protective ability		Potentiodynamic polarisation curves		Electrochemical impedance spectroscopy
CRS	**Response**	PA after drying at 80 °C	PA after air-drying for 24 h	not considered		R_p
	Applicability	characterisation	not considered			characterisation, optimisation
Zn	**Response**	PA after drying at 80 °C	PA after air-drying for 24 h	j_{corr}	R_p	$\|Z\|$ at 0.25119 Hz
	Applicability	/	characterisation, optimisation	/	characterisati-on	characterisation, optimisation
AA5754	**Response**	PA after drying at 80 °C	PA after air-drying for 24 h	j_{corr}	R_p	$\|Z\|$ at 0.25119 Hz
	Applicability	characterisation and optimisation	characterisation (and optimisation)	/	characterisation	characterisation, optimisation

2.3.3 Surface analysis by SEM/EDS

After building an empirical model from RSM and estimating the main and possible interaction effects of particular factors, the most research-compelling samples were subjected to SEM analysis to argue particular RSM response results.

For discussional purposes, only Zr, O, and Fe contents obtained by EDS were found relevant. The atomic percentages of these elements are provided alongside the locations where EDS spectra were acquired on SEM micrographs in Figure 2.11-2.15. Complete EDS analyses can be found in Appendix A, A.5 (Figure A.6-A. 8). The coating density has a large impact on electron penetration depth. In a practical setting, the density may be notably reduced, leading to a faster arrival of the beam at the substrate, which impedes quantitative determination of light-weight elements, such as O. Our Monte Carlo simulations reveal that on the AA5754 matrix, Zn and CRS, the penetration depth is 60 nm at 3 kV, 230 nm at 5 kV, and 1560 nm at 15 kV, assuming a model thickness of 20 nm. Additionally, for AA5754 IMPs, the penetration depth is 70 nm at 3 kV, 130 nm at 5 kV, and 950 nm at 15 kV, using a model thickness of 1000 nm.

Given that the penetration depth presumably exceeds the coating thickness (typically ranging from 10 to 70 nm on all substrates, excluding IMPs [9]) for AA5754 IMPs, 15 kV is sufficient to detect the IMP. However, it is likely inadequate to grasp its thickness fully under various ZrCC factor settings. Furthermore, considering peak overlapping, especially that of F and Fe [135], assessing the quantitative impact of concentration and conversion time on ZrCC thickness is unreliable [136, 137]. Nevertheless, both thickness and coating density can be indirectly inferred. To achieve an accurate evaluation of F content, advanced techniques such as wavelength dispersive X-ray analysis (WDX) with superior energy resolution are necessary to prevent common peak overlap errors encountered in EDS analysis. Consequently, the enclosed EDS micrographs are only semi-quantitative [136, 137].

2.3.3.1 Cold-rolled steel

From Figure 2.11, it follows that a clean bare surface exhibits a nanometric-sized fine structure [32], which is presumably just grinding residues, as indicated by the same Fe and O content

throughout the whole surface. Alkaline cleaning (pH=7.4) changes the surface morphology in the form of nanometric lamellar and nodular structures, also composed of the substrate (Fe). However, FeO formation may occur [138] during alkaline cleaning based on the increased O content. Commenting on O content is uncertain for the reasons mentioned above. However, it can be used for comparative purposes in cases where the difference exceeds an order of magnitude (*vide infra*).

Figure 2.11 also shows that all ZrCCs on CRS uniformly follow the topography of the underlying substrate, exhibiting nodular morphology [148]. Uniform coating formation can be ascribed to uniform corrosion [136], where the location of anodic and cathodic sites changes continuously due to small changes in surface reactivity as the corrosion process proceeds.

The sample prepared at the shortest conversion time, 825 ppm/60 s/pH 4.0, shows low Zr content and morphology similar to the underlying morphology caused by alkaline cleaning. However, extending the conversion time from 60 to 480 s leads to an increase in Zr content along with a Fe content decrease, indicating an increase in coating thickness.

On the other hand, the effect of pH is stricter. The sample subjected to the lowest pH (3.0) exhibits almost no Zr (at least not detectable by EDS) and significantly decreased O content at the bulk of the coating (site #1) with only rarely distributed zirconia particles (site #2) over the surface and surface morphology similar to the underlying substrate, i.e., alkaline-cleaned sample. However, moving pH to slightly less acidic (3.4) and a slightly higher concentration (1226 ppm) (and accordingly shorter conversion time of 230 s) reveals at least some coating formation over the whole surface, although with a very low Zr content and the overall morphology similar to the alkaline-cleaned surface (Figure A.6).

This can be explained by a much higher corrosion rate of iron and steel at $pH < 4.0$ caused by a greater effect of hydrogen evolution reaction (HER) accompanying oxygen reduction reaction (ORR), as well as the fact that ferrous oxide, FeO (that should otherwise form and remain stable during alkaline cleaning), is soluble at $pH < 4.0$.

The above-described observations of insufficient coating formation are confirmed through EIS spectra, as only one time constant is observed with the shape and width of the capacitive loop, similar to ZrCC-free samples (Figure 2.3a). However, with such a concentration setting, an HF loop appears in EIS spectra only at extended conversion times (730 s), indicating the thickening of the ZrCC layer. From this, it can be inferred that $pH < 4.0$ generally leads to an insufficient coating formation, which can only be compensated with a combination of higher concentration (1226 ppm) and longer conversion time (730 s). On the other hand, samples prepared at $pH \geq 4.0$ exhibit sufficient coating formation, as indicated by three time constants (*vide supra*). Hence, the high-frequency time constant can indeed function as an indicator of adequate ZrCC formation.

The beam depth does not allow for differentiation between Zr content when performing conversion at different H_2ZrF_6 concentrations at the same pH and time setting ($pH > 4.0$).

Still, the samples 150 ppm/480 s/pH 4.0 and 825 ppm/480 s/pH 4.0 exhibit similar Zr contents, but the obtained topography for the former is similar to the underlying substrate, whereas a thicker layer is formed for the latter, i.e., at higher concentrations. Similarly, although not reflected in higher Zr content, the sample prepared at the highest concentration, 1500 ppm, shows higher Zr nodule density, suggesting higher thickness/compactness. Based on RSM plots (Figure 2.6), however, it seems that after immersion into the electrolyte, thicker ZrCC coatings are more prone to delamination, giving the optimal value at the centre of chosen experimental space, i.e., 825 ppm/480 s/pH 4.0 towards higher concentrations (1226 ppm) and pH (4.6). Overall, this supports the previous study on CRS, where the coating formations were promoted at pH 4.0 due to establishing a dynamic equilibrium between dissolution and precipitation [140].

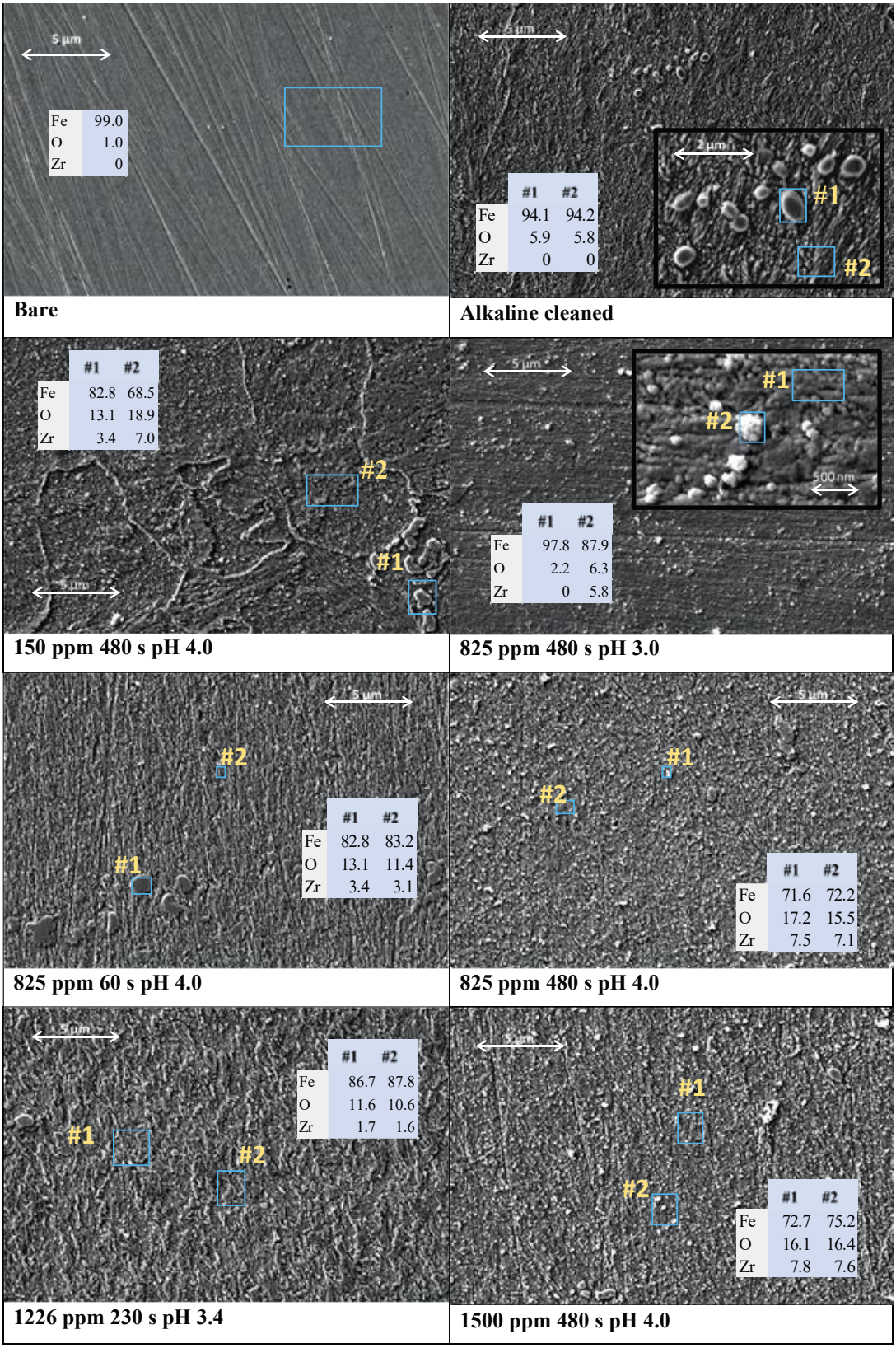

Figure 2.11: SEM micrographs of bare and alkaline-cleaned CRS samples and CRS samples subjected to various ZrCC treatments. The sites of EDS analyses are noted by blue rectangles, and the results for Fe, O and Zr are given in tables. All EDS results are given in Appendix A, A.5, Figure A.6.

2.3.3.2 Zinc

The bare Zn surface also shows a few grinding residues, confirmed through EDS analysis, having almost the same Zn content throughout the surface (Figure 2.12. After alkaline cleaning, the surface is covered with nodular ZnO. This is confirmed by higher concentrations of Zn and O at the nodular locations, as well as the presence of darker circles observed when using the CBS detector mode, all of which align with the expected results for the given pH (12.5), Figure A.7.

All Zn-ZrCC samples underwent morphological changes resembling chipping to varying extents due to acid etching. These changes are otherwise highly dependent on the solution composition and are particularly noteworthy in the design of Zn anodes [141].

Like CRS, ZrCCs on Zn exhibit nodular morphology, with the population of nodules, in general, increasing with an increase in either conversion time and H_2ZrF_6 concentration. In the case of Zn, the effect of low pH was the most prominent, where pH < 4.0 leads to excessive etching of the surface (Figure 2.13), revealing bare Zn regions and highly nodular ZnO regions. This is due to cathodic control of HER leading to significantly higher corrosion rates on Zn at pH < 4.0. In mildly acidic solutions, which accounts for pH 4.0, due to lower concentration of H^+, the influence of otherwise a large overpotential of HER on Zn prevails and shifts cathodic control to ORR, which, due to a fixed oxygen concentration, leads to almost constant corrosion throughout a wide subsequent pH range [142]. However, it should be noted that the conversion process appears to be influenced not only by pH but also by the conversion agent; for instance, molybdate conversion coatings exhibit faster deposition at pH 3.0 [143]. Interestingly, while the sample 825 ppm/480 s/pH 3.0 was only etched without any detectable ZrCC formation, the sample 1226 ppm/230 s/pH 3.4, although extensively etched, still did form a thin ZrCC layer, as indicated by low Zr content (Figure 2.13). This is probably a compromise of slightly lower corrosion rates at a slightly less acidic pH of 3.4, compared to 3.0, enabling ZrCC deposition to occur, although in a very small amount. Only conversion at pH ≥ 4.0 led to uniformly coated surfaces (Figure 2.13).

Furthermore, based on RSM results for PA (Figure 2.7 and Table A.8), Zn samples treated at pH < 4.0 showed PA within 10 minutes, which decreased after 24 hours, while ZrCC-free Zn samples showed PA only after 24 hours. Combining with EIS and SEM results, this may suggest that an etched surface rich in ZnO with higher geometry and possible hydrophobicity, along with some ZrCC formation, leads to PA in ZrCC-treated samples. However, this effect resolves after 24 hours as acidic environment within pores from the ZrCC process deteriorate the surface, leading to lower PA values compared to ZrCC-free Zn samples.

A higher pH and higher concentrations generally led to a thicker coating, as evidenced by higher Zr content. In addition, higher concentrations led to more ZrCC nodules on the surface (Figure 2.13). However, the shape of low-frequency arcs ascribed to diffusional processes in the case of Zn shows consistent trends that can be useful for Zn-ZrCC evaluation when exposed to a dilute Harrison's solution.

Bare Zn and samples having thinner ZrCCs had very large low-frequency arcs and consequently, large diffusion resistances, R_d, as a result of longer diffusion paths (Figure 2.4a-c). On the other hand, alkaline-cleaned and samples having higher ZrCC thickness, along with etched samples treated at pH < 4.0, exhibited lower low-frequency arcs due to shorter diffusion paths. This points to the fact that thicker ZrCC coatings resulted in the formation of fewer Zn corrosion products and vice versa. In addition, Zn corrosion products on bare Zn are denser and thicker than the alkaline-cleaned sample that already had a thin and homogeneous layer of ZnO on it (compare Figure 2.12 and Figure 2.13). In contrast, samples deposited at pH < 4.0 had a highly accessible surface roughened by highly porous, inhomogeneously distributed nodular ZnO. This also enabled faster diffusion, reflected in lower R_d and R_{ct} values than Zn-ZrCC samples at pH ≥ 4.0.

It can be inferred that, in general, Zn-ZrCCs at pH ≥ 4.0, at both conversion times ≥ 230 s and concentrations ≥ 825 ppm, have higher coating thickness compared to those treated at lower

settings of those factors. Thus, the width of the low-frequency arc associated with diffusion can indicate the degree of formation of Zn corrosion products, which is inversely proportional to ZrCC thickness. This implies a greater long-term predictive capacity for EIS, recognizing the influence of prolonged conversion time on thickness increase, resulting in improved corrosion resistance. This is in contrast to R_p derived from Tafel extrapolation (Figure 2.9), which places more emphasis on lower concentrations and shorter conversion times (*vide supra*) and was indeed found unsuitable according to RSM models (Appendix A, A.4.2). However, it is noteworthy that all samples treated at pH 4.0 and concentration exhibit similar values in $|Z|$, supporting the effect of ZrCC thickness on its corrosion resistance. However, it remains unresolved why the sample at 1124 ppm/230 s/pH 4.6 seemingly exhibits the least diffusion control, suggesting the most resistive ZrCC film, which may not necessarily be related to thickness but possibly to compactness (*vide infra*).

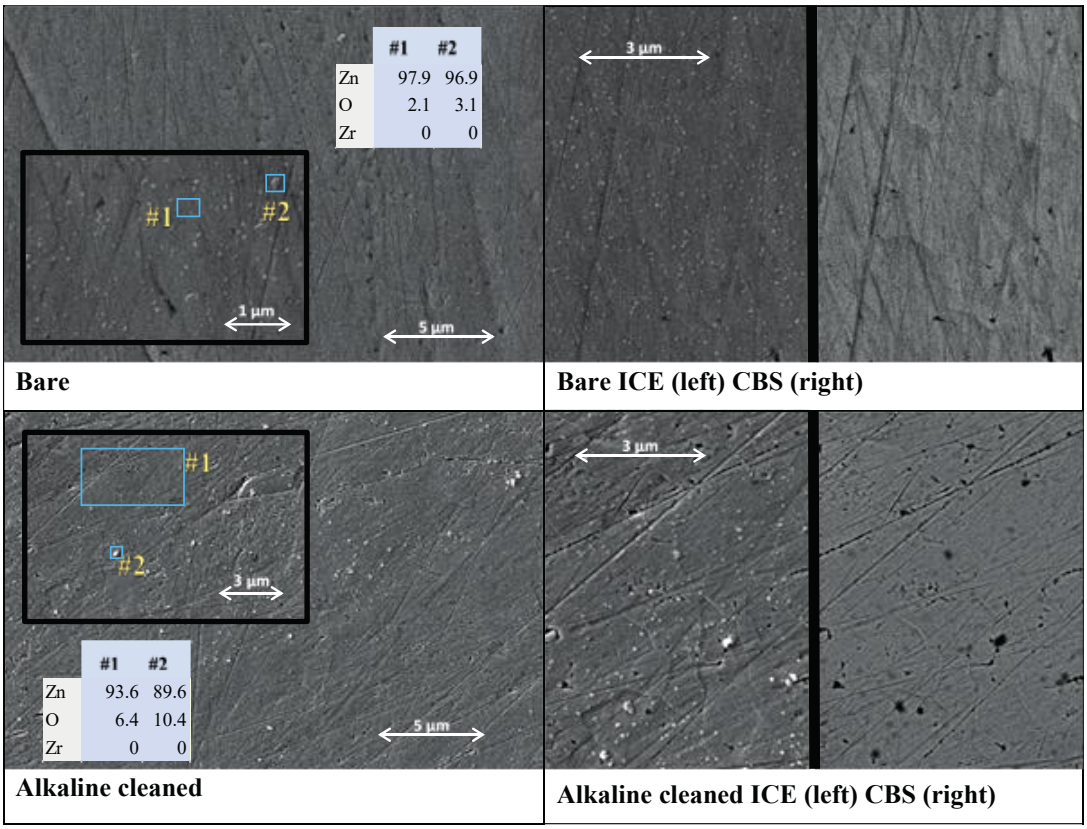

Figure 2.12: SEM micrographs of bare and alkaline-cleaned Zn ZrCC-free samples. Blue rectangles note the sites of EDS analyses, and the results for Zn, O and Zr are given in tables. Micrographs on the right side were captured using the CBS detector mode to further confirm the presence of oxide. All EDS results are given in Appendix A, A.5, Figure A.7.

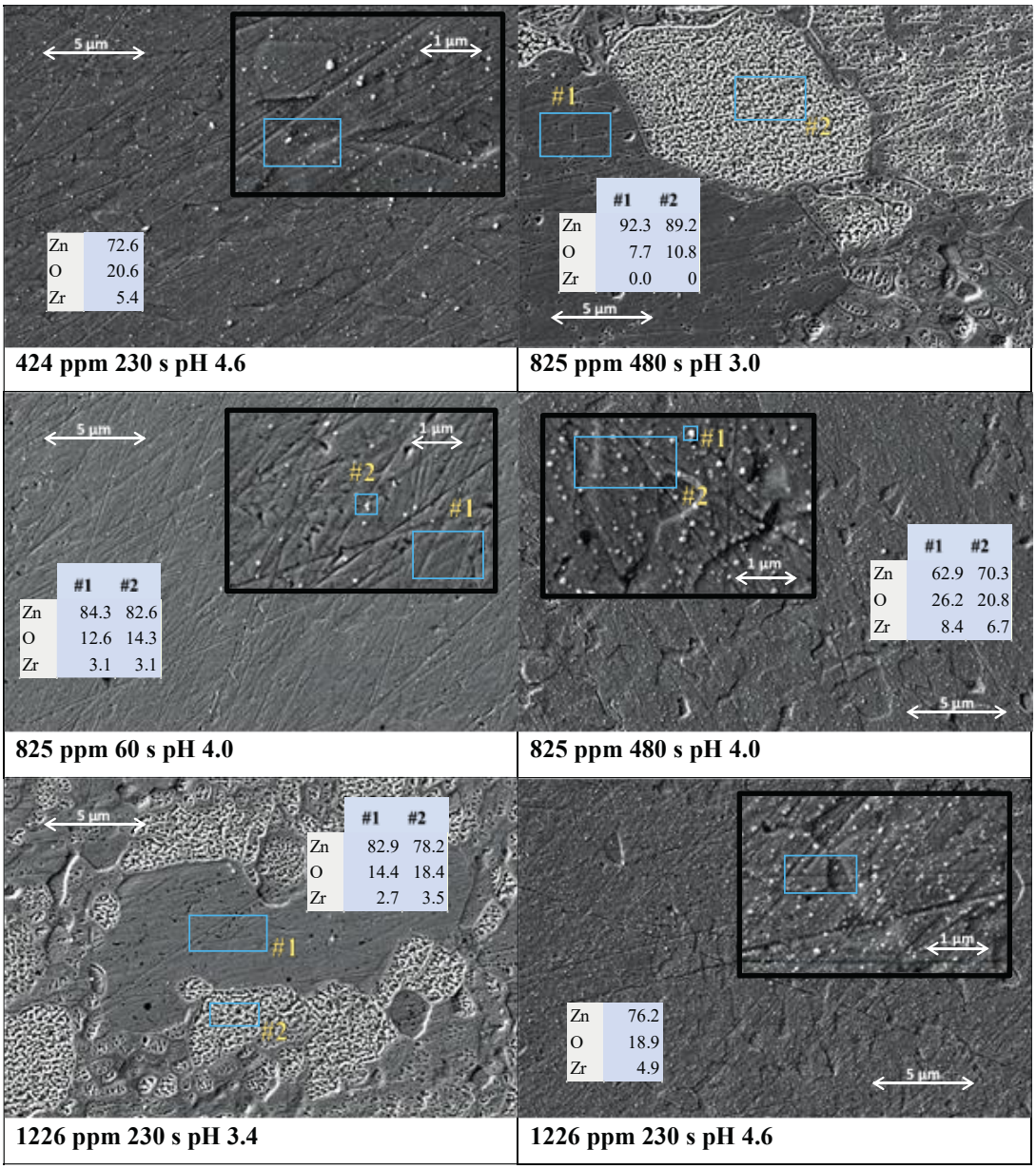

Figure 2.13: SEM micrographs of Zn ZrCC-free samples prepared under different conditions with locations of EDS spectra obtained and EDS results for Al, O and Zr. All EDS results are given in Appendix A, A.5, Figure A.7.

2.3.3.3 AA5754

For the purpose of discussion, only the Zr, O, and Al contents obtained through EDS were deemed relevant. The atomic percentages of these elements, along with the locations where EDS spectra were acquired on SEM micrographs, are presented in Figures 2.14-2.15. Comprehensive EDS analyses can be found in Appendix A, A.5, Figure A.8. The coating density significantly impacts the depth of electron penetration. In practical scenarios, the density may be noticeably reduced, leading to a faster beam arrival at the substrate.

AA5754 alloy contains $(MnFe)Al_6$, α-$(MnFe)_3SiAl_{12}$, [144] $AlFe_3$, Mg_2Si and, sporadically, Al_6CuMg_4 IMPs [145]. High Fe:Mn ratios observed from EDS spectra on bare and chemically pretreated samples (Figure 2.14) are common for AA5754, where a significant portion of Mn is substituted by Fe. The semi-quantitative nature of EDS and the strong influence of matrix signal at 15 kV [136] do not allow for identification of the exact type of IMPs except that the main

ones found to be important for conversion are Fe-containing and are referred to as Al–Fe IMPs. However, understanding the behaviour of Al-IMPs at different pH is still under research and can differ greatly for the same IMPs in different aluminium alloys in the same series [122, 146, 147, 148]. Nevertheless, Fe exhibited cathodic behaviour in all Fe-containing IMPs, which is needed for further discussion [149, 150]. Therefore, the general knowledge of Fe's behaviour can be applied to Al–Fe IMPs to explain ZrCC formation on AA5754.

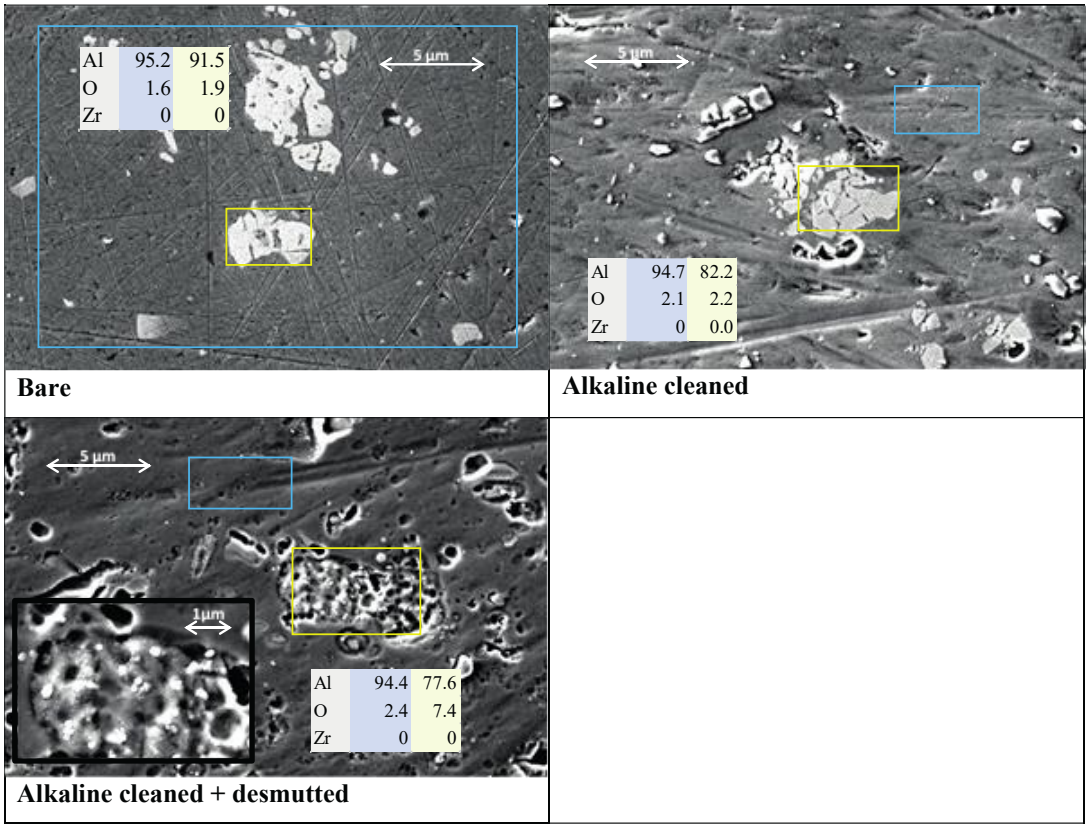

Figure 2.14: SEM micrographs of bare, alkaline-cleaned and alkaline-cleaned and desmutted AA5754 ZrCC-free samples. Blue and yellow rectangles note the locations of EDS analyses, and the results for Al, O, and Zr are given in tables. Blue sites refer to the matrix, and yellow sites to IMPs. All EDS results are given in Appendix A, A.5, Figure A.8.

In contrast to bare, chemically pretreated samples have significantly increased Fe content on Al–Fe IMPs, pointing to a possible enrichment due to the selective dissolution of Mg [151]. In addition, after desmutting, Al–Fe IMPs exhibited a rather porous structure (Figure 2.15). The current study employed a commercial desmutting step that contained H_2SO_4, HNO_3, and HF. The latter two components were previously studied by Campestrini et al. as an additional pickling step, and their results confirmed that using HF in the desmutting process leads to a severe attack on the Al-matrix, resulting in the better removal of second-phase particles and, possibly, SiC grounding residuals through a drop out [152]. Therefore, lower concentrations of local cathodes on the surface should lead to more uniform alumina formation during the alkaline cleaning and desmutting steps, as well as subsequent more uniform conversion coating deposition. This could explain the superior EIS capacitive loop observed for the desmutted sample as well as improved values of PA compared to bare and alkaline-treated samples both after 10 min and 24 h, respectively. However, although the porosity of structures formed out of IMPs presumably improves their cathodic efficiency, it also makes them more susceptible to pitting corrosion than ZrCC-treated samples, as observed in PPC results (Figure 2.2a).

The ultimate confirmation of ZrCC-samples inferior performance in EIS, when compared to ZrCC-free samples, becomes evident in SEM micrographs due to crack formation (Figure 2.5). This leads to the EIS response being exclusively governed by charge transfer through substantial defects at the OCP, which are, in fact, larger than the coating thickness (generally around 10–80 nm [9]). In contrast, extended passivation regions in AA5754-ZrCC samples can arise as a direct consequence of pores being cathodic to the substrate, thereby enabling them to contribute to passivation during the anodic scan in PPCs (Figure 2.2)

The effects of increasing concentration and conversion time at the same pH setting result in thicker coatings on AA5754, just as observed for Zn and CRS, indicated by a higher Zr content on both matrix and IMPs and lower Fe content on IMPs (compare 150 ppm/pH 4.0 at 480 s and 730 s as well as 825 ppm/pH 4.0 at 60 and 480 s). Moreover, the sample 825 ppm/60 s/pH 4.0 confirms that the conversion begins at cathodic sites (Al—Fe IMPs) as indicated by Zr detection only at the IMPs and none at the matrix. Interestingly, in contrast to PA results, electrochemical test results show that 825 ppm/60 s/pH 4.0 offers the same level of corrosion protection as ZrCC-free samples and even a slightly prolonged passivation range. When the coating blocks merely a fraction of the surface, the corrosion rate may stay the same on the remaining bare areas, as the increase in R_{ct} occurs due to a decrease in surface active area. This is already seen in (Figure 2.2), as this sample is the only one having more negative E_{corr} compared to other ZrCC samples, which is almost the same as the bare sample [140], indicating that more electrochemically active regions are present on the surface [107], and not that the coating provides sufficient protection.

Further increase of conversion time enables ZrCC growth in the lateral direction, aligned with a decreased difference in Volta potential between cathodic IMPs and anodic Al matrix [9]. The cathodic reactivity of the IMPs is suppressed after zirconia deposition, lowering the extent of microgalvanic coupling with the matrix, i.e., driving force for ZrCC deposition and allowing for cathodic reactions to continue at Al matrix, along with Al dissolution, similarly to CCCs [153].

In addition, the cathodic action of IMPs is also seen through a higher Zr content obtained at larger IMPs (825 ppm/480 s/pH 4.0). Concentrations of Zr on IMPs and matrix differ even by order of magnitude, leading to cracking of the coating around the IMPs and enabling ingress of corrosive agents to the substrate. This difference in Zr content is approximately 20 × for samples at 825 ppm and approximately 3–10 × for samples at 150 ppm, except for the sample with pH = 3.4, where the difference reaches 20 ×, as will be further discussed below.

There is also a significant difference in the morphology of ZrCC at IMPs and matrix, similar to that in CCCs. Compared to small—nodular on the Al-matrix, more compact, thicker and denser zirconia films are formed on the surfaces of IMPs. ZrCCs are cracked around IMPs, owing to a significantly higher deposition rate of ZrCC on IMPs. This behaviour has been shown for ZrCCs throughout the AA series [34]. The fact that the coatings continue to grow on both IMPs and the matrix after a long conversion time results from the permeability of the formed gel and solution access through the cracked IMPs, allowing cathodic reactions to continue [154, 155]. Nevertheless, the previously formed particles can also serve as nucleation sites for subsequent precipitation, as proposed in [156].

By comparing Zr contents obtained at low and intermediate concentration settings (150 and 825 ppm), it can be seen that lower concentration leads to a more uniform coating, reflected in a smaller difference between Zr content on the matrix and IMPs. Prolonging the conversion time at lower concentrations still results in lower Zr content on Fe IMP than shorter conversion times at higher concentrations (compare 150 ppm/730 s/pH 4.0 and 825 ppm/480 s/pH 4.0 and 825 ppm/60 s/pH 4.0 and 150 ppm/480 s/pH 4.0). This proves that the kinetics of the subsequent conversion film growth is diffusion-controlled, as lower concentrations lead to lower concentration gradients and greater depletion of H_2ZrF_6 at the surface. It can be inferred that further growth occurs until the exhaustion of the conversion agent (Zr-bearing component, in

this case, H_2ZrF_6) and local cathodes near the metal surface, making the process self-limiting. However, conversion times and concentrations used in this work do not lead to a self-limiting effect. This is in contrast to the observations made by Campestrini et al. [153] on CCC on Alclad 2024−T3, where nucleation starts on IMPs and growth proceeds on the Al-matrix, enabling CCC to reach a greater thickness on the Al-matrix than on the IMPs after a longer conversion time. The probable reason for this is the different hydrolysis and redox behaviour of Zr compared to Cr. The formation of CCC is controlled by pH and the concentration of reduced Cr(VI) and exhibits more predictable hydrolysis behaviour.

In contrast, the uncontrolled hydrolysis and condensation of Zr lead to overlapping nucleation and growth processes that occur on both the Al-matrix and IMPs with a longer conversion time, with reduction currents not dependent on Zr concentration as much as on only pH.

However, the main influential factor for the conversion process on AA5754 is most certainly pH, as shown in the RSM plots (Figure 2.8 and Figure 2.10), as it governs the reactivity of Al−Fe IMPs. Performing the conversion process at low pH and higher concentration, more precisely, 825 ppm/480 s/pH 3.0, leads to lower Zr content on both the matrix and Al−Fe IMPs, as well as more pronounced cracking compared to other samples at 825 ppm. On the other hand, a combination of low pH and concentration (150 ppm/480 s/pH 3.4) results in a high Zr content on both the Al−Fe IMP and the matrix, compared to other samples at 150 ppm. These samples exhibit a more uneven coating morphology with agglomerated zirconia nodules across the surface. This can be explained by starting the conversion process at a lower pH, which increases the cathodic reactivity of Fe-containing IMPs and the anodic activity of the subsequent aluminium matrix. A rapid accompanying formation of hydroxyls leads to localised alkalisation necessary for ZrCC deposition, albeit unevenly, leaving less time for uniform deposition of zirconia and even leading to extensive agglomeration. Although 825 ppm/480 s/ pH 3.0 conditions on AA5754 did result in coating formation, unlike CRS and Zn, it can be concluded that, in general, the prevalence of anodic activity in the form of substrate dissolution during most of the conversion time outweighs the cathodic activity enabling ZrCC deposition. In other words, a longer time is required to achieve an equilibrium between substrate dissolution and ZrCC deposition at a pH < 4. Nevertheless, as such, samples performed at pH < 4.0 are not interesting from a corrosion standpoint and were not further studied herein.

The first augmented sample, 825 ppm/230 s/pH 4.3, exhibits approximately half the amount of Zr compared to the central point, 825 ppm/480 s/pH 4.0, which can be attributed to a halved conversion time. Additionally, zirconia nodules are more concentrated at the edges of the IMPs, likely due to their proximity to the underlying cracks that facilitate cathodic reactions. Longer conversion times ($\geq$ 480 s) lead to the creation of spherical particles by agglomerated ZrO_2 nodules (Figure 2.15). pH of the 825 ppm/480 s/pH 4.3 sample is one coded unit (Appendix A, A.3) away from the best-performing pH of 4.6 and one coded unit away from the central point at pH 4.0. This suggests that the cathodic action of the IMPs does not undergo significant changes within this pH range. However, given the lower depletion rate of H_2ZrF_6 at higher concentrations and the fact that the ZrCC deposition always first starts at cathodic IMPs on aluminium alloys, with Zr deposition being greater at higher concentrations, it can be altogether inferred that the route for more accessible and better control of homogeneous ZrCC deposition on aluminium alloys is using low concentrations and pH values near zirconia precipitation.

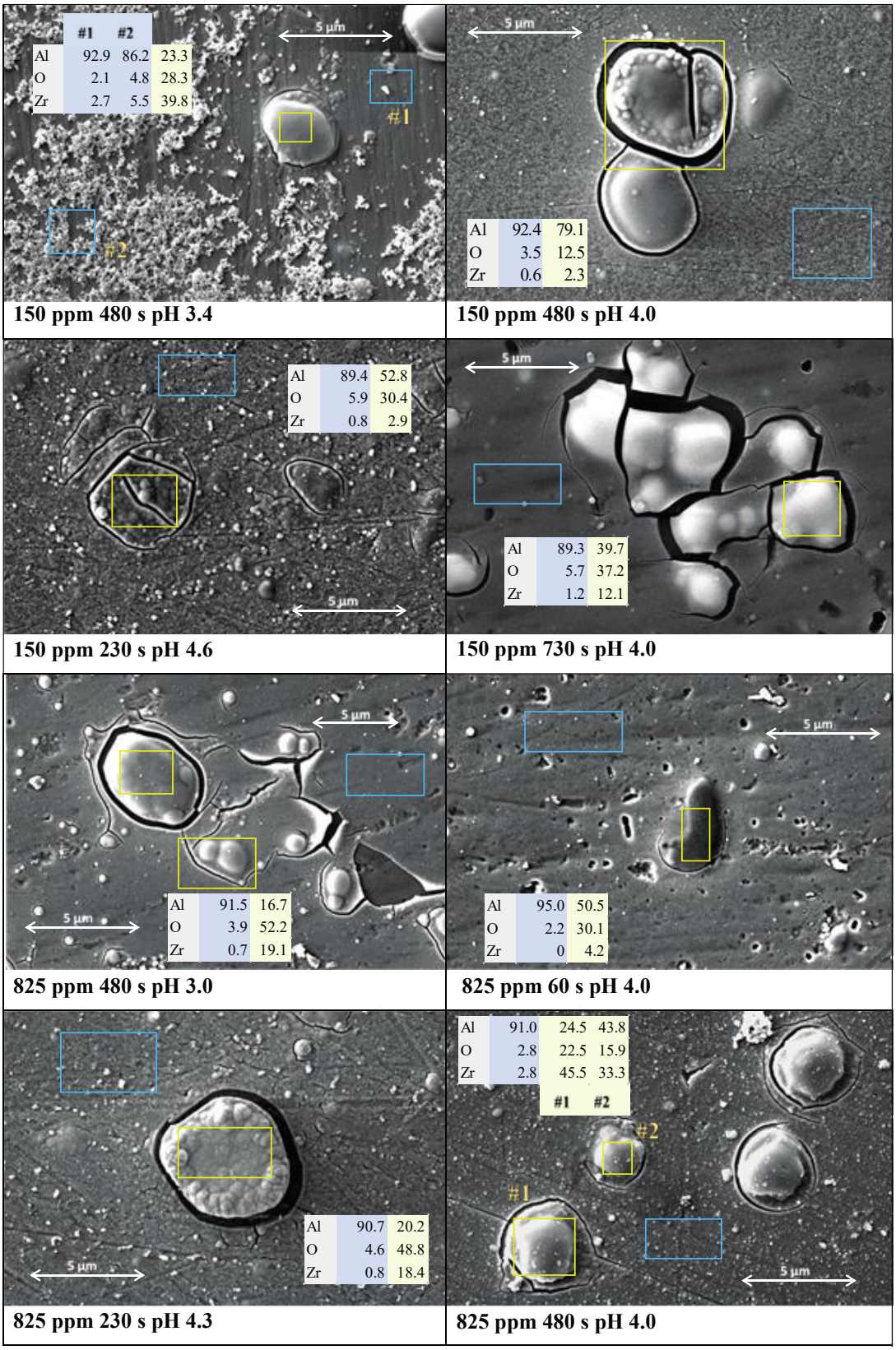

Figure 2.15: SEM micrographs of AA5754 samples subjected to various ZrCC treatments. Blue and yellow rectangles note the locations of EDS analyses, and the results for Al, O, and Zr are given in tables. Blue sites refer to the matrix, and yellow sites to IMPs. All EDS results are given in Appendix A, A.5, Figure A.8.

Finally, the second augmented sample (Figure 2.15), carried out at a low concentration, shorter conversion time, and higher pH setting (150 ppm/230 s/pH 4.6), as guided by the first RSM augmentation (Figure A.5), yields the best performance in the drop test response (Table A.9). This is further shown in SEM/EDS results (Figure 2.15) as the smallest difference in Zr content between the IMPs and matrix. Although some cracking is still present, which is likely a result of drying in SEM vacuum conditions or the fact that the coating is still too thick on the IMPs, the observed morphology corresponds to the best PPC behaviour (Figure 2.2a). On the other hand, the obtained EIS data in the region of low concentration and higher pH imply that samples with medium conversion times (480 s) exhibit improved performance (Figure 2.5). However, after observing the onset of cracking at IMPs already on the sample treated at 230 s, it can be noted that prolonged conversion times also lead to further cracking as ZrCC growth persists at IMPs. Thus, despite not achieving the best EIS performance (but near it) but the best drop test performance, the best-performing sample is, in our opinion, 150 ppm 230 s pH 4.6. The need for augmentations, i.e., narrowing of the design space, confirms the anticipated higher sensitivity of AA5754 to changes in ZrCC bath parameters compared to CRS and Zn.

It should be noted that the present study confronted RSM principles, emphasising rapid and cost-effective result acquisition. Nonetheless, this approach carries the potential risk that the genuine effectiveness of ZrCCs might be compromised within a one-day timeframe. As demonstrated by Šekularac et al. [33, 34, 43], longer immersion times in a corrosive electrolyte generally yield an increased impedance, sometimes surpassing ZrCC-free samples and reduced deviation in obtained impedances on a particular sample due to crack densification caused by corrosion products. This effect could be even more pronounced and favourable in the case of thicker coatings.

Therefore, in the context of AA5754, EIS measurements conducted within one day and near the optimal region may exhibit heightened sensitivity for predicting future corrosion resistance compared to the drop test, as thicker coatings offer improved corrosion resistance under both short and extended immersion times. This highlights the need for further research on surface pretreatments before conversion. Additionally, to achieve better refinement in pH and conversion time at lower concentrations, implementing *in-situ* local electrochemical methods would be beneficial, which will be addressed in our future research. Nevertheless, in this case, RSM demonstrated particular benefits in determining the factor settings necessary for achieving the least-cracked coating, which had not been explicitly shown before.

2.4 General Discussion

The pH is the most critical factor for the conversion process on all substrates since it governs the cathodic control of corrosion reactions. Indeed, it has been shown earlier that the interfacial pH of electrochemical processes is significantly influenced by the underlying substrate [157]. Overall, for CRS and Zn, where ZrCC deposition is guided by uniform corrosion, optimal performance is achieved at moderate (825 ppm) to high concentrations (1226 ppm) and pH levels of 4.0–4.6. In contrast, for AA5754, where cathodic reaction kinetics are entirely influenced by IMPs achieving better control of deposition kinetics, lower concentrations (150 ppm), shorter to moderate conversion times (230–480 s), and elevated pH (4.0–4.6) are needed to acquire uniform coating deposition (Table 2.4). Additionally, medium immersion times at lower concentrations could have enhanced corrosion resistance at extended exposures to corrosive environments. While the coating formation on Zn and CRS is uniform, resulting from a continuous change of local anodic and cathodic sites, sustained spatial separation of these sites in AA5754 leads to substantial cracking after long conversion times, causing continuous cathodic action within the cracks.

Table 2.4: Summary of governing mechanisms and optimal factor ranges for ZrCCs deposition on different substrates.

Substrate	Mechanism	Optimum factor range		
		Conversion time	Concentration	pH
CRS	Governed by uniform corrosion	480 s	825–1226 ppm	4.0–4.6
Zn		480–730 s	825–1226 ppm	4.0–4.6
AA5754	Governed by cathodic action of IMPs	230–480 s	150 ppm	4.0–4.6

It should be noted that the formation of nodular oxide structures, due to their porosity and catalytic activity, may promote further film growth through the enhancement of ORR [158] either on the oxide surface or substrate, as predicted by the porous oxide corrosion model [159]. Interestingly, it has been found that ZrCC nodules do not form on pure aluminium, which, along with the fact that in the case of aluminium alloys, nodular forms are present on IMPs more than matrix, points to electrocatalytic effects of ZrCC precipitation posed by IMPs, as shown by Chidambaram et al. [26]. Namely, if the growth rate of the film is significantly higher than the nucleation rate, nodular growth can be favoured when the deposition conditions or material itself leads to rapid film growth [160]. This is likely to be the case in ZrCC, given the aqueous behaviour of Zr [51].

The results imply that the Zr conversion process is primarily of a chemical rather than electrochemical nature, as demonstrated in previous studies on Cr-coatings by Zhang et al. [156] and further elaborated by Campestrini et al. [152, 153]. Removing microgalvanic coupling between the IMPs and aluminium matrix would favour the sol-gel nature of the process and lead to more homogeneous coatings. This can be established, for example, by the control of density and electroactivity of IMPs [108, 161] by application of electro-assisted deposition [162]). Nonetheless, all these findings emphasize the need for further investigations into the effect of conversion bath pH on different substrate materials. When the gelation phase of conversion coatings, like ZrCCs, is separate from drying (as in immersion application), initial products transform into stable forms through processes like Ostwald ripening (*vide infra, Chapter 3*). Prolonged exposure to air or baking dehydrates hydroxides into oxides, potentially impacting both ZrCC and the underlying substrate oxides. Unlike CCCs, which lose their self-healing ability at high temperatures due to inability of Cr to migrate through the gel coating, Zr-based (as well as Ce-based) coatings require and can withstand higher drying temperatures [163, 164]. However, the literature lacks a consensus on the specific drying conditions for ZrCCs, as the conditions appear arbitrary. Thus, further research is needed to establish standardized guidelines for ZrCC drying.

For CRS, both RSM responses indicate a slight shift in the response surface towards higher pH and concentrations with an increase in conversion time. In essence, optimal PA values can also be achieved at lower pH levels, such as 3.4, with a sufficiently extended conversion time. This is further supported by EIS results from samples under the same conditions but with extended conversion time (1226 ppm, 730 s, pH 3.4), which display a high-frequency loop, reaffirming the presence of a satisfactory coating.

This trend suggests a potential balance between the overall acidity of the solution, diminishing with higher pH and/or lower concentration and the time needed to achieve equilibrium between dissolution and precipitation. Importantly, achieving this equilibrium takes longer at lower pH values. This is further emphasized by the increased Zr availability near the surface at higher concentrations, leading to shorter yet effective conversion times, which improve corrosion protection.

The drop test was more sensitive for CRS and Zn at pH < 4.0 and for AA5754 at pH ≥ 4.0. Additionally, for Zn, the drop test conducted after air-drying for 24 h could only highlight the influence of pH, suggesting that a satisfactory coating forms at a higher pH (4.6), which is not

necessarily related to its thickness. It must be noted that PA results on Zn should be treated separately due to the use of a different reagent compared to the other two substrates.

Nevertheless, combining PA trends from all subtrates point to the fact that the drop test is predominantly influenced by the underlying substrate solubility, compactness, and Zr content rather than defects. Hence, samples treated at pH < 4.0 on AA5754 also performed relatively well in the drop test due to a high Zr content. However, the coating on these samples is the most non-uniform, as revealed by EIS and confirmed by SEM observations. In contrast, although EIS results are affected by charge transfer in large defects on AA5754, they also detect ZrCC thickness when the film is more uniform, especially at a lower concentration (150 ppm) and higher pH values (4.0; 4,6). Conversely, for Zn at pH ≥ 4.0, EIS effectively indicates the ZrCC thickness through the diffusion time constant. However, at pH < 4.0, EIS reflects the behaviour of the porous ZnO formed during conversion (Table 2.5). In particular, Zn-ZrCCs at pH ≥ 4.0 and both conversion times ≥ 230 s and concentrations ≥ 825 ppm have higher coating thickness. This implies a greater long-term predictive capacity for EIS, recognizing the influence of prolonged conversion time on thickness increase, resulting in improved corrosion resistance akin to AA5754. This is in contrast to R_p from Tafel extrapolation, which placed more emphasis on lower concentrations and shorter conversion times and nevertheless, deemed unsuitable from RSM models.

In the case of AA5754, however, R_p from Tafel extrapolation produced RSM plots similar to EIS for AA5754 within a restricted experimental range of lower concentrations, conversion time, and higher pH. This suggests that R_p might be a more suitable evaluation metric than j_{corr} for PPC measurements, likely attributed to R_p encompassing both thermodynamic and kinetic factors, enhancing its capacity to robustly discern differences. However, its feasibility for RSM models on all substrates was still shown to be poor, thereby making it an unfeasible metric for evaluating ZrCC corrosion resistance.

Nevertheless, to determine if the model-suggested optimal points, like 1224 ppm/230 s/pH 4.6 on CRS and Zn, indeed outperform the central point in terms of drop test or EIS compatibility and to discern which method best characterises ZrCCs for each substrate requires further investigation with more sensitive techniques like local electrochemistry, as will be described in *Chapter 5*.

Table 2.5: Feasibility of individual techniques for evaluation of corrosion protection ability of ZrCCs on different substrates.

Technique	Benefits and drawbacks
Drop test screening	• More sensitive for CRS and Zn at pH < 4.0 • More sensitive for AA5754 at pH ≥ 4.0
EIS	• Dependent on the corrosion mechanism of the substrate • High-frequency loop indicates sufficient ZrCC formation on CRS • Highly dependent on the size of defects on AA5754 • Sensitive to ZrCC thickness on Zn at pH ≥ 4.0 and ZnO at pH < 4.0
PPC	• Not suitable for thin films • Feasibility of PPC dependent on the nature of pores, i.e., if ZrCC is anodic or cathodic to the substrate

2.5 Conclusions

This study employed RSM to comprehensively explore the experimental space, identify optimal conditions by properly navigating the design space, and evaluate factor interactions on CRS, Zn, and AA5754 substrates under diverse ZrCC bath conditions. This approach also allowed for assessing the suitability of specific techniques and derived factors. The findings revealed that the drop test, immediately after conversion for CRS and 24 h air-drying for AA5754 and Zn, can be an effective screening method for the ZrCC behaviour when combined with EIS due to its sensitivity and non-destructive nature. In contrast, when using PPC, polarisation resistance is a more convenient evaluation factor compared to corrosion current density. While PA measuring is inherently more subjective than electrochemical measurements, the drop test method is advisable for a quick initial assessment of ZrCC performance. In particular, the drop test gives a generally accurate picture of ZrCC corrosion resistance on CRS and Zn substrates, for the latter after 24 h and at pH $\geq$ 4.0 on AA5754 substrates.

Regarding electrochemical measurements, EIS proved to be the most sensitive method for assessing interactions between conversion bath factors across various combinations. From EIS results, it can be inferred that the ZrCC corrosion behaviour of AA5754 and CRS is exclusively controlled by charge transfer resistance on the former and mostly on the latter, whereas diffusion control prevails on Zn. However, it does not always reflect the corrosion resistance behaviour of the ZrCC. In particular, on AA5754, EIS effectively characterises ZrCC only when complete coating formation is achieved (conversion time $\geq$ 230 s). On CRS, however, besides indicating higher corrosion protection, a high-frequency time constant in EIS spectra indicates satisfactory ZrCC formation. Lastly, on Zn at pH $\geq$ 4.0, EIS can effectively describe ZrCC thickness through diffusion time constant, while at pH $<$ 4.0, EIS captures the behaviour of the porous ZnO formed during conversion. Nevertheless, EIS displays the potential for effectively predicting prolonged corrosion performance depending on ZrCC thickness on A5754 substrates at lower concentrations.

While Zn and CRS possess a preference towards mid to higher concentrations (825—1226), mid to longer conversion times (480—430 s) and mid to higher pH (4.0—4.6), AA5754 is stricter, requiring exclusively lower concentrations (150 ppm), shorter immersion times (230 s) and higher pH (4.6). From this, it becomes clear that applying a one-size-fits-all optimisation strategy across different substrates is impractical, as different techniques yield inconsistent results, heavily dependent on the substrate; however, future optimisations could be adjusted towards AA5754 more at the expense of Zn and CRS. However, it seems that only EIS has the potential to be used on both substrates for both characterisation and prediction/optimisation. In any case, RSM remains valuable for identifying optimal regions and elucidating complex relationships between input factors and responses, ultimately contributing to assessing the extent of viability of each evaluation technique.

Nevertheless, in terms of the statistical applicability of the obtained RSM models, those derived from EIS can function as a universal approach for both characterisation and, to a lesser extent, optimisation of all three substrates, provided that the selection of the appropriate type of resistance from EIS as a response is carefully considered. Further investigation using more sensitive techniques like local electrochemistry is needed to confirm model-suggested optimal points and determine the best method for characterising ZrCCs on all substrates.

This study also advocates the importance of selecting appropriate electrochemical measurements and electrolytes tailored to the specific system under investigation. Additionally, it highlights the necessity of assessing the corrosion performance as a combination of ZrCC and the underlying native (hydro)oxide, especially in cases where the formed oxide does not crack. This knowledge can be extended further to formulate individual baths with even more additives to obtain the desired performance, as well as the development of multi-metal coatings. Rather than delving deeply into the statistics of DoE and RSM, we intended to promote the more

frequent application of DoE in corrosion research, enhancing the robustness of corrosion studies in general. Nevertheless, it must be remembered that in industrial applications, interpreting results requires considering both statistical and practical significance. While larger sample sizes always increase the likelihood of detecting statistical significance, this does not necessarily translate to practical significance if the effect size is small. The latter often arises when values are of comparable magnitudes, leading to minor differences between observed samples that, despite being statistically significant, could lack practical importance. However, in this case, assessing statistical significance proved valuable in unveiling process behaviour, at least from a fundamental level.

What began with the goal of identifying optimal ZrCC conditions on various substrates has, due to observed problems, evolved into a study focusing on the feasibility of different evaluation techniques. Consequently, our study stayed in the characterisation/exploration phase, focusing on identifying the main effects and interactions without advancing to model-based prediction of optimal conditions, which would require further validation, representing the ultimate application of RSM. Yet, this methodological approach was able to enhance the reliability of findings and facilitate a seamless comparison of ZrCC performance across various substrates and its evaluation techniques, ultimately improving overall research credibility and laying the groundwork for future studies.

Chapter 3

Thermodynamic Consideration of Aqueous Chemistry of Zirconium and Experimental Verification

"Water and metals are ever present. Water has the power to erode any material that might contain the metals, thereby releasing them into the water. The liberated metals can hydrolyse the water, releasing protons, the hydroxide binding to the metal. All metals can undergo this process. Nature has conspired to make many of these processes essential for life itself, utilising the unique features of some metal ions within essential mechanisms in plants and animals. Conversely, nature also conspires to make just as many of these processes able to destroy life. Moreover, the processes are important in many other scientific and industrial fields. Consequently, knowledge of hydrolytic reactions and their magnitude is seen as being essential."

Paul L. Brown, Christian Ekberg, Hydrolysis of Metal Ions, 2016 [49].

3.1 The Aqueous Chemistry of Zirconium

3.1.1 General properties and geometry of Zr compounds

Zirconium (electronic configuration [Kr] $4d^2\ 5s^2$) is the 40th element belonging to Group 4 of the periodic table, with properties closely resembling titanium and hafnium. It is a lustrous silver-grey metal, exceptionally ductile, malleable, and strong, yet lighter than steel (density 6.51 g cm^{-3}). Both Zr and its most common important derivative, crystalline ZrO_2 (zirconia), are resistant to most alkalis and acids (except HCl and H_2SO_4, and especially in the presence of F) as well as heat (melting point 1850 °C for Zr and 2710 °C for ZrO_2). In addition, the exceptional fracture toughness and chemical and heat resistance of ZrO_2 make it a perfect ceramic material, a thermal barrier coating, and a common diamond substitute.

Elemental Zr has a hexagonally close-packed crystal structure. In contrast, ZrO_2 has a monoclinic stable phase at room temperature, which changes to tetragonal above 1100 °C and cubic, fluorite-type above 2300 °C. Like other transition metals, Zr forms a wide range of inorganic compounds and coordination complexes, the most important being $ZrSiO_4$, ZrN, ZrC, ZrF_4, $ZrCl_4$, $ZrBr_4$ and ZrI_4 [46, 165, 166, 167].

Owing to its high *charge-to-radius* ratio as well as $4d^25s^2$ valence shell electron configuration, Zr is predominantly found in a tetravalent state in aqueous solutions. As is the case for all ions with charge $z \geq 4$. Zr aqueous chemistry is characterised by spontaneous and slow hydrolysis, yielding a highly acidic solution [168]. The degree of metal ion hydrolysis is affected by metal ion concentration, pH, and solution content, such as chelating agents and counterions [164].

Furthermore, having no partially filled shells leads to a lack of preferential geometry in Zr compounds. This, together with the low energy required for exchange from one geometry and coordination number to another, results in a variety of Zr species in both solid and liquid phases. In effect, Zr geometry is highly dependent on the nature of the current donor atoms (stoichiometry, size, and chelating ability) as well as vapour pressure, temperature, pH of the solution, etc. [165, 169].

3.1.2 The aqueous chemistry of zirconium: Insights into Zr—OH and Zr—F equilibria for conversion coatings

As mentioned at the very beginning in *Chapter 1*, ZrCCs are formed by pH-driven precipitation, most commonly from baths containing H_2ZrF_6. ZrCC formation can be generally expressed with Equation 3.1 [9]:

$$ZrF_6^{2-}(aq) + 4OH^- \rightarrow ZrO_2 \times 2H_2O\ (s) + 6F^- \qquad 3.1$$

While the chemistries of CCCs and PCCs have been studied in more detail using a variety of techniques throughout their use in the last century, [5, 8] research on the aqueous chemistry of Zr was not sufficiently addressed, as evidenced by a limited number of studies [47, 48, 170]. In particular, spontaneous hydrolysis and condensation (*vide infra*) of Zr slowly reaches an equilibrium state and leads to the co-existence of various mononuclear and polynuclear species in the solution. This resulted in a relatively poor agreement between literature data regarding Zr-species and their stability constants [47, 48, 170].

Brown et al. [47] gave a thorough thermochemical review of Zr and its compounds, including fluoride complexes. In an attempt to explain contradictory literature findings on Zr–OH hydrolysis by establishing a single Zr-hydrolysis model, the authors included various monomeric and polymeric species, some of which had not been experimentally confirmed, namely $Zr_3(OH)_9^{3+}$, $Zr_4(OH)_{15}^{+}$ and $Zr_4(OH)_{16}(aq)$. This resulted in hydrolysis and solubility constants of high uncertainty. Rai et al. [48] have recently developed a more comprehensive thermodynamic model by revising the available hydrolysis data for Zr and recalculating constants to be consistent with the more reliable data for its congener, Hf. As a matter of fact, producing pure Zr is challenging because its chemistry is nearly identical to Hf, which naturally occurs as an impurity in zirconium ores. The intervening lanthanide contraction leads to nearly equal atomic and ionic radii for Zr and Hf (1.45 and 0.86 Å for Zr and Zr^{4+}; 1.44 and 0.85 Å for Hf and Hf^{4+}), making Hf a perfect chemical analogue to Zr [165]. Therefore, it is reasonable to expect hydrolysis constants for both elements to be similar in magnitude [48].

For a complete elaboration of selection criteria in the Zr–OH system, readers are referred to Rai et al. [48]. For Zr–F, values reported by Brown et al. are retained, with a full elaboration of selection criteria already given therein [47].

For the reasons stated above, we intended to review and present the state-of-the-art aqueous equilibria of Zr, with a specific focus on its hydrolysis behaviour in Zr–OH and Zr–F systems. By compiling all the information, which is, in our opinion, needed to clarify conflicting study outcomes and establish a foundation for future research. Through this effort, we seek to support researchers in the field of conversion coatings, facilitating a deeper understanding of current limitations and focusing more on the solution chemistry behind Zr conversion bath constituents as it affects the final coatings' properties. The results of this *Chapter* were published in [51].

3.1.3 Experimental

3.1.3.1 Equilibria diagrams and specific ion interaction theory

All Zr chemical equilibria diagrams in this work were constructed using Spana, a HALTAFALL-based software [171]. Spana is a Java version of the former Medusa/Hydra tool, available under the GPLv3 license for free download [172, 173]. Although designed primarily for educational purposes, Spana offers a highly customisable database and an intuitive interface for generating equilibrium diagrams. Spana database contains equilibrium constants extrapolated to zero ionic strength (*I=0*). This enables equilibria calculations at different pH and ionic strength values as well as ionic strength corrections arising from pH change and hydrolysis. For ionic strength corrections, either Davies equation, simplified Helgeson-Kirkham-Flowers (HKF), or Specific Ion Interaction Theory (SIT) can be used [172, 173]. In particular, SIT accommodates both Debye-Hückel's long-range electrostatic interactions in dilute solutions and short-range non-electrostatic interactions at higher concentrations by employing ε, typically considered constant regardless of ionic strength. This makes SIT ideal for high-ionic strength solutions and complex equilibria both of which establish during Zr hydrolysis. With a few variations of the SIT equation, the most common, also embedded in Spana [172], is Equation 3.2:

$$\log(\gamma_i) = -z_i^2 \left(\frac{A\sqrt{I}}{1 + \text{å}B\sqrt{I}} \right) + \sum_k \varepsilon(i,k)\ m_k \qquad 3.2$$

where γ_i is the activity coefficient of an ion i, z_i a charge of an ion i, A_γ and B_γ are the temperature and pressure-dependent Debye-Hückel parameters, å is the ion-size parameter selected to give $\text{å}B_\gamma = 1.5$ $(\text{mol/kg})^{-½}$ at 25°C, I is the ionic strength, $\varepsilon(i,k)$ is a temperature and pressure-dependent specific ion interaction parameter between the ions i and k, and m_k is the molality of an ion k present in the solution such that $z_i \times z_k < 0$.

In the absence of all ion interaction parameters between cations and ClO_4^- in the Zr−OH system, along with Spana default calculations of ionic strength iteratively by adding sodium or chloride ions to maintain electroneutrality, we opted for ε between cations and Cl^- rather than ClO_4^-, despite known interference from complexation with Cl^-. Thus, ε for the Zr−OH system was obtained from Rai et al. and calculated for the Zr−F system by Hummel's [174] estimation method incorporated in Spana: ε (Na^+, M^Y) = 0.05 Y and ε (M^Z, Cl^-) = −0.05 + (0.1 Z), where Z and Y are the cation ($Z > 0$) and anion ($Y < 0$) electric charges, respectively.

Hence, Zr species with pertaining equilibrium constants and ε with Na^+ and Cl^- counterions for I corrections in aqueous NaCl solutions were taken from Rai et al. [48] for Zr–OH calculations (Table 3.1) and Brown et al. [175] for Zr–F calculations (Table 3.2), respectively. Therefore, all equilibria here are referred to aqueous NaCl solutions as a background electrolyte.

Nevertheless, since SIT is recommended by the Thermochemical Database (TDB) project of the Organisation for Economic Co-operation and Development - Nuclear Energy Agency (OECD-NEA TDB [176]) and was also used to derive equilibrium constants by Brown et al. [47] and Rai et al. [48], the choice was made to exclusively employ SIT in this work as well.

Regarding the Zr–F system, in order to replicate H_2ZrF_6 stoichiometry in Spana, ZrF_6^{2-} was exchanged with Zr^{4+} as an input component, while F concentration was set to 0, assuming the initial resistance of ZrF_6^{2-} to hydrolysis.

As will be shown, using calculated and literature data using SIT, the obtained diagrams confronted the theoretically expected regions for Zr−OH and Zr−F species, respectively. More information on SIT, alongside other ionic strength correction models and reaction modelling in aqueous systems, can be found in [172, 177].

Table 3.1: Selected SIT ion-interaction parameters (ε) for modelling Zr–OH species at 25 °C [47].

Species	ε (kg mol^{-1})
H^+, Cl^-	0.12
Na^+, Cl^{-}	0.03
Na^+, OH^-	0.04
Zr^{4+}, Cl^-	0.33
$ZrOH^{3+}$, Cl^-	0.22
Na^+, $Zr(OH)_5^-$	0.03
Na^+, $Zr(OH)_6^{2-}$	0.07
$Zr_3(OH)_4^{8+}$, Cl^-	0.33
$Zr_4(OH)_8^{8+}$, Cl^-	1.37

Table 3.2: Selected and calculated SIT ion-interaction parameters (ε) for modelling Zr–F species at 25 °C.

Species	ε (kg mol^{-1})	Reference
H^+, Cl^-	0.12	[47]
Na^+, Cl^-	0.03	[47]
Na^+, OH^-	0.04	[47]
Zr^{4+}, Cl^-	0.33	[47]
ZrF^{3+}, Cl^-	0.25	[173, 174]
ZrF_2^{2+}, Cl^-	0.15	[174, 178]
ZrF_3^+ , Cl^-	0.05	[174, 178]
Na^+, ZrF_5^-	− 0.05	[174, 178]
Na^+, ZrF_6^{2-}	− 0.1	[174, 178]

3.1.3.2 Computational method

Ab initio calculations in the gas phase of the Zr tetramer, $Zr_4(OH)_8^{8+}$, (*vide infra*) were performed within the framework of Density-Functional-Theory (DFT) using an MN15 energy functional [179] as implemented within the Gaussian16 program package [180]. Zr tetramer structure shown herein was obtained from the structure proposed by Rai et al. [48]. All atoms were described by the all-electron Def2TZVP basis set of Ahlrichs [181]. Standard geometry optimisation was performed to obtain a stable rearrangement of atoms and water molecules. An optimised structure was obtained using forces and the second derivative matrix (Hessian matrix) standard criteria implemented in the Gaussian program package on the atoms, optimising the molecular structure to the local energy minimum [181]. Molecular graphics were produced by the XCRYSDEN graphical package [182]. Figure 3.1 shows the Zr−tetramer structure with first−shell water molecules treated explicitly. To this end, structural and electronic properties based on molecular modelling were not investigated. DFT calculations in the scope of this thesis were performed for illustration purposes only and are not meant to obtain nor describe any new phenomena.

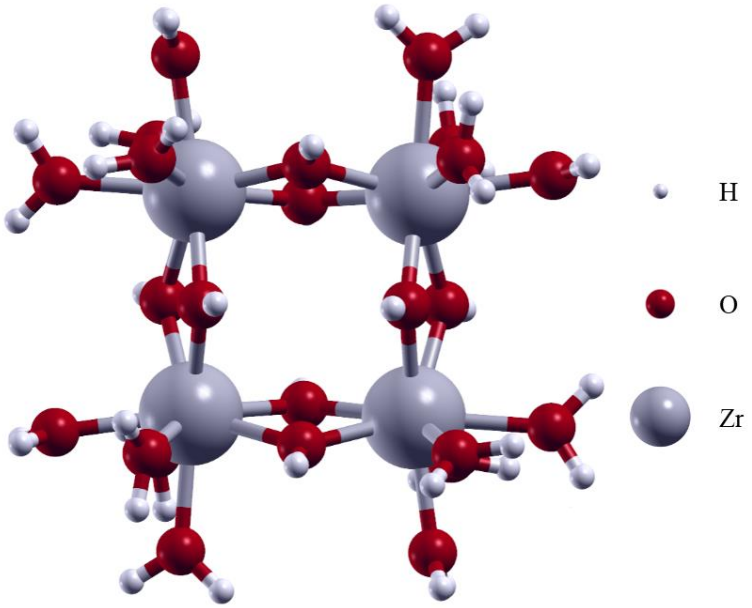

Figure 3.1: The optimised geometry of Zr tetramer, $[Zr_4(OH)_8(H_2O)_{16}]^{8+}$, calculated using the DFT method. (Courtesy of Matjaž Dlouhy from the Jožef Stefan Institute).

3.1.4 Results and discussion

3.1.4.1 Hydrolysis and Zr–OH speciation

The Zr–OH predominance diagram is presented in Figure 3.2, and the related reactions are presented in Table 3.3.

Note that it does not make much sense to discuss the exact predominance regions for species present outside 0 (or even 2) > pH > 12 due to uncertainty in activity coefficients [49]; however, the outer regions are kept for qualitative discussion. Measuring the exact pH values lower than 2 and higher than 12 is complicated due to a significant change in water concentration, resulting in an incomplete dissociation of a strong acid/base and inconsistent activity coefficients. Thus, it would be more correct to represent the results in terms of acid/alkali molality on the abscissa [48, 177]. However, reaching these values is possible, [183, 184] and they are retained herein to demonstrate Zr behaviour in hyper-acidic and -alkaline conditions, respectively. Although irrelevant for most environmental conditions, including conversion coatings, polymeric species serve here as a reminder for precipitation zirconia through a condensation process.

The constructed predominance diagram agrees with the general aqueous chemistry of Zr. Pure/free aqua ion Zr^{4+}, i.e. $[Zr(OH_2)_8^{4+}]$, practically does not exist except in hyper–acidic solutions, resulting in quite an acidic (pH < 0.5) onset of hydrolysis and precipitation, occurring at pH ≈ 2–4 [47, 49, 138, 165]. $ZrOH^{3+}$ stands out as the most important mononuclear species, followed by a less important $Zr(OH)_2^{2+}$ [48], both conferring to the previously observed existence of monomeric species at concentrations lower than 10^{-4} M [138]. In the literature, we have occasionally noticed incorrect records when conversion mechanisms were described using Zr^{4+} ion. It is clear by now that this is incorrect since Zr^{4+} is stable only at pH levels lower than usually used in conversion baths. A brief but thorough discussion on correct inorganic chemistry nomenclature with emphasis on records for charge and oxidation states for various types of ions has been given recently [185].

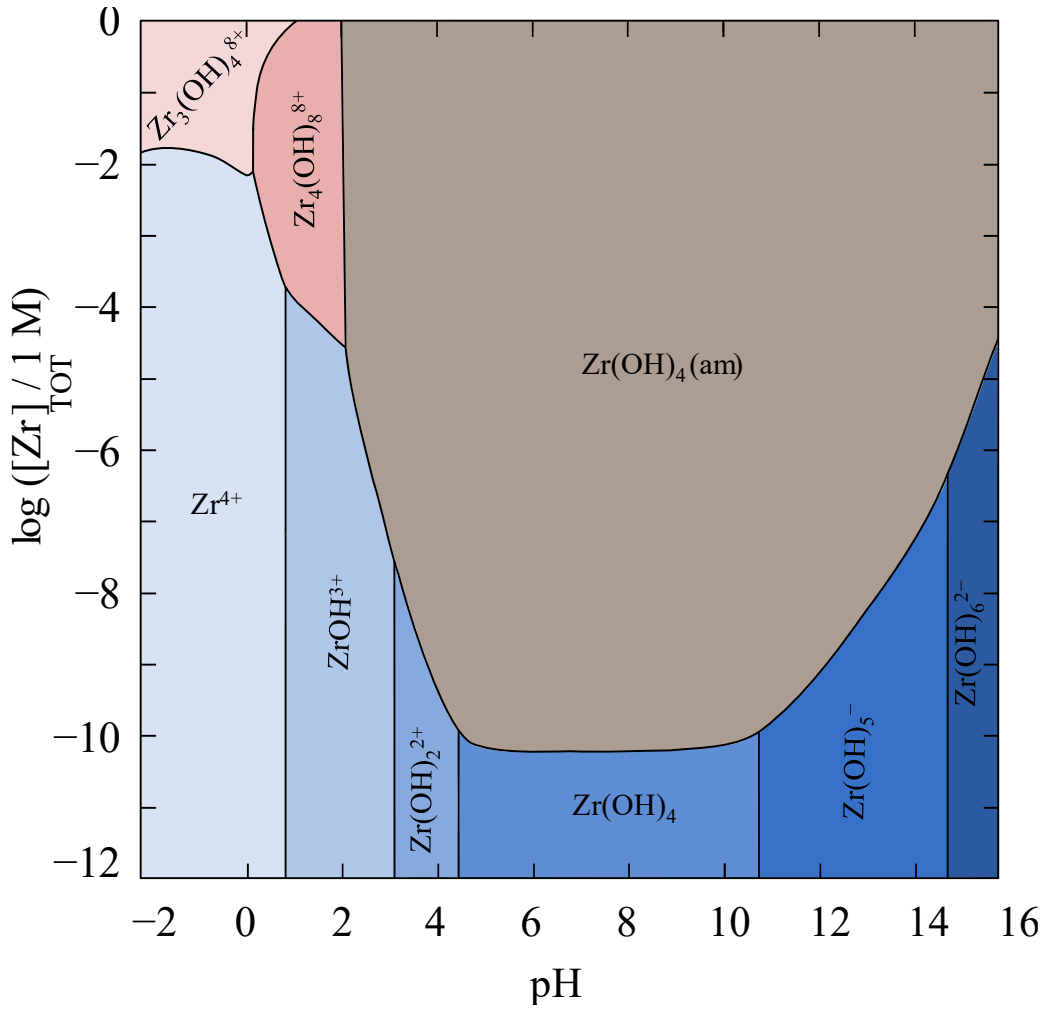

Figure 3.2: The updated predominance diagram for Zr(IV) species (with varying ionic strength in NaCl) at 25 °C.

Table 3.3: Selected cumulative stability and solubility constants ($\log_{10} K^0$) at $I = 0$ for modelling Zr–OH system at 25 °C [47].

Reaction / species	**$\log_{10} K^0$**
Mononuclear Zr hydrolysed species:	
$Zr^{4+} + 4H_2O \rightleftharpoons Zr(OH)_4(am) + 4H^+$	0.182
$Zr^{4+} + H_2O \rightleftharpoons ZrOH^{3+} + H^+$	0.32
$Zr^{4+} + 2H_2O \rightleftharpoons Zr(OH)_2^{2+} + 2H^+$	$\lesssim -2.304$
$Zr^{4+} + 4H_2O \rightleftharpoons Zr(OH)_4(aq) + 4H^+$	< -10.12
$Zr^{4+} + 5H_2O \rightleftharpoons Zr(OH)_5^- + 5H^+$	-19.66
$Zr^{4+} + 6H_2O \rightleftharpoons Zr(OH)_6^{2-} + 6H^+$	-33.29
Polynuclear Zr hydrolysed species:	
$3Zr^{4+} + 4H_2O \rightleftharpoons Zr_3(OH)_4^{8+} + 4H^+$	0.40
$4Zr^{4+} + 8H_2O \rightleftharpoons Zr_4(OH)_8^{8+} + 8H^+$	6.52

As pH increases, the formation of polynuclear species through hydrolysis and condensation proceeds continuously via charge compensation, where water molecules, being highly labile, are progressively substituted by hydroxide ligands [186]. The enclosed diagram thus contains

predominance areas only for $Zr_3(OH)_4^{8+}$ and $Zr_4(OH)_8^{8+}$ polymeric species, which in contrast agrees well with previous findings for the existence of Zr—polymeric species above 10^{-4} M [187]. Zr polymerization paths starting from monomers, dimers, tetramers to octamers [186], or even up to dodecamers have been suggested [188]. The polymerisation was found to be highly dependent on solution starting conditions, especially concentration, ageing, pH, and the presence of complexing agents [186, 188, 189]. With many possible co-existing polymeric species, the diagram in Figure 3.2 contains predominance areas only for $Zr_3(OH)_4^{8+}$ and $Zr_4(OH)_8^{8+}$ to present the existence of Zr polymeric species above 10^{-4} M, aligned with previous findings [190]. Furthermore, a special focus was given as this species has indeed been found with varying prevalence in most Zr-solution-based studies [48, 169, 170, 186, 188, 189, 191, 192, 193, 194, 195, 196, 197, 198, 199, 200, 201, 202] (*vide infra*), regardless of starting conditions. Even though Rai et al. demonstrated that equilibrium constants values for the trimer ($Zr_3(OH)_4^{8+}$) and tetramer ($Zr_4(OH)_8^{8+}$) were significantly overestimated in [47] due to highly uncertain ion-interaction parameter values, making them irrelevant in a very extensive H^+ concentration range (10^{-1}—$10^{-15.4}$ mol kg^{-1}), values from [47] for the aforementioned polymers are retained in the light of describing further polymerisation paths, as $Zr_4(OH)_8^{3+}$ is indeed the most experimentally studied and structurally confirmed Zr aqueous species. It is also noteworthy that a recent Car-Parrinello molecular dynamics (CPMD) study has shown that trimer, although present here, may be a transient species rather than an essential component from which the tetramer is formed [170, 193].

Finally, hydrolysis of Zr ends with the precipitation of a fresh hydroxide amorphous phase, often referred to as "hydrated zirconia". Fresh hydroxides are almost exclusively amorphous, which is additionally enhanced with increasing metal ion valency [203]. Ageing or refluxing Zr-solutions for extended periods leads to conversion from amorphous to more stable cubic or monoclinic crystalline hydrous zirconias, having intrinsically much lower values of solubility constants, i.e., being far less soluble [189, 203]. Kobayashi et al. speculated that room temperature precipitation of fresh $Zr(OH)_4$(am) occurs via nanometric primary particles generated from weak electrostatic stacking of several $[Zr_2(OH)_4]^{4+}$ and $[Zr_4(OH)_8]^{8+}$ [191]. These aggregated primary particles are randomly oriented and inhomogeneously dispersed. Tetramers have also been demonstrated to self-organize into cylindrical shapes, depending on pH and Zr precursor content [9].

Hydrated zirconia precipitates at the aforementioned pH ≈ 2–4, with a large predominance region up to 10^{-10} M and a broad pH range from 2 to 16 [48]. In hyper-alkaline conditions, Zr hydroxylation yields anionic species $Zr(OH)_5^-$ and $Zr(OH)_6^{2-}$ with concentrations from 10^{-10} to 10^{-5} M. Zirconate ion can be noted either as ZrO_3^- or $Zr(OH)_6^{2-}$, due to current inability to distinguish between the two in solution-based solubility studies [49]. The latter is preserved here, along with its equilibrium parameters from [48].

Zr, along with all highly charged tetravalent ions of *d*-block elements, acts as a strong acid, polarising both aqua and hydroxo ligands. Hence, formed amorphous hydroxide is not stable and undergoes spontaneous dehydration, resulting in more or less hydrated oxyhydroxide of ill-defined composition, most correctly denoted as $ZrO_{2-x}(OH)_{2x}$,yH_2O [168]. However, in the literature, the Zr amorphous hydroxide phase is usually represented as either hydrous oxide ($ZrO_2 \times 2H_2O$ (s), hydroxide ($Zr(OH)_4$ (s)/(am) or zirconia amorphous oxide (ZrO_2 (am)) [9, 166, 204]. In this thesis, we choose to represent it as $Zr(OH)_4$ (am). Finally, in hyper-alkaline conditions, Zr hydroxylation yields anionic species $Zr(OH)_5^-$ and $Zr(OH)_6^{2-}$ with concentrations from 10^{-10} to 10^{-5} M.

Taking hydrolysis strictly as a reaction with water, a general hydrolysis model for mononuclear and polynuclear Zr-species can be derived from [168] as Equation 3.3:

$$Zr(H_2O)_N^{4+} + qH_2O \rightleftharpoons Zr(OH)_q(H_2O)_{N-q}^{(4-q)+} + qH^+ \qquad 3.3$$

For the sake of simplicity, aqua ligands in Zr hydroxoaqua complexes contained in the first hydration sphere are left out in this thesis. This gives a simplified Equation 3.4 [47]:

$$m\mathrm{Zr}^{4+} + q\mathrm{H_2O} \rightleftharpoons \mathrm{Zr}_m(\mathrm{OH})_q^{(4m-q)+} + q\mathrm{H}^+ \qquad 3.4$$

The second hydration sphere was not even considered, as its identification is in general, impeded by rapid exchange with the molecules in the bulk, expected to be especially pronounced in the case of Zr [168]. For more, refer to [168, 202, 205].

It can be inferred that the free aqua $[Zr]^{4+}$ ion spontaneously hydrolyses, forming a monomer $[Zr(OH)]^{3+}$, which in turn condenses by olation, forming the cyclic tetramer $[Zr_4(OH)_8]^{8+}$ and possibly, even higher polynuclear forms, depending on particular experimental conditions. The degree of Zr polymerisation through hydrolysis increases with pH, and polynuclear species begin to predominate only at higher Zr concentrations ($> 10^{-4}$ M) [190], with the tetramer ($Zr_4(OH)_8^{8+}$) being of particular interest and a common denominator in all Zr-solution-based studies [48, 169, 170, 186, 188, 189, 191, 192, 193, 194, 195, 196, 197, 198, 199, 200, 201, 202].

3.1.4.2 The tetramer, $Zr_4(OH)_8^{8+}$

The tetramer, $Zr_4(OH)_8^{8+}$ (more precisely, $[Zr_4(OH)_8(H_2O)_{16}]^{8+}$), obtains an eight-fold coordination, where four Zr atoms occupy corners of a distorted square linked along each edge by two bridging hydroxo groups (Figure 3.1), thus exhibiting antiprismatic geometry [168, 206]. $Zr_4(OH)_8^{8+}$ has indeed been detected in both liquid and solid states [207, 208] probably as a result of high kinetic stability arising from its high symmetry and cyclisation [169, 186, 202]. Nevertheless, ZrO_8, with a highly disordered lattice, has also been proposed [205]. Short-distance ordering, applicable to amorphous phases, is expected to differ significantly in the case of Zr as a result of its variability in geometry and coordination that highly depends on the starting solution conditions, thus disabling the establishment of a general precipitation model [209, 210, 211, 212, 213]. However, assuming the existence of a generic link between the aqueous species and the formed solid, the seemingly ubiquitous $Zr_4(OH)_8^{8+}$ could be considered the representative of all other polynuclear species and a fundamental building block of the solid phase (amorphous and crystalline). To sum up, depending on particular experimental conditions, Zr precipitates are formed from $Zr_4(OH)_8^{8+}$ (see Figure 3.6) either via electrostatic stacking or further change of its geometry [186, 191, 205].

3.1.4.3 Updated *E*–pH Pourbaix diagram for Zr

The original *E*–pH diagram for Zr is presented in Figure 3.3. Zr has a very negative reduction potential, disabling production from aqueous solutions by electrolysis [138]. This makes the Pourbaix diagram of Zr just an inset from its general predominance diagrams at certain concentrations. If following Pourbaix's practice, those come down to 10^{-6}, 10^{-4}, and 10^{-2} M.

In brief, the original Pourbaix diagram contained Zr^{4+} cation in highly acidic solutions, hydrolysing to followed by a zirconyl ion, ZrO^{2+}, representing all other aqueous species, both mono- and poly-nuclear [138] in the range from pH $\approx$ 2–4, depending on concentration. The stable solid compound was represented as hydrated zirconium(IV) oxide, $ZrO_2{\cdot}2H_2O_{(s)}$, extending through a broad pH $\approx$ 2–13. At pH $>$ 13, Zr was represented to dissolve as a zirconate ion, $HZrO_3^-$.

The updated *E*–pH Pourbaix diagram (Figure 3.4) was constructed in Spana based on equilibrium data in Table 3.3. The polynuclear Zr species should be excluded from the Pourbaix diagram by default, given that they are not in equilibrium. However, to establish the aforementioned transition from mononuclear to polynuclear species at Zr concentration $> 10^{-4}$ M [190], we opted to represent the former with $ZrOH^{3+}$ and the latter with $Zr_4(OH)_8^{3+}$, respectively. In this way, the thermodynamic stability of $Zr_4(OH)_8^{3+}$ was deliberately exchanged

for its aforementioned kinetic stability. In concentrated solutions, according to the SIT equation, some values of log γ_i can become linearly dependent on the concentrations being calculated, thus impeding calculations at extreme values of pH or E_h, i.e. outside the stability range of H_2O. In the latter case, unrealistically large amounts of O_2 (aq) or H_2 (aq) are calculated, resulting with $\sum m_k$ in Equation 3.5 also becoming unrealistically large, thus creating convergence problems [173].

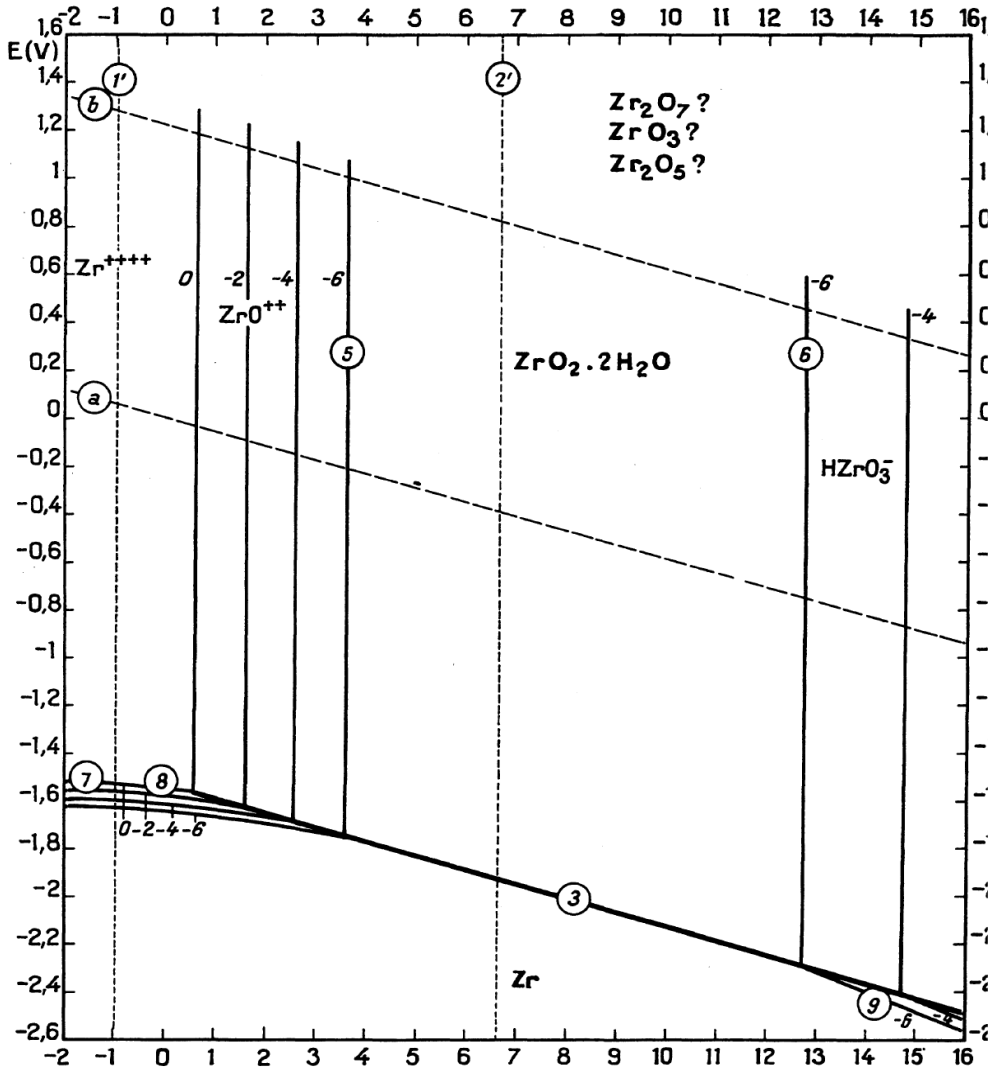

Figure 3.3: The original E–pH Pourbaix Zr–H_2O diagram at 25 °C [138]. *Reprinted from the book "Atlas of Electrochemical Equilibria in Aqueous Solutions" by Marcel Pourbaix, NACE, Cebelcor (Houston, Brussels), 1974, publisher National Association of Corrosion Engineers, with permission from AMPP Global Center, Inc.*

Here, it must be noted that although SIT model experienced convergence problems due to a large amount of H_2 (aq) and O_2 (aq) developed at extreme values of electrode potentials, i.e., outside the stability region of water, [173] taking into account ionic strength effects by applying this very model made it possible to create Pourbaix diagrams that conform well to the original one and the expected stability range of tetramer (Zr concentrations $> 10^{-4}$ M) [190].

In general, an updated diagram (Figure 3.4) shares many similarities with the original one (Figure 3.3.) [138], mostly regarding the passive region ranging from pH 2–13. However, ZrO^{2+} existence had been conclusively disproven in both the aqueous and solid states [207, 208, 214]. A stable solid compound in the passive region is denoted as $Zr(OH)_4$(am), as discussed above.

Zirconate ion, $HZrO_3^-$ or ZrO_3^- from the original Pourbaix diagram, is denoted here as $Zr(OH)_6^{2-}$, although it can also be noted as ZrO_3^-.

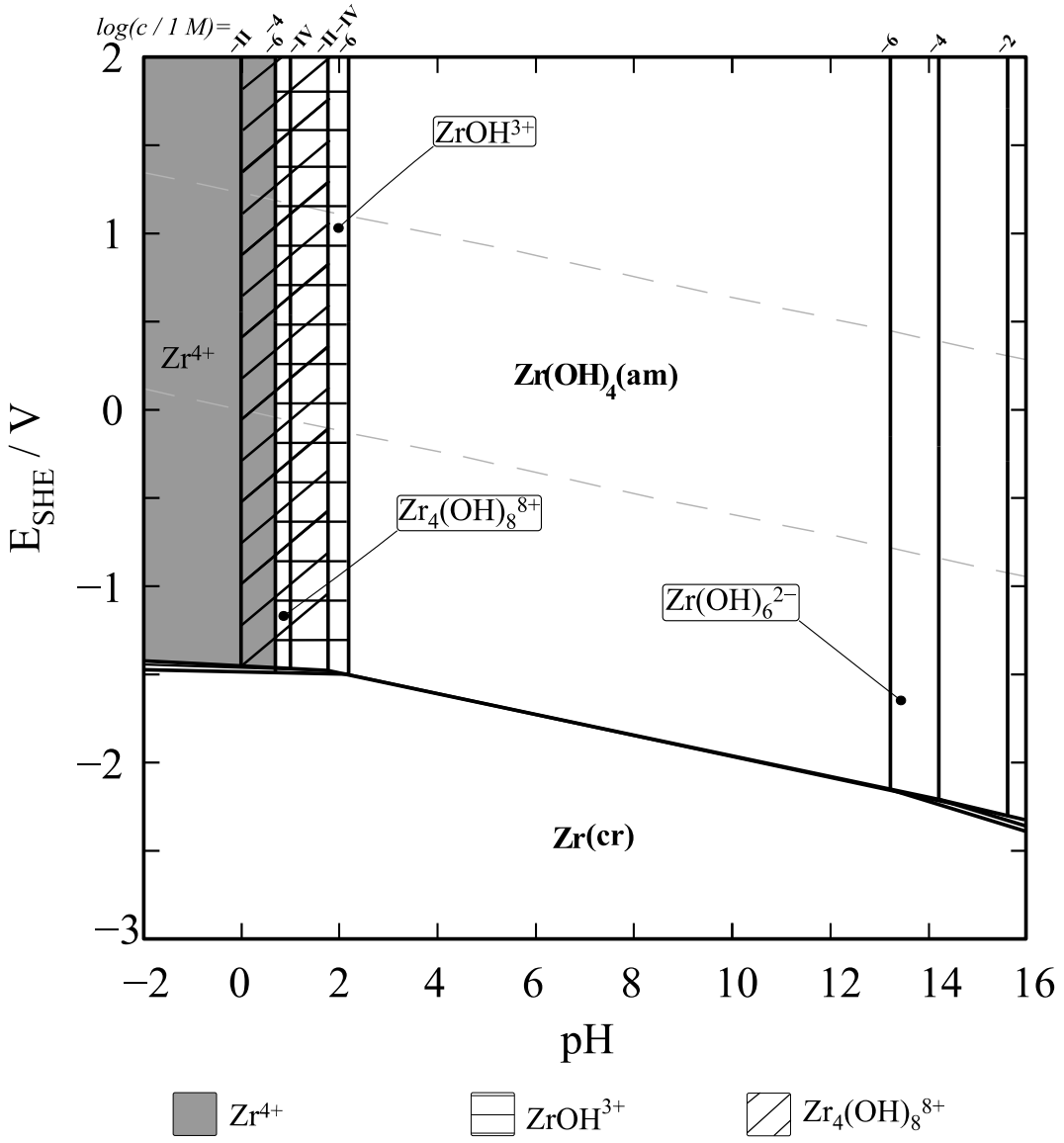

Figure 3.4: The updated E–pH Pourbaix Zr–H_2O diagram (with varying ionic strength in NaCl) at 25 °C. Callouts are added to point to the species. For easier reading, a legend is given at the bottom due to overlapping regions of monomeric and tetrameric species. In addition, the Roman numerals on top of the diagram indicate concentrations at which Zr tetramer exists. For all other species, the concentrations are given in Arabic numerals.

Note that the existence of Zr aqueous compounds with a valency different than 4 that could theoretically occur in its oxide derivatives, especially at higher potentials, is unlikely. In addition, ZrH_2, due to its extreme stability, should eclipse the field of Zr. However, we opted to follow Pourbaix's practice and show the elementary state of the metal in relation to its corrosion products [138].

Looking from ZrCCs perspective, the absence of soluble Zr species of higher valency above the $Zr(OH)_4$ region excludes the possibility of self-healing for Zr, in contrast to Cr. However, Zr non–toxicity and environmental friendliness, along with a wider passivity region (pH ≈ 2–13), compared to metallic substrates on which ZrCCs are applied (steel, galvanised steel, aluminium

and its alloys), [215, 216, 217] and as shown in Figure 1.2 before, make it an attractive replacement, especially in terms of developing multi-metal coatings.

3.1.4.4 Zr–F speciation, hydrolysis and influence of F in the conversion bath

Following the Hard and Soft Acids and Bases (HSAB) principle, [218] Zr–F complexes are quite stable fluoro-complexes, [219, 220] with complexation proceeding up to ZrF_6^{2-}, (also antiprismatic) [169], according to Equation 3.5 [47]:

$$Zr^{4+} + qF^- \rightleftharpoons ZrF_q^{4-q} \qquad 3.5$$

It is thus not surprising that fluoride ions had been frequently added in Zr-containing solutions to prevent the early onset of hydrolysis, [221] and have indeed made the development of Zr-based conversion coatings easier. If using all other Zr salts, dissolution in concentrated acids would be required. In contrast, by introducing hexafluorozirconate ZrF_6^{2-} anion that keeps Zr solvated in the form of a fluoride complex, this matter was solved all at once [222, 223]. Today, ZrCC baths have hexafluorozirconate commonly added as a salt or acid, i.e., K_2ZrF_6 or H_2ZrF_6 [9]. Table 3.4 contains equilibrium constants for the Zr–F complexes from Brown et al. [47] with calculated SIT parameters (Table 3.2) based on [174] from which a Zr–F predominance diagram in Figure 3.5 was constructed.

Table 3.4: Selected cumulative stability constants ($\log_{10}\beta^0$) at I=0 for modelling Zr–F system at 25 °C [47].

Reaction / species	$\log_{10}\beta^0$
$Zr^{4+} + F^- \rightleftharpoons ZrF^{3+}$	10.12
$Zr^{4+} + 2F^- \rightleftharpoons ZrF_2^{2+}$	18.55
$Zr^{4+} + 3F^- \rightleftharpoons ZrF_3^{+}$	24.72
$Zr^{4+} + 4F^- \rightleftharpoons ZrF_4$	30.11
$Zr^{4+} + 5F^- F^- \rightleftharpoons ZrF_5^-$	34.60
$Zr^{4+} + 6F^- \rightleftharpoons ZrF_6^{2-}$	38.11

It can be seen that stable Zr–F complexation in H_2ZrF_6, occurring at concentrations $> 10^{-4}$ M, raises the precipitation pH (compare Figure 3.2 and Figure 3.5), which is further increased with H_2ZrF_6 concentration. However, performing conversion with high H_2ZrF_6 concentrations would lead to insufficient pH rise, a decrease in the Zr content [50, 224] as well as an increase in F^- content. Consequently, ZrCCs have been produced most commonly in the pH range from pH 4–4.6 [9] and concentrations recalculated to Zr ion within 10–30 wt.% [225, 226, 227, 228], depending on the substrate.

The little reference that has been given to ZrF_6^{2-} solutions is summarized as follows: ZrF_6^{2-} was shown to be the only mononuclear species present in solutions containing ZrF_5^- and ZrF_7^{3-} ions, thus suggesting its high stability [229]. After adding alkali to aqueous solutions of ZrF_6^{2-}, only ZrF_6^{2-} and F^- ions were detected, with no additional hydrolysis species. A part of Zr and F was shown to transform into forms not observed in ^{19}F NMR, while the remainder precipitated rapidly as colloidal polynuclear fluorohydroxocomplexes (PFHCs) with a Zr: F ratio of 1:3, thus suggesting a high lability of ZrF_6^{2-} [230]. It was shown that Zr–F does not undergo complete hydrolysis [231], which altogether supports general XPS findings on ZrCCs composition as a mixture of primary ZrO_2 with lower amounts of ZrF_4, oxyhydroxide and/or oxyfluorides [42, 50].

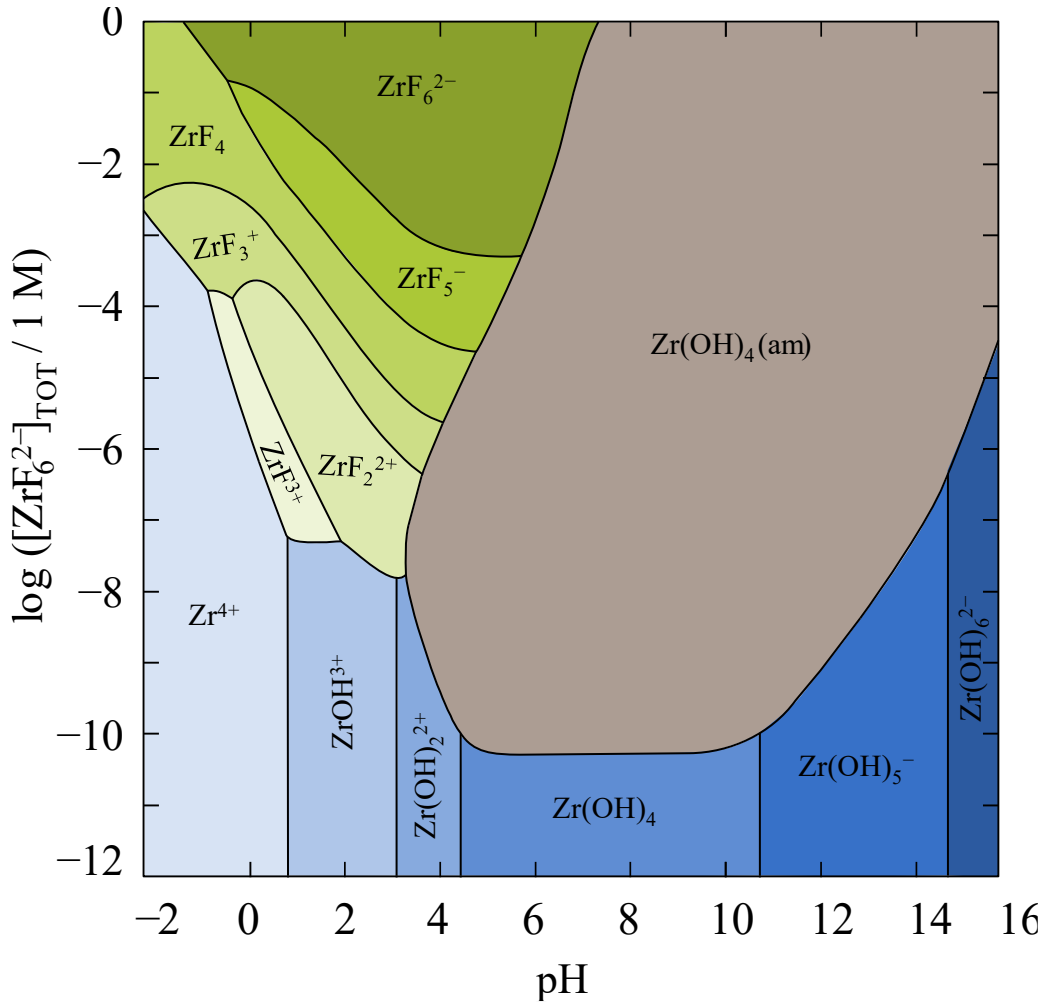

Figure 3.5: The updated predominance diagram for Zr–F species (with varying ionic strength in NaCl) at 25 °C.

As one can see, the speciality of ZrF_6^{2-} that enabled the development of ZrCCs seems to lie in its simultaneous stability and lability (note that the lability is a kinetic parameter and indicates how fast a metal ligand is exchanged, whereas stability is a thermodynamic parameter, defined by the formation constant) [232]. Nevertheless, hydrolysis of ZrF_6^{2-} is complicated by the existence of F^- as a complexing agent in the inner ligand sphere. For comparison, Cl^- ions occupy only the outer ligand sphere during complexation with Zr and are thus more prone to rapid exchange with solution molecules than F^- [208]. However, F^- is more electronegative than water; thus, the nature of the Zr–F bond is more ionic and more susceptible to ionic dissociation along with a high exchange rate with OH^- ion due to similarities in ionic radii [233]. Therefore, hydrolysis of H_2ZrF_6 can be best described as an isomorphic substitution of F^- with OH^-, which has already been shown for antimony and silicon fluoride complexes, [234, 235] with subsequent condensation, as will be further discussed.

As ZrF_6^{2-} ions have shown to be significantly less aggressive than free F^- in terms of oxide film thinning, their primary role in ZrCC baths appears to be surface activation via a significant increase in its wettability. In contrast, the synergistic action of acid and free F^- (the latter added in the formulation or has been recovered from the reaction) leads to metal and native (hydro)oxide film thinning, thus enabling electron tunnelling, the latter being crucial for Al and its alloys [26]. However, on Mg alloy, it has been shown that free F^- suppresses Zr–film formation by inhibiting the reaction of Zr with OH^- liberated by cathodic reaction at the interface rather than by substituting the existing surface OH^- [50]. High hydrophilicity and acidity thus make

ZrCCs ideal for improving subsequent adhesion but not corrosion protection properties at the same time [236].

3.1.4.5 Sol-gel and electrochemical perspectives of the formation of Zr (hydr)oxide formed by conversion

As mentioned at the beginning of this *Chapter*, ZrCC formation can be generally expressed withEquation 3.6, representing a simplified precipitation mechanism of Zr oxide in ZrCCs. In the hitherto published literature, much of the emphasis on the precipitation of Zr oxide in ZrCCs has been given to the consequent electrochemical properties of the substrate/coating system only. In this process, as hydroxylation is induced by the cathodic reactions and consequent rise in pH. However, the progress of the coating formation and the overall process is indeed based on sol-gel chemistry. Therefore, understanding the coatings' formation from both sol-gel and electrochemical perspectives is a prerequisite for improving their overall performance.

3.1.4.6 Sol-gel perspective

Self-hydrolysis and thermally induced hydrolysis of Zr, both being relatively slow processes, can lead to homogeneous and higher-ordered structures [168, 189]. Zr hydrolysis is thus made faster by forced hydrolysis through alkalisation, resulting in disordered structures. In particular, a diffusion-controlled hydroxylation by alkalinisation (essentially present during ZrCC formation during the cathodic reaction of hydrogen and oxygen reduction at the cathodic sites of a heterogeneous alloy surface) is exceptionally rapid [237], with overlapping nucleation and growth processes. In other words, rapid base addition leads to the formation of local pH gradients, i.e., random distribution of hydroxyls on the tetramer. Consequently, polymerisation occurs in many directions simultaneously, as there is not enough time to form an ordered array of tetramers. As a result, the obtained product is an amorphous gel rather than a crystal [168, 189]. Theoretically, amorphous films offer significant corrosion resistance over crystalline ones due to the absence of grain boundaries, dislocations, and inclusions, providing fewer conductive paths to the substrate. However, their thinness often makes them suitable only for temporary use. In practice, the choice between amorphous and crystalline forms depends on the application, where crystalline forms can also offer corrosion protection and improved adhesion due to a higher roughness enabled by a more structured surface, as seen with PCCs [73, 74].
The two described scenarios are presented in Figure 3.6 based on the report by Clearfield [238]. It can be observed that the tetrameric network expands as free water molecules at the edges are allowed to hydrolyse continuously. Further polymerisation and/or stacking of tetrameric [186, 191, 205] units thus lead to precipitation of the solid phase, as the conditions allowing the nucleophilic substitution on the growing oligomer are no longer present [168].

It should be noted that a higher electrical charge, as in the case of $Zr_4(OH)_8^{8+}$ tetramer, limits the formation of condensed species, whereas neutral precursors can condense freely to solid (virtually infinitely). Precipitation can occur over a wide range of acidity, frequently much outside the predominance zone of a noncharged metal species. In the case of Zr, this might occur via species such as $Zr(OH)_4$ (aq) or tetrameric $Zr_4(OH)_{16}$ (aq), for the latter of which no solid evidence exists. However, it was also found that Zr precipitation can occur via species of lower charge than $Zr_4(OH)_8^{8+}$ [186]. While there is no significant change in charge as pH rises, Walther et al. demonstrated that a decrease in tetrameric species concentration with an increase of higher polynuclear species (pentamers, octamers) concentration, as well as a decrease in their mean charge value to 2 near the solubility limit, supports precipitation of $Zr(OH)_4$ (am) by larger, yet less charged species than $Zr_4(OH)_8^{8+}$ [186].

The sol phase results from forming the aforementioned colloidal particles, whereas the gel phase results from their subsequent aggregation into a three-dimensional structure.

1. Condensation of purely aquocomplexes does not occur, as aqua ligand, being very labile, acts only as a leaving group.
2. In aquahydroxo complexes, however, hydroxo ligand acts as a nucleophilic entering group inducing substitution of aqua ligand in another complex. Formed hydroxo bridges are referred to –ol groups to distinguish them from terminal hydroxo ligands, and the whole condensation process is thus referred to as olation (Equation 3.6):

$$M-OH \ + \ M-OH_2 \ \rightarrow \ M-OH-M \ + \ H_2O \qquad 3.6$$

3. The hydroxo ligand may also act as a leaving group forming an aqua ligand when the aqua ligand is absent, as in the case of oxohydroxo complexes. In this case, condensation proceeds with the formation of an oxo bridge by reaction of terminal OH^- groups, which is referred to as oxolation, (Equation 3.7) and can indeed occur in the case of Zr [168]:

$$M-OH \ + \ OH-M \ \rightarrow \ M-O-M \ + \ H_2O \qquad 3.7$$

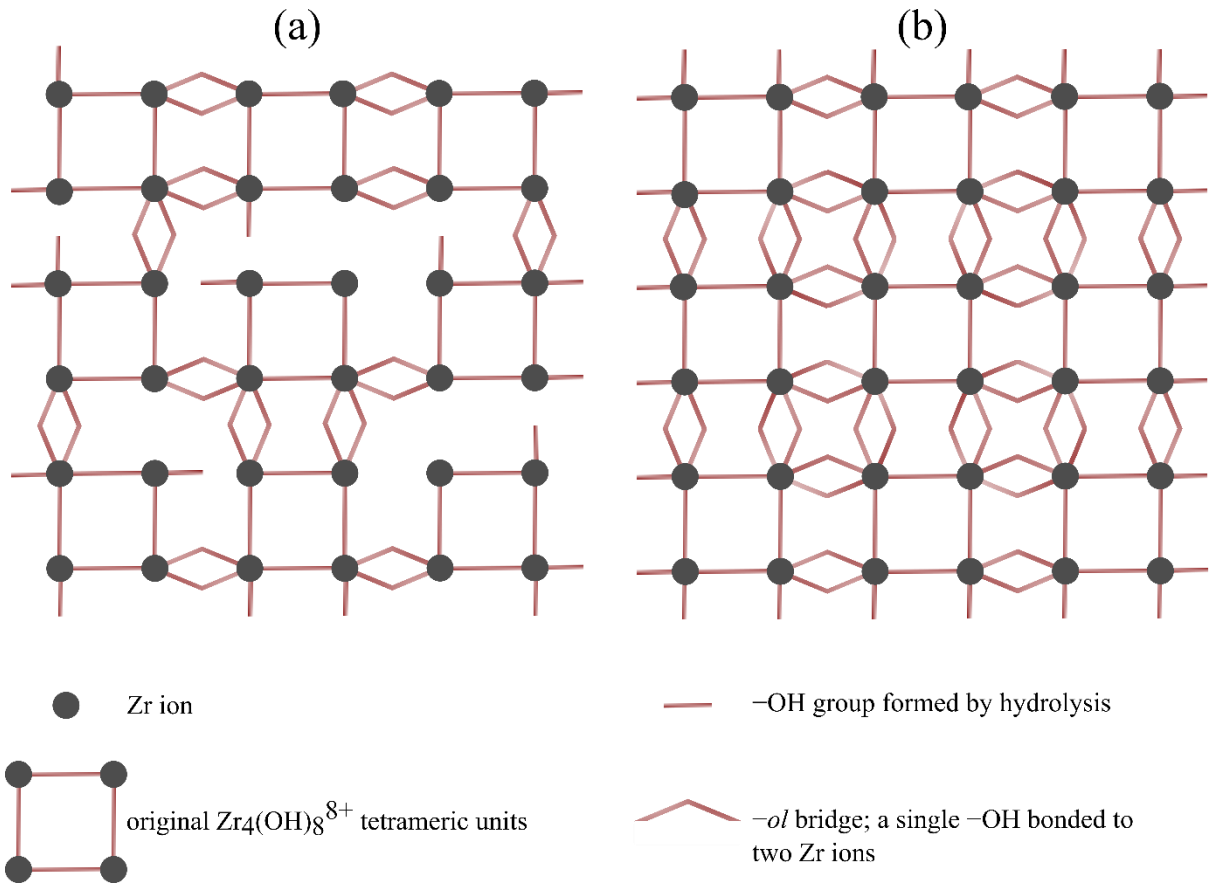

Figure 3.6: Schematic illustration of two-dimensional Zr tetramer condensation. (a) Randomly formed polymer obtained by fast hydrolysis, such as base addition (including ZrCCs). (b) Ordered sheet polymer produced by slow hydrolysis, such as heating. Figure modified from [238].

However, conforming to the general observations for competition between olation and oxolation, the rate constant of oxolation of Zr is much slower, i.e., by two orders of magnitude than olation [239]. Nevertheless, the tendency toward oxolation increases with an increase in pH, so a sufficient rise during conversion could lead to oxolation [212].

Conventional sol-gel synthesis is also applied in several examples on zirconium conversion coatings [240, 241, 242, 243], most often including alkoxy precursors, enabling fine-tuning of

hydrolytic rate and path through the ratio of alkoxy precursors to water as well as the addition of various complexing agents [233]. This leads to separated sol and gel stages. In contrast, in ZrCC, the precipitation is based on H_2ZrF_6, where sol and gel stages occur consecutively in the vicinity of the metal surface, thus not leaving much space for control of distinctive stages or reaction rates. Therefore, a better understanding of the aqueous thermodynamics of Zr should be the first step in elucidating the control of Zr hydrolytic rate and path.

3.1.4.7 Electrochemical perspective

A part of the matrix metal surface (bare metal and metal oxide) comprising anodic areas undergoes oxidation, accompanied firstly by hydrogen and followed by oxygen reduction at cathodic areas (such as IMPs and grain boundaries), eventually leading to surface alkalisation and final precipitation. Thus, ZrCC preferentially deposits at cathodic areas and grows in the lateral direction until full metal coverage. As a result, ZrCCs have an inconsistent thickness, ranging between 10 and 80 nm, which is significantly lower and could be disadvantageous compared to its ancestor technologies [9].

One can try applying the sol-gel chemistry of Zr–OH to Zr–F as follows: supposing the isomorphic substitution of F^- with OH^- during hydroxylation of ZrF_6^{2-} results in the formation of aquahydroxo/aquafluorohydroxo complexes. Hydroxo, ligand, in turn, acts as a nucleophilic entering group inducing substitution of aqua ligand in another complex. Condensation initiated by alkalisation from H_2ZrF_6 solutions should thus include discrete polycationic species starting from monomers, proceeding with dimers and, most probably, ending with some form of tetramers. More substantial evidence was given in older studies on thermo- and alkali-hydrolysis of Zr oxyfluorides, at least in the crystalline phase [244, 245, 246]. Figure 3.6a can thus be used for describing ZrCC precipitation as well. All in all, it is hard to postulate any exact species involved in the hydrolysis and precipitation of H_2ZrF_6 solutions, as the polymerisation path significantly depends on starting solution conditions, in this case, F^- as a complexing agent [189].

After the layer of a condensed sol containing polynuclear particles has been created, the resulting gel exhibits high permeability, ionic conductivity, open structure, and high water retention that allow for continued gelation and film growth through alkalisation and nucleation via formed colloidal particles [233, 247].

The conversion process should thus occur until the exhaustion of the conversion agent (Zr-bearing components) and suppression of local cathodic activity at the metal surface, making the process self-limiting [226, 248, 249].

Hence, studies of conversion coating processes should be directed toward managing the electrochemical aspects, especially those that would allow control of pH increase during conversion (e.g., through the control of density and electroactivity of IMPs, [250] electro–assisted deposition [30], etc.), as well as its sol-gel nature, as already elaborated for Cr conversion coating [164, 247, 251, 252] s.

When gelation is separated from drying, as is the case for immersion application of ZrCCs, initially formed kinetic products are allowed to form more stable species via Ostwald ripening, syneresis, phase separation etc. [164, 233].

As seen from reaction in Equation 3.1, the ZrCC process is accompanied by the regeneration of the hydrofluoric acid. Determining total and free-fluoride content is crucial for establishing equilibrium between the former and hydrolysis reaction, as too high concentration leads to excess metal dissolution, while too low concentration leads to insufficient coating formation. In addition, F^- retained in the coating is detrimental to the underlying substrate [9, 253]. Nevertheless, hydrated zirconia has ionic exchange properties, and the amount of retained anions (anions are always retained when precipitation occurs at $pH < 7$) in the precipitate decreases with an increase in the final precipitation pH [189, 196]. In the case of F^-, due to the aforementioned high lability, proper rinsing with clean deionised water can significantly minimise F^- content [225, 253, 254].

Moreover, the amount of F^- in commercial ZrCCs is minimised by blending with other additives, such as Cu, Zn, Mn, Co, alkaline earth metal ions [255] and H_3BO_3 [256]. To sum up, nowadays, F^- is an essential component of ZrCC baths yet detrimental to the underlying substrate, which requires thorough studies on Zr–OH and ZrF_6^{2-} solutions. However, the determination of solvated ion structures requires various scattering, absorption and resonance spectroscopy methods combined with computer simulations. These include X-ray diffraction, neutron diffraction, electron diffraction, small-angle X-ray and neutron scattering as well as quasi-elastic neutron scattering, spectroscopic methods (extended X-ray absorption fine structure and X-ray absorption near edge structure, nuclear magnetic resonance, Mössbauer spectroscopy, infrared, Raman, and Raleigh-Brillouin spectroscopies) [257]. Most of those methods are not readily available or require synchrotron radiation, which, along with fast hydrolysis and exchange of Zr geometry and coordination, makes the deduction of exact polymerisation paths and species involved in the process still challenging. Although some of the methods have been successfully employed for Zr–OH systems without F [186, 191, 192, 202, 205, 258, 259], to the best of our knowledge, no absorption or scattering studies have explicitly been conducted on Zr–F complexes, which would considerably help to reveal ZrCC coating formation.

3.1.5 Conclusions

Limited knowledge of ZrCC chemistry directly results from limited knowledge of Zr aqueous chemistry. The high tendency of zirconium to hydrolyse, along with a rapid exchange of geometry, coordination, and sensitivity to solution composition, significantly impedes the study of the composition and geometry of Zr compounds. The primary function of hexafluorozirconate is to provide an activated metal surface while also adjusting the pH from severely acidic to that acceptable for conversion. In this study, revised predominance areas for Zr–OH and Zr–F aqueous speciation concerning the Zr amorphous phase were established as a foundation for describing the ZrCC formation mechanism. The tetramer, $Zr_4(OH)_8^{8+}$, was used to represent all other polynuclear species and a fundamental building block of the solid phase. Revised Zr equilibria were the basis for the updated *E*–pH diagram, comprising $ZrOH^{3+}$ and $Zr_4(OH)_8^{8+}$ instead of formerly employed ZrO^{2+}.

We believe this study can serve as a starting point for future extensions to other additives utilised in ZrCC baths, as well as the elucidation of their effects and interactions. This could, at the very least, direct field researchers to focus their research on the final coating and the solution chemistry behind Zr conversion bath components. The electrochemical nature of the conversion process is reflected only in its initiation; however, the core of the process is indeed based on hydrolysis and condensation. Thus, future efforts to identify ways to control both electrochemical and sol-gel chemistry could be critical in increasing the overall performance of ZrCCs.

3.2 Structural Analysis of Zirconium Conversion Coatings with ToF-SIMS

3.2.1 Literature review

Some degree of comprehension of polymerisation paths and species involved in Zr−OH systems has been achieved by applying sophisticated scattering, absorption, and resonance spectroscopy methods coupled with computer simulations [260, 261, 262, 263, 264, 265, 266]. However, to the best of our knowledge, no experimental studies have focused on the speciation of polymeric species in Zr−F solutions related to zirconium conversion baths.

To experimentally validate the proposed concept involving the tetrameric Zr as the main building block of the precipitating ZrCC in our previous study [51] featured above *in Chapter 3.1*, we employed a more accessible technique, ToF-SIMS, to investigate ZrCCs prepared at selected bath operating conditions. So far, ToF-SIMS has been used to investigate zirconium oxide distribution in conversion layers produced by the trivalent chromium process (TCP) [267, 268, 269]. Recognised for its exceptional surface sensitivity, ToF-SIMS provides structural insights based on mass fragments, thus being able to identify polymeric Zr species [270, 271, 272].

3.2.1.1 Sample preparation and chemicals

For EIS measurements, the same CRS samples and their preparation have been used as described in *Chapter 2.* For ToF-SIMS analysis, the samples were cut to dimensions ≤ 1 cm^2. Three different ZrCC bath parameter combinations, determined through RSM in our previous work presented in *Chapter 2,* were employed. At bath concentration of 825 ppm H_2ZrF_6, ZrCCs were prepared at two conversion times (60 s and 480 s) and pH values (3.0 and 4.0): (i) pH of 3.0 leads to inadequate coating formation, (ii) pH of 4.0 with 60 s conversion time leads to a very thin, non-corrosion−resistant coating, and (iii) pH of 4.0 with 480 s conversion time results in a thicker coating, exhibiting improved corrosion resistance compared to bare samples.

3.2.1.2 ToF-SIMS

ToF-SIMS analysis was conducted using a ToF-SIMS 5 spectrometer (IONTOF GmbH, Münster, Germany) under a base pressure of 5×10^{-9} mbar. The data acquisition and post−processing analysis were performed using SurfaceLab software v7. The spectrometer was run in high current (HC) bunched mode with a high mass resolution (DM/M around 7000, measured on Si peak). The exact mass values of at least five known species were used to calibrate the data acquired in the negative ion polarity. All samples were cleaned before introduction into the spectrometer. Mass spectra were recorded within the mass-to-charge ratio (m/z) range of 0–550 using a pulsed 25 keV Bi^+ primary ion source delivering a target current of 1.2 pA over a 500 µm × 500 µm area with a 45° incidence angle to the specimen surface. Bi^+ primary ion dose below 10^{12} ions cm^{-2} was used to ensure static analysis conditions.

The depth profiles were recorded by interlacing the pulsed primary ion source (1.2 pA over a 100 µm × 100 µm area) with sputtering using a 0.5 keV Cs^+ source beam delivering 17 nA of target current over a 300 mm × 300 mm area. The intensity of the ionised fragments, all measured quasi-simultaneously, was plotted vs. the Cs^+ ion sputtering time. Both ion beams were set at an incidence angle of 45° with respect to the sample surface, well-aligned to ensure analysis at the centre of the sputtered crater. All acquisitions were conducted in negative polarity. The depth profiles were recorded at two separate regions on the surface of each sample to ensure reproducibility.

3.2.1.3 EIS

Simulated acid rain was used as an electrolyte with pH ≈ 5 adjusted with 0.1 M H_2SO_4 (96 %, Carlo Erba reagents, Barcelona, Spain). It was prepared by mixing 0.2 g/L Na_2SO_4 (99%, Acros Organics, Hampton, NH, USA) + 0.2 g/L $NaHCO_3$ (Sigma Aldrich, Saint Louis, MO, USA) + 0.2 g/L $NaNO_3$ (99%, Sigma Aldrich, Saint Louis, MO, USA). Simulated acid rain herein is another way to replicate atmospheric conditions, being less aggressive in terms of chloride content, allowing a comparison of corrosion properties among different ZrCCs, similar to using a dilute Harrison's solution in *Chapter 2.3.1.2.1*. Given their susceptibility to noticeable corrosion even at open circuit potential (OCP), CRS samples were allowed to attain a stationary state, defined as ΔOCP<5 mV/10 min, established at approximately 20 min [96]. Thorough EIS experimental details are given in *Chapter 2.2.5.2.1*.

3.2.2 Results and discussion

3.2.2.1 ToF-SIMS results

Figure 3.7 presents overlapped mass spectra in the m/z range 0–540 measured on ZrCCs prepared on cold rolled steel at the three combinations of bath parameters (pH of 3.0 (red), pH of 4.0 with 60 s (blue) and 480 s (grey) conversion time). A peak selection encompassing monomeric, dimeric, trimeric, and tetrameric Zr fragments of the type $Zr_nO_m(OH)_p^-$ is also indicated in Figure 3.7. Notably, high-intensity mass peaks herein are evident in the 380—400, 400—420, 500—520, and 520—540 mass ranges (m/z) for coatings prepared at pH = 4.0. This observation implies that polymerised ZrCC layers form at pH = 4.0.

A comprehensive list of negative ion fragments obtained in the 0–540 m/z mass range, along with their corresponding masses, is presented in Table 3.5, with selected ToF-SIMS mass spectra in Figure 3.8.

Table 3.5 additionally provides information on the potential existence of $Zr_nO_m(OH)_pF_q^-$ along with certain specific $Zr_nO_m(OH)_p^-$ species, as fluoride is demonstrated to incorporate into ZrCCs in the form of oxyfluorides [42, 273]. We believe the most likely mechanism involves the isomorphic substitution of F^- with OH^- during the hydroxylation of ZrF_6^{2-}, resulting in the formation of aquahydroxo/aquafluorohydroxo complexes, leading to condensation and ultimately precipitation [51].

The ToF-SIMS depth profiles of $Zr_nO_mH_p^-$ and $Zr_nO_mH_pF_q^-$ species* in Figure 3.9 were selected based on the highest signals observed in the sample at 825 ppm/480 s/pH 4.0, further reflecting the results in Figure 3.7 and Figure 3.8. The Fe_2^- signal originating from the metallic substrate is also added since it allows the ZrCC/substrate interface to be positioned (vertical line in Figure 3.9). As the conversion time and pH increase, the thickness of the ZrCC increases, following this trend: 250 s for the sample 825 ppm/480 s/pH 3.0, 820 s for 825 ppm/60 s/pH 4.0, and 1800 s for 825 ppm/480 s/pH 4.0, that corresponds to 5 nm, 16.5 nm, and 36 nm, respectively (assuming a constant sputtering rate of 0.02 nm/s, estimated from previous work on a TCP conversion coating [267]). Looking deeper at the ZrCC layer, it can be observed that the maximum intensities of all Zr-containing species increase from pH = 3.0 to pH = 4.0, suggesting that the ZrCC, in addition to being of low thickness, does not fully cover the substrate at pH 3.0. Additionally, the intensities of Zr peaks decrease from monomeric to tetrameric species, likely due to fragmentation. The primary Zr peak observed is ZrO_2^-, consistent with similar ToF-SIMS studies at lower m/z [34]. The Fe_2^- signal, associated with the metallic substrate, exhibits a steeper increase with sputtering time for the coating prepared at shorter conversion times and lower pH. This suggests the broadening of the ZrCC/substrate interface, presumably due to the

* Note that a more precise record would be $Zr_nO_m(OH)_p^-$ and $Zr_nO_m(OH)_pF_q^-$. However, since ToF–SIMS cannot differentiate between oxygen originating from oxide or hydroxide, we opted for a simpler record $Zr_nO_mH_p^-$ and $Zr_nO_mH_pF_q^-$.

increased roughness with the ZrCC layer thickness. Additionally, detecting FeO_2^- (and $FeOOH^-$, results not shown in the figure) signals between the substrate and ZrCC suggests the presence of an intermediate layer of ferrous oxide/hydroxide at the interface, likely resulting from the alkaline cleaning step.

Table 3.5: List of main peak position extracted from ToF-SIMS mass spectra with possible assignments (selection of peaks). In addition to ZrCC- and substrate-originating fragments, those related to alkaline pretreatments are presented (C, P and S).

Ion fragment	*m / z*	Ion fragment	*m / z*	Ion fragment	*m / z*	Ion fragment	*m / z*
C	12.00	ZrO_2^-	121.90	$Zr_2O_4H_4F^-$	266.83	$Zr_4O_7H_7^-$	478.63
F^-	18.99	ZrO_2H^-	122.91	$Zr_2O_5H_4F^-$	282.84	$Zr_4O_9H_3^-$	506.60
S^-	31.97	ZrO_3^-	137.90	$Zr_2O_5H_5F^-$	283.83	$Zr_4O_9H_4^-$	507.62
O_2^-	31.99	ZrO_3H^-	138.90	$Zr_2O_4H_3F_2^-$	284.82	$Zr_4O_9H_5^-$	508.61
OF^-	34.99	$ZrO_3H_2^-$	139.91	$Zr_2O_3H_2F_3^-$	286.82	$Zr_4O_9H_6^-$	509.60
PO_2^-	62.97	$ZrO_3H_3^-$	140.90	$Zr_3O_7H^-$	382.70	$Zr_4O_9H_7^-$	510.61
FeO^-	71.93	$ZrO_4H_2^-$	155.90	$Zr_3O_7H_2^-$	383.70	$Zr_4O_9H_8^-$	511.57
$FeOH^-$	72.94	$ZrO_4H_5^-$ / $ZrO_3H_2F^-$	158.88	$Zr_3O_7H_3^-$	384.70	$Zr_4O_9H_9^-$	512.60
PO_3^-	78.96	$ZrO_4H_7^-$ / $ZrO_3H_4F^-$	160.93	$Zr_3O_7H_4^-$	385.70	$Zr_4O_7H_6F_2^-$ / $Zr_4O_6H_3F_3^-$	515.62
FeO_2^-	87.93	$Zr_2O_4H_2^-$	245.81	$Zr_3O_7H_7^-$	388.70	$Zr_4O_{10}H_9^-$ / $Zr_4O_9H_6F^-$	528.61
$FeOOH^-$	88.93	$Zr_2O_5H_3^-$	262.83	$Zr_3O_8H_9^-$	406.72	$Zr_4O_{10}H_{10}^-$ / $Zr_4O_9H_7F^-$	529.61
$FeO_2H_2^-$	89.94	$Zr_2O_5H_4^-$	263.84	$Zr_3O_8H_{10}^-$ / $Zr_3O_7H_7F^-$	407.73	$Zr_4O_{10}H_{11}^-$ / $Zr_4O_9H_8F^-$	530.61
$C_4H_4F_2^-$	90.00	$Zr_2O_4H_2F^-$	264.82	$Zr_3O_8H_{11}^-$ / $Zr_3O_7H_8F^-$	408.73	$Zr_4O_7H_4F_3^-$	532.61
Fe_2^-	111.87	$Zr_2O_4H_3F^-$	265.83				

To reiterate, the tetrameric structure proposed by Clearfield for amorphous zirconia [206], as applied to ZrCCs in our previous study [51], contained above in this *Chapter,* is identified as $Zr_4(OH)_8^{8+}$, with the possibility of higher polynuclear forms and less charged species [263]. However, ToF-SIMS measurements do not allow the exact ionic hydration structure to be deducted. Thus, our primary objective was to identify polymeric fragments and, most importantly, to confirm tetrameric ones, as their higher kinetic stability, facilitated through cyclisation, is the most probable cause for their incorporation from solution to precipitate [51].

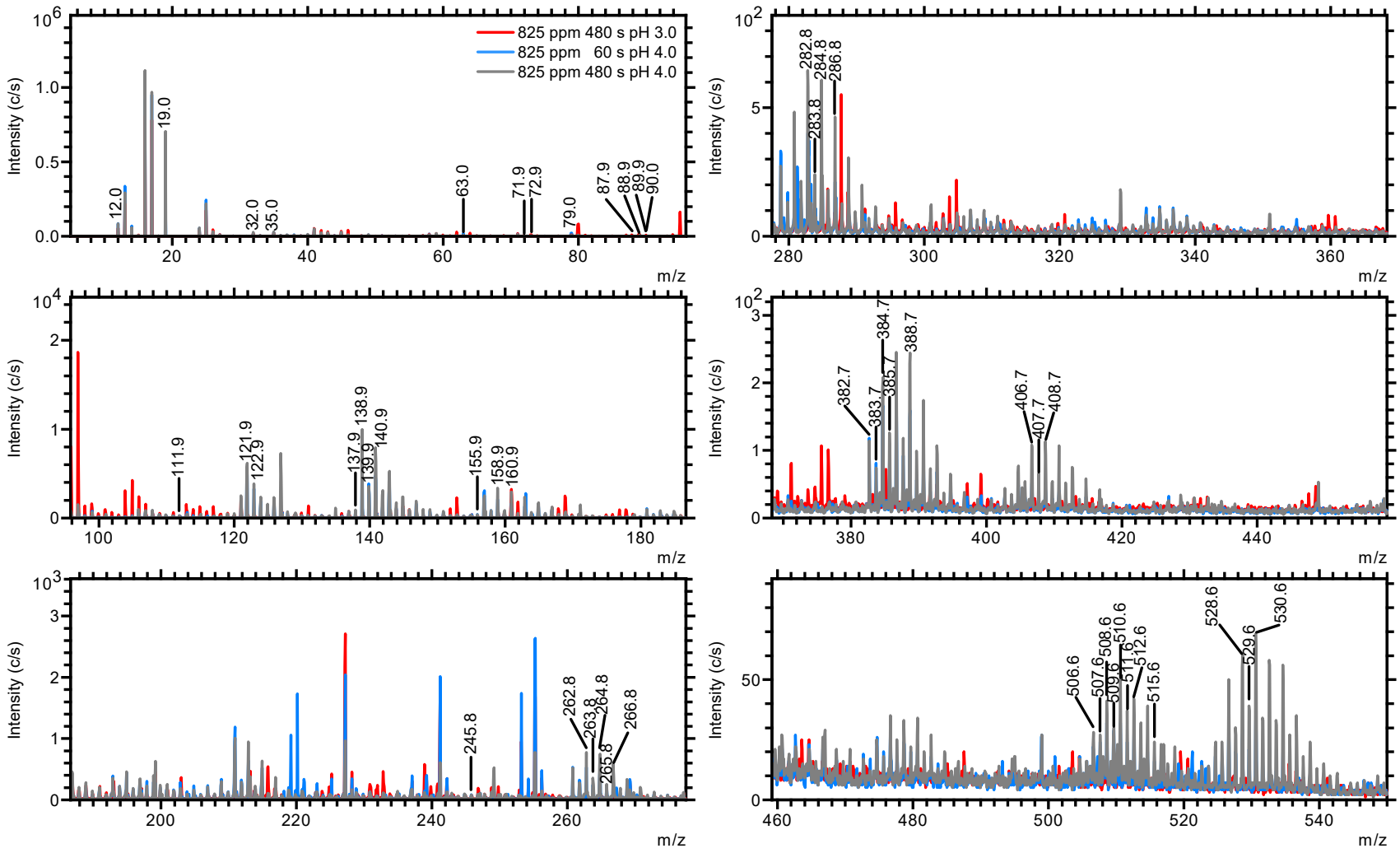

Figure 3.7: Mass spectra (negative polarity) in the m/z range 0–540 measured on ZrCCs prepared on cold rolled steel at three combinations of bath parameters as indicated in the legend. Characteristic ion fragments are presented in Table 3.5.

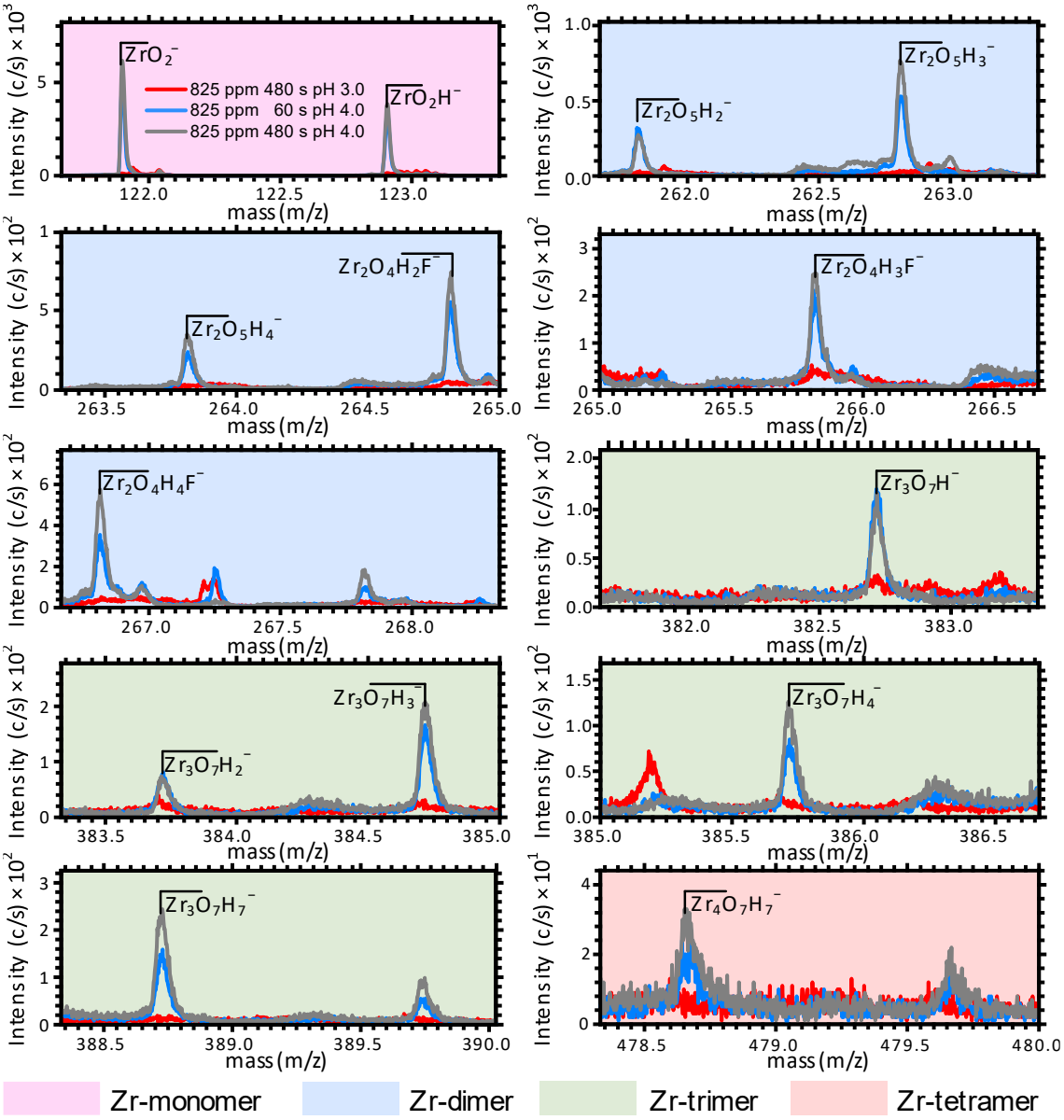

Figure 3.8: ToF-SIMS negative ion spectra of ZrCCs prepared at various combinations of bath parameters on cold rolled steel. Characteristic fragmentation ions are assigned.

Although not measured in the solution, ToF-SIMS allows us to infer a plausible connection between the aqueous species involved in the solid-phase formation in the precipitate and confirm the proposed structure of ZrCCs. The tetrameric peak, although not the most intensive among polymeric species (Figure 3.9), can undoubtedly confirm that ZrCC contains Zr in the tetrameric form, considering its fragmentations during ToF-SIMS measurements. Finally, and most notably, trimeric and tetrameric structures are present in samples obtained at higher pH, strongly suggesting that not only does the ZrCC thickness increase with longer conversion times but also that polymerised coating forms at pH = 4.0, and presumably, above, as indicated in *Chapter 2*. Also, the intensities of Zr peaks in the case of pH = 3.0 are very low, suggesting that almost no conversion layer is formed at pH = 3.0 (vide infra).

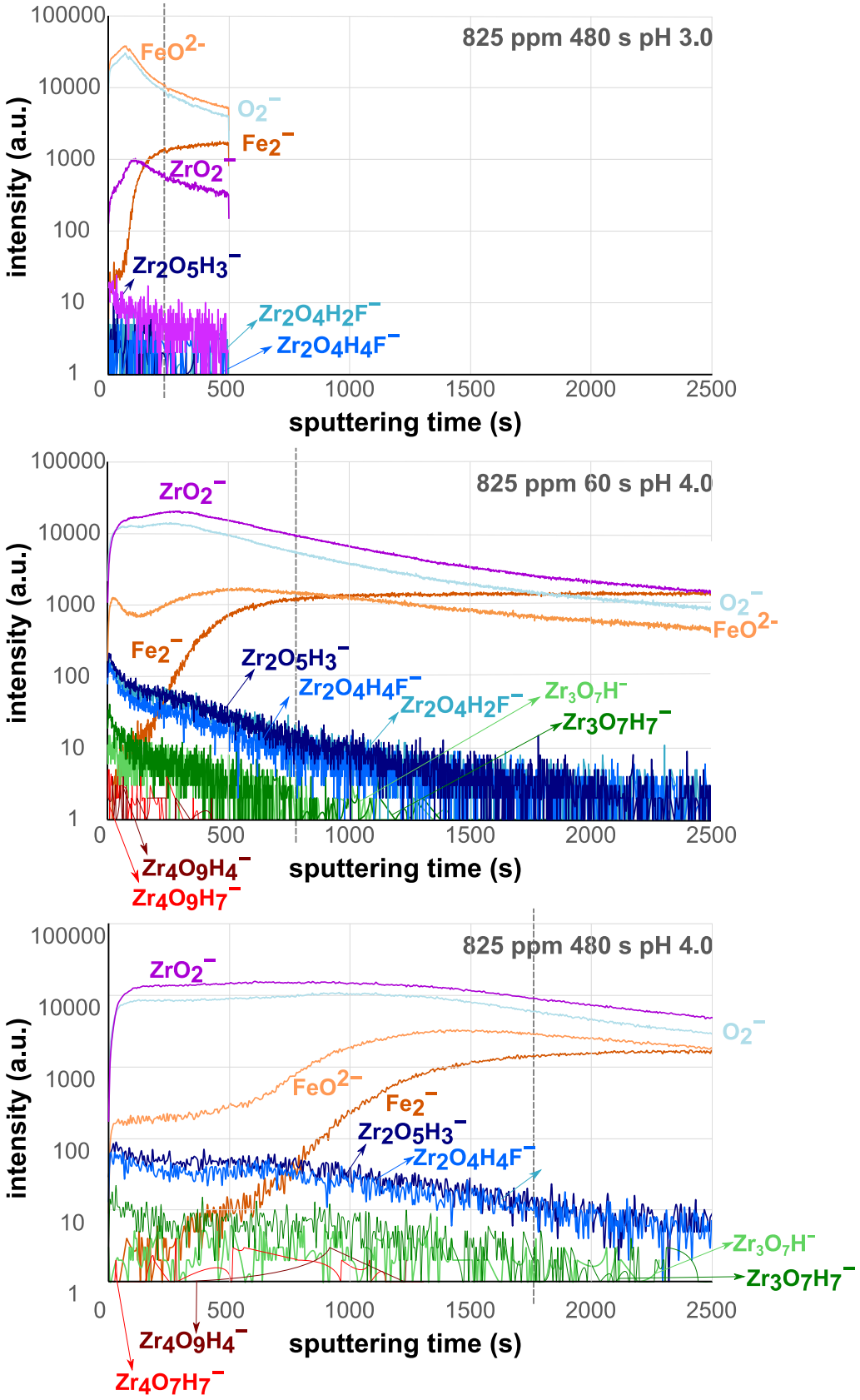

Figure 3.9: ToF-SIMS depth profiles of selected Zr and Fe fragments of ZrCCs prepared at three combinations of bath parameters. Gray dashed vertical lines indicate the ZrCC thickness obtained from the drop of the oxygen intensity peak value to half.

3.2.2.2 EIS results

The EIS results (Table 3.6) obtained for the chosen ZrCC bath parameter combinations, albeit in a slightly more acidic medium of simulated acid rain (pH ≈ 5) presented in Figure 3.10, show similar Nyquist plot shapes for the samples prepared in the same manner in dilute Harrison's solution (pH 5.2). The EIS fitting procedure and discussion, thoroughly elaborated therein, can be seamlessly applied herein. Equivalent electrical circuits (EECs) used for fitting are given in Figure 3.10a-b. In this context, either one (Figure 3.10a) or three (Figure 3.10b) time constants are presumed to indicate appropriate ZrCC formation, with the sum of resistances giving the overall polarisation resistance (R_p). A small capacitive loop at high frequency (Figure 3.10c) was not fitted due to its negligible value and high-frequency effects induced by the reference electrode. For cases with three time constants, the EEC with only two time constants was used (Figure 3.10b). In that case, the sum of two time constants gives the value of R_p, as elaborated thoroughly in *Chapter 2.3.1.2.1.* Specifically, the high-frequency loop (Figure 3.10c) indicates complete ZrCC coating formation for 825 ppm/480 s/pH 4.0. Further, the second middle-frequency time constant (Figure 3.10b) can be attributed to the charge transfer resistance of faradaic reactions inside defects, while the third low-frequency time constant refers to the response of corrosion products. This contrasts the EEC with a single time constant (Figure 3.10b) observed for the bare sample and the samples with inadequate coating formation (exhibiting either a too thin coating in the case of 825 ppm/60 s/pH 4.0 and no coating with only some spots featuring ZrCC nodules for 825 ppm/480 s/pH 3.0), which also reflects in their lower R_p values.

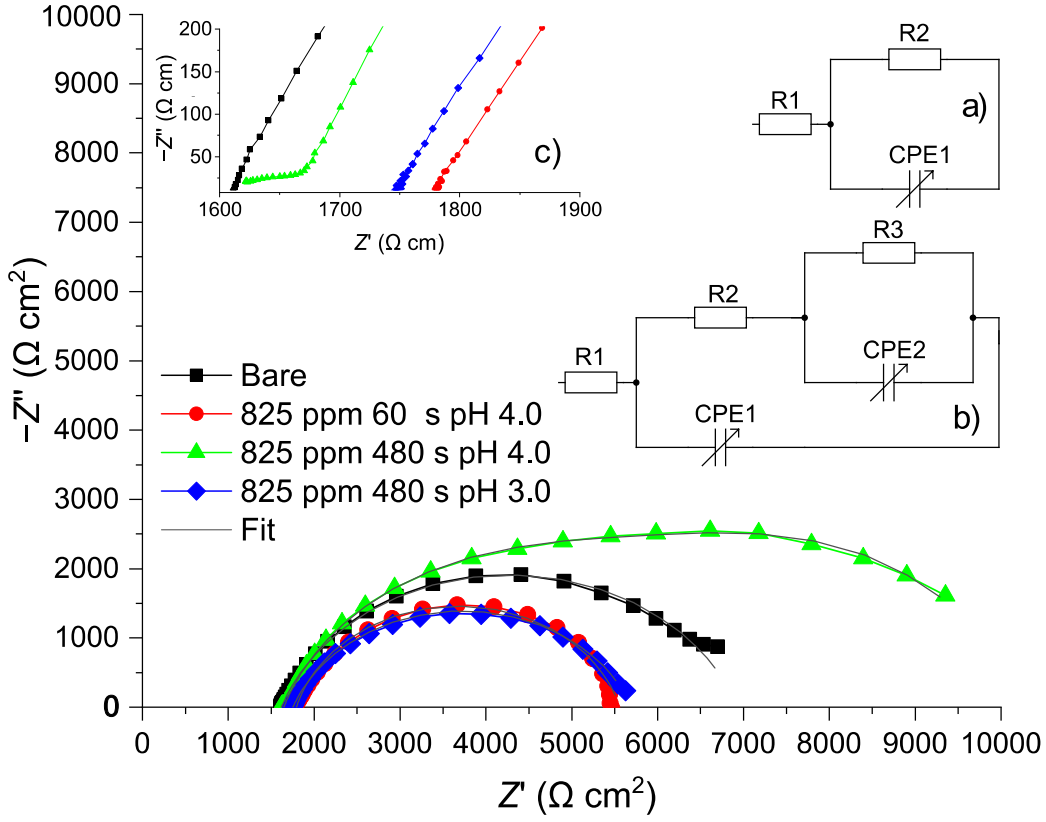

Figure 3.10: EIS spectra measured in simulated acid rain (pH ≈ 5) on ZrCCs prepared on cold rolled steel at three combinations of bath parameters. The enclosed EECs (a,b) were utilised for fitting. Only EEC in (b) was applied on 825 ppm/480 s/pH 4.0; the remaining samples were fitted with EEC in (a). The inset (c) displays high-frequency spectra.

Table 3.6: EIS fitting results employing EECs in Figure 3.10.

Sample	R1 (Ω cm^2)	R2 (Ω cm^2)	Y_0 CPE 1 (Ω^{-1} s^n)	CPE 1 n	R3	Y_0 CPE 2 (Ω^{-1} s^n)	CPE 2 n	χ^2	R2+R3(Ω cm^2)
Bare	1618	5315	208	0.79				0.015	6933
825 ppm/480 s/pH 3.0	1753	3947	248	0.78				0.015	5660
825 ppm/480 s/pH 4.0	1648	6104	161	0.80	2408	1833	0.96	0.017	7752
825 ppm/60 s/pH 4.0	1794	3766	134	0.84				0.029	5560

3.2.3 Conclusions

EIS and ToF-SIMS results suggest that adequate ZrCCs are those that are polymerised and contain a tetrameric structure but are also obtained at longer conversion times. Using ToF-SIMS, the presence of polymerised film, including tetrameric species, in ZrCCs was confirmed. Evidently, ToF-SIMS showed that tetrameric structures are found in ZrCCs prepared at pH = 4.0, increasing with longer conversion times. This is further confirmed by EIS data in simulated acid rain, suggesting that adequate ZrCC formation requires a pH of 4.0 and a specific conversion time (480 s herein) for the desired thickness. The thickness adequacy is affirmed by a high-frequency EIS loop, emphasising the significance of specific pH and conversion time conditions for effective ZrCC formation. Nevertheless, understanding the hydration numbers of ions, rates of exchange of coordinated water molecules around ions, and interaction energies between ions and water molecules requires advanced scattering methods. Therefore, fully unravelling the ZrCC formation mechanism awaits future research work.

Chapter 4

Influence of Fluoride and Chloride Ions on the Corrosion Resistance on Various Substrates

4.1 Literature Review

The behaviour of fluoride and chloride ions in corrosion has been extensively studied on aluminium and its alloys and, to a lesser extent, on steel and zinc substrates. In acidic solutions containing F^-, passive films on Fe were shown to dissolve uniformly due to the increased stability of HF complexes with surface Fe cations in more acidic environments, while at pH > 5, pitting corrosion occurs [274, 275]. This was ascribed to decreased formation and transfer of soluble F-complexes, leading to less pronounced oxide layer thinning and localized attack in less acidic to basic conditions [274, 276]. For chlorides, it was observed that Cl-induced pitting on Fe occurs above a critical Cl^- concentration of 0.3 mM and below a critical pH of 10.4 [277].

It is widely recognised that fluoride ions can effectively remove aluminium oxide films by forming aluminium-fluoride complexes and soluble AlF_3 films [278, 279, 280]; this process is essential in conversion coating solutions [281]. In contrast, Cl^- ions initiate a more localised attack in the form of pitting [278, 279, 282, 283, 284]. Similarly, it was demonstrated that Cl^- ions enhance corrosion by promoting the breakdown of air-formed oxide films and by assisting in maintaining an aggressive pitting microenvironment on carbon steel [285].

Xue et al. [280] found that in H_2SO_4 solutions with F^- ions, aluminium forms various Al—F complexes, influenced by fluoride concentration and solution pH, while zinc and iron remain unaffected by fluoride. This was further supported by the construction of *E*–pH (Pourbaix) diagrams.

The presence of Cl^- ions in F^- solutions further complicates this interaction, with studies by Carroll et al. [284] demonstrating that fluoride ions can modify aluminium oxide surfaces within specific concentration ranges, increasing susceptibility to Cl-induced corrosion. On the other hand, the study by Trompette et al. [286] offered a refined perspective by proposing that the corrosiveness of halide ions, including fluoride and chloride, should be evaluated beyond their ionic size, focusing instead on their interactions with water molecules. In particular, F^- ions (at pH=8.1), acting as cosmotropes, form robust bonds with water, thereby stabilising its structure and mitigating corrosion by preserving their hydration shells. In contrast, Cl^- ions (at pH=6.6), characterised as chaotropic, weaken structural integrity of water, making it easier to dehydrate and

infiltrate metal oxides, thus promoting pitting corrosion on Al. This was further observed on Fe in alkaline solutions (pH=10), where the kinetics of F^- attack is significantly lower than Cl^- [287].

The observed corrosion aggressiveness of fluoride ions is in the context of ZrCCs taken advantage of as they lead to surface activation of aluminium by removal of the native film, thus priming it for more uniform ZrCC deposition. Concurrently, the less aggressive ZrF_6^{2-} ions, otherwise the primary Zr-bearing component, improve the surface wettability for the successful deposition of subsequent layers [26]. In addition, fluoride complexation with ZrF_6^{2-} uniquely extends the ZrCC operational window by delaying the onset of Zr hydrolysis and precipitation to more manageable pH levels, as shown in *Chapter 3.1* [51]. Nevertheless, it was also indicated that ZrF_6^{2-} has an etching effect, albeit at high concentrations (10^{-2}—10^{-1} M [288, 289]).

In contrast to fluoride, chloride ions are not so commonly used as additives in conversion coating baths. However, there are some instances of providing titanium conversion coatings, which are similar to ZrCCs, with chloride sources like $TiCl_4$ [69, 290, 291, 292, 293]. Nevertheless, it is difficult to apprehend how this is accomplished, considering the vigorous nature of $TiCl_4$ [294]. Additionally, ZrCC baths often include ammonium bicarbonate as a pH adjuster and buffer, highlighting the complex interplay of various additives in corrosion processes. Given all this intricate interaction, a nuanced understanding of the individual and combined effects of fluoride and chloride ions on different substrates and in the presence of other solution additives is essential.

Building upon our previous research featured in *Chapter 2*, our initial goal was to compare the effects of free fluoride and chloride ions, deliberately excluding ZrF_6^{2-} due to their mild nature. This endeavour has expanded into a detailed study of their corrosion effects, in conjunction with the buffering agent, further supported by equilibrium calculations that consider the entire solution composition and ion interactions in much more complex equilibria. To the best of our knowledge, no study has yet investigated the combined effects of fluoride and chloride solutions with ammonium bicarbonate on these particular substrates. In our opinion, this approach not only highlights the importance of evaluating all species present in the solution at their respective concentrations but also lays a foundational framework for future corrosion studies involving complex solutions, particularly those incorporating conversion agents and additives in conversion coating baths.

4.2 Experimental

4.2.1 Materials, chemicals, preparations

Solutions were prepared to closely resemble those used in *Chapter 2*. but without H_2ZrF_6, thereby mimicking a "blank" H_2ZrF_6 solution to minimise the impact on the electrochemical double layer composition. The decision not to study the combination of halide ions with the conversion agent was made not only because of its demonstrated non-activating and less aggressive nature (vide supra) but also to avoid immediate surface passivation with ZrCCs at the OCP, which would make polarisation measurements unfeasible.

As noted at the beginning, free F^- ions, both pre-existing in formulations and released through the hydrolysis of H_2ZrF from previous conversion processes, enable surface activation. Consequently, in this study, we deliberately adjusted F^- concentrations to mirror the highest and lowest levels used in *Chapter 2* (0.007 and 0.070 M). This adjustment was made under the assumption of complete H_2ZrF_6 hydrolysis, which typically does not occur (*vide infra*), resulting in F^- levels six times higher than the selected H_2ZrF_6

concentrations of 0.007 and 0.070 M, giving 0.0042 and 0.0420 M, respectively. These concentrations fall within the lower range observed in commercial ZrCC set-ups, as indicated by some of the available Safety Data Sheet (SDS) information. Typically, literature reports mention the use of concentrates containing H_2ZrF in the range of 10^{-2} to 10^{-1} M, with or without free F^- at levels around 10^{-2} M [295, 296, 297, 298, 299, 300]. Since usually 1 % of these concentrates are recommended for the preparation of commercial ZrCC baths, this translates to concentrations approximately ranging from 10^{-4} to 10^{-3} M for H_2ZrF_6 and 10^{-3} M for free F^-, respectively [295, 296, 297, 298, 299, 300]. However, for improved corrosion protection properties, it is advisable to also consider higher concentrations of H_2ZrF_6, both in commercial settings [299, 300] and as demonstrated in *Chapter 2*. Thus, this may lead to the adjustment of higher free F^- (10^{-2} M) concentration ranges that match those employed in the current study. Nonetheless, it was shown that higher concentrations (10^{-1}–10^{-2} M) of free F^- are detrimental to the film formation of ZrCC [288]. However, this observation was explicitly made on magnesium alloy and at significantly lower pH levels [288] and would require a further separate study on other materials.

For further consistency with *Chapter 2*, a pH level of 4.0 was chosen, an intermediary value that conclusively promotes ZrCC deposition on all three substrates employed. This intermediary pH not only favours the deposition of ZrCC on various substrates but also ensures the complete dissociation of HF into free fluoride ions (pK_a value of HF = 3.18 [301]). Finally, NH_4HCO_3 was used as the pH-adjusting agent, consistent with its common use in both commercial and homemade zirconium conversion baths [9] (*vide supra*), resulting in concentrations of 0.0030 M and 0.0300 M, which are presumably of a similar order of magnitude to those used in analogous H_2ZrF_6 solutions.

For comparison, identical concentrations of Cl^- were employed alongside the same buffering agent and pH.

4.2.2 Electrochemical measurements

Electrochemical experiments were carried out in the same setup described in *Chapter 2*. One series of samples was allowed to rest at the OCP for 1 h to reach a quasi-steady state before performing PPC measurements to assess the influence of the OCP stabilisation. PPC measurements were conducted in the same manner as described in *Chapter 2*. Tafel extrapolation method to extract corrosion parameters (corrosion potential, E_{corr}, and corrosion current density, j_{corr}) from PPCs was performed using NOVA 2.1 software, from which R_p and corrosion rates were calculated according to the standard ASTM G59–97 [97]. The repeatability of the measurements was satisfactory; representative results from repetitions are presented here. For corrosion rate calculations, equivalent weights (EW), defined as the molar mass divided by the number of transferred electrons, were those of the main alloy elements as follows: For CRS, the EW of Fe (27.92 g/mol); for AA5754, the EW of Al (8.99 g/mol); and for Zn, the EW of Zn (32.69 g/mol). These values were accompanied by the respective element densities, namely 7.85 g/cm^3 for Fe, 2.66 g/cm^3 for Al, and 7.13 g/cm^3 for Zn.

Electrochemical measurements were conducted in solutions containing free F^- and Cl^-. Specifically, electrolytes were prepared using 0.00422 M and 0.0420 M solutions of hydrofluoric acid (HF 39.5 %, Carlo Erba, Val de Reuil Cedex, France) and hydrochloric acid (HCl 37 %, VWR International S.A.S, Fontenay-sous-Bois, France), respectively. These solutions were further adjusted to a pH of 4.0 using approximately 0.0030 M and 0.0300 M of ammonium bicarbonate (NH_4HCO_3) for each acid, with the rationale behind this electrolyte composition explained before.

Given its relatively high concentrations, comparable in magnitude to those of halide ions, the influence of NH_4HCO_3 on the equilibrium calculations was also considered. Consequently, separate calculations were conducted for the metal-h_2O, metal–F, metal–Cl, metal–NH_4HCO_3–F, and metal–NH_4HCO_3–Cl systems, presented in the form of *E*–pH diagrams.

4.2.3 Equilibria diagrams

The *E*–pH predominance diagrams presented were produced again using Spana (*vide supra*, *Chapter 3.1*), without any modifications or omissions of species or equilibrium constants from its default database. The database for species of interest herein contains mostly work from B. Beverskog and I. Puigdomenech [302, 303], the Organisation for Economic Co-operation and Development-Nuclear Energy Agency (OECD-NEA) [304, 305], National Institute of Standards and Technology (NIST) standard Reference Database [306], Brown and Ekberg [49], Baes and Mesmer [237] and Nordstrom and May [307] as well as other newer geochemical sources, including [308, 309].

While Davies equation represents the simplest between them and is convenient for concentrations ≤ 0.1 molal, the HKF model generally performs well at low ionic strengths, as demonstrated with electrolytes at ≤ 0.2 molal [172] and a wide range of temperatures, making it suitable for the conditions herein in addition to its ease-of-use. On the other hand, SIT uses ε chosen to fit experimental data at 25°C (*vide supra*, *Chapter 3.1*). Moreover, the SIT model, in addition to being a recommended default in the TDB project of the OECD-NEA [177, 310] and shown to produce useful results in *Chapter 3* led to the inclusion of incorporation of a larger number of complexes when applied in this context. This, in our view, more accurately reflects the observed behaviour, thereby justifying its use in this study as well (*vide infra*). In addition, default Hummel's estimation method [311] for ε (*vide supra*, *Chapter 3.1*) was maintained due to the ongoing uncertainty in updated SIT coefficients, especially concerning Fe-halide complexes, as indicated recently by NEA-OECD [304]. However, it is worth noting that despite convergence issues at extreme electrode potentials, i.e., outside the stability region of water [173], the SIT model, by considering ionic strength effects, led to the occurrence of certain complexes (e.g., fluoride ones with Fe at lower potentials) in Pourbaix diagrams, similar to the findings of Xue et al. [280] albeit without formation of solid fluorides.

The total concentrations of dissolved substrate ions, namely Fe, Al, and Zn, used for constructing *E*–pH diagrams, were determined from an electrochemical quartz crystal microbalance (EQCM) study [32] of both commercial and homemade ZrCC baths, where a rough recalculation for the magnitude order for Fe dissolution gives the concentration of 10^{-6} M. This was particularly noted after 5-minute conversion time, with mass losses increasing but staying within the same magnitude for longer times (more precisely, 9.13×10^{-7} M after 5 min, closer to industrially used conversion time, and 4.20×10^{-6} M after 30 min, respectively). Al and Zn were assumed to follow the same magnitude due to minor differences in mass losses compared to Fe. It should be noted that this study [32] only mentioned the use of Henkel's TecTalis® process [312] containing Cu without explicitly stating if the solutions used contained pre-added free fluoride. However, based on this limited data, we can infer the expected magnitude to perform equilibrium calculations that can further support our electrochemical findings (*vide infra*). Nevertheless, this very concentration is also the standard threshold for corrosion defined by Pourbaix [138] and was used as the only concentration level for metal ions herein.

4.3 Results and Discussion

4.3.1 Electrochemical results

Figure 4.1a,c,e presents OCP curves as a function of immersion time for CRS, AA5754 and Zn in Cl^- and F^- solutions of two concentrations. The OCP stabilisation occurs more rapidly at higher concentrations (0.0420 M) of both ions. In the case of the CRS substrate (Figure 4.1a), all OCP values at the end of the 1 h-stabilization period show a minimal variation, with differences around 30 mV. The influence of F^- on the AA5754 substrate (Figure 4.1c) reflects a noticeable reduction in OCP in the presence of F^-, with the most pronounced difference between concentrated F^- and Cl^- solutions being 665 mV and 314 mV for less concentrated solutions, both suggestive of a pronounced galvanic effect, probably the removal of native Al (hydro)oxide by etching effect of acidic F^-. For Zn substrates (Figure 4.1e), Cl^- ions lead to a more negative OCP, with the largest difference being about 80 mV when compared to a 0.0042 M F^- and a 50 mV difference observed within F^- solutions, neither of which suggests a notable galvanic effect [313].

Figure 4.1b,d,f shows that none of the substrates achieves proper passivation, as indicated by the high limiting current density values levelling off at more positive potentials, suggesting the formation of less protective surface films or adsorbed species. This is undoubtedly underscored by the formation of films directly from halide ion solutions without the pre-passivation in a halide-free medium, which would benefit the protective film development [287, 314]. The respective OCP and PPC data, along with their below-described results from Tafel extrapolation, are further illustrated in Figure 4.2. Complete Tafel extrapolation results, with corrosion current densities recalculated to corrosion rates for inter-substrate comparison, are provided in Table 4.1.

A concentration of 0.0420 M of both Cl^- and F^- increases corrosion rates and decreases polarisation resistance across all substrates, while stabilisation at OCP generally mitigates corrosion rates (Figure 4.1 and Table 4.1).

In particular, from Figure 4.1, Figure 4.2 and Table 4.1, it is observed that CRS (Figure 4.1b, Figure 4.2.) exhibits marginally higher corrosion rates with F^- than with Cl^-, especially at 0.0420 M, although E_{corr} remains stable at approximately −0.70 V. The absence of OCP 1 h-stabilization, however, leads to an increase in corrosion rates of 0.0420 M F^- solutions. For AA5754 (Figure 4.1d, Figure 4.2), F^- pronouncedly increases corrosion rates more than Cl^-, reflected also in more negative E_{corr} (up to −1.306 V for F^- versus around −0.65 V for Cl^-), indicating a less noble surface conducive to its activation role in the ZrCC process. Moreover, both ions at 0.0420 M increase Zn corrosion rates (Figure 4.1f, Figure 4.2), with F^- reaching rates of AA5754 and Cl^- exceeding those rates on both CRS and AA5754. However, the E_{corr} of Zn remains relatively unaffected, ranging between −0.982 and −1.085 V, though the highest Zn corrosion rates occur with 0.0420 M F^- without OCP stabilisation.

However, although OCP stabilisation does not significantly alter corrosion rates, there is a subtle difference in the onset of limiting current (mass-transport controlled), specifically in the magnitude of limiting currents on CRS (Figure 4.1b). Solutions containing Cl^- typically initiate limiting regions at higher current densities, except in 0.0042 M, non-OCP-stabilised case. Conversely, F^- solutions generally induce limiting region onset at lower current densities. Only in the case of 0.0420 M, OCP-stabilized F^- solution, the onset of the limiting region occurs at the same magnitude as that observed with Cl^- solutions.

Table 4.1: OCP and Tafel extrapolation results of PPCs for CRS, AA5754, and Zn in various solutions of F^- and Cl^-, with NH_4HCO_3 buffer at pH=4.

Substrate	Halide ion	Concentration (M)	OCP stabilization	E_{corr} (V)	i_{corr} (µA)	j_{corr} (µA/cm^2)	$\lvert b_a \rvert$ (V/dec)	$\lvert b_c \rvert$ (V/dec)	Polarisation resistance (Ωcm^2)	Corrosion rate (mm/year)
CRS	**F^-**	0.0042	no	−0.695	11.60	14.80	0.170	0.410	4491	0.17
	F^-	0.0420	no	−0.677	37.70	48.00	0.126	0.298	1019	0.56
	F^-	0.0042	**yes**	−0.697	6.07	7.73	0.102	0.466	6007	0.09
	F^-	0.0420	**yes**	−0.674	20.30	25.90	0.107	0.203	1496	0.30
	Cl^-	0.0042	no	−0.679	7.45	9.49	0.219	0.471	8706	0.11
	Cl^-	0.0420	no	−0.696	21.70	27.60	0.104	0.388	1647	0.32
	Cl^-	0.0042	**yes**	−0.693	4.45	5.67	0.138	0.444	10286	0.07
	Cl^-	0.0420	**yes**	−0.687	13.70	17.50	0.080	0.326	2033	0.20
AA5754	**F^-**	0.0042	no	−1.168	7.01	8.93	0.281	0.227	7780	0.10
	F^-	0.0420	no	−1.276	57.90	73.80	0.244	0.197	818	0.82
	F^-	0.0042	**yes**	−1.056	2.67	3.40	0.188	0.208	16094	0.04
	F^-	0.0420	**yes**	−1.306	51.70	65.90	0.256	0.214	979	0.73
	Cl^-	0.0042	no	−0.651	0.77	0.98	0.166	0.158	45699	0.01
	Cl^-	0.0420	no	−0.652	1.17	1.50	0.041	0.175	12249	0.02
	Cl^-	0.0042	**yes**	−0.718	1.54	1.96	0.204	0.231	30503	0.02
	Cl^-	0.0420	**yes**	−0.643	0.84	1.08	0.043	0.204	18197	0.01
Zn	**F^-**	0.0042	no	−0.986	6.67	8.49	0.160	0.226	6092	0.13
	F^-	0.0420	no	−1.045	52.20	59.10	0.113	0.150	602	0.89
	F^-	0.0042	**yes**	−0.982	46.40	7.73	0.181	0.439	9183	0.12
	F^-	0.0420	**yes**	−1.051	36.40	46.40	0.141	0.136	825	0.70
	Cl^-	0.0042	no	−1.024	6.36	8.10	0.174	0.211	6512	0.12
	Cl^-	0.0420	no	−1.086	36.90	47.00	0.178	0.167	1014	0.71
	Cl^-	0.0042	**yes**	−1.070	11.10	14.20	0.220	0.178	3848	0.21
	Cl^-	0.0420	**yes**	−1.075	34.80	44.30	0.173	0.154	1020	0.66

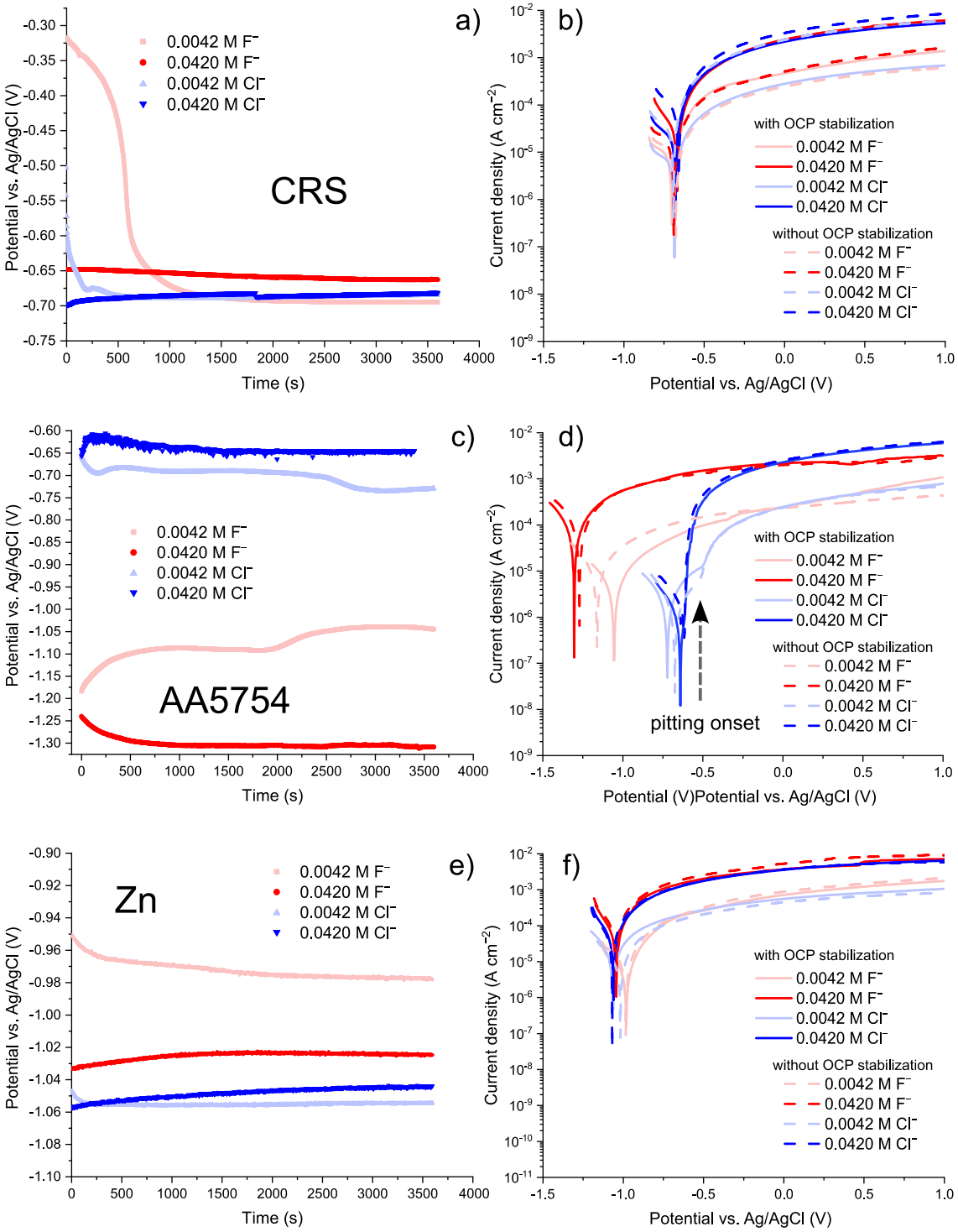

Figure 4.1: OCP (left) and PPC (right) measurements of CRS (a,b), AA5754 (c,d), and Zn (e,f) in various solutions of F^- and Cl^-, with NH_4HCO_3 buffer at pH=4.0. Note that in (b), the solid red curve overlaps with the solid blue curve.

For AA5754 (Figure 4.1d and Figure 4.2), F^- at 0.0420 M results in significantly higher corrosion current densities compared to equivalent concentrations of Cl^-, although lower F^- concentrations (0.0042 M) lead to similar current densities to Cl^- solutions. However, Cl^- solutions at 0.0420 M lead to pitting at around −0.5 V, whereas F^- solutions, despite higher corrosion current densities, exhibit extended limiting current density regions.

Lastly, in the case of Zn (Figure 4.1f and Figure 4.2), there is a notable impact of 0.0420 M of both ions on higher corrosion current densities, regardless of OCP stabilization. This suggests a general influence of ion concentration on corrosion rates.

It can be summarised that higher ion concentrations (0.0420 M) increase corrosion rates across all substrates. Ion type has no significant impact on CRS and Zn substrates but significantly influences the AA5754 substrate, where both ion type and concentration notably affect corrosion rates. However, further attention is needed to understand the effect of OCP stabilisation (*vide infra*).

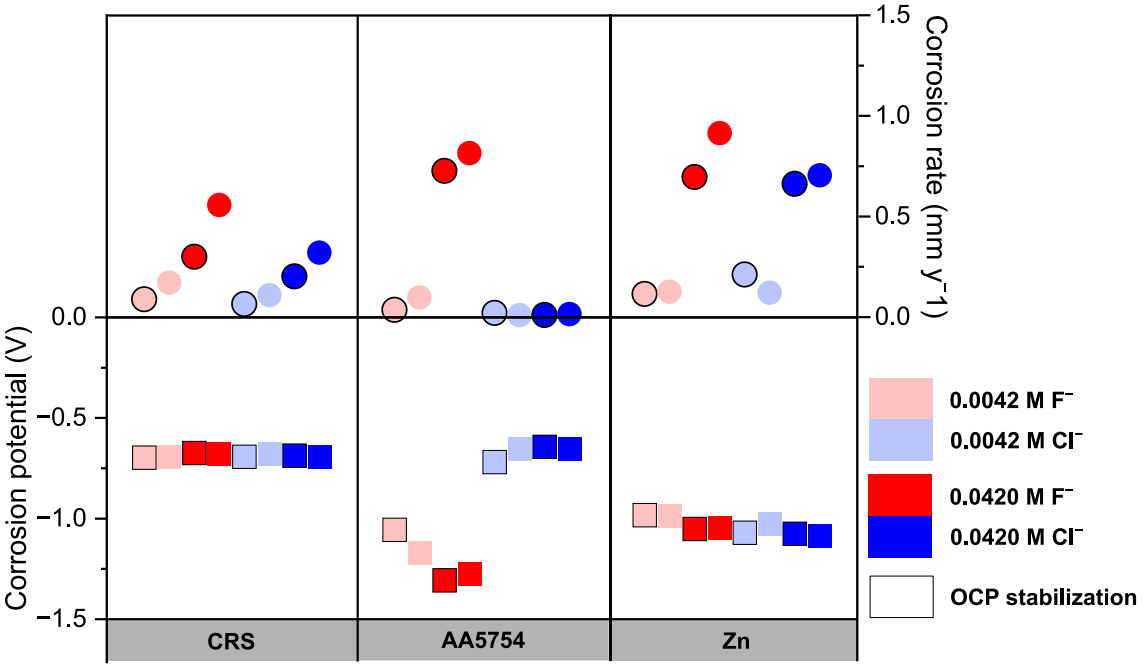

Figure 4.2: Presentation of corrosion potential and corrosion rate for CRS, AA5754 and Zn substrates in F^- and Cl^- solutions of two concentrations (0.0420 and 0.0420 M) with and without 1 h-stabilisation at OCP. All electrochemical data are presented in Table 4.1.

4.4 Equilibrium Calculations Results

The enclosed *E*–pH diagrams for metal-h_2O systems[†] (Figure 4.3) correspond fairly well with the existing ones [138, 302, 303]. In addition, using the SIT model agrees fairly well with applying HKF models for Fe and Zn [302, 303].

[†] As shown in *Chapter 3,* here is a significant difference in solubility between crystalline oxides and amorphous hydroxides. Amorphous hydroxides typically form initially at room temperature from fresh hydroxides, then slowly recrystallize into less soluble and stable crystal solids [173]. In addition, do not confuse neutral species with solid ones, as the state of the latter is clearly indicated by respective labels.

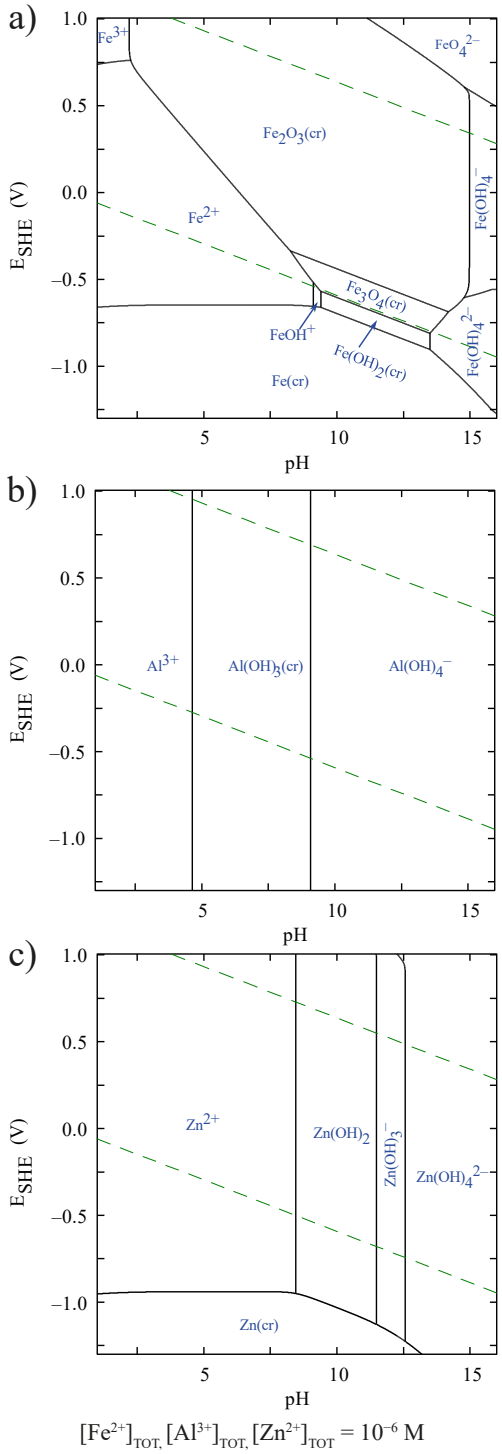

Figure 4.3: Constructed E–pH diagrams for Fe (a), Al (b) and Zn (c) in H_2O at 10^{-6} M.

4.4.1 *E*–pH diagrams for Fe-H_2O, Al-H_2O and Zn-H_2O

Figure 4.3a shows that iron dissolves in acidic environments, forming Fe^{2+} and evolving hydrogen gas. At higher potentials in such conditions, Fe^{2+} oxidises to Fe^{3+} and $FeOH_2^+$, with Fe^{3+} only present at pH levels above zero. In alkaline solutions, iron achieves passivity, forming anionic complexes like $Fe(OH)_4^{2-}$ and $Fe(OH)_4^-$. In the passive region, ferrous hydroxide ($Fe(OH)_2$ (cr)) can oxidise to magnetite (Fe_3O_4 (cr)) at higher potentials, which

can further oxidise to hematite (Fe_2O_3 (cr)), the most stable form at 25 degrees Celsius. Finally, hematite dissolves at extremely high potentials to $Fe(OH)_4^{2-}$ [302].

E–pH diagram for Al is taken as a representation of AA5754. Figure 4.3b shows aluminium dissolved as trivalent Al^{3+} ions in very acidic solutions and aluminate $Al(OH)_4^-$ ions in alkaline conditions. Between pH 4 and 9, it forms an oxide film, typically of complex nature [138].

Figure 4.3c shows that zinc does not passivate at a concentration of 10^{-6} M due to incorporating the uncharged aqueous hydrolysis complex $Zn(OH)_2$ in the *E*–pH diagrams. However, it is worth noting that zinc undergoes passivation at concentrations of $10^{-5.7}$ M, i.e., 2.51×10^{-6} M or higher, forming the oxide form, ZnO, that stabilises within a pH range of 8.2–12.1 at room temperature [303]. Since it is not impossible to achieve these concentrations in ZrCC conversion baths, further studies employing dissolution data on different substrates in ZrCCs are needed. It has been demonstrated that within the pH range 1–4, zinc corrosion is primarily controlled by cathodic mechanisms, with the hydrogen evolution reaction kinetics dictating the overall corrosion rates. From pH 4 to 11, Zn corrosion rates stabilize, attributed to the transition in the cathodic reaction from HER to ORR. However, the oxides formed in this range do not provide adequate corrosion protection [142]. In particular, at pH 12, the formation of an inner ZnO layer and an outer $Zn(OH)_2$ precipitated layer both contribute to a stable structure that acts as an effective anodic barrier. Conversely, at pH 13, the formation of soluble $Zn(OH)_3^-$ and $Zn(OH)_4^{2-}$ phases destabilizes the precipitated layer, leading to accelerated zinc corrosion. This layer further facilitates the catalysis of oxide growth through cathodic reactions [158].

4.4.2 *E*–pH diagrams for metal–F, metal–Cl, metal–NH_4HCO_3–F, and metal–NH_4HCO_3–Cl systems

From further comparison of *E*–pH diagrams within different systems (Figures 4.3–4.6), it becomes apparent that while there is no discernible disparity in the visual representation between –H_2O and –Cl systems (Figure 4.5), a notable contrast emerges within –F systems, particularly concerning CRS and AA5754 (Figure 4.4a,b) in terms of F-complexation. Applying the Hard and Soft Acids and Bases principle (HSAB) [315], similar to *Chapter 3* [51], F-complexation leads to stable complexes, thereby extending the onset of hydrolysis and precipitation. In terms of corrosion, stable complexes may passivate the metal surface and inhibit further corrosion, while less stable complexes may dissolve and provide limited protection.

For Fe, a predominant F-complexation is observable, displacing the active region at higher potentials, which is in the absence of F^- occupied by Fe^{3+} (Figure 4.4a). This phenomenon is further evident within the active corrosion region of Fe^{2+}, particularly pronounced in 0.0420 M F^- solution (Figure 4.4b), leading to the formation of FeF_3 complexes, which also aligns with the E_{corr} region measured herein. Dashed lines mark the FeF^+ region disrupted by SIT convergence issues, likely due to model complexity. Furthermore, for Fe, there is scarce available data for aqueous fluoride complexes [304], which is further complicated by the fact that virtually no data are available below an ionic strength of 0.5 mol dm^{-3}. This makes extrapolation to zero ionic strength difficult due to the established dependence of ion interaction coefficients of halide anions and Fe^{3+} on ionic strength, which is most pronounced for ionic strengths ≤ 0.5 molal [305]. This poses a question of the feasibility of the SIT model in this case. However, only the use of the SIT model resulted in the incorporation of F species in the OCP region, supporting electrochemical findings. Hence, while the HKF model balances accuracy with computational efficiency, the SIT model is preferred for systems exhibiting notable specific

ion interactions, such as concentrated electrolytes or those with complex ions, precisely the case here, providing a more detailed description of solution behaviour (*vide supra*).

In the case of Al (Figure 4.4c,d), as anticipated, the active corrosion region of Al^{3+} ions is significantly extended due to the presence of a series of F-complexes (AlF_2^+, AlF_3, AlF_4^-). This extension notably shrinks the passive region, with complexation intensifying at 0.0420 M and higher potentials (Figure 4.4d), ultimately obscuring the original passive region altogether. This aligns with findings from Chidambaram et al. [26], who observed that no passive Al film develops in solutions containing 0.024 M free F^-. This effect has otherwise significant applications in electrowinning in Zn electrolytes, where F^- facilitates Zn deposition on Al surfaces by removing the oxide layer from pure Al through F-complexation, as demonstrated by Xue et al. [280] and Paula et al. [316].

Conversely, the integration of NH_4HCO_3 to equilibrium calculations of –F and –Cl systems, as presented in Figure 4.6 and Figure 4.7, demonstrates minimal impact on CRS and AA5754, with the former exhibiting negligible formation of iron carbonate complexes, discernible as a narrow region between Fe^{2+} and Fe_2O_3 (cr). However, a substantial difference arises with Zn, where a series of carbonate and ammonium complexes are formed (Figure 4.6e,f and Figure 4.7e,f). The complexation with ammonium ions is especially pronounced at a bicarbonate concentration of 0.0420 M, with regions that, under increased Zn concentrations, would be replaced by solid Zn carbonate and oxide species.

The graphs obtained contradict those of Xue et al. [280], wherein solid FeF_2 and ZnF_2 species are observed at F^- concentrations as low as 0.01 M. In our view, this inconsistency stems from several factors. Firstly, older studies, including that from Xue et al., relied on equilibrium constants available at the time. Secondly, their calculations were conducted without ionic strength corrections, using equilibrium constants measured at varying ionic strengths. Additionally, Xue et al. focused on solids‡, rather than metal ion concentrations, coupled with limited consideration of aqueous species such as various hydrolysis products for iron and neutral aqueous complexes for zinc, as well as the omission of ions like sulphate ions.

4.4.3 Comparison of electrochemical and equilibrium data

The integration of electrochemical and thermodynamic data indicates that the effects of complexation on corrosion rates vary with the concentration of complexing ions and substrate type. Specifically, the formation of stable F-complexes on CRS at 0.0420 M may reduce corrosion rates by decreasing the amount of free dissolved Fe, especially at higher potentials during the anodic scan, and OCP/E_{corr} (Figure 4.4a,b). Contrary to expectations, this F^- concentration does not result in lower limiting currents but rather corresponds to those observed in Cl^- solutions. In Cl^- solutions, in turn, the typically higher limiting currents compared to F^- solutions can be attributed to the absence of predominant complexation of Fe with Cl^-, likely resulting in more Fe available for oxidation during the anodic scan, except for the 0.0042 M non-OCP stabilized solution (Figure 4.5a,b). Therefore, the additional F-complexation step at 0.0420 M, beginning at OCP and further enhanced by stabilisation, might delay the formation of the oxide layer during the anodic scan. Conversely, in Cl^- solutions, the absence of OCP stabilization at 0.0042 M not only leads to a lower amount of dissolved Fe but also seems to be low enough not to prevent the formation of the oxide surface layer. Here, the cosmo/chao-tropic nature of Cl^- and F^-

‡ Studying metal complex formation and solubility at low concentrations, like 10^{-6} M, offers a clearer insight into metal behaviour in solutions, avoiding the complications from surface phenomena and microstructural effects seen in solid species. Nonetheless, the latter is crucial for precipitation studies [173].

observed at alkaline pH [287] is not feasible due to complexation and subsequent passivation, both beginning in acidic solutions.

Similarly, for AA5754, no predominant Cl-complexation is observed (Figure 4.5c,d), supporting quite low corrosion rates obtained. However, F-complexation (Figure 4.4c,d) is significant throughout the entire active corrosion region of Al and becomes more pronounced at 0.0420 M and higher potentials. The complexation, which starts already at lower pH levels than those examined here and continues throughout the observed OCP and E_{corr} regions for both concentrations, might explain the negligible impact of OCP stabilization on the corrosion rates (Figure 4.2). The lower corrosion current densities observed with 0.0420 M F^- compared to 0.0042 M F^- can be ascribed to the continuous formation of soluble F-complexes without any predominant tendency to form a passive region. On the contrary, Cl^- induces pitting at 0.0420 M (Figure 4.1d). Since E—pH diagrams, as predominance equilibria diagrams, do not represent kinetic and local effects, the possibility of the formation of Cl-complexes due to local effects within the pit cannot be excluded. Modelling pit behaviour would employ higher metal concentration to replicate pit conditions by constructing additional equilibrium diagrams, like fractional or logarithmic ones, similar to Thomas et al. [142]. Based on the literature reviewed, the corrosiveness of F^- towards Al predominantly manifests as complexation, resulting in more uniform corrosion, while its cosmotropic nature mitigates the aggressiveness towards pitting.

In contrast, the impact of Cl^- is not observed in corrosion rates but rather in localized pitting, which is attributed to its chaotropic nature [286]. A higher affinity of Cl^- towards pitting on Al has been elaborated by Nguyen and Foley [317] and more recently by Natishan and O'Grady [282] as initial adherence to the surface oxide layer through electrostatic interactions at pH < 9. It was shown that Cl^- ions not only adsorb on the surface but are also incorporated into the oxide film, moving across a range of electrical potentials, both below and above the pitting potential. This movement destabilizes the protective oxide layer by altering the film resistivity and semiconducting properties, thereby making Al more susceptible to pitting. This can also lead to other physical disruptions, such as oxide blistering.

Lastly, the comparable effects of Cl^- and F^- on the corrosion rates of Zn, regardless of OCP stabilization, further enhanced at 0.0420 M can be rather attributed to the effect of NH_4HCO_3, resulting in extensive hydrolysis of Zn with carbonate and ammonium species at higher and lower potentials, respectively. The question remains whether the pH for this complexation is indeed reached during polarisation, given its higher values compared to Fe and Al. Hence, it can be articulated that corrosion rates of Zn increase with solution ionic strength. In terms of ZrCCs, however, this complexation would occur at a pH higher than that of zirconia precipitation, as shown in *Chapter 3* [51], thus not affecting the conversion process.

Predicting effects of Cl^- and F^- on ZrCC can be explained through incomplete hydrolysis of H_2ZrF_6 [318], as well as incomplete removal during rinsing through an exchange with hydroxide ions, leading to the existence of a certain amount of residual F^- in the form of zirconium oxyfluorides in ZrCCs [154]. However, F^- tends to exchange less rapidly than Cl^-, enabling the latter to eventually replace fluoride in the ZrCC films through the outer ligand sphere [319] over time, as confirmed by Šekularac et al. [33, 43]. Interestingly, while XPS revealed the presence of ZrO_2, ZrF_4, and other compounds in Zr conversion coating [42, 273] s, analogous Ti conversion coatings employing H_2TiF_6 were found only to incorporate TiO_2 [273].

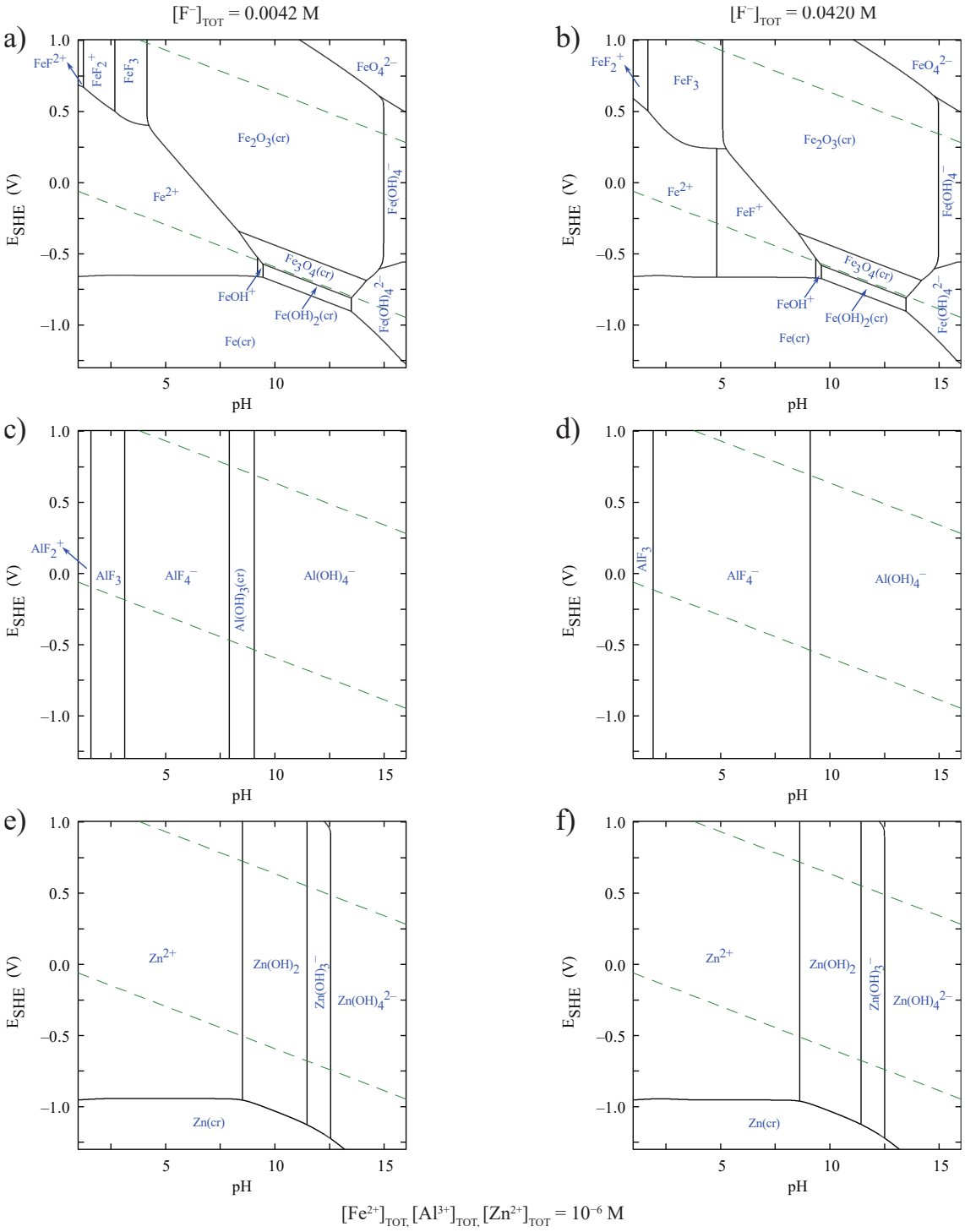

Figure 4.4: Constructed E–pH diagrams for Fe (a,b), Al (c,d) and Zn (e,f) in the presence of F^- at 0.0042 M (left) and 0.0420 M (right).

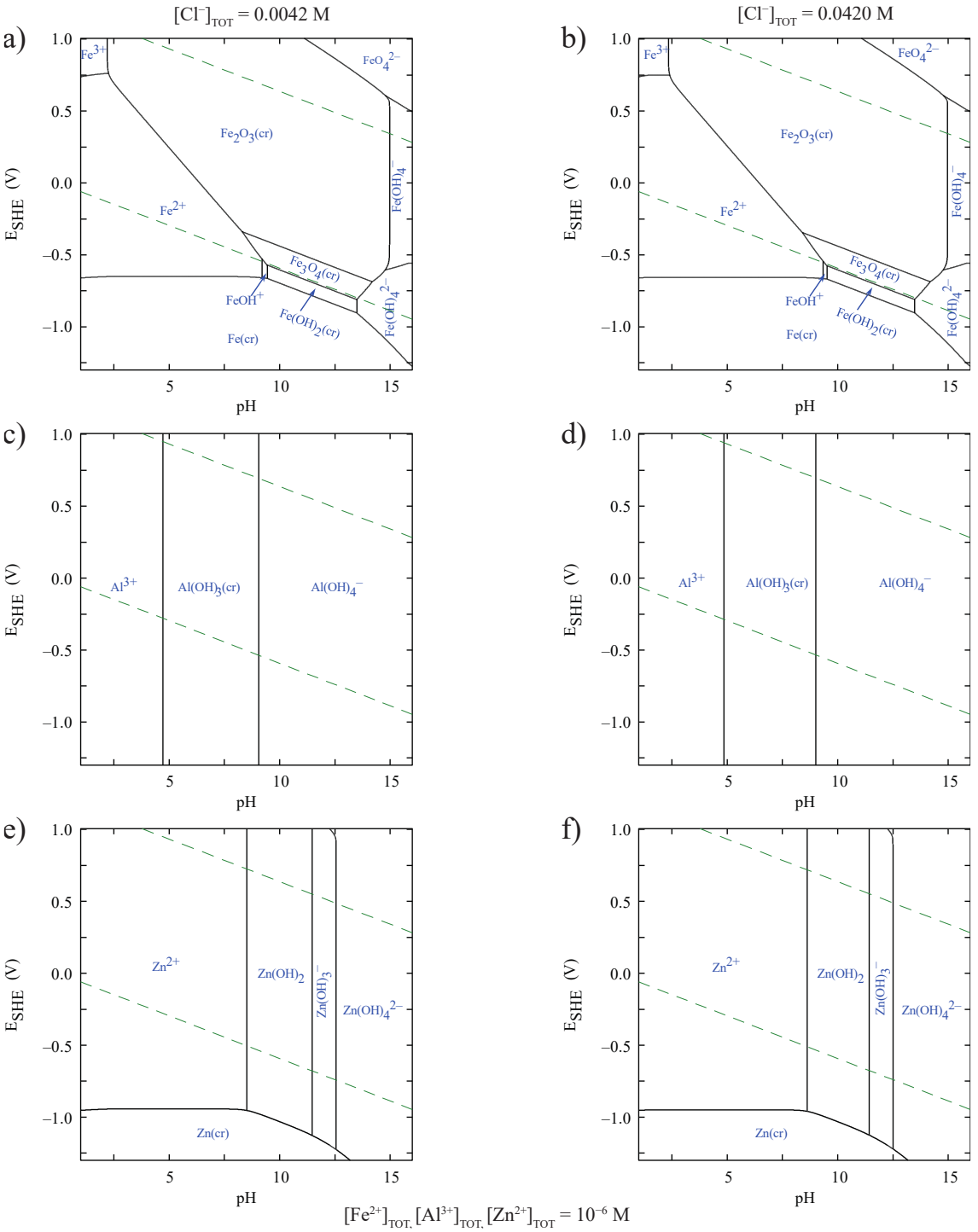

Figure 4.5: Constructed *E*–pH diagrams for Fe (a,b), Al (c,d) and Zn (e,f) in the presence of Cl^- at 0.0042 M (left) and 0.0420 M (right).

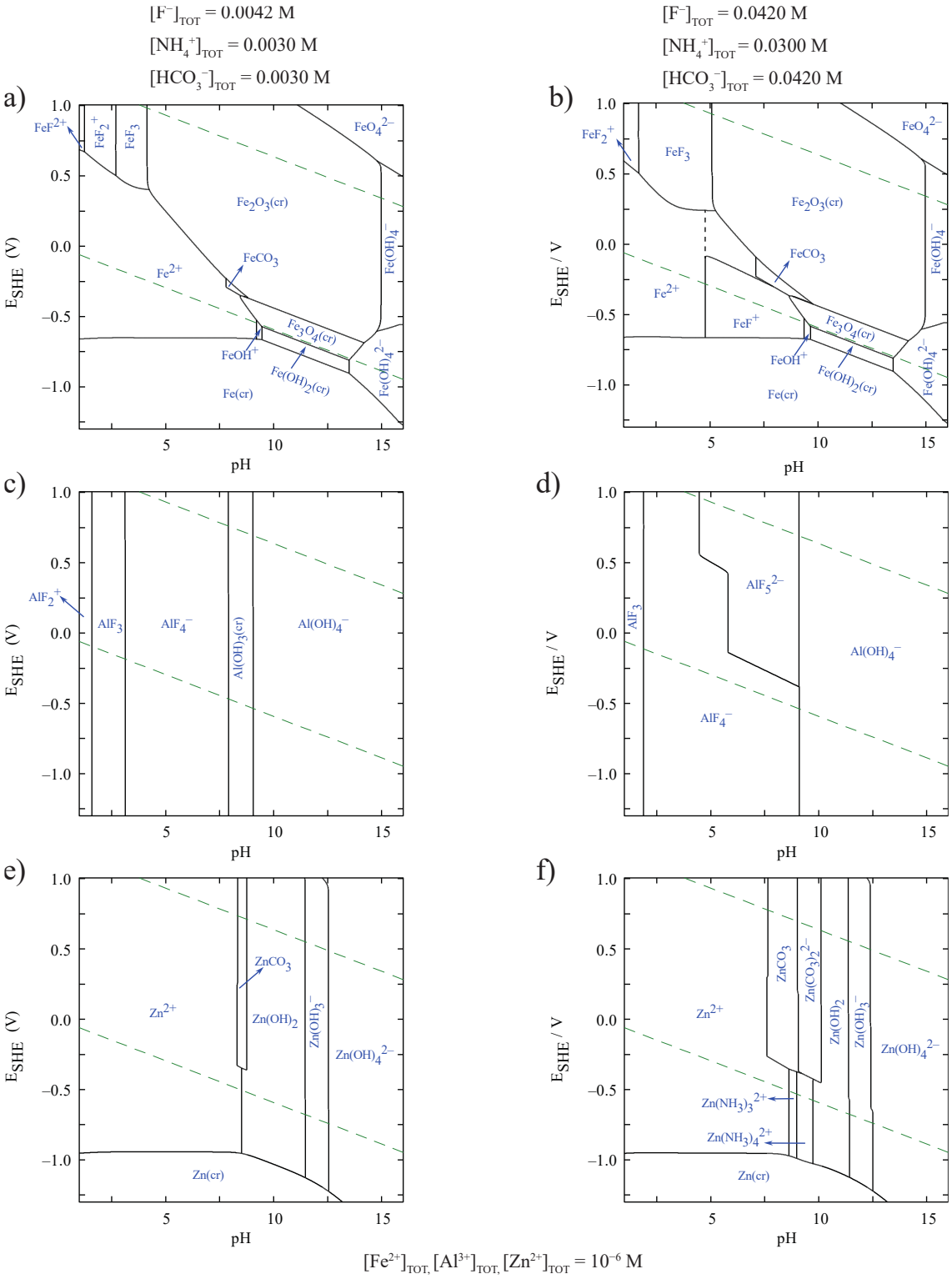

Figure 4.6: Constructed *E*–pH diagrams for Fe (a,b), Al (c,d) and Zn (e,f) in the presence of F^- and NH_4HCO_3 at 0.0042 M (left) and 0.0420 M (right).

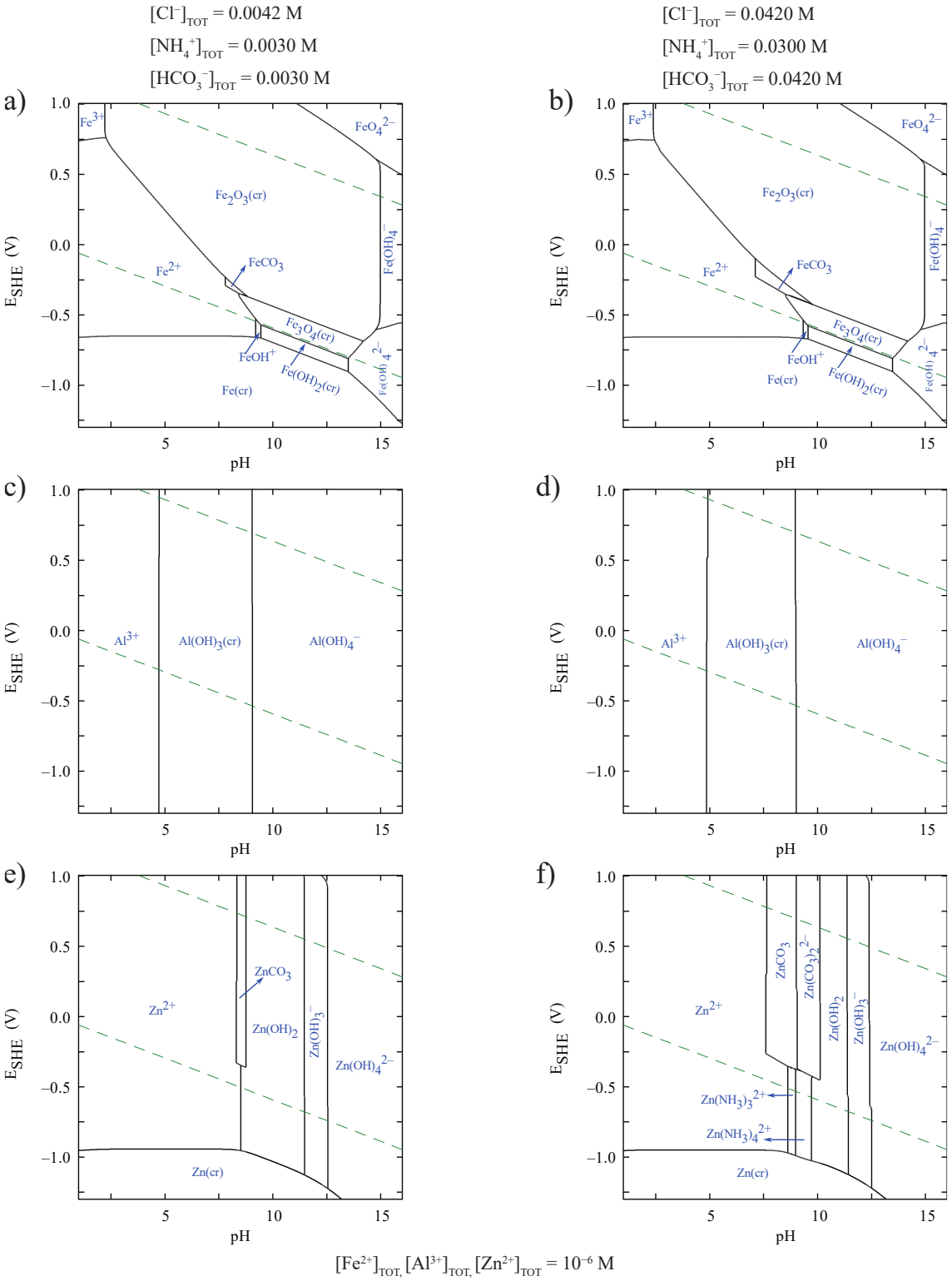

Figure 4.7: Constructed *E*–pH diagrams for Fe (a,b), Al (c,d) and Zn (e,f) in the presence of F^- and NH_4HCO_3 at 0.0042 M (left) and 0.0420 M (right).

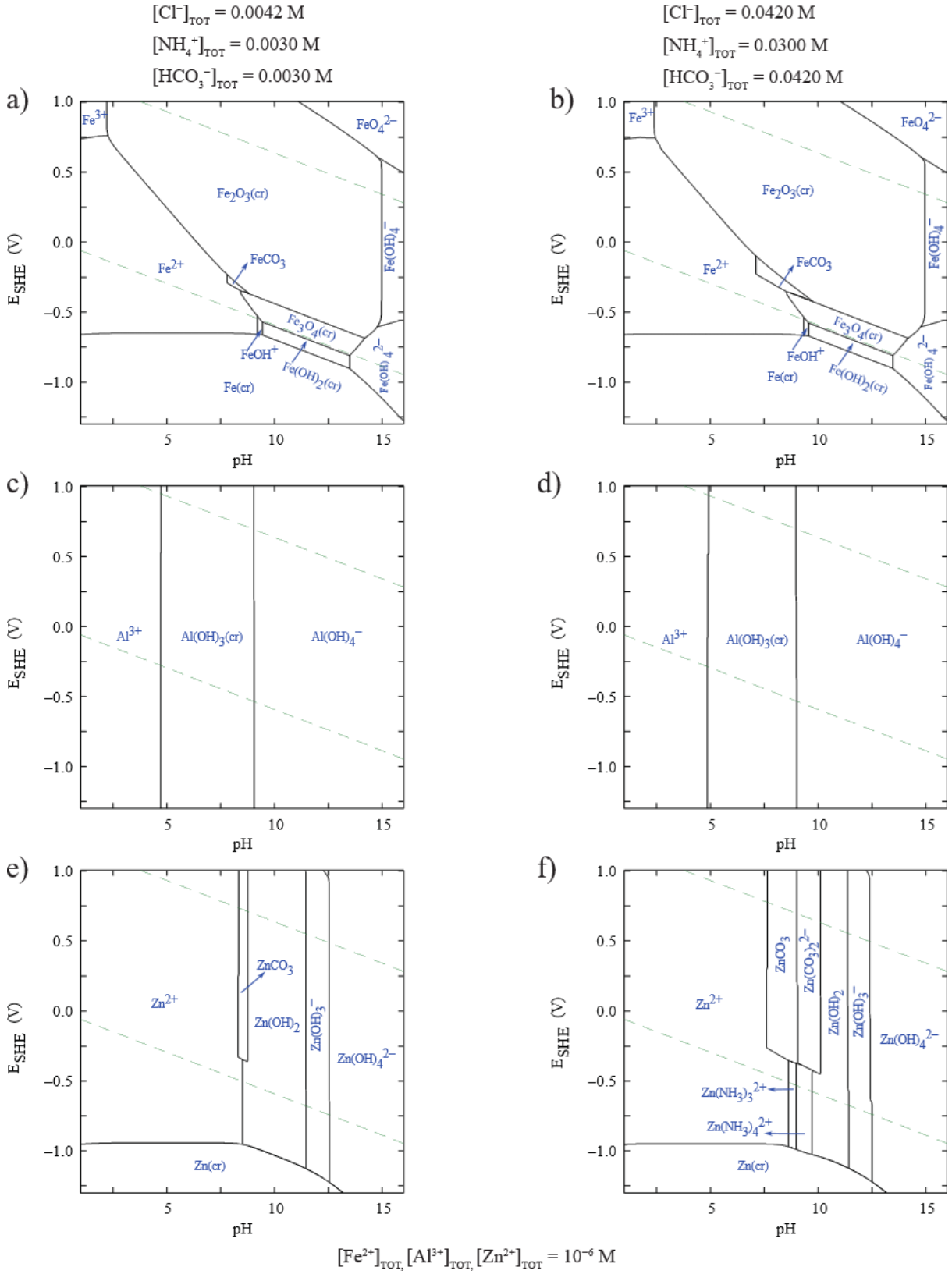

Figure 4.8: Constructed *E*–pH diagrams for Fe (a,b), Al (c,d) and Zn (e,f) in the presence of Cl^- and NH_4HCO_3 at 0.0042 M (left) and 0.0420 M (right).

4.5 Conclusions

This study investigated the corrosion behaviour of three substrates: CRS, AA5754 and Zn in environments containing F^- and Cl^- at 0.0042 and 0.0420 M concentrations in the presence of 0.0030 and 0.030 M ammonium bicarbonate at pH = 4.0, both with and without OCP stabilization. The generally observed electrochemical actions of F^- and Cl^- have been confirmed herein; however, they are further supported by thermodynamic calculations that considered the entire solution composition and ion interactions in much more complex equilibria.

For CRS, stable F-complex formation reduces corrosion rates by decreasing the amount of freely dissolved iron during anodic scans, thereby aiding the formation of the surface layer with insufficient protective properties. However, when complexation occurs in OCP-stabilized 0.0420 M F^- solution, this process is less pronounced. Conversely, Cl^- ions only reduce corrosion rates in 0.0042 M Cl^- non-OCP stabilized solution, indicating a balance between reduced free Fe availability and Cl^- concentration that does not interfere with the formation of the surface layer.

With AA5754, the effect of ion concentration is more pronounced. The concentration of F^- at 0.0420 M results in considerably greater corrosion rates than Cl^- due to complexation. At 0.0042 M, however, the corrosive effects of F^- and Cl^- are similar. Notably, Cl^- at 0.0420 M leads to pitting corrosion, while F^- induces a more extended limiting current range, suggesting a more uniform corrosion process, conforming to their inherent differences in cosmo/chao-tropic behaviour.

In the case of Zn, corrosion rates appear to be unaffected by the type of halide ion. Here, the advantage of thermodynamic calculations truly becomes apparent, as they indicate that the observed corrosion phenomenon can be due to the buffer, i.e., the formation of complexes with ammonium and carbonate ions, which further increases at 0.0420 M of NH_4HCO_3.

F-complexation, presented in predominance diagrams and reflected in uniform corrosion of Fe and Al, occurs at pH levels achievable during polarisation. However, for Zn, buffer-complexation occurs at a higher pH that might not be encountered during polarisation, thereby making it safer to say its behaviour is influenced by higher ionic strength.

Nevertheless, despite the inability to account for pitting behaviour in thermodynamic diagrams, considering complex equilibria supports the stabilisation effects on OCP and the differences in corrosion rates. Most importantly, it also aids in explaining that corrosion behaviour of Zn is influenced by ammonium bicarbonate complexation rather than by halide ions.

As such, this study emphasises the significance of accounting for complex equilibria in corrosion analysis, offering a framework for future studies, particularly those addressing intricate solutions with conversion agents and additives in coating baths.

Chapter 5

Comparative Study of ZrCC Formation on Various Substrates via Scanning Micro-probe Techniques

5.1 Introduction

Being electrochemically and pH-triggered, as shown in *Chapter 3.1* the ZrCC formation process requires *in-situ* monitoring of pH and oxygen changes to reveal its mechanism. To reiterate, shortly after immersion into a ZrCC bath, the metal surface becomes activated as outer oxyhydroxide layers are replaced by fluorides, facilitating further anodic dissolution. Simultaneously, hydrated metal oxides precipitate at micro-cathodic sites due to an interfacial pH increase caused by HER and/or ORR [9]. In that sense, cathodic reactions feed the ongoing metal oxidation. The use of scanning micro-probe technique (SPM) can be crucial in this research for its ability to analyse real-time cathodic and anodic reactions, facilitating the study of local pH and oxygen variations during ZrCC formation. This technique employs a vibrating conductive probe to measure potential differences in the electrolyte in contact with corroding metal, allowing for precise monitoring of *in-situ* pH and O_2 variations. The paramount ability of measurement of local pH and local concentration of dissolved oxygen lies in detecting minute electric fields generated by ion and electron flow during corrosion. Thus, in this preliminary study, the *in-situ* development of ZrCCs using scanning micro-probe techniques based on the scanning probe microscopy (SPM) was monitored on all three substrates of interest in this PhD thesis: CRS, Zn, and AA5754, under selected concentrations of H_2ZrF_6 and pH levels.

5.2 Experimental

5.2.1 Samples and chemicals

The same CRS, Zn and AA5754 samples from *Chapter 2* were cut to 1×1 cm dimensions to accommodate the scanning micro-probe techniques setup. The samples were embedded in epoxy resin (Buehler, EpoxiCure™, USA) with a round face along with wires to construct a working electrode. The subsequent sample preparation until conversion treatment was identical to the preparation for electrochemical measurements in *Chapter 2*. The working area was delimited with beeswax to prevent crevice corrosion, and the edge of the resin was encased with sticky tape to create a container for the electrolyte with a height of 3 mm. To corroborate the findings from *Chapter 2*, only specific H_2ZrF_6 bath conditions were chosen, namely 825 ppm/pH 4.0, identified as the optimal condition for CRS and Zn based on *Chapter 2* findings, thereby serving

as a benchmark. For comparative analysis, pH = 3.0 was also tested due to its known adverse effects on coating quality. The impact of concentration at a constant pH was assessed by exploring 150 ppm at pH = 4.0.

Additionally, the effect of pH at varying concentrations was examined by studying conditions at pH = 4.6 with both 150 ppm and 1226 ppm. The 150 ppm concentration, deemed the most suitable for AA5754, was consistently applied across all substrates to facilitate comparison. Conversely, the 1226 ppm level was chosen for CRS and Zn, as it was also pointed out as a region where optimum can be achieved in RSM and its distinctive EIS response in Zn, which suggested minimal diffusion control.

5.2.2 Local measurements

Local pH was measured using a commercial glass-type pH microelectrode (Unisense, pH-10) with a tip diameter of 10 µm in conjunction with a mini-Ag/AgCl reference electrode. Local O_2 concentration, i.e., dissolved oxygen (DO) was monitored using a needle-type retractable fibre-optic O_2 micro–optode (OXR50-UHS) with a tip diameter of 50 µm, connected to a FireSting O_2 oxygen logging meter, both supplied by Pyroscience™. Integrating the pH microelectrode and DO micro–optode into a commercial scanning vibrating electrode technique (SVET) and the scanning ion-selective electrode technique (SIET) system (Applicable Electronics™) facilitated probe movement. Data acquisition was performed concurrently using LV4 software from Sciencewares™ and PyroOxygenLogger from Pyroscience™. The distance between the pH microelectrode and DO micro-amperometric oxygen sensor was precisely controlled at 50-150 µm in a horizontal plane using custom-made dual-head stage micromanipulators, enabling in situ simultaneous monitoring of pH and DO concentration evolution [320]. The distance between the microprobes and the surface was controlled to be 20 µm. An additional mini-Ag/AgCl electrode was employed for the open circuit potential (OCP) monitoring, connected to the working electrode (WE) solution via a saline bridge. Due to rapid surface passivation resulting from ZrCC deposition, only point measurements were feasible, precluding mapping measurements for identifying anodic and cathodic regions. The test setup schematic is presented in Figure 5.1.

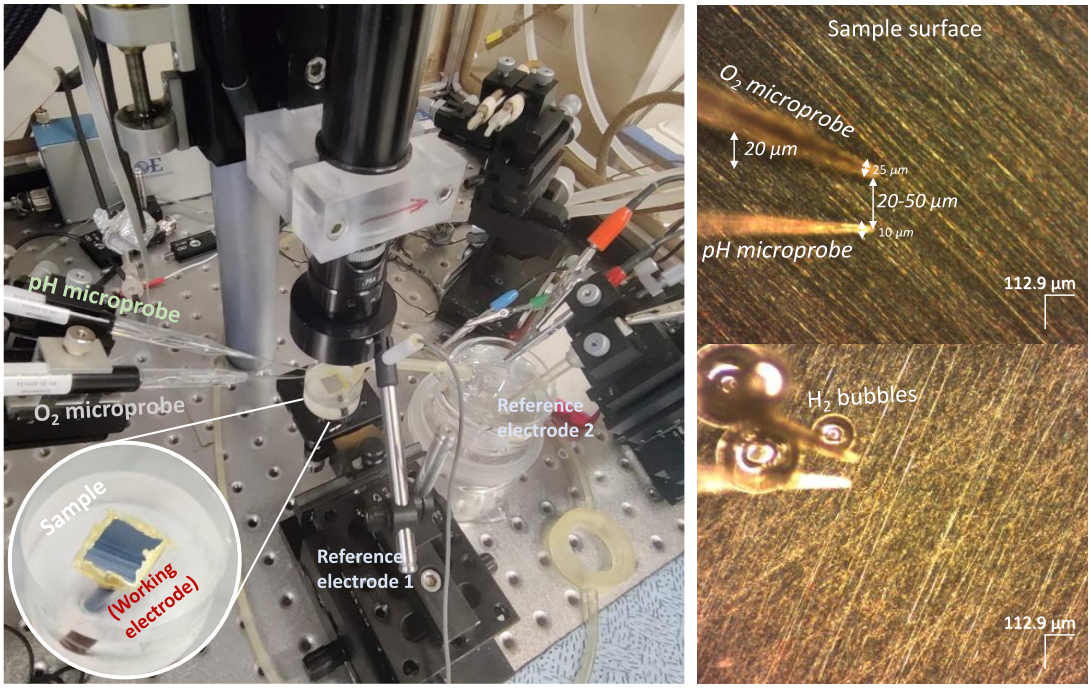

Figure 5.1: Experimental setup for monitoring *in-situ* ZrCC formation using scanning micro-probe techniques.

5.3 Results and Discussion

Figure 5.2a-i displays original DO, pH and OCP profiles during 5000 s conversion, where conversion times up to 1000 s are especially intriguing from a ZrCC formation standpoint as its formation is known to start immediately upon immersion. Table 5.1 contains the characteristic profile parameters as a function of immersion time, selected for discussion. These parameters include the time and DO concentration at the minimum and plateau, the pH peak and plateau, and the minimum and plateau of the OCP curve.

5.3.1 Cold-rolled steel

The DO profiles presented in Figure 5.2a reveal that oxygen consumption depends on concentration and pH values. Upon immersion, the lines DO vs. time show a minimum DO concentration after several hundred s, followed by a more or less steep increase and a plateau. In particular, at the minimum, for samples treated at pH $\geq$ 4.0, the highest level of oxygen consumption was recorded at 825 ppm/pH of 4.0, followed by 150 ppm/pH 4.6, 1226 ppm/pH 4.6, and 150 ppm/pH 4.0, the sequence of the latter three being harder to discern Table 5.1. A higher level of oxygen consumption is reflected by a smaller DO concentration and is indicative of an increased ORR. Values of DO stabilise between 180 and 560 s, indicative of sufficient ZrCC formation, as already shown in *Chapters 2.3.1.2.1, 2.3.2.4.1* and *2.3.3.1.*

Although not interesting from a ZrCC formation standpoint, as longer immersion times lead to significant cracking, some consistent trends in original profiles to 5000 s warrant further comment. Specifically, overall DO profiles suggest that the increase in DO, indicating inhibiting further ORR, is dependent on pH, with a less steep increase at pH = 4.6 and even less so at higher concentrations than pH = 4.0. Remarkably, at 825 ppm/pH 4.0, a steep increase in DO begins already around 340 s, indicating the most suppressed ORR, likely due to the formation of a highly protective ZrCC layer. This supports the findings from *Chapter 2* of this condition being optimal, suggesting an interplay between pH and concentration, leading to rapid and dense ZrCC deposition, which effectively prevents further cathodic processes, particularly ORR. Alternatively, this could also imply that the majority of H_2ZrF_6 is consumed at the outset due to favourable kinetics provided by intermediate pH and concentration levels.

The behaviour of the 825 ppm/pH 3.0, which does not lead to ZrCC formation, requires a separate discussion. In this case, the reduced remaining DO (around 2.4 ppm) is attributed to the more pronounced HER at lower pH levels (Figure 5.3), as evidenced by hydrogen bubbles consistently observed throughout the experiment.

Furthermore, it can be seen in Figure 5.2a that for samples treated at pH $\geq$ 4.0, regions of the highest reduction in the remaining DO overlap with regions with the highest pH for each treatment (Figure 5.2b), confirming ZrCC formation. All pH values begin to stabilise relatively quickly, approximately within 300 s, a duration demonstrated in *Chapter 2* to produce satisfactory coatings. The pH range established at the plateau is between 4.8 and 6.4 (Table 5.1). Contrary to the consensus in the literature that ZrCC occurs due to surface alkalization, the pH actually remains slightly acidic. The order of pH stabilisation is as follows: 150 ppm/pH 4.6 > 825 ppm/pH 4.0 > 1226 ppm/pH 4.6 > 150 ppm/pH 4.0 (Table 5.1). This can be partly attributed to the inverse buffering capacity of solutions, with the lowest being for the 150 ppm/pH 4.6, thus leading to the greatest pH increase during cathodic reactions. In contrast, 150 ppm/pH 4.0 exhibits the smallest pH increase, wherein the buffering capacity may be hindered by the insufficient supply of Zr at less concentrated but more acidic H_2ZrF_6 solutions. The notable exception is again 825 ppm/pH 3.0, which stabilises at pH $\approx$ 4.5, where ZrCC formation is evidently absent, leading to minimal pH increase due to predominant HER (Figure 5.3) and etching without ZrCC deposition. Additionally, HER tends to also occur at higher concentrations, 825 ppm and 1226 ppm (Figure 5.3), likely due to increased total acidity.

However, this does not appear to be linked to coating quality, at least when compared with findings from *Chapter 2*.

On the other hand, OCP profiles (Figure 5.2e) do not appear to show any clear trends, stabilising quickly after 100 s at approximately –0.705 to –0.685 V, except for 825 ppm/pH 3.0, which stabilises around –0.645 V. This is likely due to a higher concentration of oxidised species, particularly hydrogen ions (H^+) governing OCP according to the Nernst equation [321]. In this context, the minima and OCP plateaus are indistinguishable.

5.3.2 Zinc

The behaviour of Zn closely resembles that of CRS, likely due to their shared uniform corrosion that initiates ZrCC deposition. Specifically, the highest reduction in the remaining DO (Figure 5.2d) was observed at 825 ppm/pH 4.0, followed in order by 1226 ppm/pH 4.6, 150 ppm/pH 4.6, and 150 ppm/pH 4.0. In general, DO profiles stabilise at around 2 ppm after 500 s for 825 and 1226 ppm and around 3 ppm for 150 ppm (Table 5.1) combinations. This suggests that higher concentrations may lead to a quicker and more substantial formation of ZrCC due to increased cathodic activity. However, observed DO values are generally higher than on CRS, suggesting less rapid ZrCC formation. In addition, the DO profiles in the case of Zn exhibit two peaks, with the latter being higher than the former, likely indicative of bilayer formation. Specifically, the emergence of the first DO peak ($\lesssim$160 s) could imply the interaction with ZnO previously formed during alkaline cleaning with the H_2ZrF_6 bath, given that this occurrence does not align with sufficient Zn-ZrCC formation, as shown in *Chapter 2*. The second DO peak (also, the overall DO minimum) can then be attributed to the formation of ZrCC. Due to issues with the probe, accurate DO measurements at pH = 3.0 on Zn could not be conducted, leading to the exclusion of these results at the moment. Nevertheless, we believe the data from the other two substrates provides sufficient insights and it is assumed that the behaviour would be similar to CRS since all the other behaviour is indeed similar between Zn and CRS due to the aforementioned shared uniform corrosion mechanism. Moreover, they are less significant for ZrCC formation, as it has been demonstrated that they result in the poorest coating quality, evident in surface etching on CRS and Zn or the most inhomogeneous ZrCC on AA5754.

Furthermore, the appearance of peaks starting in the order 825 ppm/pH 4.0 > 150 ppm/pH 4.0, > 1226/ and 150 ppm/pH 4.6 (Table 5.1) highlights a pH dependence, suggesting more rapid ZrCC formation kinetics at lower pH. Similarly, profiles at longer immersion times, as seen with CRS, samples treated at pH = 4.6 demonstrate a more gradual increase in DO, suggesting sustained cathodic activity [322, 323, 324]. This is likely due to the slower corrosion kinetics at higher pH, which facilitates the formation of ZrCC, thereby supporting continuous ORR. However, this does not necessarily correlate with the coating quality. Instead, it merely suggests the potential for ongoing ZrCC deposition through ORR. This does not contradict EIS findings in *Chapter 2* for Zn-ZrCC which indicated diffusion-controlled corrosion behaviour in a dilute Harrison's solution, primarily resulting from Zn corrosion products rather than from ORR, as the latter was in turn not shown to occur under diffusion control in PPCs. Therefore, it also remains ambiguous in the case of CRS discussed above whether a pH of 4.6 at 1226 ppm is more detrimental if it exhibits sustained cathodic reactions, as the RSM models presented in *Chapter 2* suggest that optimal region may exist at these conditions as well. In any case, it must be borne in mind that longer conversion times may result in increased ZrCC thickness but without any apparent benefit and could potentially introduce greater stress, making the coating more prone to cracking when exposed to corrosive electrolytes.

EIS results from *Chapter 2* further suggested that Zn-ZrCCs treated at pH $\geq$ 4.0 at both conversion times $\geq$ 230 s and concentrations $\geq$ 825 ppm exhibit higher coating thickness, as evidenced by the width of the diffusion constant, implying sufficient ZrCC formation and consequently higher corrosion resistance compared to those treated at lower settings of those factors. In other words, it is postulated that higher thickness of treating samples at pH $\geq$ 4.0 and

concentrations ≤. 825 ppm is hard to compensate for higher conversion times (at least in the region ≥ 230−730 s). Now, integrating them with DO profiles, it can be assumed that sufficient coating formation reflects in lower DO plateau values and not the DO minima (Table 5.1), as 825 ppm and 1226 ppm led to lower DO plateau values (approx. 2.20 and 2.35 ppm at 550 and 380 s, respectively). This also explains why performing conversion near or in the DO stabilisation region (at 230 and 730 s for 1226 ppm and 480 and 900 s for 825 ppm) in *Chapter 2* led to similar values in $|Z|$ at 0.25119 Hz, which is presumably due to a sufficient coating formation. However, it remains unclear why the sample with 1226 ppm/230 s/pH 4.6, despite having a $|Z|$ at 0.25119 Hz comparable to those of adequately formed ZrCC coatings, exhibited the least diffusion influence. The conversion time in that instance falls very near the DO minimum, a phase where ZrCC formation still occurs but other treatments failed to exhibit effective resistance. At present, it can only be asserted that a combination of higher concentration and pH levels allows for more controlled and denser ZrCC coating formation, at least seen as denser and smaller ZrCC nodules in the SEM images from *Chapter 2*.

Similar to CRS, the pH profiles for Zn (Figure 5.2e) demonstrate a partial dependence on buffering capacity, though the pH values increase and stabilize at lower levels compared to CRS, namely in the range 5.1–6.2. Specifically, the sequence of these pH levels at the first minimum is as follows: 150 ppm/pH 4.6 > 1226 ppm/pH 4.6 > 825 ppm/pH 4.0 > 150 ppm/pH 4.0, coinciding with lower reduction in the remaining DO observed in comparison to CRS (Table 5.1). In addition, a close alignment of pH peaks with DO minima, albeit slightly delayed, is observed. However, both 825 ppm and 1226 ppm concentrations distinctly display pH valleys at 5.5 and 5.7, respectively, suggesting mild acidification. This is likely due to the combined effect of increased overall reduction in the remaining DO associated with denser and more rapid ZrCC formation at higher concentrations. Consequently, the pH stabilization values observed after the aforementioned valleys were around 5.6–5.9. As pH values do not increase to the high levels required for ZnO formation included also in *Chapter 3*, it can be safely concluded that ZnO does not form during the conversion process.

Lastly, OCP profiles for Zn (Figure 5.2f), like those for CRS, offer minimal information, with stabilisation occurring between −1.055 and −1.077 V. An exception is again observed on 825 ppm/pH 3.0, where a valley forms after an initial OCP drop to −1.067 V, before increasing and stabilising at −1.054 V, likely due to etching and enhanced HER activity (Figure 5.3). In this context, the minima and OCP plateaus are again indistinguishable. This makes OCP an inadequate parameter for tracking the ZrCC process of CRS and Zn substrates.

By combining all the results obtained so far, it can be inferred that a path to optimisation of ZrCCs includes reaching not only DO minimum but also sufficiently low DO stabilisation values, which are achievable only at higher concentrations. To verify these findings, it is necessary to conduct conversion processes that are very close to both the DO minimum and the DO plateau. Consequently, future studies would include EIS measurements at the DO minimums (≈ 130 and 260 s) and plateaus (≈ 550 and 380 s) for concentrations of 825 and 1226 ppm, along with other advanced techniques.

5.3.3 AA5754

In contrast, the behaviour of AA5754 differs markedly, as expected. DO profiles (Figure 5.2g) clearly show the emergence of two peaks for all samples treated at pH ≥ 4.0, with 150 ppm/pH 4.6 being the easiest to distinguish. The appearance of the first DO peak (140−340 s) also follows the same trend 150 ppm/pH 4.6 followed by 150 ppm/pH 4.0 and 825 ppm/pH 4.0 while the second DO peak follows the reverse trend with the greatest separation between the two peaks for 150 ppm/pH 4.6 (Table 5.1). Thus, in this case, the overall lowest DO is observed at 150 ppm/pH 4.6. This could support assumptions from *Chapter 2* regarding the rapid formation of ZrCC at higher pH levels and lower concentrations, which effectively regulate cathodic reactions at IMPs and matrix. Conversely, other conditions result in more cracks, allowing ongoing ORR

inside them and leading to lower oxygen concentration. Nevertheless, 825 ppm/pH 3.0 also results in relatively low DO levels (the lowest being around 3.2 ppm), though without distinctive peaks and with the DO minimum appearing much later (around 1710 s, Table 5.1). This results from the least controlled ZrCC deposition kinetics, leading to the least uniform ZrCC coating and the greatest number of cracks due to the thickest ZrCC on IMPs, thereby intermittently enabling cathodic reactions.

The pH profiles in Figure 5.2h generally inversely correlate with DO, reflecting consumption due to cathodic reactions and the buffering capacity of the solution. This leads to higher pH values in less acidic solutions, following the order of pH stabilization: 150 ppm/pH 4.0 > 150 ppm/pH 4.6 > 825 ppm/pH 4.0. Additionally, the first pH bumps around 150–260 s suggest a dissolution phase, aligning well with the OCP minima (Table 5.1).

As already confirmed throughout the literature, OCP profiles in Figure 5.2i exhibit typical dissolution of the substrate/precipitation of the ZrCC behaviour, with dissolution indicated by a drop to a minimum OCP value and precipitation by a subsequent increase until a plateau is reached. The latter in turn signals a dynamic equilibrium between dissolution and precipitation. The appearance of OCP minima, ranging from −1.290 to −1.350 V, thus leading to HER in all samples (Figure 5.3) follows the order: 825 ppm/pH 3.0 > 825 ppm/pH 4.0 > 150 ppm/pH 4.6 > 150 ppm/pH 4.0 with the reverse order for reaching OCP plateaus (Table 5.1). This reflects dissolution kinetics, which are faster at lower pH and higher concentrations while the width of peaks following the same order suggests that more intense dissolution takes longer to balance with precipitation, as postulated in *Chapter 2*. Lastly, the occurrence of OCP plateaus between 410 and 830 s appears to depend solely on concentration, with plateaus at higher concentrations emerging earlier, indicating denser precipitation (Table 5.1).

Given that the point measurements herein likely represent average reactions across both IMPs and the matrix, the first DO peak likely corresponds to ZrCC formation on IMPs, with the second peak indicating ZrCC extension onto the matrix or bilayer structure formation. However, considering that *Chapter 2* demonstrated optimal ZrCC formation with minimal cracking at 150 ppm/230 s/pH 4.6, which falls between the two DO peaks, it is more likely that the first DO peak could be more indicative of complete ZrCC deposition at both IMPs and the matrix. Moreover, current data from *Chapter 2* demonstrate exclusive ZrCC formation on IMPs for 825 ppm/pH 4.0 treated for 60 s, which does not contradict herein the occurrence of the first DO peak between 140–340 s (Table 5.1). In contrast, the second DO peak should be attributed to another phenomenon, which may be revealed through observations of OCP plateaus that tend to occur slightly after the second DO peaks, and particularly more after in the case of 150 ppm/pH 4.0 (830 s, Table 5.1). This may provide an additional explanation to those previously discussed, suggesting that while ZrCC formation on the matrix may be complete, ZrCC deposition could still occur in the cracks, likely concluding at the OCP plateau. The notably extended time required to reach the OCP plateau for 150 ppm/pH 4.0, which exhibits intermediate ZrCC precipitation behaviour in both pH and DO profiles, could be hence attributed to the delayed filling of cracks resulting from the initially higher consumption of H_2ZrF_6 at the lower pH level. In contrast, the notably lowest observed DO value of the second DO peak at 150 ppm/pH 4.6 can imply easier filling of the cracks, owing to the initially more uniform deposition of ZrCC. This highlights the necessity of considering the position and values of both DO peaks in the optimisation process. Nevertheless, bearing in mind that RSM models from EIS in *Chapter 2* recommend higher conversion times (150 ppm/480 s/pH 4.6) that are aligned herein with the second DO peak and OCP plateau, future research should focus on these conversion times, specifically around the DO minimum and plateau at around 460 s and 700 s, respectively. In this regard, tracking OCP is not indicative of ZrCC uniformity but rather of its compactness, which could be attributed to the filling of cracks. As such, it cannot be the sole criterion for assessing homogeneous ZrCC precipitation. On the other hand, the conversion time before the second DO peak may indicate uniform ZrCC formation, while the second DO peak

may signify the completion of filling IMPs within cracks. Therefore, DO remains the most reliable parameter for investigating ZrCC, while the most promising guideline towards optimisation appears to be the position of the first DO peak and the value of DO at the second DO peak.

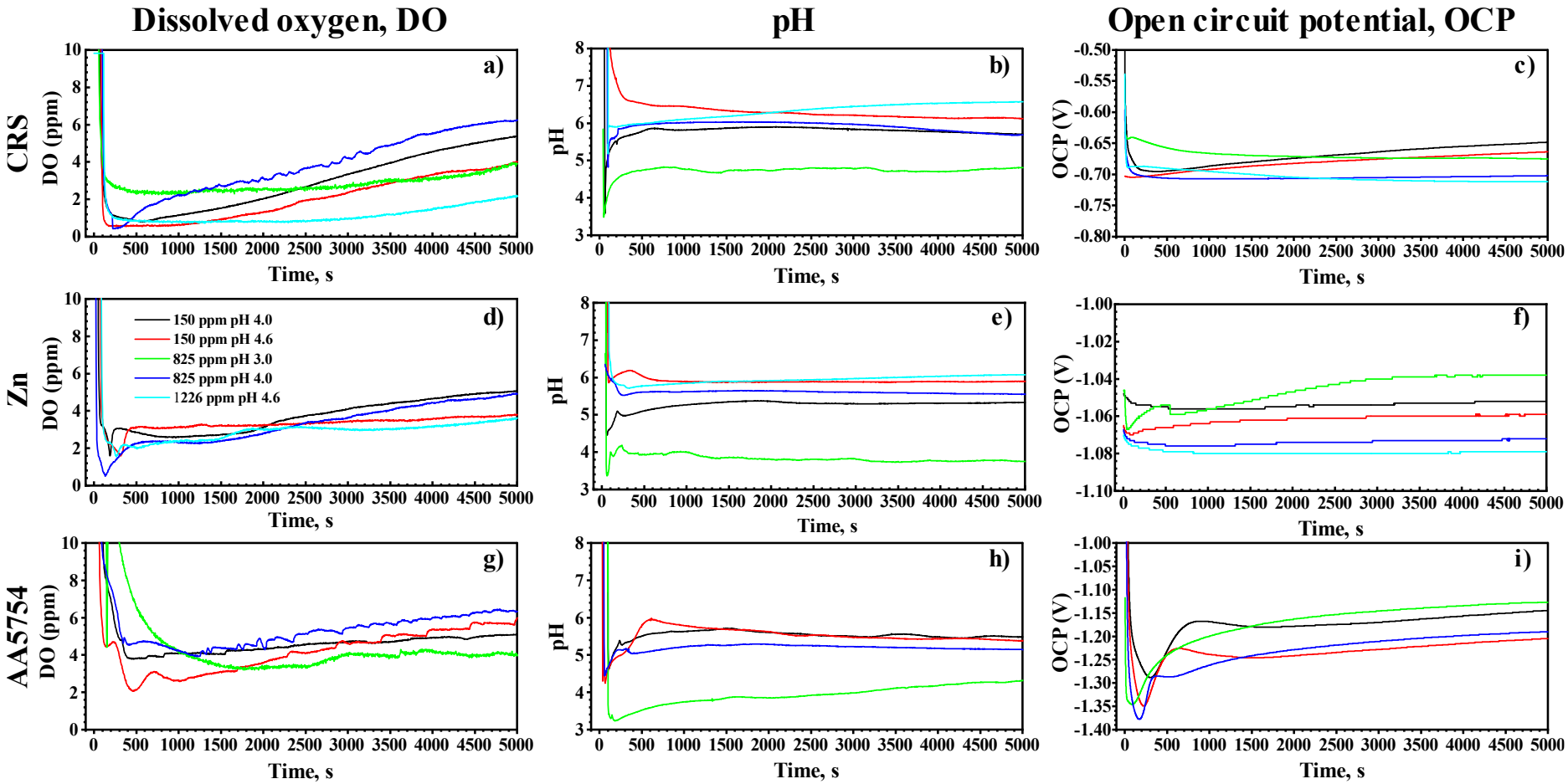

Figure 5.2: Evolution of DO, pH and OCP profiles during *in-situ* ZrCC formation at different H_2ZrF_6 combinations using corresponding scanning micro-probe techniques. Note that 0 indicates addition of the ZrCC formulation, capturing the very first seconds of ZrCC contact with the substrate surface.

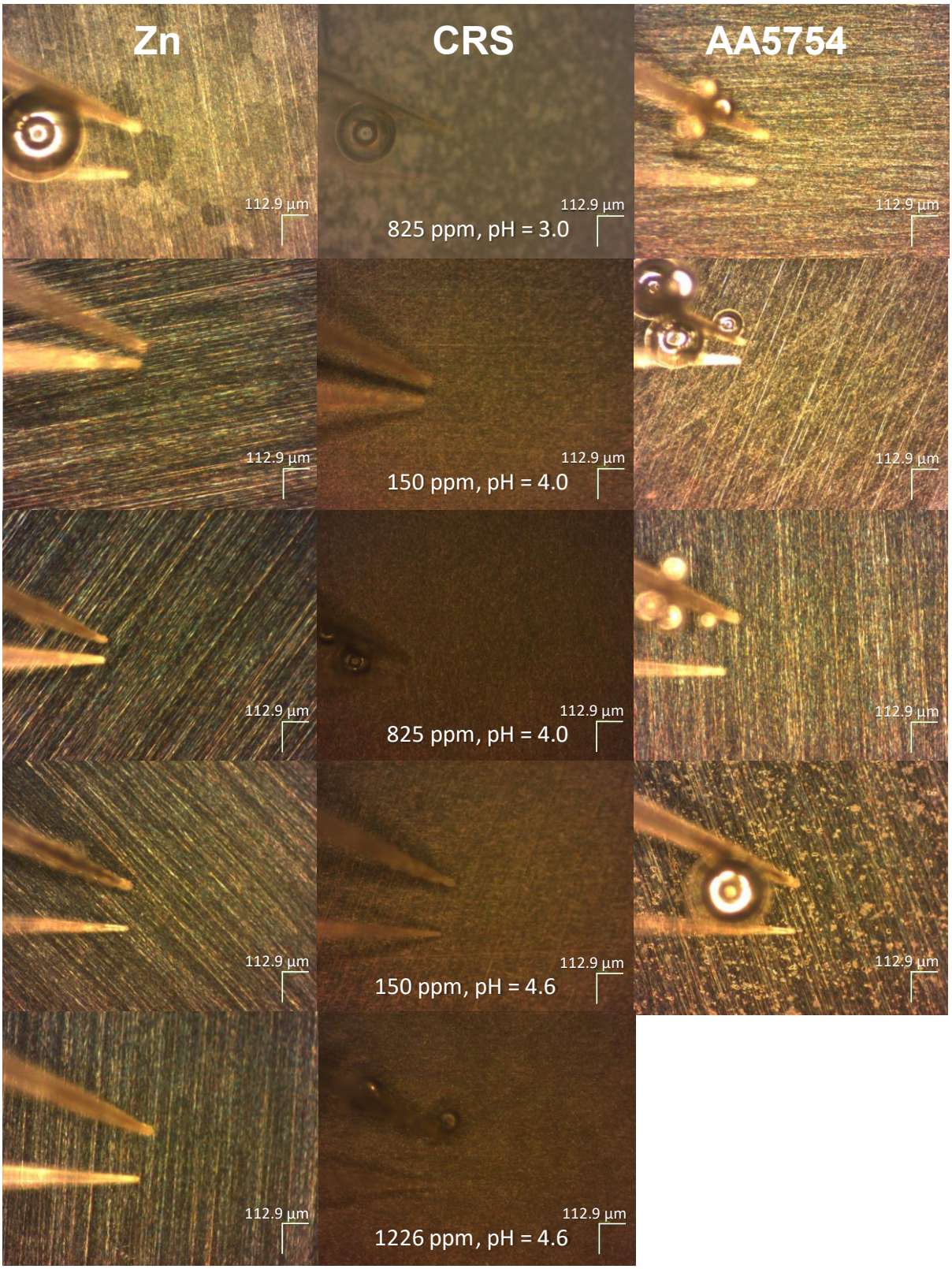

Figure 5.3: A visual appearance of samples during *in-situ* ZrCC formation at different H_2ZrF_6 combinations using scanning micro-probe techniques.

Table 5.1: Selected characteristic DO, pH and OCP peaks observed during ZrCC formation at different H_2ZrF_6 combinations.

	H_2ZrF_6 setting	The first DO peak / s	The first DO peak / ppm	The second DO peak / s	The second DO peak / ppm	DO plateau / s	DO plateau / ppm	The first pH peak / s	The first pH peak	The second pH peak / s	The second pH peak	pH plateau / s	pH plateau	OCP minimum /	OCP minimum / V	OCP plateau / s	OCP plateau / V
CRS	150 ppm pH 4.0	530	0.8	/	/	530	0.8	≈ 300	5.8	/	/	/	/	indistinguishable; OCP minimum = OCP plateau			
	150 ppm pH 4.6	180	0.5	/	/	180	0.5	≈ 300	6.5	/	/	/	/				
	825 ppm pH 3.0	560	2.4	/	/	560	2.4	≈ 300	4.8	/	/	/	/				
	825 ppm pH 4.0	220	0.4	/	/	> 340	1.7	≈ 300	6.0	/	/	/	/				
	1226 ppm pH 4.6	400	0.8	/	/	400	0.8	≈ 300	6.1	/	/	/	/				
Zn	150 ppm pH 4.0	78	3.2	185	1.6	280	3.0	180	5.1	/	/	850	5.3	indistinguishable; OCP minimum = OCP plateau			
	150 ppm pH 4.6	160	2.3	315	1.6	460	3.2	330	6.2	/	/	610	6.0				
	825 ppm pH 3.0	/	/	/	/	/	/	220	4.2	/	/	345	4.0				
	825 ppm pH 4.0	50	1.5	130	0.5	550	2.4	250	5.5	/	/	500	5.6				
	1226 ppm pH 4.6	160	2.3	260	1.5	380	2.2	310	5.7	/	/	1300	5.9				
AA5754	150 ppm pH 4.0	310	4.8	420	3.8	450	3.8	213	5.4	/	/	≈ 1300	5.7	300	−1.290	830	
	150 ppm pH 4.6	140	4.4	460	2.0	700	3.1	215	5.0	617	5.95	≈ 1300	5.7	220	−1.35	630	
	825 ppm pH 3.0	1770	3.2	1710	3.2	1850	3.3	150	3.4	/	/	≈ 1300	3.8	70	−1.345	1850	
	825 ppm pH 4.0	340	4.6	410	4.5	410	4.7	260	5.1	/	/	≈ 1300	5.3	167	−1.379	410	

5.3.4 General discussion

In general, CRS and Zn substrates exhibit similar patterns, with optimal conditions for ZrCC formation identified at 825 ppm/pH of 4. In contrast, AA5754 shows a preference for higher pH levels and lower concentrations (150 ppm/pH 4.6), indicating a distinct localized corrosion mechanism and different dynamics in ZrCC formation. This confirms the optimal regions identified through RSM in *Chapter 2*. Furthermore, the Zr–F predominance diagram constructed in *Chapter 3,* Figure 3.5 indicates that ZrCC precipitation occurs within the concentration range of 150−1226 ppm at pH levels between 5.80−6.10. This aligns closely with the stabilisation pH values observed on CRS and Zn substrates, indicating a more effective film formation that buffers further pH changes, as demonstrated, for example, in the cases of Zn- and Fe-alloys, with film formation occurring during exposure to various electrolytes [322, 323, 324]. In contrast, AA5754 exhibits generally lower pH increases, indicating less effective buffering, likely due to the formation of a more porous coating. Nevertheless, in all cases of H_2ZrF_6 formulations at pH ≥ 4.0, the pH remains within the range where the conversion of ZrF_6/ZrF_5 (aq) to $Zr(OH)_4$ (am) occurs, as calculated in *Chapter 3,* Figure 3.5. This is further supported by the findings of *Chapter 4*, as complexation with buffering agents or fluorides occurs at pH levels different from those of ZrCC deposition. An exception is noted across all substrates at 150 ppm/pH 4.6, where a higher pH increase is observed, likely due to less effective buffering of the solution. This further confirms that effective film formation requires pH ≥ 4.0. For CRS and Zn, this can be supported with thermodynamic data as an insufficient increase for adequate ZrCC precipitation. In the case of AA5754, where ZrCCs do form at a pH of 3.0, yet are of poor quality, rather indicate inadequate buffering due to a marked increase in porosity and defects. As such, pH values may indicate larger porosity and defect formation when coupled with lower reduction in the remaining DO. Therefore, by integrating DO profiles and pH stabilisation values, it can be inferred that ZrCC formation on the CRS substrate is the most uniform, rapid, and protective compared to other substrates. Future research could further explore these relationships, integrating additional analytical techniques to refine the optimisation parameters for ZrCC formation.

5.4 Conclusions

In this preliminary study, *in-situ* development of ZrCCs on CRS, Zn and AA5754 under various H_2ZrF_6 concentrations and pH levels was followed using scanning micro-probe techniques. Both Zn and CRS exhibited similar patterns of ZrCC deposition due to their shared mechanism of uniform corrosion, while AA5754 exhibited distinct behaviour. For CRS and Zn, ZrCC deposition is more prominent at the lowest DO levels on 825 ppm/pH 4.0, particularly for CRS. For AA5754, the most notable deposition occurs at 150 ppm/pH 4.6. This confirms the optimal conditions for ZrCC deposition, as identified in *Chapter 2*, highlighting the crucial interaction between pH and concentration for effective ZrCC deposition that hinders further cathodic processes. The tracking of DO levels emerges as the key parameter for monitoring ZrCC formation progress. For AA5754, the initial DO peak may signal complete ZrCC coverage, with subsequent peaks and OCP plateau positions indicating ZrCC deposition in cracks and their eventual sealing. In this study,

pH values provided less information about dynamics of ZrCC process compared to DO profiles, suggesting pH is more related to significant defects and porosity, while DO indicates ongoing ZrCC formation potential. However, a very important finding is that the pH during the ZrCC process from an H_2ZrF_6 bath is not alkaline and is determined by the pH of zirconia precipitation, in accordance with the predictions from *Chapter 3.1.* Future research should focus on optimising conditions based on these findings, particularly at DO minima and plateaus. More advanced surface analysis techniques, such as TEM, can be utilised to elucidate the composition of the formed ZrCCs and cross-sectioning with FIB on IMPs to assess the possibility of filling the cracks. Additionally, using the recently established electrochemical quartz crystal microbalance method in our laboratory for real-time mass change measurements pertinent to Zr−film species could greatly improve the understanding of the kinetics involved in ZrCC deposition.

Chapter 6

Improving Corrosion Resistance of Zirconium Conversion Coatings with Si- and Zr-based Treatments

6.1 Literature Review

It becomes clear by now that although ZrCCs are not designed primarily for corrosion protection, their corrosion-resistant properties cannot be enhanced by merely adjusting the concentration, conversion time, and pH levels of H_2ZrF_6. To effectively improve ZrCCs, a holistic approach involving pre- and posttreatment processes, as well as the incorporation of various additives, is essential for addressing the issues related to ZrCC deposition from H_2ZrF_6 solutions. However, it seems like the literature has not adequately addressed those issues. Within this context, the sealing process, a customary industrial procedure, encompasses the application of a sealant layer, often composed of a polymer or an alternative conversion coating, onto the surface previously subjected to conversion. Notably, certain literature studies have demonstrated that the posttreatment of a Zr-based conversion coating with $NiSO_4$ significantly enhances the corrosion resistance of coated CRS [39]. Nonetheless, other sealing methods, such as sodium silicate (Na_2SiO_3) solution posttreatment [40], simple boiling water sealing or air-drying, also prove effective [41]. Concurrently, research from our group has revealed the significant effects of air drying or immersion in sodium chloride on the electrochemical behaviour of ZrCCs, highlighting the importance of exploring posttreatments for ZrCCs. Conversely, pretreatments have received even less attention in the literature [34, 42, 43, 325]. Hence, in this preliminary study, we examine the sol-gel behaviour assumed to be intrinsic to the ZrCC process by employing colloidal nanoparticles. Our hypothesis is centred on the notion that these nanoparticles can act as nucleation sites for the subsequent deposition of ZrCC. Given that the ZrCC process is believed to involve both electrochemical and chemical mechanisms, as demonstrated in *Chapter 3*, ideally, the non-specific chemical adsorption of colloids across the entire surface could result in a more uniform deposition of ZrCC, contrasting with the selective deposition on microcathodic sites, most commonly IMPs, particularly in aluminium alloys.

This approach might indeed seem familiar, as it draws parallels with the historical use of Jernstedt's salts in phosphate conversion coatings. Jernstedt's salts are typically prepared by dissolving disodium orthophosphate in water and adding titanium as a soluble salt [44]. In this context, an ion exchange mechanism, where sodium ions on the surface of

titanium colloids are replaced by cations from the substrate, catalyses the conversion process, thus facilitating the formation of finer-sized crystals [326].

Our method, drawing from another patent [327], utilizes nano-sized, anionically charged colloidal metal nanoparticles as a pretreatment step, offering advantages such as extended shelf-life, broad temperature, and pH stability, reduced negative effects of cationic substances in the pretreatment bath, as well as lower limitations on metal contact times due to improved nanoparticle agglomeration resolution. Furthermore, this pretreatment step can be incorporated during cleaning and degreasing and is adaptable to using various agents, surfactants, and additives.

Conversely, the formation of zirconate and syloxyl linkages (...—O—Zr—O—Si—O—Si—...) shown by Nikol'skii et al. [328] has been suggested in some earlier patents [40, 329, 330], as a posttreatment for ZrCCs. This treatment enhances corrosion resistance but significantly reduces paint adhesion due to the resultant hydrophobic surface, contrasting with the inherently hydrophilic nature of ZrCCs. However, it is specifically with sodium silicates (commonly known as water glass) that an additional layer of corrosion protection is achieved by forming a siloxane linkage network during drying while maintaining the hydrophilic characteristic of the surface [40]. The described formation of Si—Zr networks has also been demonstrated more recently in coatings referred to as TMZ (based on tetraethyl orthosilicate (TEOS), 3-methacryloxypropyltrimethoxy silane (MAPTMS), zirconium tetrapropoxide (ZTP) and methacrylic acid (MAA)), where Zr enhances the kinetics of hydrolysis and condensation reactions, leading to the formation of Si—O—Zr heterometallic bonds and a reduction in the number of free silanol groups [331]. Indeed, $Si(OH)_4$ condenses with any solid surface possessing OH—groups available for reaction, thereby forming a silicate under the specified pH conditions [332].

Considering the role of Si, this preliminary study examines pretreatment with both SiO_2 and ZrO_2 nanocolloids, the latter being a primary component of ZrCCs and thus a representative of ZrCC colloidal nanoparticles alongside a sodium silicate posttreatment. These were applied to previously optimised ZrCC coatings derived from H_2ZrF_6 bath on AA5754 in *Chapter 2* to elucidate the chemical nature of the ZrCC process and subsequently enhance its performance. At this stage, the focus was on observing the possible effects of the above-described treatments for improving the ZrCC process to lay the groundwork for future studies on its compatibility following the application of subsequent organic layers.

Note that in this initial study, the focus was solely on observing the effects of the treatments. Therefore, comparative measurements on non-treated samples will be completed in the future.

6.2 Experimental

6.2.1 Chemicals, materials, and methods

All solutions were prepared from analytical grade reagents except for Na_2SiO_3, which was of technical grade. AA5754 substrates of the same composition were used, cut, and surface-prepared for ZrCC deposition and electrochemical testing, as well as for SEM, in the same manner described in *Chapter 2*, where only 24 h air-dried samples were used. Additional pre- and posttreatment steps were carried out on the optimal conversion conditions (150 ppm, 230 s, pH 4.6), obtained in *Chapter 2*, as follows: Bare and alkaline-cleaned + desmutted samples, as well as the optimal conversion conditions (150 ppm, 230 s, pH 4.6) obtained in *Chapter 2*, were again presented for comparison in dilute Harrison's solution with additional measurements performed in 3.5 % NaCl solution (*vide infra*).

Pretreatment:
After the acid desmutting step, the water-rinsed samples were submerged for 30 s in solutions containing either 10, 30, or 300 ppm of SiO_2 colloidal nanoparticles (LUDOX® HS-40, Sigma-Aldrich Chemie GmbH, Taufkirchen, Germany, 40 wt.% aqueous suspensions, 20 nm particle size, sodium-stabilised), with a specific pH, designated as "SiO_2 pretreatment". Alternatively, the samples were immersed in solutions of 10, 30, or 300 ppm of ZrO_2 colloidal nanoparticles (NYACOL® Zr10/20NH4 alkaline zirconia sol, NYACOL® Nano Technologies, Inc., Ashland, Massachusetts, 18—20 wt.% aqueous suspension, 5—20 nm particle size, ammonia/organic acid-stabilised), also with a specific pH, designated as "ZrO_2 pretreatment". Following this, they were immediately placed in an H_2ZrF_6 bath under the optimal conditions determined in *Chapter 2* (150 ppm, 230 s, pH 4.6), designated as "optimal H_2ZrF_6".
Posttreatment:

After obtaining optimal H_2ZrF_6 samples, the samples were immersed into a 10 % Na_2SiO_3 solution (water glass solution, SILKEM d.o.o., Kidričevo, Slovenia, 35—38 % Na_2SiO_3 content) for 5 min at 48 °C under 150 rpm stirring rate on a C-MAG HS 7 magnetic hotplate stirrer (IKA®-Werke GmbH & Co. KG, Staufen, Germany), designated as "Na_2SiO_3 posttreatment".

Where applicable to both treatments, SiO_2 colloid and Na_2SiO_3 posttreatment, or ZrO_2 colloid and optimal H_2ZrF_6 treatment, will be simply referred to as Si- and Zr-treatments, respectively.

6.2.2 Electrochemical impedance spectroscopy

EIS measurement was conducted in the same manner as in *Chapter 2* (i.e., using dilute Harrison's solution) with additional comparison in 3.5 % NaCl solution (> 99.5 %, AppliChem GmbH, Darmstadt, Germany) in the best-observed pretreatment in Harrison's solution (30 ppm of SiO_2, *vide infra*). Fitting was not performed at the moment. Considering the preliminary nature of this study, EIS measurements were conducted over several days until a significant drop in impedance was observed, indicating coating failure.

6.2.3 SEM/EDS

The same procedure for SEM sample preparation was applied as that described for AA5754 in *Chapter 2*. SEM analyses were conducted using two different instruments: a JEOL JSM 7600 F equipped with an Inca Oxford 350 EDS SDD for EDS and a Thermo Fisher Verios 4G HP field emission SEM, equipped with Ultim Max 350 SDD for EDS. Images were captured in both SE and back-scattered modes, employing a CBS detector. A beam voltage of 5 kV was utilised to improve the detection of intermetallic particles on AA5754 (as mentioned earlier). Additionally, to mitigate charging effects, samples were coated with a thin layer of carbon before analysis.

6.3 Results and Discussion

6.3.1 Electrochemical impedance spectroscopy

The EIS results recorded up to 5 days of immersion presented in Figure 6.1 demonstrate an overall improvement in performance when using pre- and posttreatments compared to bare and samples treated solely with H_2ZrF_6. Specifically, in dilute Harrison's solution, the application of 30 ppm for both colloids seems to yield the best results compared to other concentrations; however, SiO_2 pretreatment by far shows superior performance. Notably,

in the case of the SiO_2 pretreatment, the impedance arcs display a single time constant, indicative of charge transfer control. The impedance values increase with immersion time for concentrations of 30 and 300 ppm and are the highest initially but decrease at 10 ppm, with a notable distinction in the day 2 measurement at 30 ppm, meriting further investigation as it has not been observed in other solutions. Moreover, Na_2SiO_3 posttreatment achieves impedance values comparable to those of the SiO_2 pretreatment on day 5. However, only one spectrum is presented because the coating degraded after one day. This supports the observation of impedance spectra with two time constants: the first associated with the post-treatment layer forming a Si—Zr network, and the second with charge transfer resistance through cracks. Notably, these cracks demonstrably form when using H_2ZrF_6 without pretreatment. Future studies should thus explore the combined effects of SiO_2 pretreatment and Na_2SiO_3 posttreatment with or without the application of subsequent organic layers.

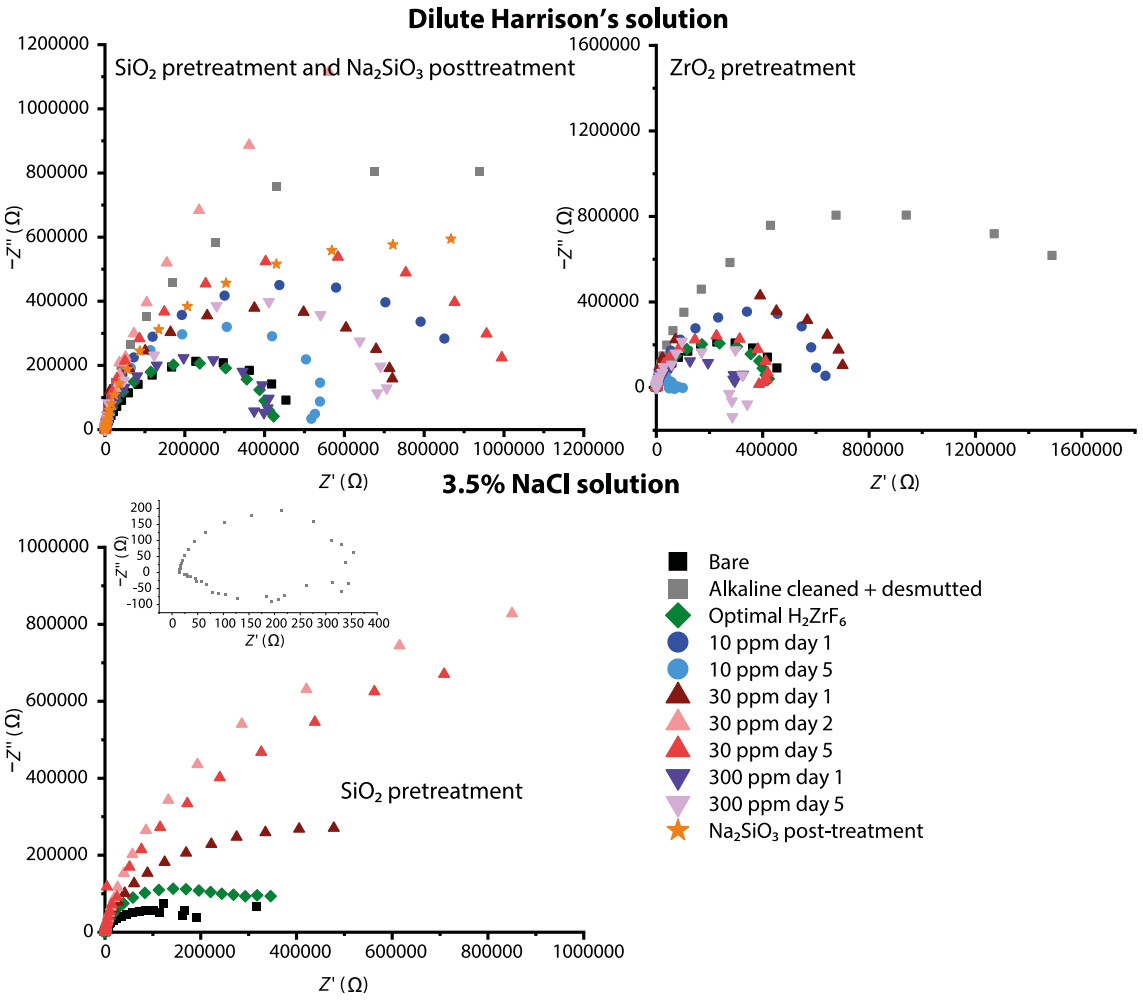

Figure 6.1: EIS results of AA5754 with different treatments for ZrCC in dilute Harrison's solution (above) and 3.5 % NaCl (below).

In contrast, for ZrO_2 pretreatment, impedance values decrease with immersion time across all concentrations, with 30 ppm showing the best and 300 ppm the worst performance, likely due to stronger interactions with the electrolyte. Furthermore, after 5 days, the impedance values at 30 ppm drop to those of samples treated only with H_2ZrF_6 after 1 day, indicating only a marginal enhancement. However, the values for ZrO_2 are

lower than those for SiO_2 pretreatment. Consequently, the sample prepared using the latter pretreatment (30 ppm of SiO_2) was tested in a more corrosive 3.5 % NaCl solution for up to 5 days, where a similar trend was observed, albeit with two time constants, possibly due to the aggressive environment leading to separation in the first time constant associated with the SiO_2 pretreatment layer and the second with charge transfer resistance inside defects. This condition also demonstrated a more consistent impedance value over time, evidenced by a smaller decrease from day 2 to 5, indicating the beneficial effect of the Si—Zr combination in forming networks, thus providing enhanced and prolonged corrosion protection.

Interestingly, it can also be seen that desmutted samples exhibit superior performance in dilute Harrison's solution compared to those discussed in *Chapter 2*. However, they demonstrated significant inferiority in a 3.5 % NaCl solution. This observation highlights the need for further investigation in future studies, as it suggests a potential sensitivity to chloride concentration.

6.3.2 SEM/EDS

The EIS results obtained are further supported by SEM micrographs (Figure 6.2) and EDS analysis (Figure 6.3). For the reasons elaborated upon in *Chapter 2*, the discussion focuses solely on the elements Al, Zr, Si, and O. In scientific research, unexpected deviations (in this case the use of SiO_2 as a substitute for ZrO_2) often lead to significant discoveries. Figure 6.2 demonstrates that the SiO_2 pretreatment uniquely results in a transformation of the ZrCC morphology into a uniform, crack-free coating. However, nodular structures remain on the IMPs, albeit at a reduced density compared to Zr-treatments. This is attributed to the expected agglomeration due to increased cathodic activity at the IMPs. The EDS results (Figure 6.3) further confirm that SiO_2 pretreatment leads to the most uniform and thinnest coatings, as indicated by the smaller difference in Al content between the matrix and the IMPs (cca. 2 times compared to 2.5 times without the SiO_2 pretreatment and by the smallest reduction in Al content relative to other treatments, respectively. Moreover, it results in the highest Zr content and lowest O content, suggesting the formation of a Si—Zr network.

Contrary to expectations, the ZrO_2 pretreatment maintains the ZrCC morphology and composition seen with H_2ZrF_6 treatment alone (as shown in Figure 6.2 and 6.3). This suggests a limited effect on corrosion protection, contradicting the hypothesis that it would facilitate nucleation sites for more uniform ZrCC deposition. The likely cause is the slow kinetics of ZrCC growth on existing ZrO_2 nuclei compared to nucleation and growth after electrochemically induced alkalization on IMPs, at least at the concentrations tested. Interestingly, despite not causing significant morphological changes compared to Zr treatments (Figure 6.2), only Na_2SiO_3 posttreatment results in a Zr content that is twice as high as that of other treatments (Figure 6.3). This likely stems from unreacted Zr during the conversion, where the alkaline pH of the posttreatment enhances zirconia precipitation, consistent with the previously discussed Zr precipitation behaviour in *Chapter 3* [51]. This could explain the higher impedance values observed, which, however, diminish more quickly due to the presence of cracks. In this context, the formation of Si—Zr networks cannot be explained solely by the oxygen content. Rather, it could be understood qualitatively through the significant reduction in F content observed in both Si treatments, as shown in Figure 6.3. However, this reduction is likely also due to higher alkalinity in posttreatment, enhancing the removal of F^- through ion exchange with OH^- as the amount of retained anions in zirconia decreases with an increase in the final precipitation pH [154, 236, 333, 334].

These results imply that morphological and corrosion improvements in ZrCCs can be achieved only through the formation of Si—Zr networks, where already a small content of Si significantly leads to improvement. Si/Zr content in Si treatments generally differs by one order of magnitude in the matrix and two orders of magnitude in IMPs, as shown in Figure 6.3. This suggests that the rapid electrochemical formation step of ZrCC can be more efficiently slowed down by introducing another fast chemical reaction step, like the formation of Si—Zr networks, as the growth rate of ZrCC on preexisting ZrO_2 particles does not exceed the rate of alkalization occurring during cathodic reactions in IMPs, thereby not being sufficient for homogeneous ZrCC deposition.

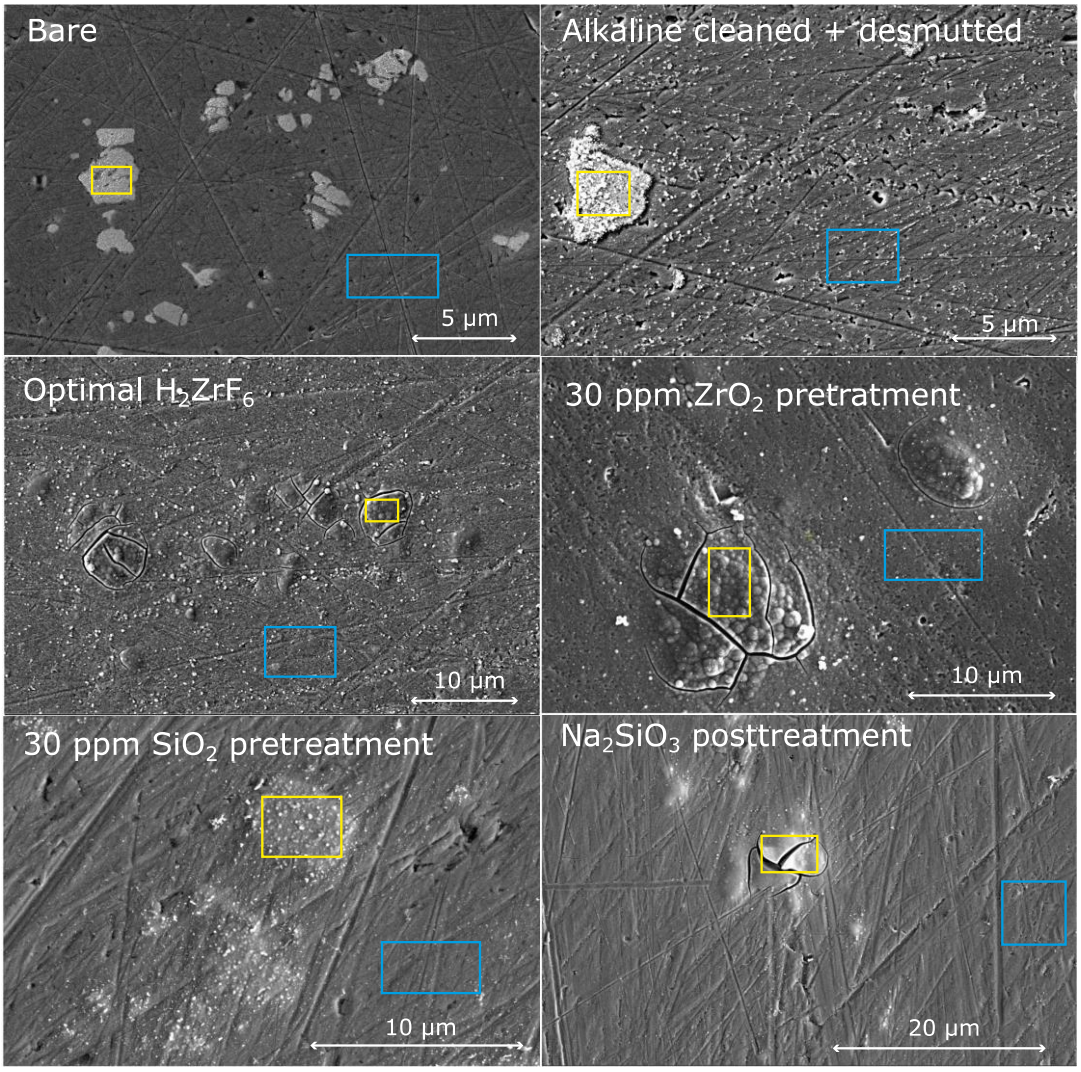

Figure 6.2: SEM micrographs of AA5754 with different treatments for ZrCC.

6.4 Conclusions

The integration of SiO_2 pretreatment significantly improves the corrosion resistance of ZrCCs. The optimal concentration was determined to be 30 ppm, as confirmed by EIS in both dilute Harrison's solution and 3.5 % NaCl. This finding is further supported by SEM analyses, highlighting its efficacy in forming uniform, crack-free ZrCC layers and suggesting the potential of Si—Zr network formation for corrosion resistance enhancement. Despite the less promising results from ZrO_2 pretreatment and Na_2SiO_3 posttreatment, the overall

findings indicate the promising potential of applying colloidal chemistry to enhance ZrCCs. Future research will focus on the long-term effects of SiO_2 pretreatment and investigate the combined effects of SiO_2 and Na_2SiO_3 treatments, with or without additional organic layers, to further enhance the corrosion resistance and adhesion properties of ZrCCs.

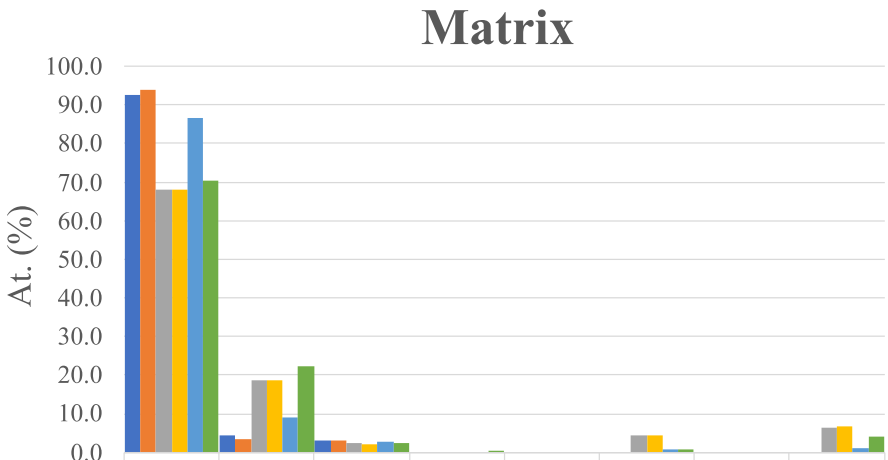

	Al	O	Mg	Si	Fe	F	Cu	Zr
Bare	92.5	4.4	3.1	0.0	0.0	0.0	0.0	0.0
Desmutted	93.8	3.3	3.0	0.0	0.0	0.0	0.0	0.0
optimal H_2ZrF_6	68.2	18.6	2.4	0.0	0.0	4.5	0.0	6.3
optimal $H_2ZrF_6 + ZrO_2$	68.1	18.6	2.1	0.0	0.0	4.4	0.0	6.8
optimal $H_2ZrF_6 + SiO_2$	86.5	9.1	2.7	0.0	0.0	0.6	0.0	1.1
optimal $H_2ZrF_6 + Na_2SiO_3$	70.2	22.2	2.3	0.5	0.0	0.6	0.0	4.2

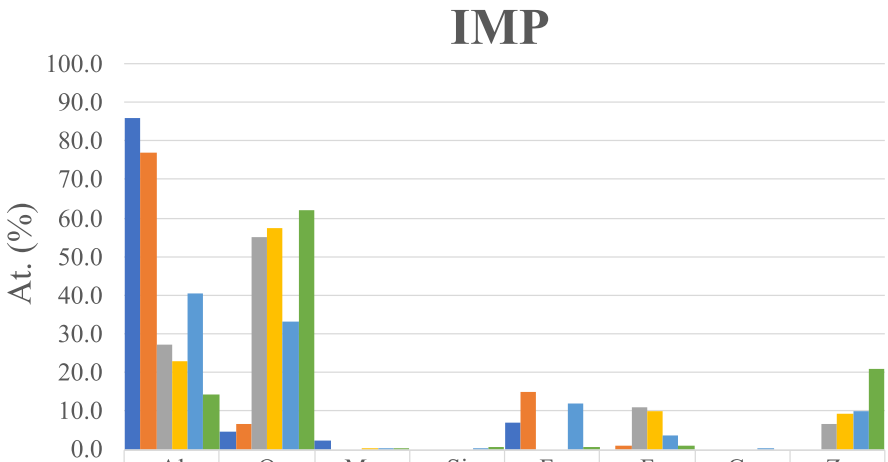

	Al	O	Mg	Si	Fe	F	Cu	Zr
Bare	86.0	4.7	2.3	0.0	6.9	0.0	0.0	0.0
Desmutted	77.0	6.8	0.0	0.0	15.1	1.1	0.0	0.0
optimal H_2ZrF_6	27.1	55.2	0.0	0.0	0.0	11.0	0.0	6.7
optimal $H_2ZrF_6 + ZrO_2$	22.8	57.4	0.5	0.0	0.0	9.9	0.0	9.4
optimal $H_2ZrF_6 + SiO_2$	40.4	33.1	0.3	0.4	12.0	3.5	0.3	10.0
optimal $H_2ZrF_6 + Na_2SiO_3$	14.3	61.9	0.4	0.6	0.7	1.1	0.0	20.9

Figure 6.3: EDS results of AA5754 with different treatments for ZrCC. Matrix (above) and IMP (below).

Chapter 7

Conclusions

The development and optimisation of zirconium conversion coatings (ZrCCs) on cold-rolled steel (CRS), zinc, and aluminium alloy AA5754 substrates were successfully studied and discussed. This chapter provides conclusions in the form of hypotheses confirmation.

1. **Utilising response surface methodology (RSM) explores ZrCC design space on CRS, Zn, and AA5754, identifying optimal condition ranges and factor interactions to enhance corrosion resistance.**

   RSM results revealed that CRS and Zn favoured mid to higher concentrations (825–1226 ppm), longer conversion times (430–480 s), and mid to higher pH levels (4.0–4.6), while AA5754 favoured significantly lower concentrations (150 ppm), shorter immersion times (230 s), and a higher pH (4.6). This is attributed to its higher sensitivity towards conversion bath parameters and the preferential, thicker ZrCC deposition on IMPs, leading to cracking. When evaluating the performance of ZrCC coatings, using a quick drop test method is recommended for initial assessment as it accurately predicts corrosion resistance at specific ZrCC formulation pH levels. Among electrochemical methods, electrochemical impedance spectroscopy (EIS) is sensitive for studying conversion bath effects, but it does not always reflect ZrCC corrosion behaviour. On AA5754, EIS works well after complete coating formation (conversion time $\geq$ 230 s) and has the potential for predicting long-term corrosion on AA5754 with varying ZrCC thickness at lower concentrations. On CRS, a high-frequency time constant indicates good ZrCC formation and higher corrosion protection. On Zn, EIS at pH $\geq$ 4.0 describes coating thickness, while at pH $<$ 4.0, it captures porous ZnO behaviour during conversion. Nevertheless, RSM models derived from EIS were the most effective for both characterising and optimising ZrCCs on all substrates, suggesting it as the most universal ZrCC evaluation technique.

   This hypothesis was confirmed in Chapter 2.

2. **Conducting electrochemical measurements in less aggressive media (e.g., dilute Harrison's solution and simulated acid rain) yields reliable corrosion parameter evaluations and a deeper understanding of ZrCCs' corrosion behaviour.**

   This was especially demonstrated through the evolution of different time constants on CRS in both media. The high-frequency loop indicated the presence of ZrCC in addition to rust layer formation at low frequency, the evolution of which is trackable over time due to the less aggressive nature of the electrolyte.

   This hypothesis was confirmed in Chapters 2 and 3.

3. **Aqueous chemistry in Zr—OH and Zr—F systems illuminates the importance of considering sol-gel chemistry in ZrCC formation beyond electrochemical aspects.**

   Extensive Zr-hydrolysis was presented in the form of revised Zr—OH and Zr—F predominance diagrams. In the latter case, the role of hexafluorozirconic acid, H_2ZrF_6, was shown to suppress the early onset of Zr hydrolysis, thereby adjusting the pH from severely acidic to a level acceptable for the metal substrate during conversion.

   This hypothesis was confirmed in Chapter 3.

4. **Zirconia in ZrCCs exhibits a tetrameric form, confirmable with Time-of-Flight secondary ion mass spectrometry (ToF-SIMS).**

   The implied tetrameric structure from equilibrium diagrams was confirmed with ToF-SIMS and further supported by EIS in simulated acid rain, revealing that not only does ZrCC contain the tetrameric form, but also that it forms only at pH values leading to adequate ZrCC formation, demonstrated at pH = 4.0.

   This hypothesis was confirmed in Chapter 3.

5. **The influence of F^- and Cl^- is different on different substrates, which is reflected in the ZrCC process.**

   F-induced corrosion results from significant complex formation on CRS and AA5754, the latter leading to a narrowing of the Al passive region. However, a comprehensive analysis of the solution content and complex equilibria reveals that Zn corrosion is primarily influenced by the overall ionic strength of the solution and further complexation with the buffering agent at higher pH levels, should these conditions occur during corrosion. In contrast, the effect of Cl^- does not involve complexation and thus does not lead to uniform corrosion but rather to localized corrosion, primarily causing pitting on AA5754 at higher concentrations. Additionally, thermodynamic equilibria analysis highlights the subtle differences in the stabilization effects of open circuit potential on CRS and AA5754.

   This hypothesis was confirmed in Chapter 4.

6. **Non-preferential adsorption of colloidal particles on the metal surface ensures their uniform distribution, acting as nucleation sites for ZrCC precipitation, resulting in a uniform ZrCC coating on AA5754. Thus, applying colloidal SiO_2 or ZrO_2 pretreatment enhances the corrosion resistance of the formed ZrCCs.**

   Using SiO_2 pretreatment enhances the corrosion resistance of ZrCCs, with the best performance identified at 30 ppm, as confirmed by EIS in both dilute Harrison's solution and 3.5 % NaCl. SEM analysis further showed uniform, crack-free ZrCC layers and suggested Si—Zr network formation needed for corrosion resistance. Contrary to the initial hypothesis, ZrO_2 seemed to have no effect, probably due to much faster cathodic activity during conversion compared to the growth of ZrCC, which is effectively mitigated with the formation of Si—Zr networks.

   This hypothesis was partially confirmed in Chapter 5.

7. **Local pH and dissolved oxygen (DO) concentration measurements using scanning micro-probe techniques assist in deciphering the complete ZrCC mechanism on various substrates, based on the premise that different substrates yield different results even under similar ZrCC conversion bath parameters.**

Here, the optimal conditions obtained in *Chapter 2* were confirmed. Both CRS and Zn showed similar deposition patterns due to uniform corrosion, with CRS having more significant deposition at 825 ppm DO and pH = 4.0. In contrast, AA5754 showed optimal deposition at 150 ppm DO and pH = 4.6. DO levels were revealed as the most essential parameter for tracking ZrCC formation, where initial DO peaks for AA5754 indicate complete ZrCC coverage, with subsequent peaks and shifts in OCP suggesting the sealing of cracks.

Appendix A

Supplementary Data for Chapter 2

A.1 Experimental Procedure

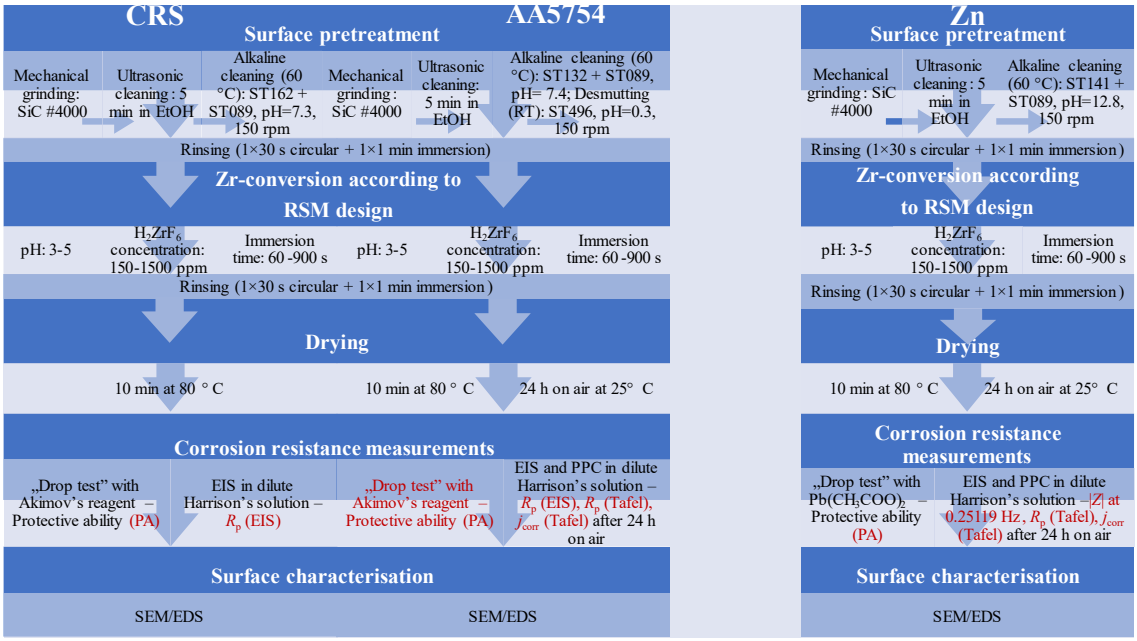

Figure A.1: Schematic summary of the experimental procedure.

A.2 Electrochemical Results

Table A.1: PPC results for CRS: corrosion current density, corrosion potential, anodic and cathodic Tafel slopes and polarisation resistance.

Conditions	j_{corr} (µA/cm²)	E_{corr} (V)	$\lvert b_a \rvert$ (V/dec)	$\lvert b_c \rvert$ (V/dec)	R_p (Ω cm²)
424 ppm 230s pH 3.4	3.10	−0.745	0.062	0.122	7252
825 ppm 480s pH 4.0	3.22	−0.732	0.097	0.139	9802
Alkaline cleaned	5.06	−0.764	0.083	0.190	6298
Bare	6.04	−0.758	0.080	0.161	4909

Table A.2: PPC results for Zn: corrosion current density, corrosion potential, anodic and cathodic Tafel slopes and polarisation resistance.

Conditions	j_{corr} (µA/cm²)	E_{corr} (V)	$\lvert b_a \rvert$ (V/dec)	$\lvert b_c \rvert$ (V/dec)	R_p (Ω cm²)
1226 ppm 230 s pH 3.4	9.76	−1.088	0.106	0.100	2923
1226 ppm 230 s pH 4.6	13.57	−1.090	0.081	0.075	1592
1226 ppm 730 s pH 3.4	10.98	−1.092	0.070	0.104	2114
1226 ppm 730 s pH 4.6	9.20	−1.091	0.092	0.082	2602
150 ppm 480 s pH 4.0	9.97	−1.098	0.122	0.110	3213
1500 ppm 480 s pH 4.0	7.26	−1.098	0.096	0.074	3190
424 ppm 230 s pH 3.4	11.24	−1.093	0.074	0.102	2108
424 ppm 230 s pH 4.6	8.90	−1.102	0.112	0.099	3261
424 ppm 730 s pH 3.4	11.13	−1.086	0.072	0.101	2083
424 ppm 730 s pH 4.6	8.90	−1.092	0.078	0.084	2525
825 ppm 480 s pH 3.0	11.45	−1.098	0.074	0.112	2157
825 ppm 480 s pH 4.0_1	9.40	−1.094	0.088	0.083	2517
825 ppm 480 s pH 4.0_2	9.28	−1.089	0.094	0.097	2846
825 ppm 480 s pH 4.0_3	7.64	−1.088	0.077	0.091	3020
825 ppm 480 s pH 4.0_4	6.71	−1.083	0.056	0.087	2799
825 ppm 480 s pH 4.0_5	6.77	−1.091	0.080	0.077	3219
825 ppm 480 s pH 4.0_6	7.20	−1.073	0.047	0.105	2497
825 ppm 480 s pH 5.0	8.77	−1.094	0.093	0.085	2810
825 ppm 60 s pH 4.0	11.71	−1.097	0.163	0.102	2967
825 ppm 900 s pH 4.0	9.99	−1.092	0.073	0.082	2143
Alkaline cleaned	19.14	−1.091	0.092	0.130	1555
Bare	16.28	−1.095	0.064	0.081	1215

Table A.3: PPC results for AA5754: corrosion current density, corrosion potential, anodic and cathodic Tafel slopes and polarisation resistance.

Conditions	j_{corr} (µA/cm²)	E_{corr} (V)	$\lvert b_a \rvert$ (V/dec)	$\lvert b_c \rvert$ (V/dec)	R_p (Ω cm²)
1226 ppm 230 pH 3.4	0.46	−0.763	0.464	0.217	179350
1226 ppm 230 pH 4.6	0.20	−0.804	0.378	0.169	329520
1226 ppm 730 s pH 3.4	0.34	−0.831	0.365	0.168	186850
1226 ppm 730 s pH 4.6	0.17	−0.811	0.330	0.159	356780
150 ppm 230 s pH 4.6_1	0.15	−0.721	0.257	0.228	454900
150 ppm 230 s pH 4.6_2	0.11	−0.765	0.211	0.222	565350
150 ppm 355 s pH 4.3	0.09	−0.732	0.235	0.196	676990
150 ppm 480 s pH 3.4	0.38	−0.857	0.364	0.183	176480
150 ppm 480 s pH 4.0	0.16	−0.768	0.458	0.178	457460
150 ppm 480 s pH 4.6	0.08	−0.842	0.374	0.149	722340
150 ppm 730 s pH 4.0	0.36	−0.923	0.471	0.166	187500
1500 ppm 480 s pH 4.0	0.27	−0.897	0.290	0.153	204310
424 ppm 230 s pH 3.4	0.38	−0.799	0.466	0.298	263810
424 ppm 230 s pH 4.6	0.12	−0.805	0.474	0.167	552980
424 ppm 730 s pH 3.4	0.40	−0.874	0.320	0.191	164540
424 ppm 730 s pH 4.6	0.20	−0.771	0.285	0.190	313770
650 ppm 420 s pH 4.4	0.21	−0.906	0.206	0.205	268740
825 ppm 230 s pH 4.3_1	0.10	−0.743	0.239	0.224	625140
825 ppm 230 s pH 4.3_2	0.13	−0.794	0.240	0.233	485750
825 ppm 355 s pH 4.0_1	0.32	−0.815	0.398	0.186	218190
825 ppm 355 s pH 4.0_2	0.39	−0.914	0.387	0.171	166940
825 ppm 355 s pH 4.0_3	0.36	−0.785	0.413	0.225	225020
825 ppm 480 s pH 3.0	0.50	−0.748	0.411	0.244	169360
825 ppm 480 s pH 4.0_1	0.27	−0.843	0.256	0.162	204480
825 ppm 480 s pH 4.0_2	0.29	−0.781	0.327	0.201	234570
825 ppm 480 s pH 4.0_3	0.19	−0.837	0.380	0.192	367930
825 ppm 480 s pH 4.0_4	0.19	−0.906	0.400	0.147	318060
825 ppm 480 s pH 4.0_5	0.23	−0.953	0.313	0.153	242480
825 ppm 480 s pH 4.0_6	0.15	−0.828	0.286	0.125	325720
825 ppm 480 s pH 5.0	0.38	−0.778	0.382	0.203	191870
825 ppm 60 s pH 4.0	0.17	−0.695	0.393	0.221	455090
825 ppm 900 s pH 4.0	0.39	−0.864	0.333	0.166	156200
Alkaline cleaned	0.06	−0.669	0.192	0.233	1010000
Alkaline cleaned + desmutted	0.04	−0.611	0.193	0.166	1410000
Bare	0.12	−0.695	0.203	0.142	374290

Table A.4: EIS results for CRS.

Conditions	R1 (Ω cm^2)	R2 (Ω cm^2)	Y_0 CPE 1 ($\mu\Omega^{-1}$ s^n)	CPE 1 n	R3 (Ω cm^2)	R2 +R3 (Ω cm^2)	Y_0 CPE 2 ($\mu\Omega^{-1}$ s^n)	CPE 2 n	χ^2
1226 ppm 230 s 3.4 pH	235	2276	226	0.75		2276			0.014
1226 ppm 230 s 4.6 pH	275	3513	329	0.73	1503	5015	6020	0.96	0.010
1226 ppm 730 s 3.4 pH	231	2307	512	0.71	1406	3713	5240	0.83	0.005
1226 ppm 730 s 4.6 pH	272	2779	366	0.69	820	3598	4600	0.77	0.056
150 ppm 480 s 4.0 pH	247	4694	309	0.74	2052	6746	3990	0.8	0.005
1500 ppm 480 s 4.0 pH	217	2232	461	0.7	860	3092	5250	0.86	0.006
424 ppm 230 s 3.4 pH	210	2994	222	0.77		2994			0.009
424 ppm 230 s 4.6 pH	247	3444	307	0.75	2371	5816	2330	0.67	0.006
424 ppm 730 s 3.4 pH	236	3293	446	0.71	1519	4812	7550	0.92	0.010
424 ppm 730 s 4.6 pH	263	2733	430	0.7	562	3295	6680	0.92	0.014
825 ppm 480 s 3.0 pH	125	3451	195	0.78		3451			0.159
825 ppm 480 s 4.0 pH_1	236	2879	296	0.75	2994	5872	1380	0.54	0.014
825 ppm 480 s 4.0 pH_2	265	4551	304	0.74	3174	7725	3900	0.76	0.008
825 ppm 480 s 4.0 pH_3	282	4530	330	0.71	1471	6000	8670	0.95	0.049
825 ppm 480 s 4.0 pH_4	245	3879	349	0.73	2444	6323	4040	0.82	0.012
825 ppm 480 s 4.0 pH_5	273	4042	340	0.73	2982	7024	4360	0.76	0.037
825 ppm 480 s 4.0 pH_6	252	3681	312	0.72	1848	5529	2890	0.67	0.011
825 ppm 480 s 5.0 pH	227	3351	375	0.72	1548	4899	4720	0.88	0.004
825 ppm 60 s 4.0 pH	172	3078	311	0.73		3078			0.084
825 ppm 900 s 4.0 pH	251	1472	458	0.71	851	2323	1440	0.66	0.029
Alkaline cleaned	230	3114	181	0.79		3114			0.027
Bare	238	2189	276	0.75		2189			0.018
Time resolved evolution of ZrCC corrosion									
825 ppm 480 s 4.0 pH_0 h	252	3681	312	0.72	1848	2276	2889	0.67	0.011
825 ppm 480 s 4.0 pH_24 h	251	3788	273	0.74	820	5016	14779	1.00	0.027

To support the assessment of those time constants, a change of the aforementioned time constants was observed on one selected sample presumed to have a satisfactory ZrCC coating, namely 825 ppm/480 s/pH 4.0 after 24-h immersion in dilute Harrison's solution, Figure A.2. This led to wider complex impedance and increased n values (Table A.4), indicative of rust layer growth on the electrode area, increasing capacity with concurrent decrease in R due to accumulation of more porous and not so adherent rust which is yet non protective. Despite rust formation, the first and second time constants remained mostly stable, signifying the preservation of ZrCC related to the first time constant whereas the second time constant, associated with charge transfer resistance, remains unchanged due to the presence of a non-protective rust layer. Furthermore, a clearer separation between the last two time constants corresponds with the formation of a thicker rust layer on the ZrCC, suggesting a less dense structure. This contrasts with the more overlapping time constants observed immediately after exposure, which imply a denser arrangement between the ZrCC and the developing corrosion products, similar to protective film growth observations in Fe- and Zn-based alloys [322, 335].

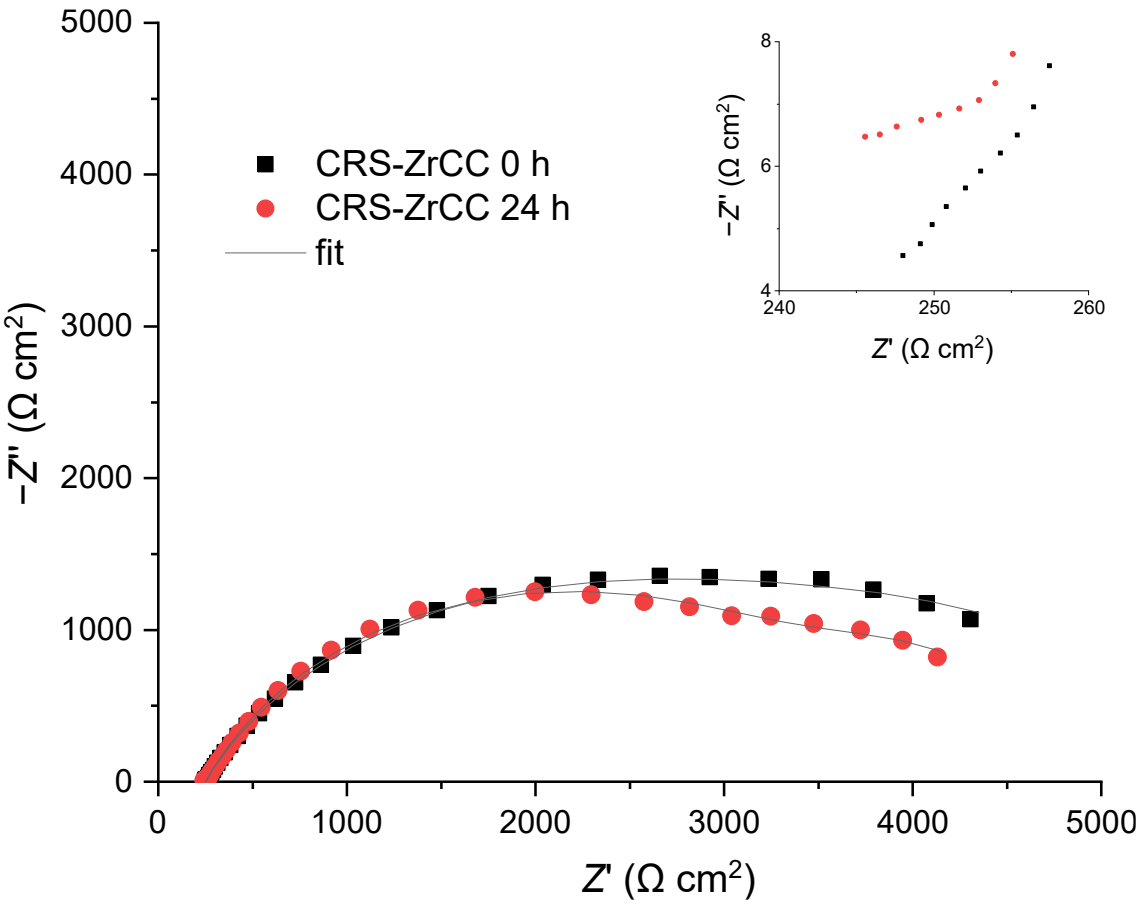

Figure A.2: Time evolution of EIS spectra measured for CRS-ZrCCs during 24 h with inserted high-frequency region (right) and table of EEC fitting results (above).

Table A.5: EIS results for Zn.

Conditions	$\|Z\|$ at 0.25119 Hz (Ω cm^2)
1226 ppm 230 s pH 3.4	1079
1226 ppm 230 s pH 4.6	1201
1226 ppm 730 s pH 3.4	950
1226 ppm 730 s pH 4.6	1450
150 ppm 480 s pH 4.0	642
1500 ppm 480 s pH 4.0	1377
424 ppm 230 s pH 3.4	561
424 ppm 230 s pH 4.6	788
424 ppm 730 s pH 3.4	778
424 ppm 730 s pH 4.6	697
825 ppm 480 s pH 3.0	574
825 ppm 480 s pH 4.0_1	916
825 ppm 480 s pH 4.0_2	1212
825 ppm 480 s pH 4.0_3	875
825 ppm 480 s pH 4.0_4	1025
825 ppm 480 s pH 4.0_5	800
825 ppm 480 s pH 4.0_6	895
825 ppm 480 s pH 5.0	1452
825 ppm 60 s pH 4.0	588
825 ppm 900 s pH 4.0	1297
Alkaline cleaned	655
Bare	304

Table A.6: EIS results for AA5754.

Conditions	R1 (Ω cm²)	R2 (Ω cm²)	Y_0 CPE 1 ($\mu\Omega^{-1}$ s^n)	CPE 1 *n*	χ^2
1226 ppm 230 pH 3.4	228	112520	5.63	0.93	0.102
1226 ppm 230 pH 4.6	243	171100	4.37	0.93	0.093
1226 ppm 730 s pH 3.4	209	91541	5.61	0.93	0.072
1226 ppm 730 s pH 4.6	238	221720	4.91	0.93	0.063
150 ppm 230 s pH 4.6_1	237	443400	4.65	0.93	0.173
150 ppm 230 s pH 4.6_2	237	443400	4.65	0.93	0.173
150 ppm 355 s pH 4.3	258	650830	4.98	0.94	0.073
150 ppm 480 s pH 3.4	252	107120	5.88	0.93	0.033
150 ppm 480 s pH 4.0_1	214	147140	5.85	0.92	0.032
150 ppm 480 s pH 4.0_2	232	331670	5.55	0.92	0.062
150 ppm 480 s pH 4.6	252	471630	4.63	0.94	0.133
150 ppm 730 s pH 4.0	231	115150	5.07	0.94	0.092
1500 ppm 480 s pH 4.0	212	123820	5.64	0.94	0.031
424 ppm 230 s pH 3.4	238	166660	5.46	0.94	0.066
424 ppm 230 s pH 4.6	244	324030	4.55	0.93	0.108
424 ppm 730 s pH 3.4	224	112390	5.81	0.95	0.018
424 ppm 730 s pH 4.6	259	196040	5.47	0.94	0.036
650 ppm 420 s pH 4.4	249	210370	5.03	0.94	0.196
825 ppm 230 s pH 4.3_1	245	504890	4.55	0.93	0.128
825 ppm 230 s pH 4.3_2	241	338530	5.45	0.93	0.130
825 ppm 355 s pH 4.0_1	245	147090	5.33	0.93	0.066
825 ppm 355 s pH 4.0_2	229	113930	6.06	0.94	0.021
825 ppm 355 s pH 4.0_3	238	144130	5.25	0.94	0.104
825 ppm 480 s pH 3.0	210	90900	5.29	0.95	0.120
825 ppm 480 s pH 4.0_1	231	139570	5.76	0.95	0.025
825 ppm 480 s pH 4.0_2	213	156280	5.53	0.94	0.037
825 ppm 480 s pH 4.0_3	244	268900	5.01	0.94	0.050
825 ppm 480 s pH 4.0_4	252	182880	4.70	0.94	0.116
825 ppm 480 s pH 4.0_5	229	166890	5.07	0.95	0.038
825 ppm 480 s pH 4.0_6	240	199190	5.29	0.93	0.064
825 ppm 480 s pH 5.0	227	128890	5.66	0.93	0.027
825 ppm 60 s pH 4.0	170	716410	5.05	0.95	0.057
825 ppm 900 s pH 4.0	239	98866	6.20	0.93	0.040
Alkaline cleaned	229	1735700	6.47	0.93	0.039
Alkaline cleaned + desmutted	244	1778300	4.19	0.96	0.033
Bare	231	502990	7.94	0.87	0.084

A.3 RSM Procedure and Theoretical Background

Experiments serve three primary purposes: exploration, estimation, and confirmation. Exploration involves understanding the generated data, estimation identifies how process variables influence the output, and confirmation validates predicted results, often for optimisation purposes [67], the latter being the main purpose of RSM. In brief, during the modelling phase, data is collected and a mathematical model is created to map the relationship between input factors and the response. The model is then analysed for accuracy and fit. Once validated, optimisation techniques are used to find the conditions that optimise the response. These conditions are finally tested through additional experiments to confirm the real-world accuracy of the model. Guided by Occam's razor principle, the design and analysis were kept as simple as possible. It is out of the scope of this thesis to describe all the use of these tools, as they are readily available and user-friendly, with explanations provided in conventional DoE statistical tools like Design Expert. For detailed information on performing proper statistical analysis in DoE, refer to [36, 37, 67, 131].

In DoE, including RSM, factors are simultaneously varied at different levels based on a planned experimental design matrix in which experimental runs are both orthogonal and randomised. Orthogonality guarantees the independence of factors, ensuring that changing the level of one factor does not interfere with the variation caused by another factor. This is achieved by matching each level of each factor with an equal number of levels of other factors. Conversely, randomization involves assigning experimental conditions randomly to different runs or trials, reducing the impact of unknown and uncontrolled influences on the results.

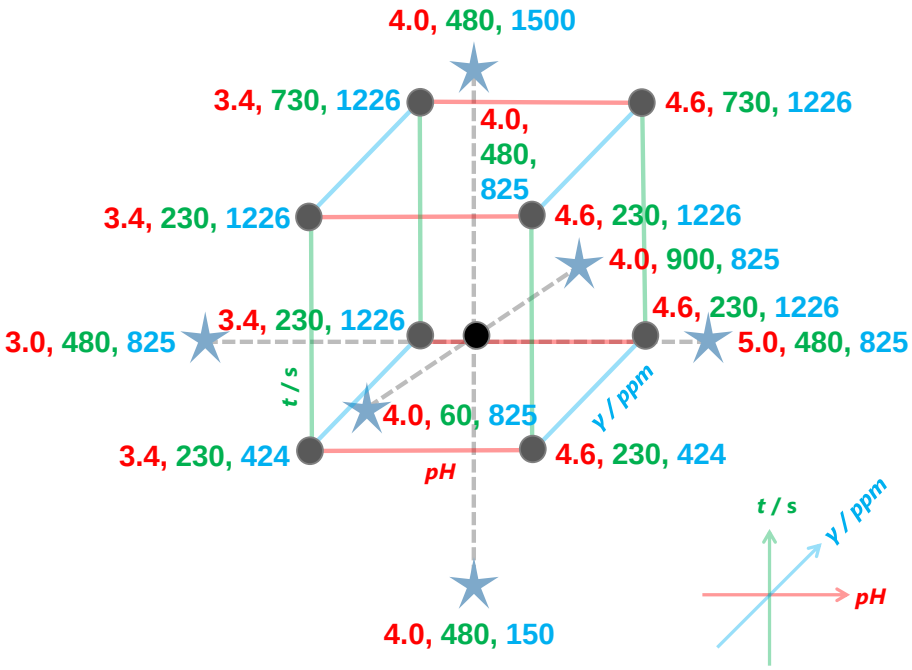

Figure A.3: The initial CCD design (without augmentation) employed for all substrates.

The central composite design (CCD), the most common RSM design that strikes a balance between complexity and efficiency, was employed in this work. Despite involving a greater number of experiments, CCD was economically and practically feasible in this

case. The CCD used is presented in Figure A.3. It includes factorial points at the centre and extremes of the design space, along with axial points, presented as "stars". The central point (825 ppm 480 s pH 4.0) represents conditions at the middle of all factor levels, facilitating the curvature estimation. Meanwhile, strategically placing axial points at a certain distance from the centre enables efficient estimation of both curvature and interaction effects as well as exploration of regions of interest without measuring all possible points. The curvature can arise from either a main effect exhibiting a quadratic response or interactions between two factors. Both situations are possible in the case of ZrCCs. Signs of curvature, particularly in the ZrCC process, can be observed from earlier OFAT results on pH, concentration, and conversion time, such as [43, 140], where responses show an inflexion point, representing either a minimum or maximum at a particular setting before changing again. RSM plots thus involve three factors, two plotted on the x and y axes, and the response variable shown as contours or a surface. The third factor is typically represented by keeping it constant, while the other two factors vary. In that way, 3D plots help in understanding the overall trend and interaction effects.

Factor ranges were entered in terms of alphas, where the alpha value represents a distance from the centre of the design space along each design axis (set herein to the commonly used value of 1.68). The factors are designated as follows: **A: pH, B: t (s), and C: γ (ppm), i.e., pH, conversion time and H_2ZrF_6 concentration**. The experimental runs were divided into 3 blocks (3 days of measurement for each substrate), conforming to both orthogonality and randomization principles. The design matrix and corresponding responses for each substrate are shown in Tables A.7–A.9. In DoE, the primary objective, in general, is to understand the relationship between variables and the response rather than achieving high precision. Emphasising an adequate number of runs effectively models this relationship, making it unnecessary to repeat all measured points. Typically, only centre points are repeated, enabling the estimation of pure error needed for the lack of fit test, which, in turn, is necessary to assess the reliability of the model. This approach is also advantageous because one may expect the optimum at the middle of the design space, thus improving prediction capability in that region. However, if needed, this does not limit the user from performing replication runs in their region of interest.

The effectiveness of the RSM model indeed lies in its ability to utilise ANOVA (Analysis of Variance). As such, ANOVA is implemented in the RSM statistical tools of Design Expert, and was employed herein to determine whether there are statistically significant differences between the means of the samples. By addressing noise in experimental data, ANOVA helps to discern and accommodate variability in the model. Moreover, in situations with limited data, ANOVA assists the RSM model in relying on neighbouring data points, even in regions of sparse or inconsistent information, contributing to a more robust analysis. Finally, the consideration of variable interactions through ANOVA enables the RSM model to identify an optimum that may differ from the direct experimental point with the best response, providing a nuanced understanding of complex relationships. In simpler terms, the second or third best measured responses can be found to be closer to the optimal condition [36, 37, 131].

While RSM is primarily used for optimisation, the irreproducible nature of ZrCCs made achieving precise optimal conditions challenging, requiring a high confidence level in the predictive model. Consequently, we shifted our focus to the exploration and estimation phases to gain a more comprehensive understanding of ZrCC behaviour, rather than prediction of specific optimal conditions. It is important to note that experimenters often elect optimal conditions based on factors like costs or environmental impact rather than pursuing the "true" process optimum. Thus, greater emphasis was placed on modifying the model to satisfy parameters used for evaluating its significance and its ability to navigate the design space effectively, such as adequate precision (*vide infra*). This approach

ultimately allowed us to identify directions for improvement, indicate optimum regions, and identify factor interactions, ultimately explaining the behaviour of the obtained data.

In particular, model validation was conducted using graphical and numerical analysis tools. The focus was on the model maximising the adjusted R^2 and the predicted R^2. Each analysis began with a quadratic model, and an automatic model selection tool in Design Expert was used to algorithmically choose the terms to include in the model. Models based on maximising the adjusted R^2 were found the most suitable, resulting in hierarchical models that may contain insignificant factors to preserve hierarchy. This is because, in a hierarchical model, all lower-order terms contained in a term must also be present in the model [336]. The decision to ignore certain data points, make transformations, or even ignore blocks can be justified under specific circumstances to ensure a proper understanding of the system behaviour. Ignoring outliers or extreme data points not representative of the system true behaviour can help prevent undue influence on the model.

In the case of AA5754, the obtained models revealed the direction of improvement to higher pH, lower conversion times and lower concentrations, requiring further experiments. To achieve this, the existing design was augmented with additional runs in the desired experimental space using an automatic algorithm provided by the Design Expert software. The first augmentation involved factor settings of 150 ppm/480 s/pH 3.4, 150 ppm/730 s/pH 4.0, 150 ppm/480 s/pH 4.6 and triplicated point at 825 ppm/355 s/pH 4.0. As optimal results were not achieved after this augmentation, the second one was conducted, which involved factor settings of 150 ppm 230 s pH 4.6, the duplicated point at 150 ppm/ 355 s/pH 4.3, 656 ppm/418 s/pH 4.4 and duplicated point at 825 ppm/230 s/pH 4.3. This design refination resulted in a so-called "D-optimal design" where the quality of the data obtained during the augmentation process is enhanced to provide the most precise and efficient estimation of model parameters and the best prediction accuracy for response variables. The obtained final augmented model, based on 32 experiments, suggested using a cubic model to describe the process. Higher-order polynomials, like cubic ones, can indeed be described using RSM, but they introduce complexities with multiple terms raised to various powers, making it difficult to estimate their effects uniquely. Consequently, certain measurements, specifically those taken before augmentations (*vide infra*), were excluded from the RSM analysis. This decision was made to revert to simpler, lower-ordered models and to investigate the design space of interest, which includes lower concentrations, shorter conversion times, and higher pH levels. This approach was necessary because the results from the previous models were significantly influenced by the cracking of ZrCCs. Therefore, modifications to the models were grounded in scientific reasoning, prioritizing a thorough comprehension of the system over mere statistical improvements. In addition, cubic terms become aliased with lower-order terms due to insufficient data from the experimental design as well as suggesting overfitting of the data (overfitting occurs when the model fits the experimental data noise too closely, leading to overly optimistic precision estimates that do not hold up on new data). Yet, by applying the sparsity-of-effects principle, it has been observed that most natural phenomena involve interactions between at most two factors [131]. Therefore, while higher-order polynomials are possible, they are often impractical for describing specific processes, including ZrCC formation.

Similarly, transformations can help linearise relationships, making the model assumptions more plausible and the interpretation of results more meaningful. In cases where certain experimental blocks introduce confounding effects that do not contribute to the primary factors of interest, their exclusion can enhance the clarity of the analysis. The transformations employed in this study encompassed inverse square root and power transformations (*vide infra*).

Nevertheless, although statistics can be manipulated to portray desired outcomes, the primary objective of RSM is to model and optimise complex systems accurately by

thoroughly exploring the response surface. Therefore, it is of utmost importance to ensure that the model outcomes hold practical significance. The revealed relationships should align with both domain knowledge and the involved variables and all modifications to the model should be founded on scientific rationale, emphasising a thorough grasp of the system rather than mere statistical enhancement.

A.3.1 Terminology

A.3.1.1 Fit statistics

Adequate precision measures the signal-to-noise ratio. A ratio greater than 4 is desirable, indicating an adequate signal, i.e., that the model can be used to navigate the experimental space.

Requiring a difference below 0.2 between adequate and predicted R^2 could serve as a heuristic against overfitting. Overfitting arises when a model closely fits training data but struggles to generalize to new data. A significant adequate and predicted R^2 difference might signal overfitting, wherein the model learns noise and patterns specific to training data, not applicable to new data. If the main aim is, however, describing variable relationships in the measured data, with less focus on predicting new data, the mentioned difference becomes less important.

A.3.1.2 The final equation in terms of actual factors

The equation in terms of actual factors can be used to make predictions about the response for given levels of each factor. Here, the levels should be specified in the original units for each factor. This equation should not be used to determine the relative impact of each factor because the coefficients are scaled to accommodate the units of each factor and the intercept is not at the centre of the design space.

A.3.1.3 Transformations

Power transformations encompass raising each data point to a specific exponent, which can assume any real value. Common power transformations encompass square root, cube root, logarithmic, and reciprocal transformations.

Inverse transformations are used when the relationship between variables is expected to be inversely proportional. Applying this transformation can help make the relationship more linear. They are also, at times, employed for normalizing data exhibiting exponential growth patterns.

The inverse square root transformation finds application in scenarios where data exhibits escalating variance as response variable values increase. This transformation compresses data at higher values, diminishing dispersion and fostering greater consistency in variance throughout the response variable range. It particularly proves beneficial for counting data or measurements with increasing proportional variance at higher values.

A.4 RSM Results

In tables, Std refers to Standard Order, a predetermined sequence of experimental runs based on an experimental design matrix. Run order refers to the actual order in which experiments are run, whether randomised or not. Experiments were run in 3 blocks (3 days of measurement for each substrate).

Text in `code style` represents outputs from Design Expert software.

A.4.1 Cold-rolled steel

Table A.7: RSM matrix for CRS and non-RSM responses.

Substrate: CRS			Factors			Protective ability	Polarisation resistance	Non-RSM responses	
Std	**Block**	**Run**	**A: pH**	**B: t (s)**	**C: γ (ppm)**	**PA after 10 min (s)**	**R_p EIS (Ω cm²)**	**ZrCC color****	**Drop color *****
1	Day 1	1	3.4	230	424	7	2994	gold	red
6	Day 1	2	4.6	230	1226	11	5016	gold	pink
4	Day 1	3	4.6	730	424	7	3295	purple	red
7	Day 1	4	3.4	730	1226	6	3713	gold	red
10	Day 1	5	4.0	480	825	11	5872	gold	pink
9	Day 1	6	4.0	480	825	12	7725	gold	pink
12	Day 2	7	4.0	480	825	12	6000	gold	pink
11	Day 2	8	4.0	480	825	13	6323	gold	pink
3	Day 2	9	3.4	730	424	10	4812	gold−purple	pink
5	Day 2	10	3.4	230	1226	7	2276	gold	red
8	Day 2	11	4.6	730	1226	10	3599	gold−purple	pink
2	Day 2	12	4.6	230	424	10	5816	gold	pink
17	Day 3	13	4.0	480	150	12	6746	gold	pink
15	Day 3	14	4.0	60	825	9	3078	light gold	red
14	Day 3	15	5.0	480	825	10	4899	gold	pink
13	Day 3	16	3.0	480	825	8	3451	light gold	pink
20	Day 3	17	4.0	480	825	12	7024	gold	pink
19	Day 3	18	4.0	480	825	12	5529	gold	red
18	Day 3	19	4.0	480	1500	11	3092	gold	pink
16	Day 3	20	4.0	900	825	9	2323	purple, smeared	red
Bare						19	/	red	red
Alkaline cleaned						11*	/	red	red

*Hydrophobic surface caused by alkaline cleaning.
**Colour changes from gold to purple with the increase in thickness.
*** Colour of the drop during copper reduction in the drop test.

A.4.1.1 Response 1: PA after 10 min (s)

ANOVA for Reduced Quadratic model

Source	Sum of Squares	df	Mean Square	F-value	p-value	
Block	7.03	2	3.51			
Model	67.56	7	9.65	16.69	0.0002	significant
A-pH	9.46	1	9.46	16.36	0.0029	
B-t	0.2929	1	0.2929	0.5066	0.4946	
C-c	0.0664	1	0.0664	0.1148	0.7425	
AB	4.50	1	4.50	7.78	0.0211	
AC	8.00	1	8.00	13.84	0.0048	
A^2	25.59	1	25.59	44.26	< 0.0001	
B^2	25.59	1	25.59	44.26	< 0.0001	
Residual	5.20	9	0.5781			
Lack of Fit	4.20	6	0.7005	2.10	0.2894	not significant
Pure Error	1.0000	3	0.3333			
Cor Total	79.79	18				

This row was ignored for the analysis:
19
Factor coding is Coded.
Sum of squares is Type III - Partial
The model F-value of 16.69 implies that the model is significant. There is only a 0.02 % chance that an F-value this large could occur due to noise.
Based on p-values, A, AB, AC, A^2, and B^2 are significant model terms.
The lack of fit F-value of 2.10 implies that the lack of fit is not significant relative to the pure error. There is a 28.94 % chance that a lack of fit F-value this large could occur due to noise. The model fits.

Fit Statistics

Std. Dev.	0.7603	R^2	0.9285
Mean	9.89	Adjusted R^2	0.8729
C.V. %	7.68	Predicted R^2	0.6308
		Adequate Precision	10.1216

The predicted R^2 of 0.6308 is not as close as the adjusted R^2 of 0.8917; i.e., the difference is more than 0.2. Adequate precision of 10.122 indicates that this model can be used to navigate the experimental space.

Final Equation in Terms of Actual Factors

$$\text{PA after 10 min / s} = -56.63771 + 31.39522 \times \text{pH} + 0.040724 \times t - 0.016559 \times c - 0.005051 \times (\text{pH} \times t) + 0.004190 \times (\text{pH} \times c) - 3.87855 \times \text{pH}^2 - 0.000022 \times t^2$$

A.4.1.2 Response 2: R_p EIS / Ω cm²

ANOVA for Reduced Quadratic model

Source	Sum of Squares	df	Mean Square	F-value	p-value	
Block	22574.22	2	11287.11			
Model	4.420×10^7	5	8.841×10^6	19.42	< 0.0001	significant
A-pH	2.968×10^6	1	2.968×10^6	6.52	0.0268	
B-t	2.792×10^5	1	2.792×10^5	0.6135	0.4500	
AB	6.467×10^6	1	6.467×10^6	14.21	0.0031	
A^2	1.098×10^7	1	1.098×10^7	24.11	0.0005	
B^2	2.759×10^7	1	2.759×10^7	60.61	< 0.0001	
Residual	5.007×10^6	11	4.552×10^5			
Lack of Fit	2.120×10^6	8	2.650×10^5	0.2755	0.9357	not significant
Pure Error	2.886×10^6	3	9.622×10^5			
Cor Total	4.923×10^7	18				

This row was ignored for the analysis:
19
Factor coding is Coded.
Sum of squares is Type III - Partial
The model F-value of 19.42 implies that the model is significant. There is only a 0.01 % chance that an F-value this large could occur due to noise.
Based on p-values, A, AB, A^2, and B^2 are significant model terms.
The lack of fit F-value of 0.28 implies that the lack of fit is not significant relative to the pure error. There is a 93.57 % chance that a lack of fit F-value this large could occur due to noise. The model fits.

Fit Statistics

Std. Dev.	674.66	R^2	0.8983
Mean	4762.68	Adjusted R^2	0.8520
C.V. %	14.17	Predicted R^2	0.7670
		Adeq Precision	9.6717

The predicted R^2 of 0.7670 is in reasonable agreement with the adjusted R^2 of 0.8520; i.e., the difference is less than 0.2. Adequate precision of 9.672 indicates that this model can be used to navigate the experimental space.

Final Equation in Terms of Actual Factors

$$R_p \text{ EIS} = -53598.94370 + 23842.75498 \times \text{pH} + 45.38111 \times t - 6.05502 \times (\text{pH} \times t) - 2519.04561 \times \text{pH}^2 - 0.022639 \times t^2$$

Ignoring the outlier (Run 19) was suggested after analysing the externally studentized residuals, which improved fit statistics for both responses. Notably, this point (1500 ppm/480 s/pH 4.0) is an axial point that lies outside the design space, indicating that

extrapolation to higher concentrations is not advisable. However, ignoring this point did not change the shape or the direction toward the optimum of the response surface. Therefore, it can be summarized that the design for CRS is generally good; the model for PA after 10 min is of average quality, still usable for characterisation. On the other hand, the model for R_p EIS is excellent and can be employed for both characterisation and, potentially, optimization.

A.4.2 Zn

Table A.8: RSM matrix for Zn.

Substrate: Zn			**Factor**			**Protective ability**		**Corrosion current density**	**Polarisation resistance**	**Absolute impedance**
Std	**Block**	**Run**	**A: pH**	**B: t (s)**	**C: γ (ppm)**	**PA after 10 min (s)**	**PA after 24 h (s)**	**j_{corr} (µA cm^{-2})**	**R_p Tafel (Ω cm²)**	**$\|Z\|$ at 0.25119 Hz (Ω cm²)**
1	Day 1	1	3.4	230	424	24	10	11.24	2108	561
6	Day 1	2	4.6	230	1226	17	27	13.57	1592	1201
4	Day 1	3	4.6	730	424	10	21	8.90	2525	697
7	Day 1	4	3.4	730	1226	20	11	10.98	2114	950
10	Day 1	5	4.0	480	825	24	22	9.40	2517	916
9	Day 1	6	4.0	480	825	24	25	9.28	2846	1212
12	Day 2	7	4.0	480	825	23	20	7.64	3020	875
11	Day 2	8	4.0	480	825	21	15	6.71	2799	1025
3	Day 2	9	3.4	730	424	17	13	11.13	2083	778
5	Day 2	10	3.4	230	1226	18	12	9.76	2923	1079
8	Day 2	11	4.6	730	1226	18	19	9.20	2602	1450
2	Day 2	12	4.6	230	424	24	21	8.90	3261	788
17	Day 3	13	4.0	480	150	21	22	9.97	3213	642
15	Day 3	14	4.0	60	825	24	22	11.71	2967	588
14	Day 3	15	5.0	480	825	23	23	8.77	2810	1452
13	Day 3	16	3.0	480	825	9	2	11.45	2157	574
20	Day 3	17	4.0	480	825	18	22	6.77	3219	800
19	Day 3	18	4.0	480	825	21	17	7.20	2497	895
18	Day 3	19	4.0	480	1500	21	15	7.26	3190	1377
16	Day 3	20	4.0	900	825	19	15	9.99	2143	1297
Bare						0	11	16.28	1215	304
Alkaline cleaned						0	12	19.14	1555	655

A.4.2.1 Response 1: PA after 10 min (s)

ANOVA for Reduced Quadratic model

Source	Sum of Squares	df	Mean Square	F-value	p-value	
Block	1.53	2	0.7667			
Model	205.74	5	41.15	3.38	0.0388	significant
A-pH	13.43	1	13.43	1.10	0.3139	
B-t	51.07	1	51.07	4.20	0.0630	
C-c	0.2929	1	0.2929	0.0241	0.8792	
BC	72.00	1	72.00	5.92	0.0315	
A^2	68.94	1	68.94	5.67	0.0347	
Residual	145.93	12	12.16			
Lack of Fit	139.43	9	15.49	7.15	0.0664	not significant
Pure Error	6.50	3	2.17			
Cor Total	353.20	19				

Factor coding is Coded.
Sum of squares is Type III - Partial
The model F-value of 3.38 implies there is a 3.88 % chance that an F-value this large could occur due to noise.
Based on p-values, BC and A^2 are significant model terms.
The lack of fit F-value of 7.15 implies that the lack of fit is not significant relative to the pure error. There is a 6.64 % chance that a lack of fit F-value this large could occur due to noise. The model fits, however, this relatively low probability (<10%) is troubling.

Fit Statistics

Std. Dev.	3.49	R^2	0.5850
Mean	19.80	Adjusted R^2	0.4121
C.V. %	17.61	Predicted R^2	-1.1379
		Adeq Precision	5.5694

A negative predicted R^2 implies that the overall mean may be a better predictor of the response than the current model.
The adequate precision of 5.569 indicates that this model can be used to navigate the experimental space.

Final Equation in Terms of Actual Factors

$$\text{PA after 10 min} = -67.61150 + 50.72683 \times \text{pH} - 0.032436 \times t - 0.014731 \times c + 0.000030 \times (t \times c) - 6.13235 \times \text{pH}^2$$

A.4.2.2 Response 2: PA after 24 h (s)

ANOVA for Reduced Linear model

Source	Sum of Squares	df	Mean Square	F-value	p-value	
Block	24.03	2	12.02			
Model	437.73	1	437.73	29.62	< 0.0001	significant
A-pH	437.73	1	437.73	29.62	< 0.0001	
Residual	236.44	16	14.78			
Lack of Fit	206.94	13	15.92	1.62	0.3843	not significant
Pure Error	29.50	3	9.83			
Cor Total	698.20	19				

Factor coding is Coded.
Sum of squares is Type III - Partial
The model F-value of 29.62 implies the model is significant. There is only a 0.01 % chance that an F-value this large could occur due to noise.
Based on p-values, A is a significant model term.
The lack of fit F-value of 1.62 implies that the lack of fit is not significant relative to the pure error. There is a 38.43 % chance that a lack of fit F-value this large could occur due to noise. The model fits.

Fit Statistics

Std. Dev.	3.84	R^2	0.6493
Mean	17.70	Adjusted R^2	0.6274
C.V. %	21.72	Predicted R^2	0.4293
		Adeq Precision	11.0769

The predicted R^2 of 0.4293 is in reasonable agreement with the adjusted R^2 of 0.6274; i.e., the difference is less than 0.2.
The adequate precision of 11.077 indicates that this model can be used to navigate the experimental space.

Final Equation in Terms of Actual Factors

PA after 24 h = −20.33557 + 9.52139 × pH

A.4.2.3 Response 3: j_{corr} (μA cm^{-2})

ANOVA for Reduced Quadratic model

Source	Sum of Squares	df	Mean Square	F-value	p-value	
Block	10.13	2	5.07			
Model	39.19	6	6.53	4.93	0.0110	significant
A-pH	3.47	1	3.47	2.62	0.1339	
B-t	2.76	1	2.76	2.08	0.1770	
C-c	0.0882	1	0.0882	0.0666	0.8011	
AC	5.35	1	5.35	4.04	0.0697	
A^2	11.03	1	11.03	8.33	0.0148	
B^2	18.89	1	18.89	14.26	0.0031	
Residual	14.57	11	1.32			
Lack of Fit	14.04	8	1.75	9.89	0.0429	significant
Pure Error	0.5321	3	0.1774			
Cor Total	63.89	19				

Factor coding is Coded.
Sum of squares is Type III - Partial
The model F-value of 4.93 implies that the model is significant. There is only a 1.10 % chance that an F-value this large could occur due to noise.
Based on p-values, A^2, and B^2 are significant model terms.
The lack of fit F-value of 9.89 implies that the lack of fit is significant. There is a 4.29 % chance that a lack of fit F-value this large could occur due to noise. The model does not fit.

Fit Statistics

Std. Dev.	1.15	R^2	0.7290
Mean	9.49	Adjusted R^2	0.5811
C.V. %	12.13	Predicted R^2	-0.0113
		Adeq Precision	7.1759

A negative predicted R^2 implies that the overall mean may be a better predictor of the response than the current model. In some cases, a higher order model may also predict better.
The adequate precision of 7.176 indicates that this model can be used to navigate the experimental space.

Final Equation in Terms of Actual Factors

$$j_{corr} = 67.50939 - 23.38176 \times \text{pH} - 0.019342 \times t - 0.013902 \times c + 0.003426 \times (\text{pH} \times c) + 2.46351 \times \text{pH}^2 + 0.000018 \times t^2$$

A.4.2.4 Response 4: R_p Tafel extrapolation (Ω cm^2)

ANOVA for Reduced 2FI model

Source	Sum of Squares	df	Mean Square	F-value	p-value	
Block	1.024×10^6	2	5.120×10^5			
Model	2.255×10^6	6	3.759×10^5	4.15	0.0200	significant
A-pH	2.508×10^5	1	2.508×10^5	2.77	0.1242	
B-t	2.776×10^5	1	2.776×10^5	3.07	0.1078	
C-c	45205.09	1	45205.09	0.4992	0.4945	
AC	7.425×10^5	1	7.425×10^5	8.20	0.0154	
A^2	5.804×10^5	1	5.804×10^5	6.41	0.0279	
B^2	4.430×10^5	1	4.430×10^5	4.89	0.0491	
Residual	9.960×10^5	11	90549.37			
Lack of Fit	6.569×10^5	8	82117.08	0.7265	0.6819	not significant
Pure Error	3.391×10^5	3	1.130×10^5			
Cor Total	4.275×10^6	19				

Factor coding is Coded.
Sum of squares is Type III - Partial
The model F-value of 4.15 implies the model is not significant relative to the noise. There is a 2.00 % chance that an F-value this large could occur due to noise.
Based on p-values, AC, A^2, and B^2 are significant model terms.
The lack of fit F-value of 0.73 implies that the lack of fit is not significant relative to the pure error. There is an 68.19 % chance that a lack of fit F-value this large could occur due to noise. The model fits.

Fit Statistics

Std. Dev.	300.91	R^2	0.6936
Mean	2629.38	Adjusted R^2	0.5265
C.V. %	11.44	Predicted R^2	-0.0154
		Adeq Precision	6.8256

A negative predicted R^2 implies that the overall mean may be a better predictor of the response than the current model.
The adequate precision of 6.826 indicates that this model can be used to navigate the experimental space.

Final Equation in Terms of Actual Factors

R_p Tafel extrapolation = −11549.00877 + 5801.10995 × pH + 2.11536 × t + 4.96291 × c − 1.27656 × (pH × c) − 565.00305 × pH^2 − 0.002798 × t^2

A.4.2.5 Response 5: $|Z|$ at 0.25119 Hz (Ω cm^2)

ANOVA for Linear model

Source	Sum of Squares	df	Mean Square	F-value	p-value	
Block	17787.21	2	8893.61			
Model	1.221×106	3	4.070×105	14.61	0.0001	significant
A-pH	3.692×105	1	3.692×105	13.25	0.0027	
B-t	1.517×105	1	1.517×105	5.44	0.0351	
C-c	7.000×105	1	7.000×105	25.12	0.0002	
Residual	3.901×105	14	27864.76			
Lack of Fit	3.304×105	11	30040.84	1.51	0.4075	not significant
Pure Error	59657.41	3	19885.80			
Cor Total	1.629×106	19				

Factor coding is Coded.
Sum of squares is Type III - Partial
The model F-value of 14.61 implies that the model is significant. There is only a 0.01 % chance that an F-value this large could occur due to noise.
Based on p-values, A, B, and C are significant model terms.
The lack of fit F-value of 1.51 implies that the lack of fit is not significant relative to the pure error. There is a 40.75 % chance that a lack of fit F-value this large could occur due to noise. The model fits.

Fit Statistics

Std. Dev.	166.93	R^2	0.7579
Mean	957.75	Adjusted R^2	0.7060
C.V. %	17.43	Predicted R^2	0.4882
		Adeq Precision	11.6897

The predicted R^2 of 0.4882 is not as close to the adjusted R^2 of 0.7060; i.e., the difference is more than 0.2.
However, the adequate precision of 11.690 indicates that this model can still be used to navigate the experimental space.

Final Equation in Terms of Actual Factors

$|Z|$ at 0.25119 Hz = −815.78636 + 276.53202 × pH + 0.422036 × t + 0.564076 × c

Overall, for Zn, if we exclude the poor replication at the central point (Run 8) and an external point (Run 13), some improvement is observed in the fit statistics for PA after 10 min, j_{corr}, and R_p Tafel extrapolation after design analysis. However, these improvements are not significant enough to make the results useful for optimization, nor do they alter the appearance of RSM plots. In fact, this adjustment worsens the models for PA after 10 min and $|Z|$ at 0.25119 Hz, which is why we chose to include all data points for ANOVA analysis. The latter two techniques mentioned have more scientifically explainable potential for yielding more convenient results. Therefore, the models for PA after 10 minutes, j_{corr}

and R_{p} Tafel extrapolation are unusable for anything beyond navigating the design space/characterisation. In contrast, the models for PA after 24 h and $|Z|$ at 0.25119 Hz are usable and applicable for both characterization and potentially, optimization.

A.4.3 AA5754

Table A.9: RSM matrix for AA5754.

Substrate: AA5574			Factors			Protective ability		Corrosion current density	Polarisation resistance	
Std	**Block**	**Run**	**A: pH**	**B: t (s)**	**C: γ (ppm)**	**PA after 10 min (s)**	**PA after 24 h (s)**	**j_{corr} (µA cm^{-2})**	**R_p Tafel (Ω cm²)**	**R_p EIS (Ω cm²)**
1	Day 1	1	3.4	230	424	24	50	0.38	263810	166660
6	Day 1	2	4.6	230	1226	21	45	0.20	329520	171100
4	Day 1	3	4.6	730	424	21	38	0.20	313770	196040
7	Day 1	4	3.4	730	1226	11	30	0.34	186850	91541
10	Day 1	5	4.0	480	825	14	25	0.29	234570	156280
9	Day 1	6	4.0	480	825	14	29	0.27	204480	139570
12	Day 2	7	4.0	480	825	13	33	0.19	367930	268900
11	Day 2	8	4.0	480	825	14	35	0.19	318060	182880
3	Day 2	9	3.4	730	424	10	45	0.40	164540	112390
5	Day 2	10	3.4	230	1226	18	50	0.46	179350	112520
8	Day 2	11	4.6	730	1226	22	37	0.17	356780	221720
2	Day 2	12	4.6	230	424	27	50	0.12	552980	324030
17	Day 3	13	4.0	480	150	22	53	0.16	457460	331670
15	Day 3	14	4.0	60	825	32	38	0.17	455090	716410
14	Day 3	15	5.0	480	825	19	27	0.38	191870	128890
13	Day 3	16	3.0	480	825	13	38	0.50	169360	90900
20	Day 3	17	4.0	480	825	14	32	0.23	242480	166890
19	Day 3	18	4.0	480	825	14	35	0.15	325720	199190
18	Day 3	19	4.0	480	1500	12	35	0.27	204310	123820
16	Day 3	20	4.0	900	825	17	13	0.39	156200	98866
First augmentation										
21	Day 4	21	3.4	480	150	11	52	0.38	156200	107120
26	Day 4	22	4.0	355	825	9	30	0.32	218190	147090
25	Day 4	23	4.0	355	825	10	32	0.36	225020	113930
22	Day 4	24	4.6	480	150	14	51	0.08	722340	472000
24	Day 4	25	4.0	355	825	9	29	0.39	166940	144130
23	Day 4	26	4.0	730	150	8	46	0.36	187500	115150
Second augmentation										
31	Day 5	27	4.3	230	825	8	45	0.14	485750	504890
27	Day 5	28	4.6	230	150	20	80	0.11	565350	443400
28	Day 5	29	4.6	230	150	19	60	0.15	454900	443400
29	Day 5	30	4.3	355	150	17	47	0.09	676990	650830
30	Day 5	31	4.4	420	650	5	33	0.21	268740	210370
32	Day 5	32	4.3	230	825	9	51	0.10	625140	338530
Bare						11	12	0.12	374290	502990
Alkaline cleaned						28	36	0.06	1010000	1735700
Alkalined cleaned + desmutted						35	52	0.04	1410000	1778300

A.4.3.1 Before augmentation

In (Figure A.4), the extent of results is represented on colour scales above the graphs. Measured points denoted by red and pink circles are located above or below predicted values, respectively.

A.4.3.1.1 Response 1: PA after 10 min (s)

ANOVA for Reduced Quadratic model

Source	Sum of Squares	df	Mean Square	F-value	p-value	
Block	1.09	2	0.5458			
Model	592.94	6	98.82	23.24	< 0.0001	significant
A-pH	106.24	1	106.24	24.99	0.0004	
B-t	192.15	1	192.15	45.19	< 0.0001	
C-c	52.66	1	52.66	12.39	0.0048	
AB	32.00	1	32.00	7.53	0.0191	
BC	24.50	1	24.50	5.76	0.0352	
B^2	185.38	1	185.38	43.60	< 0.0001	
C^2	46.77	11	4.25			
Residual	46.27	8	5.78	34.70	0.0071	significant
Lack of Fit	0.5000	3	0.1667			
Pure Error	640.80	19				
Cor Total	1.09	2	0.5458			

Factor coding is Coded.

Sum of squares is Type III - Partial

The model F-value of 23.24 implies that the model is significant. There is only a 0.01 % chance that an F-value this large could occur due to noise.

Based on p-values, A, B, C, AB, BC, and B^2 are significant model terms.

The lack of fit F-value of 34.70 implies that the lack of fit is significant. There is only a 0.71 % chance that a lack of fit F-value this large could occur due to noise. The model does not fit.

Fit Statistics

Std. Dev.	2.06	R^2	0.9269
Mean	17.60	Adjusted R^2	0.8870
C.V. %	11.72	Predicted R^2	0.6841
		Adequate Precision	15.7555

The predicted R^2 of 0.6841 is not as close to the adjusted R^2 of 0.8870 as one might normally expect, i.e., the difference is more than 0.2.

Even though excluding block effects and outliers would achieve the necessary difference between predicted R^2 and adjusted R^2, the model still does not fit well after model reduction and response transformation. This suggests a problem with the data related to the chosen response variable. Specifically, using protective ability measurements after a 10-minute interval to predict ZrCC corrosion behaviour is not feasible.

However, adequate precision of 15.7555 indicates that this model can be used to navigate the experimental space at lower concentrations, higher pH values and longer conversion times (Figure A.4).

Final Equation in Terms of Actual Factors

PA after 10 min = 53.54226 - 1.77424 x pH - 0.138024 x t - 0.013273 x pH x t + 0.013469 x t x γ + 0.000017 x t^2 + 0.000057 x pH^2

A.4.3.1.2 Response 2: PA after 24 h (s)

ANOVA for Reduced Quadratic model

Source	Sum of Squares	df	Mean Square	F-value	p-value	
Block	212.76	2	106.38			
Model	1431.83	5	286.37	14.61	< 0.0001	significant
A-pH	40.44	1	40.44	2.06	0.1765	
B-t	554.80	1	554.80	28.30	0.0002	
C-c	192.49	1	192.49	9.82	0.0086	
A^2	80.21	1	80.21	4.09	0.0660	
C^2	598.41	1	598.41	30.53	0.0001	
Residual	235.21	12	19.60			
Lack of Fit	220.71	9	24.52	5.07	0.1042	not significant
Pure Error	14.50	3	4.83			
Cor Total	1879.80	19				

Factor coding is Coded.
Sum of squares is Type III - Partial
The model F-value of 14.61 implies that the model is significant. There is only a 0.01 % chance that an F-value this large could occur due to noise.
Based on p-values, B, C, and C^2 are significant model terms.
The lack of fit F-value of 5.07 implies a 10.42 % chance that a lack of fit F-value this large could occur due to noise. Lack of fit is bad - we want the model to fit. This relatively low probability (<10 %) is troubling.

Fit Statistics

Std. Dev.	4.43	R^2	0.8589
Mean	36.90	Adjusted R^2	0.8001
C.V. %	12.00	Predicted R^2	0.5422
		Adequate Precision	12.8693

Although the predicted R^2 of 0.5422 is not as close to the adjusted R^2 of 0.8001 as one might normally expect, i.e., the difference is more than 0.2, it is not excessively distant either. Ignoring block effects and model reduction would satisfy this required difference but also result in a notable lack of fit, with term B being the only significant model term. Thus, we opted for a model that includes more terms in order to navigate the experimental space to regions that involve more interactions among the chosen input factors more successfully.

Nevertheless, the adequate precision of 12.869 indicates that this model can navigate the experimental space to lower concentrations and shorter conversion times, with a very high influence for the former and a slight for the latter (Figure A.4).

Final Equation in Terms of Actual Factors

$$PA\ after\ 24\ h = 196.18891 - 56.02813 \times pH - 0.025522 \times t - 0.075053 \times pH^2 + 6.64178 \times \gamma^2 + 0.000040 \times t^2$$

A.4.3.1.3 Response 3: j_{corr} (μA cm^{-2})

ANOVA for Reduced Quadratic model

Source	Sum of Squares	df	Mean Square	F-value	p-value	
Block	0.0028	2	0.0014			
Model	0.1593	2	0.0797	14.81	0.0003	significant
A-pH	0.0873	1	0.0873	16.23	0.0011	
A^2	0.0721	1	0.0721	13.39	0.0023	
Residual	0.0807	15	0.0054			
Lack of Fit	0.0773	12	0.0064	5.68	0.0894	not significant
Pure Error	0.0034	3	0.0011			
Cor Total	0.2428	19				

Factor coding is Coded.
Sum of squares is Type III - Partial
The model F-value of 14.81 implies that the model is significant. There is only a 0.03 % chance that an F-value this large could occur due to noise.
Based on p-values, A, and A^2 are significant model terms.
The lack of fit F-value of 5.68 implies that the lack of fit is not significant relative to the pure error. There is an 8.94 % chance that a lack of fit F-value this large could occur due to noise. The model fits, although it is near the recommended limit for lack of fit (< 10 %).

Fit Statistics

Std. Dev.	0.0733	R^2	0.6638
Mean	0.2730	Adjusted R^2	0.6190
C.V. %	26.87	Predicted R^2	0.1852
		Adequate Precision	9.9794

The predicted R^2 of 0.1852 is not as close to the adjusted R^2 of 0.6190 as one might normally expect, i.e., the difference is more than 0.2, which can be achieved after excluding two suggested outliers, ignoring block effects and reducing the model to linear. This improves the lack of fit values; however, it does not enhance the overall response surface behaviour since the only significant factor identified is A, which does not yield a notably different plot when compared to the model incorporating A^2 as a significant term as well.

The adequate precision of 9.979 indicates that this model can be used to navigate the experimental space towards higher pH values (Figure A.4).

Final Equation in Terms of Actual Factors

$$j_{corr} = 3.93425 - 1.72047 \times pH + 0.198252 \times pH^2$$

A.4.3.1.4 Response 4: R_p Tafel extrapolation (Ω cm^2)

ANOVA for Reduced Linear model

Source	Sum of Squares	df	Mean Square	F-value	p-value	
Block	1.473×10^{10}	2	7.365×10^{9}			
Model	9.405×10^{10}	2	4.703×10^{10}	5.38	0.0173	significant
A-pH	4.644×10^{10}	1	4.644×10^{10}	5.32	0.0358	
B-t	4.761×10^{10}	1	4.761×10^{10}	5.45	0.0339	
Residual	1.310×10^{11}	15	8.733×10^{9}			
Lack of Fit	1.258×10^{11}	12	1.049×10^{10}	6.10	0.0815	not significant
Pure Error	5.161×10^{9}	3	1.720×10^{9}			
Cor Total	2.398×10^{11}	19				

Factor coding is Coded.

Sum of squares is Type III - Partial

The model F-value of 5.38 implies that the model is significant. There is only a 1.73 % chance that an F-value this large could occur due to noise.

Based on p-values, A and B are significant model terms.

The lack of fit F-value of 6.10 implies that the lack of fit is not significant relative to the pure error. There is a 8.15 % chance that a lack of fit F-value this large could occur due to noise. The model fits.

Fit Statistics

Std. Dev.	93452.05	R^2	0.4179
Mean	2.838×10^{5}	Adjusted R^2	0.3403
C.V. %	32.93	Predicted R^2	-0.0889
		Adequate Precision	6.4737

A negative predicted R^2 implies that the overall mean may be a better predictor of the response than the current model.

Nevertheless, adequate precision of 6.474 indicates that this model can navigate the experimental space.

The overall response plot can be used for the experimental space navigation towards higher pH values and shorter conversion times Figure A.4.

Final Equation in Terms of Actual Factors

$$R_p \text{ Tafel extrapolation} = 5911.19185 + 98068.53995 \times \text{pH} - 236.43852 \times t$$

A.4.3.1.5 Response 5: R_p EIS (Ω cm^2)

ANOVA for Reduced Quadratic model

Transform: Power

Lambda: -1.3, Constant: 0

Source	Sum of Squares	df	Mean Square	F-value	p-value	
Block	5.263×10^{-15}	2	2.632×10^{-15}			
Model	1.383×10^{-13}	4	3.458×10^{-14}	14.35	0.0001	significant
A-pH	4.806×10^{-14}	1	4.806×10^{-14}	19.94	0.0006	
B-t	3.683×10^{-14}	1	3.683×10^{-14}	15.29	0.0018	
C-c	2.229×10^{-14}	1	2.229×10^{-14}	9.25	0.0095	
A^2	3.115×10^{-14}	1	3.115×10^{-14}	12.93	0.0033	
Residual	3.133×10^{-14}	13	2.410×10^{-15}			
Lack of Fit	2.876×10^{-14}	10	2.876×10^{-15}	3.36	0.1736	not significant
Pure Error	2.567×10^{-15}	3	8.557×10^{-16}			
Cor Total	1.749×10^{-13}	19				

Factor coding is Coded.

Sum of squares is Type III - Partial

The model F-value of 14.35 implies that the model is significant. There is only a 0.01 % chance that an F-value this large could occur due to noise.

Based on p-values, A, B, C, and A^2 are significant model terms.

The lack of fit F-value of 3.36 implies that the lack of fit is not significant relative to the pure error. There is a 33.63 % chance that a lack of fit F-value this large could occur due to noise. The model fits.

Fit Statistics

Std. Dev.	4.909×10^{-8}	R^2	0.8154
Mean	1.836×10^{-7}	Adjusted R^2	0.7585
C.V. %	26.73	Predicted R^2	0.4696
		Adequate Precision	12.5896

The predicted R^2 of 0.4696 is not as close to the adjusted R^2 of 0.7585; i.e., the difference is more than 0.2.

However, the adequate precision of 12.590 indicates that this model can be used to navigate the experimental space. The results from EIS seem to be the most sensitive, already predicting the optimum at low concentration, higher pH values and shorter conversion times (Figure A.4).

Excluding the outlier (Run 11) would likely improve the model F-values and the lack of fit value, achieving the necessary difference between the predicted R^2 and adjusted R^2. However, the response surface would remain largely unchanged, and the significant model terms would still be the same.

Final Equation in Terms of Actual Factors

$$(R_p\ \mathrm{EIS})^{-1.3} = 2.45320\times10^{-6} - 1.14254\times10^{-6}\times \mathrm{pH} + 2.07951\times10^{-10}\times t + 1.00655\times10^{-10}\times \gamma + 1.30347\times10^{-7}\times \mathrm{pH}^2$$

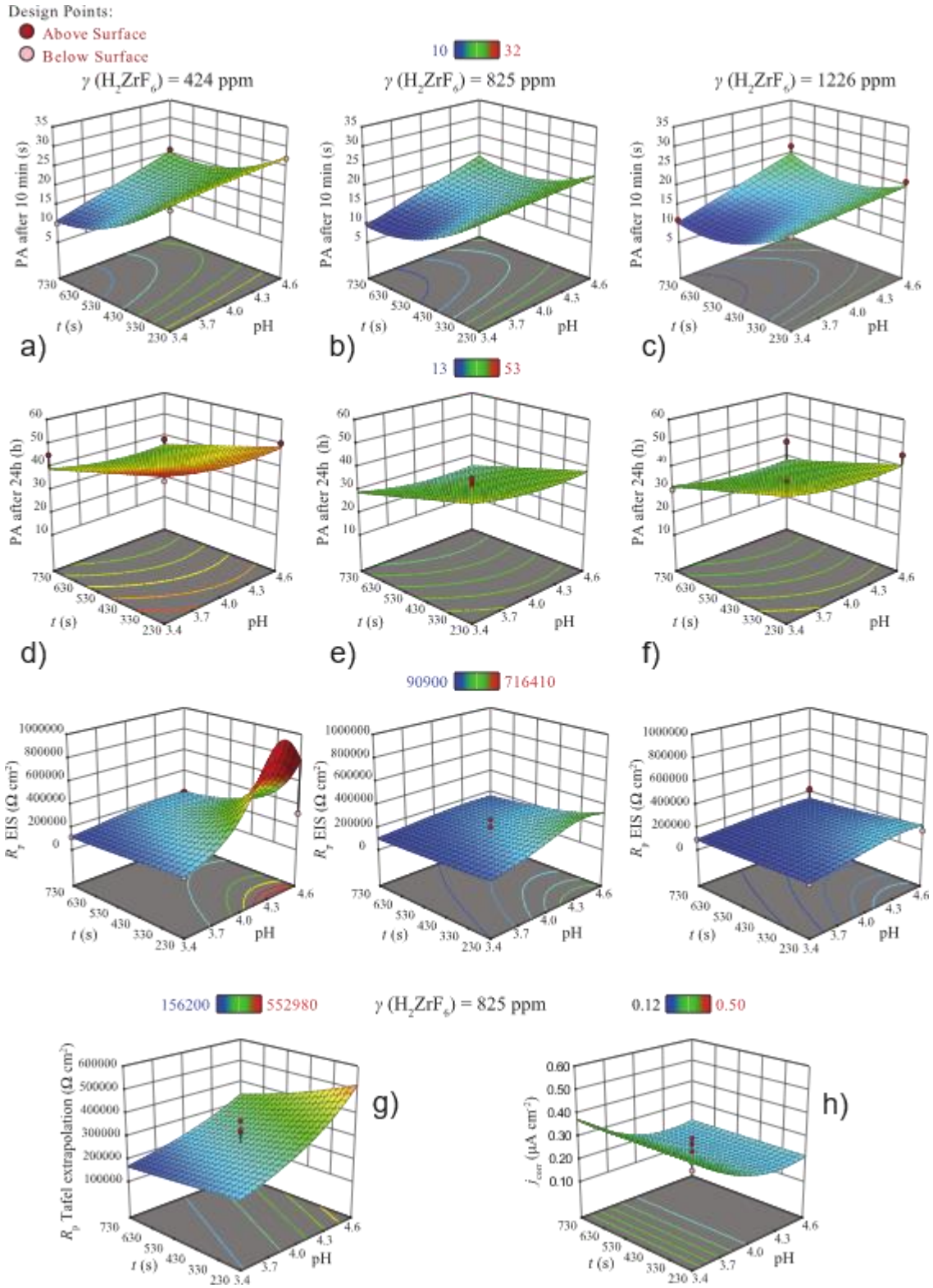

Figure A.4: RSM plots for AA5754 before augmentation for different responses: (a-c) PA after 10 min, (d–f) PA after 24 h, (g–i) R_p EIS, (j) R_p Tafel and (k) j_{corr} from PPCs for concentrations $\gamma(H_2ZrF_6)$ of 150, 424 and 825 ppm.

A.4.3.2 The first augmentation

In Figure A.5, the extent of results is represented on colour scales above the graphs. Measured points denoted by red and pink circles are located above or below predicted values, respectively.

A.4.3.2.1 Response 1: PA after 10 min (s)

ANOVA for Reduced Quadratic model

Source	Sum of Squares	df	Mean Square	F-value	p-value	
Block	247.46	3	82.49			
Model	637.24	8	79.65	43.41	< 0.0001	significant
A-pH	98.33	1	98.33	53.58	< 0.0001	
B-t	209.79	1	209.79	114.33	< 0.0001	
C-c	54.86	1	54.86	29.90	0.0001	
AB	32.00	1	32.00	17.44	0.0011	
BC	31.69	1	31.69	17.27	0.0011	
A^2	13.32	1	13.32	7.26	0.0184	
B^2	177.57	1	177.57	96.77	< 0.0001	
C^2	11.70	1	11.70	6.37	0.0254	
Residual	23.86	13	1.84			
Lack of Fit	22.69	8	2.84	12.15	0.0069	significant
Pure Error	1.17	5	0.2333			
Cor Total	908.56	24				

This row was ignored for this analysis:
15
Factor coding is Coded.
Sum of squares is Type III - Partial
The model F-value of 43.41 implies that the model is significant. There is only a 0.01 % chance that an F-value this large could occur due to noise.
Based on p-values, A, B, C, AB, BC, A^2, B^2, and C^2 are significant model terms.
The lack of fit F-value of 12.15 implies that the lack of fit is significant. There is only a 0.69 % chance that a lack of fit F-value this large could occur due to noise. The model does not fit.

Fit Statistics

Std. Dev.	1.35	R^2	0.9639
Mean	15.76	Adjusted R^2	0.9417
C.V. %	8.60	Predicted R^2	0.7920
		Adequate Precision	24.1128

The predicted R^2 of 0.7920 is in reasonable agreement with the adjusted R^2 of 0.9417; i.e., the difference is less than 0.2. However, model reduction, response transformation, and outliers would still not render a satisfactory lack of fit for the model. This suggests an inherent problem with the data concerning the chosen response variable. Specifically, measuring protective ability after 10 min cannot be used to predict the ZrCC corrosion behaviour, and the response surface is almost the same as for the original design (compare

Figures A.4 and A.5). However, the adequate precision of 22.484 indicates that this model can navigate the experimental space.

Final Equation in Terms of Actual Factors

$$\text{PA after 10 min} = 107.23154 - 29.04663 \times \text{pH} - 0.138280 \times t - 0.020919 \times \text{pH} \times t + 0.013469 \times t \times \gamma + 0.000018 \times t^2 + 3.46759 \times \text{pH}^2 + 0.000057 \times \gamma^2 + 4.62891 \times 10^{-6}$$

A.4.3.2.2 Response 2: PA after 24 h (s)

ANOVA for Reduced Quadratic model

Source	Sum of Squares	df	Mean Square	F-value	p-value	
Model	193.94	3	64.65			
A-pH	2000.13	5	400.03	32.18	< 0.0001	significant
B-t	1.10	1	1.10	0.0882	0.7703	
C-c	570.10	1	570.10	45.86	< 0.0001	
A^2	210.38	1	210.38	16.92	0.0008	
C^2	124.60	1	124.60	10.02	0.0060	
Residual	733.12	1	733.12	58.98	< 0.0001	
Lack of Fit	198.89	16	12.43			
Pure Error	179.73	11	16.34	4.26	0.0608	not significant
Cor Total	19.17	5	3.83			

This row was ignored for this analysis:
15
Factor coding is Coded.
Sum of squares is Type III - Partial
The model F-value of 32.18 implies that the model is significant. There is only a 0.01 % chance that an F-value this large could occur due to noise.
Based on p-values, B, C, A^2, and C^2 are significant model terms.
The lack of fit F-value of 4.26 implies that the lack of fit is not significant relative to the pure error. There is a 6.08 % chance that a lack of fit F-value this large could occur due to noise. The model fits.
However, this relatively low probability (<10%) is troubling.

Fit Statistics

Std. Dev.	3.53	R^2	0.9096
Mean	38.04	Adjusted R^2	0.8813
C.V. %	9.27	Predicted R^2	0.7350
		Adequate Precision	17.1383

The predicted R^2 of 0.7350 is in reasonable agreement with the adjusted R^2 of 0.8813; i.e., the difference is less than 0.2.
The adequate precision of 17.138 indicates that this model can be used to navigate the experimental space.

Ignoring the outlier, as suggested after analysing externally studentized residuals (Row 15), led to an insignificant lack of fit. However, it must be noted that this modification did not substantially impact the response surface.

Final Equation in Terms of Actual Factors

$$PA\ after\ 24\ h = 245.03694 - 84.89330 \times pH - 0.024863 \times t - 0.068676 \times pH^2 + 10.54412 \times \gamma^2 + 0.000036 \times t^2$$

A.4.3.2.3 Response 3: j_{cor} (μA cm^{-2})

ANOVA for Reduced Linear model

Source	Sum of Squares	df	Mean Square	F-value	p-value	
Block	0.0122	3	0.0041			
Model	0.2013	1	0.2013	41.64	< 0.0001	significant
A-pH	0.2013	1	0.2013	41.64	< 0.0001	
C-c	0.0967	20	0.0048			
Residual	0.0908	15	0.0061	5.16	0.0398	significant
Lack of Fit	0.0059	5	0.0012			
Pure Error	0.3103	24				
Cor Total	0.0122	3	0.0041			

This row was ignored for this analysis:
15
Factor coding is Coded.
Sum of squares is Type III - Partial
The model F-value of 41.64 implies that the model is significant. There is only a 0.01 % chance that an F-value this large could occur due to noise.
Based on p-values, A is a significant model term.
The lack of fit F-value of 5.16 implies that the lack of fit is significant. There is only a 3.98 % chance that a lack of fit F-value this large could occur due to noise. The model does not fit.

Fit Statistics

Std. Dev.	0.0695	R^2	0.6755
Mean	0.2788	Adjusted R^2	0.6593
C.V. %	24.94	Predicted R^2	0.5001
		Adequate Precision	10.3852

The predicted R^2 of 0.5001 is in reasonable agreement with the adjusted R^2 of 0.6593; i.e., the difference is less than 0.2.
The adequate precision of 10.385 indicates that this model can be used to navigate the experimental space.

After analyzing externally studentized residuals and excluding the outlier (Run 15), improvements were observed in the model F-values and the required difference between the predicted R^2 and adjusted R^2 was achieved. This enhancement enhanced the overall response surface and its effectiveness in navigating the experimental space toward higher pH and shorter conversion times (Figure A.5). The improvement stemmed from including

the term C in the model, which, despite being statistically insignificant, supported the hierarchy. However, the lack of fit value remained significant.

Final Equation in Terms of Actual Factors

j_{corr} = 1.12801 - 0.214092 × pH

A.4.3.2.4 Response 4: R_p Tafel extrapolation (Ω cm²)

ANOVA for Linear model

Transform: Inverse

Source	Sum of Squares	df	Mean Square	F-value	p-value	
Block	3.062×10^{-12}	3	1.021×10^{-12}			
Model	3.828×10^{-11}	3	1.276×10^{-11}	15.96	< 0.0001	significant
A-pH	2.607×10^{-11}	1	2.607×10^{-11}	32.60	< 0.0001	
B-t	8.591×10^{-12}	1	8.591×10^{-12}	10.74	0.0042	
C-c	5.105×10^{-12}	1	5.105×10^{-12}	6.38	0.0211	
Residual	1.439×10^{-11}	18	7.996×10^{-13}			
Lack of Fit	1.209×10^{-11}	13	9.297×10^{-13}	2.02	0.2262	not significant
Pure Error	2.306×10^{-12}	5	4.612×10^{-13}			
Cor Total	5.574×10^{-11}	24				

This row was ignored for this analysis:

15

Factor coding is Coded.

Sum of squares is Type III - Partial

The model F-value of 15.96 implies that the model is significant. There is only a 0.01 % chance that an F-value this large could occur due to noise.

Based on p-values, A, B and C are significant model terms.

The lack of fit F-value of 2.02 implies that the lack of fit is not significant relative to the pure error. There is a 22.62 % chance that a lack of fit F-value this large could occur due to noise. The model fits.

Fit Statistics

Std. Dev.	8.942×10^{-7}	R^2	0.7268
Mean	4.142×10^{-6}	Adjusted R^2	0.6812
C.V. %	21.59	Predicted R^2	0.4277
		Adequate Precision	12.4268

The predicted R^2 of 0.4277 is not as close to the adjusted R^2 of 0.6812 as one might normally expect; i.e., the difference is more than 0.2.

However, the adequate precision of 12.427 indicates that this model can navigate the experimental space.

After analysing externally studentised residuals and excluding the outlier (Run 15), notable improvements were observed in the model F-values. Additionally, the lack of fit became insignificant, resulting in a closer alignment with the required difference between

the predicted R^2 and adjusted R^2. This, in turn, enhanced the overall response surface and its effectiveness in navigating the experimental space while also improving the sensitivity compared to the previous plot in terms of optimum achievement at low concentrations, higher pH and shorter conversion times (compare Figures A.4 and A.5).

Final Equation in Terms of Actual Factors

$1/(Rp \text{ Tafel extrapolation}) = +0.000011 - 2.43604\times10^{-6} \times \text{pH} + 3.01850\times10^{-9} \times t + 1.34146\times10^{-9} \times \gamma$

A.4.3.2.5 Response 5: R_p EIS (Ω cm^2)

ANOVA for Linear model

Transform: Inverse

Source	Sum of Squares	df	Mean Square	F-value	p-value	
Block	6.572×10^{-12}	3	2.191×10^{-12}			
Model	1.315×10^{-10}	3	4.382×10^{-11}	22.93	< 0.0001	significant
A-pH	7.818×10^{-11}	1	7.818×10^{-11}	40.91	< 0.0001	
B-t	3.599×10^{-11}	1	3.599×10^{-11}	18.83	0.0004	
C-c	2.386×10^{-11}	1	2.386×10^{-11}	12.49	0.0024	
Residual	3.440×10^{-11}	18	1.911×10^{-12}			
Lack of Fit	2.966×10^{-11}	13	2.282×10^{-12}	2.41	0.1699	not significant
Pure Error	4.734×10^{-12}	5	9.469×10^{-13}			
Cor Total	1.724×10^{-10}	24				

This row was ignored for this analysis:
15
Factor coding is Coded.
Sum of squares is Type III - Partial
The model F-value of 22.93 implies that the model is significant. There is only a 0.01 % chance that an F-value this large could occur due to noise.
Based on p-values, A, B, and C are significant model terms.
The lack of fit F-value of 2.41 implies that the lack of fit is not significant relative to the pure error. There is an 16.99 % chance that a lack of fit F-value this large could occur due to noise. The model fits.

Fit Statistics

Std. Dev.	1.382×10^{-6}	R^2	0.7926
Mean	6.531×10^{-6}	Adjusted R^2	0.7580
C.V. %	21.17	Predicted R^2	0.5472
		Adequate Precision	15.8234

The predicted R^2 of 0.5472 is not as close to the adjusted R^2 of 0.7580 as one might normally expect; i.e. the difference is more than 0.2. An adequate

precision of 14.138 indicates that this model can be used to navigate the experimental space.

The response surface is actually very similar for the polarisation resistance obtained from Tafel, suggesting the feasibility of the two methods for ZrCC evaluation (compare Figure A.4 and Figure A.5.

Final Equation in Terms of Actual Factors:

$1 / (R_p \text{ EIS}) = 0.000018 - 4.21878\times10^{-6} \times \text{pH} + 6.17807\times10^{-9} \times t + 2.90006\times10^{-9} \times \gamma$

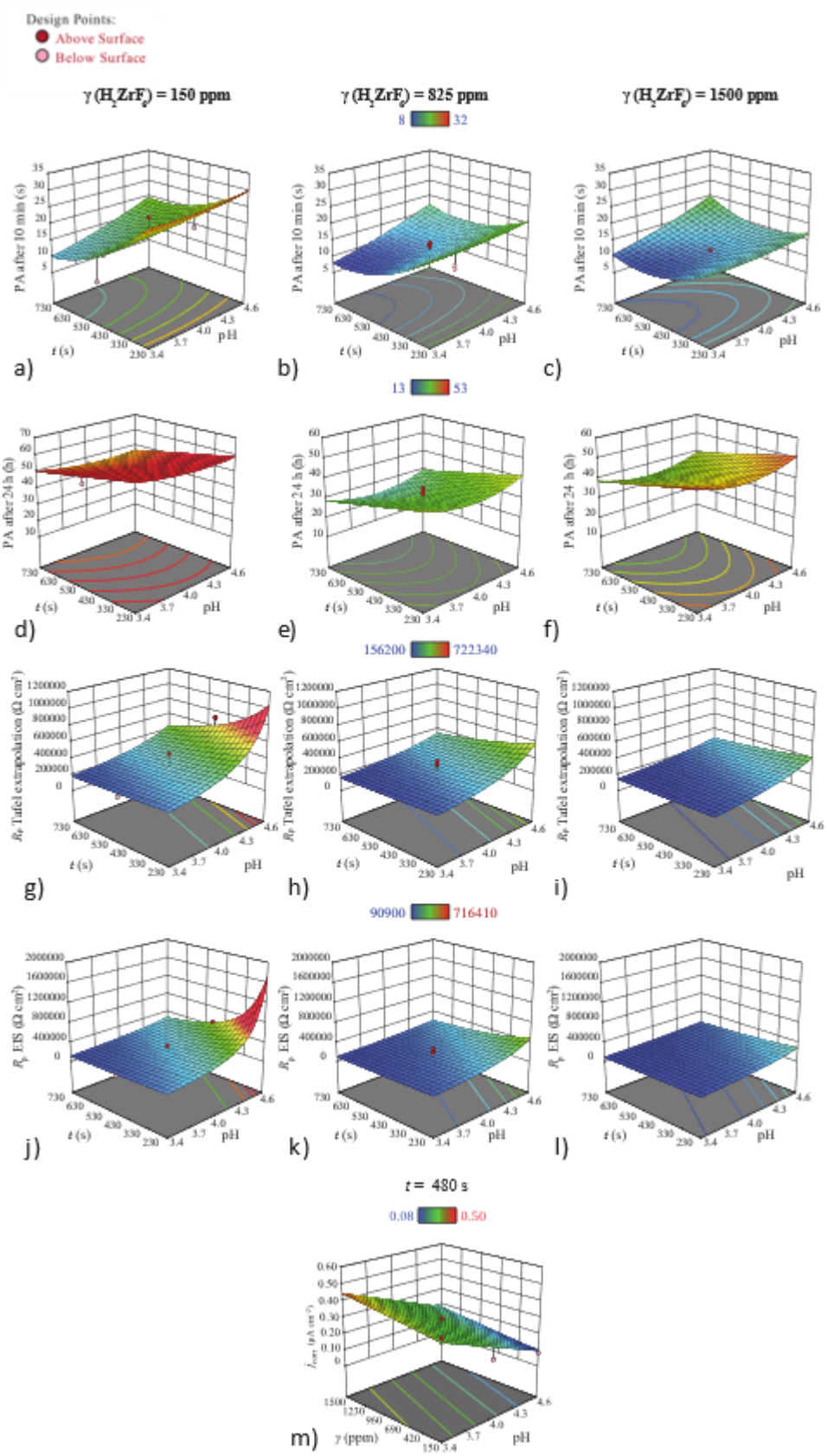

Figure A.5: RSM plots for AA5754 before augmentation for different responses: (a-c) PA after 10 min, (d–f) PA after 24 h, (g–i) R_p EIS, (j–l) R_p Tafel and (m) j_{corr} from PPCs for concentrations $\gamma(H_2ZrF_6)$ of 150, 424 and 825 ppm.

A.4.3.3 The second augmentation

At this stage, the focus shifted away from achieving an insignificant lack of fit and instead centred on providing a reasonable description of the process behaviour using the collected data. Consequently, the generated models were computed within a narrower experimental range, encompassing only concentrations of 150–825 ppm, pH values of 4–4.6, and conversion times of 230–480 s. All other data points were excluded from the analysis.

A.4.3.3.1 Response 1: PA after 10 min (s)

ANOVA for Reduced Linear model

Source	Sum of Squares	df	Mean Square	F-value	p-value	
Block	164.02	4	41.00			
Model	426.33	2	213.16	98.24	< 0.0001	significant
B-t	118.97	1	118.97	54.83	< 0.0001	
C-c	281.89	1	281.89	129.91	< 0.0001	
Residual	28.21	13	2.17			
Lack of Fit	26.04	6	4.34	14.02	0.0014	significant
Pure Error	2.17	7	0.3095			
Cor Total	618.55	19				

These rows were ignored for this analysis:
2, 3, 4, 9, 10, 11, 14, 15, 16, 19, 20, 26
Factor coding is Coded.
Sum of squares is Type III - Partial
The model F-value of 98.24 implies that the model is significant. There is only a 0.01 % chance that an F-value this large could occur due to noise.
Based on p-values, B and C are significant model terms.
The lack of fit F-value of 14.02 implies that the lack of fit is significant. There is only a 0.14 % chance that a lack of fit F-value this large could occur due to noise. The model fits.

Fit Statistics

Std. Dev.	1.47	R^2	0.9379
Mean	14.35	Adjusted R^2	0.9284
C.V. %	10.27	Predicted R^2	0.8438
		Adequate Precision	22.9519

The predicted R^2 of 0.8438 is in reasonable agreement with the adjusted R^2 of 0.9284; i.e., the difference is less than 0.2. Adequate precision of 22.952 indicates that this model can be used to navigate the experimental space.

Final Equation in Terms of Actual Factors

$$\text{PA after 10 min} = 34.56116 - 0.029606 \times t - 0.013064 \times \gamma$$

A.4.3.3.2 Response 2: PA after 24 h (s)

ANOVA for Reduced Linear model

Transform: Inverse Sqrt

Constant: 0

Source	Sum of Squares	df	Mean Square	F-value	p-value	
Block	0.0028	4	0.0007			
Model	0.0062	2	0.0031	27.18	< 0.0001	significant
B-t	0.0011	1	0.0011	9.44	0.0089	
C-c	0.0048	1	0.0048	42.11	< 0.0001	
Residual	0.0015	13	0.0001			
Lack of Fit	0.0011	6	0.0002	3.45	0.0649	not significant
Pure Error	0.0004	7	0.0001			
Cor Total	0.0106	19				

These rows were ignored for this analysis:
2, 3, 4, 9, 10, 11, 14, 15, 16, 19, 20, 26

Factor coding is Coded.

Sum of squares is Type III - Partial

The model F-value of 27.18 implies that the model is significant. There is only a 0.01 % chance that an F-value this large could occur due to noise.

Based on p-values, B and C are significant model terms.

The lack of fit F-value of 3.45 implies a 6.49% chance that a lack of fit F-value this large could occur due to noise. However, this relatively low probability (<10 %) is troubling.

Fit Statistics

Std. Dev.	0.0107	R^2	0.8070
Mean	0.1584	Adjusted R^2	0.7773
C.V. %	6.76	Predicted R^2	0.5536
		Adequate Precision	11.0638

The predicted R^2 of 0.5536 is not as close to the adjusted R^2 of 0.7773 as one might normally expect, i.e., the difference is more than 0.2, however, it is close. Adequate precision of 11.064 indicates that this model can be used to navigate the experimental space.

Final Equation in Terms of Actual Factors

$$1 / (\text{Sqrt (PA after 24 h)}) = +0.093508 + 0.000089 \times t + 0.000054 \times \gamma$$

A.4.3.3.3 Response 3: j_{cor} (μA cm^{-2})

ANOVA for Reduced 2FI model

Source	Sum of Squares	df	Mean Square	F-value	p-value	
Block	0.1211	4	0.0303			
Model	0.0714	5	0.0143	7.53	0.0036	significant
A-pH	0.0035	1	0.0035	1.86	0.2027	
B-t	0.0071	1	0.0071	3.74	0.0818	
C-c	0.0106	1	0.0106	5.57	0.0400	
AC	0.0086	1	0.0086	4.51	0.0597	
BC	0.0191	1	0.0191	10.08	0.0099	
Residual	0.0190	10	0.0019			
Lack of Fit	0.0115	3	0.0038	3.59	0.0742	not significant
Pure Error	0.0075	7	0.0011			
Cor Total	0.2115	19				

These rows were ignored for this analysis:
2, 3, 4, 9, 10, 11, 14, 15, 16, 19, 20, 26
Factor coding is Coded.
Sum of squares is Type III - Partial
The model F-value of 7.53 implies that the model is significant. There is only a 0.34 % chance that an F-value this large could occur due to noise.
Based on p-values, in this case, C and BC are significant model terms.
The lack of fit F-value of 3.59 implies that there is a 7.42 % chance that a lack of fit F-value this large could occur due to noise. However, this relatively low probability (<10 %) is troubling.

Fit Statistics

Std. Dev.	0.0435	R^2	0.7902
Mean	0.2155	Adjusted R^2	0.6853
C.V. %	20.21	Predicted R^2	-0.6632
		Adequate Precision	10.0740

A negative Predicted R^2 implies that the overall mean may be a better predictor of the response than the current model. In some cases, a higher-order model may also predict better. However, adequate precision of 10.074 indicates that this model can be used to navigate the experimental space.

Final Equation in Terms of Actual Factors

$$j_{corr} = +1.93349 - 0.330014 \times pH - 0.001050 \times t - 0.002610 \times \gamma + 0.000496 \times pH \times \gamma + 1.66790\times10^{-6} \times t \times \gamma$$

A.4.3.3.4 Response 4: R_p Tafel extrapolation (Ω cm^2)

ANOVA for Reduced 2FI model

Transform: Inverse Sqrt

Constant: 0

Source	Sum of Squares	df	Mean Square	F-value	p-value	
Block	1.502×10^{-6}	4	3.754×10^{-7}			
Model	1.545×10^{-6}	5	3.091×10^{-7}	13.32	0.0004	significant
A-pH	2.879×10^{-9}	1	2.879×10^{-9}	0.1241	0.7320	
B-t	1.219×10^{-10}	1	1.219×10^{-10}	0.0053	0.9437	
C-c	5.043×10^{-7}	1	5.043×10^{-7}	21.73	0.0009	
AC	4.264×10^{-7}	1	4.264×10^{-7}	18.38	0.0016	
BC	6.951×10^{-7}	1	6.951×10^{-7}	29.96	0.0003	
Residual	2.320×10^{-7}	10	2.320×10^{-8}			
Lack of Fit	7.850×10^{-8}	3	2.617×10^{-8}	1.19	0.3797	not significant
Pure Error	1.535×10^{-7}	7	2.193×10^{-8}			
Cor Total	3.279×10^{-6}	19				

These rows were ignored for this analysis:

2, 3, 4, 9, 10, 11, 14, 15, 16, 19, 20, 26

Factor coding is Coded.

Sum of squares is Type III - Partial

The model F-value of 13.32 implies the model is significant. There is only a 0.05 % chance that an F-value this large could occur due to noise.

Based on p-values, C, AC and BC are significant model terms in this case.

The lack of fit F-value of 1.19 implies that the lack of fit is not significant relative to the pure error. There is a 37.97 % chance that a lack of fit F-value this large could occur due to noise. The model fits.

Fit Statistics

Std. Dev.	0.0002	R^2	0.8694
Mean	0.0018	Adjusted R^2	0.8042
C.V. %	8.63	Predicted R^2	0.3213
		Adequate Precision	12.1697

The predicted R^2 of 0.3213 is not as close to the adjusted R^2 of 0.8042 as one might normally expect, i.e., the difference is more than 0.2. This may indicate a large block effect or a possible problem with the model and/or data. Things to consider are model reduction, response transformation, outliers, etc.

However, adequate precision of 12.170 indicates that this model can be used to navigate the experimental space.

Final Equation in Terms of Actual Factors

$$1 / (\mathrm{Sqrt}(R_p\ \text{Tafel extrapolation})) = 0.010104 - 0.001627 \times \mathrm{pH} - 4.93342\times10^{-6} \times t - 0.000018 \times \gamma + 3.50121\times10^{-6} \times \mathrm{pH} \times \gamma + 1.00561\times10^{-8} \times t \times \gamma$$

A.4.3.3.5 Response 5: R_pEIS (Ω cm^2)

ANOVA for Reduced 2FI model

Transform: Inverse Sqrt

Constant: 0

Source	Sum of Squares	df	Mean Square	F-value	p-value	
Block	3.169×10^{-6}	4	7.922×10^{-7}			
Model	2.333×10^{-6}	5	4.666×10^{-7}	15.03	0.0002	significant
A-pH	8.837×10^{-9}	1	8.837×10^{-9}	0.2847	0.6053	
B-t	1.254×10^{-8}	1	1.254×10^{-8}	0.4040	0.5393	
C-c	9.414×10^{-7}	1	9.414×10^{-7}	30.32	0.0003	
AC	6.625×10^{-7}	1	6.625×10^{-7}	21.34	0.0010	
BC	9.518×10^{-7}	1	9.518×10^{-7}	30.66	0.0002	
Residual	3.105×10^{-7}	10	3.105×10^{-8}			
Lack of Fit	6.735×10^{-8}	3	2.245×10^{-8}	0.6464	0.6095	not significant
Pure Error	2.431×10^{-7}	7	3.473×10^{-8}			
Cor Total	5.812×10^{-6}	19				

These rows were ignored for this analysis:

2, 3, 4, 9, 10, 11, 14, 15, 16, 19, 20, 26

Factor coding is Coded.

Sum of squares is Type III - Partial

The model F-value of 15.03 implies that the model is significant. There is only a 0.02 % chance that an F-value this large could occur due to noise.

Based on p-values, C, AC, and BC are significant model terms.

The lack of fit F-value of 0.65 implies that the lack of fit is not significant relative to the pure error. There is a 60.65 % chance that a lack of fit F-value this large could occur due to noise. The model fits.

Fit Statistics

Std. Dev.	0.0002	R^2	0.8825
Mean	0.0021	Adjusted R^2	0.8238
C.V. %	8.32	Predicted R^2	0.4376
		Adequate Precision	14.2847

The predicted R^2 of 0.4376 is not as close to the adjusted R^2 of 0.8238 as one might normally expect, i.e., the difference is more than 0.2. This may indicate a large block effect or a possible problem with the model and/or data. Things to consider are model reduction, response transformation, outliers, etc.

However, adequate precision of 14.448 indicates that this model can be used to navigate the experimental space.

Final Equation in Terms of Actual Factors

$$1 / (\text{Sqrt}(R_p\ \text{EIS})) = 0.012297 - 0.001988 \times \text{pH} - 6.05195\times10^{-6} \times t - 0.000022 \times \gamma + 4.36398\times10^{-6} \times \text{pH} \times \gamma + 1.17673\times10^{-8} \times t \times \gamma$$

A.5 EDS Results

The bar graphs represent atomic percentages obtained by EDS at marked points on the enclosed SEM micrographs in the main text.

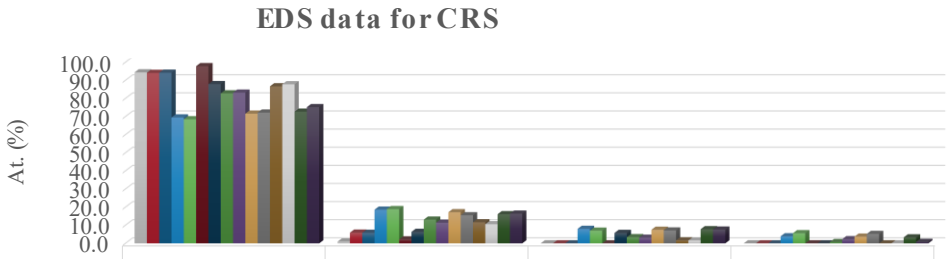

	Fe	O	Zr	F
Bare	94.4	1.0	0.0	0.0
Alkaline cleaned #1	94.1	5.9	0.0	0.0
Alkaline cleaned #2	94.2	5.8	0.0	0.0
150 ppm 480 s pH 4.0 #1	69.5	18.6	8.0	3.9
150 ppm 480 s pH 4.0 #2	68.5	18.9	7.0	5.6
825 ppm 480 s pH 3.0 #1	97.8	2.2	0.0	0.0
825 ppm 480 s pH 3.0 #2	87.9	6.3	5.8	0.0
825 ppm 60 s pH 4.0 #1	82.8	13.1	3.4	0.7
825 ppm 60 s pH 4.0 #2	83.2	11.4	3.1	2.3
825 ppm 480 s pH 4.0 #1	71.6	17.2	7.5	3.7
825 ppm 480 s pH 4.0 #2	72.2	15.5	7.1	5.2
1226 ppm 230 s pH 3.4 #1	86.7	11.6	1.7	0.0
1226 ppm 230 s pH 3.4 #2	87.8	10.6	1.6	0.0
1500 ppm 480 s pH 4.0 #1	72.7	16.1	7.8	3.3
1500 ppm 480 s pH 4.0 #2	75.2	16.4	7.6	0.8

Figure A.6: EDS results for CRS.

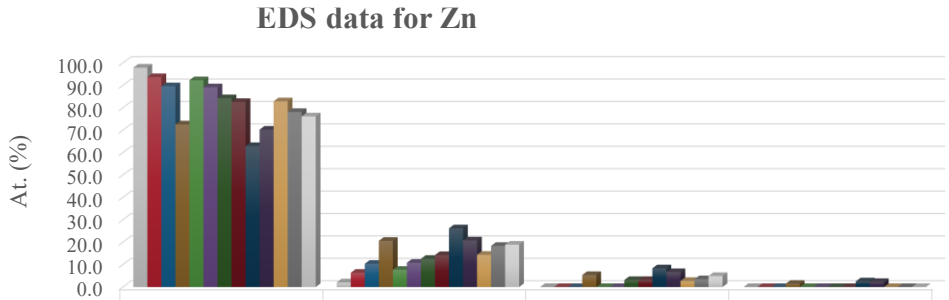

	Zn	O	Zr	F
Bare #1	97.9	2.1	0.0	0.0
Alkaline cleaned #1	93.7	6.4	0.0	0.0
Alkaline cleaned #2	89.6	10.4	0.0	0.0
424 ppm 230 s pH4.6	72.6	20.6	5.4	1.4
825 ppm 480 s pH 3.0 #1	92.3	7.7	0.0	0.0
825 ppm 480 s pH 3.0 #2	89.2	10.8	0.0	0.0
825 ppm 60 s pH 4.0 #1	84.3	12.6	3.1	0.0
825 ppm 60 s pH 4.0 #2	82.6	14.3	3.1	0.0
825 ppm 480 s pH 4.0 #1	62.9	26.2	8.4	2.5
825 ppm 480 s pH 4.0 #2	70.3	20.8	6.7	2.3
1226 ppm 230 s pH 3.4 #1	82.9	14.4	2.7	0.0
1226 ppm 230 s pH 3.4 #2	78.2	18.4	3.5	0.0
1226 ppm 230 s pH4.6	76.2	18.9	4.9	0.0

Figure A.7: EDS results for Zn.

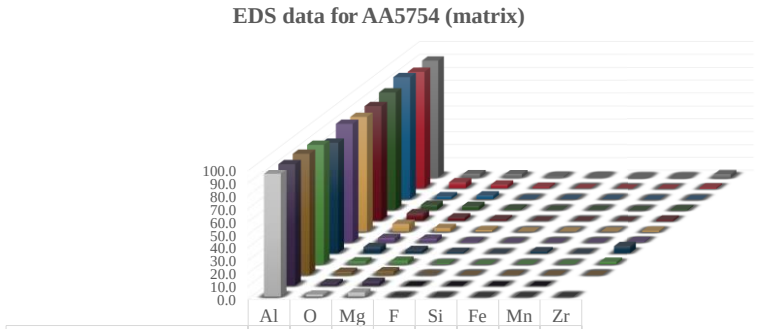

	Al	O	Mg	F	Si	Fe	Mn	Zr
Bare	95.2	1.6	3.2	0.0	0.0	0.0	0.0	0.0
Alkaline cleaned	94.7	2.1	3.2	0.0	0.0	0.0	0.0	
Alkaline cleaned + desmutted	94.4	2.4	2.9	0.0	0.0	0.2	0.1	0.0
150 ppm 480 s pH 3.4 #1	92.9	2.1	2.7	0.5	0.0	0.0	0.0	1.8
150 ppm 480 s pH 3.4 #2	86.2	4.8	2.5	1.0	0.0	1.6	0.0	5.5
150 ppm 480 s pH 4.0	92.4	3.5	2.9	0.6	0.0	0.0	0.0	0.6
150 ppm 230 s pH 4.6	89.4	5.9	2.8	1.1	0.0	0.0	0.0	0.8
150 ppm 730 s pH 4.6	89.3	5.7	2.6	1.2	0.0	0.0	0.0	1.2
825 ppm 480 s pH 3.0	91.5	3.9	3.1	0.8	0.0	0.0	0.0	0.7
825 ppm 60 s pH 4.0	95.0	2.2	2.8	0.0	0.0	0.0	0.0	0.0
825 ppm 230 s pH 4.3	90.7	4.6	2.8	1.0	0.0	0.0	0.0	0.8
825 ppm 480 s pH 4.0	91.0	2.8	2.7	0.7	0.0	0.0	0.0	2.8

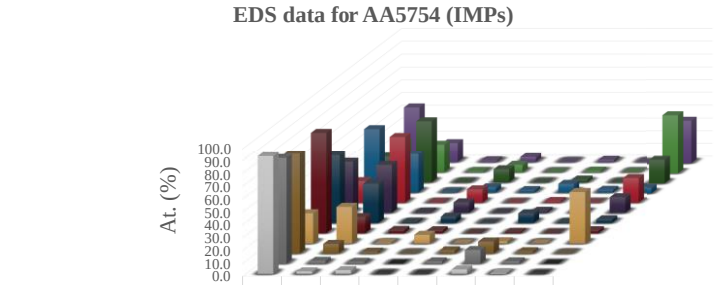

	Al	O	Mg	F	Si	Fe	Mn	Zr
Bare	91.5	1.9	2.8	0.0	0.0	3.4	0.5	0.0
Alkaline cleaned	82.2	2.2	1.5	0.0	1.8	10.6	1.8	0.0
Alkaline cleaned + desmutted	77.6	7.4	1.4	0.0	2.5	9.3	1.8	0.0
150 ppm 480 s pH 3.4	23.3	28.3	0.5	6.6	0.0	1.6	0.0	39.8
150 ppm 480 s pH 4.0	79.1	12.5	2.5	2.3	0.2	0.9	0.3	2.3
150 ppm 230 s pH 4.6	52.8	30.4	0.9	4.8	0.0	7.5	0.7	2.9
150 ppm 730 s pH 4.6	39.7	37.2	0.8	8.1	0.3	1.6	0.3	12.1
825 ppm 480 s pH 3.0	16.7	52.2	0.5	10.3	0.0	1.2	0.0	19.1
825 ppm 60 s pH 4.0	50.5	30.1	0.6	4.0	1.9	6.7	2.1	4.2
825 ppm 230 s pH 4.3	20.2	48.8	0.4	10.1	0.0	2.1	0.0	18.4
825 ppm 480 s pH 4.0 #1	24.5	22.5	0.7	5.7	0.0	1.1	0.0	45.5
825 ppm 480 s pH 4.0 #2	43.8	15.9	1.3	4.0	0.0	1.7	0.0	33.3

Figure A.8: EDS results for AA5754. (above) matrix, (below) IMPs.

A.6 FTIR Results

A.6.1 FTIR experimental procedure

FTIR spectra were obtained using a PerkinElmer Spectrum 100 instrument at a resolution of 4 cm^{-1}. Measurements were taken using the ATR sampling accessory, averaging over 4 scans. The spectra were recorded in the range of 4,000 to 600 cm^{-1} and are presented as normalised transmittances (T).

A.6.2 FTIR results

Due to the gold iridescent colour of the ZrCCs formed on CRS, visually distinguishing the formation of rust was challenging. An FTIR analysis was conducted to verify rust formation. Air-dried bare CRS and bare CRS samples subjected to 24-h corrosion in dilute

Harrison's solution as well as selected air-dried CRS-ZrCC (again 825 ppm/480 s/pH 4.0) before and post-EIS were analysed (Figure A.9). No specific peaks for $FeSO_4$, which could arise from dilute Harrison's solution, are present [337]. The peaks observed at 2925 and 2850 cm^{-1} in samples exposed to air can be attributed to the stretching vibrations of the CH_2 and CH_3 groups, originating from surface contamination by aliphatic hydrocarbons. In contrast, samples immersed in the electrolyte displayed broad shoulder between 2900–3100 cm^{-1}, characteristic of OH–groups from water [338]. The formation of lepidocrocite, strongly evident at 1021 cm^{-1} and around 744 cm^{-1} [339], was confirmed on the bare CRS after 24 h and the CRS-ZrCC post-EIS in dilute Harrison's solution. Notably, the latter sample displayed rust formations at reduced intensities, suggesting that the underlying ZrCC layer is not entirely destroyed, overall supporting EIS findings (Figure 2.3 and Figure A.2).

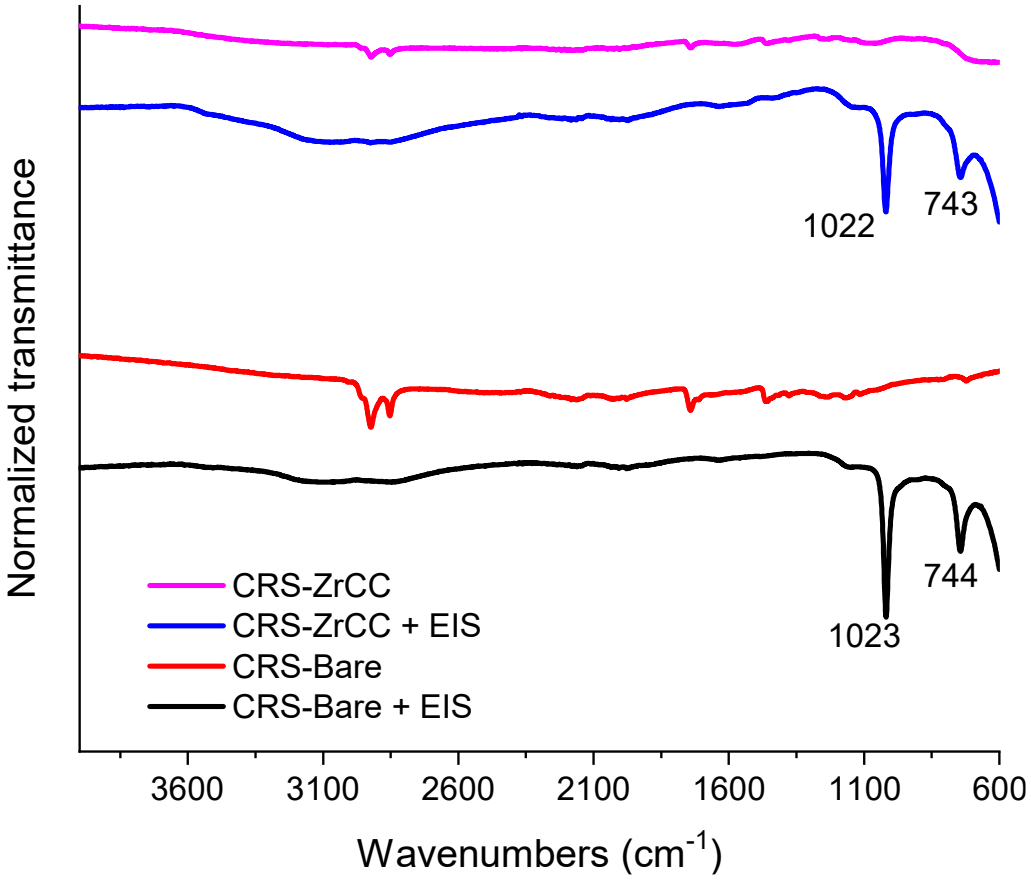

Figure A.9: FTIR results on CRS.

References

[1] P. R. Roberge, *Handbook of Corrosion Engineering*, 2nd ed. New York: McGraw-Hill Education, 2012.

[2] M. G. Fontana, *Corrosion Engineering*, 3rd ed. in Materials science and engineering series. Singapore: McGraw-Hill Book Company, 1987.

[3] A. E. Hughes, J. M. C. Mol, and R. G. B. Editors, *Active Protective Coatings*, vol. 233. in Springer Series in Materials Science, vol. 233. Dordrecht: Springer Netherlands, 2016. doi: 10.1007/978-94-017-7540-3.

[4] G. L. Song, "The grand challenges in electrochemical corrosion research," *Front Mater*, vol. 1, no. March, pp. 1–3, Mar. 2014, doi: 10.3389/fmats.2014.00002.

[5] T. S. N. S. Narayanan, "Surface pretreatment by phosphate conversion coatings - A review," *Reviews on Advanced Materials Science*, vol. 9, no. 2, pp. 130–177, 2005.

[6] K. Gerhardus, V. Jeff, N. Thopson, O. Moghissi, M. Gould, and J. Payer, "International Measures of Prevention, Application, and Economics of Corrosion Technologies Study," *NACE IMPACT Report*, pp. 1–216, 2016.

[7] S. W. Dean, "Natural Atmospheres: Corrosion," in *Encyclopedia of Materials: Science and Technology*, Elsevier, 2001, pp. 5930–5938. doi: 10.1016/b0-08-043152-6/01033-0.

[8] M. Doerre, L. Hibbitts, G. Patrick, and N. K. Akafuah, "Advances in automotive conversion coatings during pretreatment of the body structure: A review," *Coatings*, vol. 8, no. 11, p. 405, 2018, doi: 10.3390/COATINGS8110405.

[9] I. Milošev and G. S. Frankel, "Review—Conversion Coatings Based on Zirconium and/or Titanium," *J Electrochem Soc*, vol. 165, no. 3, pp. C127–C144, Feb. 2018, doi: 10.1149/2.0371803jes.

[10] U.S. Environmental Protection Agency, "Integrated Risk Information System: Chromium (VI)," NCEA, Office of Research and Development, 1998. Accessed: Apr. 16, 2024. [Online]. Available: https://iris.epa.gov/static/pdfs/0144_summary.pdf

[11] "Commission Regulation (EU) 2022/586 of 8 April 2022 amending Annex XIV to Regulation (EC) No 1907/2006 of the European Parliament and of the Council concerning the Registration, Evaluation, Authorisation and Restriction of Chemicals (REACH)." Apr. 11, 2022.

[12] "Commission Regulation (EU) No 301/2014 of 25 March 2014 amending Annex XVII to Regulation (EC) No 1907/2006 of the European Parliament and of the Council on the Registration, Evaluation, Authorisation and Restriction of Chemicals (REACH) as regards chromium VI compounds." Mar. 26, 2014.

[13] "Regulation (EC) No 1907/2006 of the European Parliament and of the Council of 18 December 2006 concerning the Registration, Evaluation, Authorisation and Restriction of Chemicals (REACH)," *2014*. Apr. 10, 2023.

[14] U.S. Environmental Protection Agency, "Integrated Risk Information System: Chromium(III), insoluble salts." NCEA, Office of Research and Development, 1998. [Online]. Available: https://iris.epa.gov/static/pdfs/0028_summary.pdf

[15] O. Gharbi, S. Thomas, C. Smith, and N. Birbilis, "Chromate replacement: what does the future hold?," *Npj Mater Degrad*, vol. 2, no. 1, p. 12, Apr. 2018, doi: 10.1038/s41529-018-0034-5.

[16] A. E. Hughes, I. S. Cole, T. H. Muster, and R. J. Varley, "Designing green, self-healing coatings for metal protection," *NPG Asia Mater*, vol. 2, no. 4, pp. 143–151, 2010, doi: 10.1038/asiamat.2010.136.

[17] "Regulation (EC) No 1907/2006 of the European Parliament and of the Council of 18 December 2006 concerning the Registration, Evaluation, Authorisation and Restriction of Chemicals (REACH)."

[18] R. Moore and B. Dunham, "Zirconization™: The future of coating pretreatment processes," *Metal Finishing*, vol. 106, no. 7–8, pp. 46–55, Jul. 2008, doi: 10.1016/S0026-0576(08)80259-0.

[19] T. R. Giles, B. H. Goodreau, W. E. Fristad, J. Kroemer, and M. Frank, "An Update of New Conversion Coating for the Automotive Industry," *SAE International Journal of Materials and Manufacturing*, vol. 1, no. 1, pp. 575–581, Mar. 2009.

[20] S. Atkinson, "Thin-film conversion coatings reduce process times and costs," *Sealing Technology*, vol. 2018, no. 12, p. 6, 2018, doi: 10.1016/s1350-4789(18)30472-0.

[21] P. Mills, "What's Cooking In Chemical Pretreatment?" Accessed: Apr. 16, 2024. [Online]. Available: https://www.powdercoatedtough.com/News/ID/572/Whats-Cooking-In-Chemical-Pretreatment

[22] Henkel Corporation, "Zirconate Coatings." [Online]. Available: https://www.henkel-adhesives.com/us/en/industries/metals/metal-pretreatment/zirconate-coatings.html

[23] Lenntech B.V., "Chromium (Cr) and water." Accessed: Apr. 16, 2024. [Online]. Available: https://www.lenntech.com/periodic/water/chromium/chromium-and-water.htm

[24] Air Force Blue Ribbon Advisory Panel, "Report on Aircraft Coatings," Nov. 1995.

[25] J. Han, D. Thierry, and K. Ogle, "Zr-based conversion coating on Zn and Zn-Al-Mg alloy coating: Understanding the accelerating effect of Cu(II) and NO3−," *Surf Coat Technol*, vol. 402, p. 126236, 2020, doi: https://doi.org/10.1016/j.surfcoat.2020.126236.

[26] D. Chidambaram, C. R. Clayton, and G. P. Halada, "The role of hexafluorozirconate in the formation of chromate conversion coatings on aluminum alloys," *Electrochim Acta*, vol. 51, no. 14, pp. 2862–2871, Mar. 2006, doi: 10.1016/j.electacta.2005.08.022.

[27] M. W. Kendig and R. G. Buchheit, "Corrosion Inhibition of Aluminum and Aluminum Alloys by Soluble Chromates, Chromate Coatings, and Chromate-Free Coatings," *CORROSION*, vol. 59, no. 5, pp. 379–400, May 2003, doi: 10.5006/1.3277570.

[28] R. W. Revie, Ed., *Uhlig's Corrosion Handbook*. Hoboken, NJ, USA: John Wiley & Sons, Inc., 2011. doi: 10.1002/9780470872864.

[29] W. S. Miller *et al.*, "Recent development in aluminium alloys for the automotive industry," *Materials Science and Engineering A*, vol. 280, no. 1, pp. 37–49, Mar. 2000, doi: 10.1016/S0921-5093(99)00653-X.

[30] V. Bonamigo Moreira, A. Puiggalí-Jou, E. Jiménez-Piqué, C. Alemán, A. Meneguzzi, and E. Armelin, "Green Nanocoatings Based on the Deposition of Zirconium Oxide: The Role of the Substrate," *Materials*, vol. 14, no. 4, p. 1043, Feb. 2021, doi: 10.3390/ma14041043.

[31] L. Li, A. L. Desouza, and G. M. Swain, "In situ pH measurement during the formation of conversion coatings on an aluminum alloy (AA2024)," *Analyst*, vol. 138, no. 15, pp. 4398–4402, 2013, doi: 10.1039/c3an00663h.

[32] S. Adhikari, K. A. Unocic, Y. Zhai, G. S. Frankel, J. Zimmerman, and W. Fristad, "Hexafluorozirconic acid based surface pretreatments: Characterization and performance assessment," *Electrochim Acta*, vol. 56, no. 4, pp. 1912–1924, Jan. 2011, doi: 10.1016/j.electacta.2010.07.037.

[33] G. Šekularac and I. Milošev, "Electrochemical Behavior and Self-Sealing Ability of Zirconium Conversion Coating Applied on Aluminum Alloy 3005 in 0.5 M NaCl Solution," *J Electrochem Soc*, vol. 167, no. 2, p. 021509, 2020, doi: 10.1149/1945-7111/ab6b0d.

[34] G. Šekularac, J. Kovač, and I. Milošev, "Comparison of the Electrochemical Behaviour and Self-sealing of Zirconium Conversion Coatings Applied on Aluminium Alloys of series 1xxx to 7xxx," *J Electrochem Soc*, vol. 167, no. 11, p. 111506, Jan. 2020, doi: 10.1149/1945-7111/aba875.

[35] F. Farnworth, S. L. Jones, and I. McAlpine, "The production, properties and uses of zirconium chemicals," *Speciality Inorganic Chemicals*, no. 40, p. 248, 1980.

[36] M. J. Anderson and P. J. Whitcomb, *DOE Simplified*, 3rd ed. New York: Productivity Press, 2017. doi: 10.1201/b18479.

[37] M. J. Anderson and P. J. Whitcomb, *RSM Simplified*, 2nd ed. New York: Productivity Press, 2016. doi: 10.1201/9781315382326.

[38] ASTM International, "ASTM G31-72(2004), Standard Practice for Laboratory Immersion Corrosion Testing of Metals." ASTM International, West Conshohocken, Oct. 22, 2012. doi: 10.1520/G0031-72R04.

[39] H. R. Asemani, A. A. Sarabi, H. Eivaz Mohammadloo, and M. Sarayloo, "Electrochemical and morphological properties of zirconium conversion coating in the presence of nickel ions on galvanized steel," *J Coat Technol Res*, vol. 13, no. 5, pp. 883–894, Sep. 2016, doi: 10.1007/s11998-016-9800-x.

[40] C. E. Tomlinson, "Conversion coatings for metal surfaces," US5380374A, Jan. 10, 1995 [Online]. Available: https://patents.google.com/patent/US5380374A/en

[41] T. G. Harvey, "Cerium-based conversion coatings on aluminium alloys: a process review," *Corrosion Engineering, Science and Technology*, vol. 48, no. 4, pp. 248–269, Jun. 2013, doi: 10.1179/1743278213Y.0000000089.

[42] G. Šekularac, J. Kovač, and I. Milošev, "Prolonged protection, by zirconium conversion coatings, of AlSi7Mg0.3 aluminium alloy in chloride solution," *Corros Sci*, vol. 169, p. 108615, 2020, doi: https://doi.org/10.1016/j.corsci.2020.108615.

[43] G. Šekularac and I. Milošev, "Electrochemical Behavior and Self-Sealing Ability of Zirconium Conversion Coating Applied on Aluminum Alloy 3005 in 0.5 M NaCl Solution," *J Electrochem Soc*, vol. 167, no. 2, p. 021509, 2020, doi: 10.1149/1945-7111/ab6b0d.

[44] Kim, Kapun, Tiringer, Šekularac, and Milošev, "Protection of Aluminium Alloy 3003 in Sodium Chloride and Simulated Acid Rain Solutions by Commercial Conversion Coatings Containing Zr and Cr," *Coatings*, vol. 9, no. 9, p. 563, Sep. 2019, doi: 10.3390/coatings9090563.

[45] G. W. Jernstedt, "Corrosion resistant coating for metal surfaces," US2310239A, Feb. 09, 1943 Accessed: Apr. 16, 2024. [Online]. Available: https://patents.google.com/patent/US2310239A/en#citedBy

[46] N. Takaomi, Y. Nagashima, and K. Shimoda, "Conditioning metal surfaces prior to phosphate conversion coating," EP0977908A1, 1998

[47] D. Lide, Ed., *CRC Handbook of Chemistry and Physics*, 84th ed. in CRC Handbook of Chemistry and Physics, 84th Ed. CRC Press, 2004.

[48] P. L. Brown, E. Curti, and B. Grambow, *Chemical Thermodynamics of Zirconium*, 1st ed. Amsterdam: Elsevier, 2005.

[49] D. Rai, A. Kitamura, M. Altmaier, K. M. Rosso, T. Sasaki, and T. Kobayashi, "A Thermodynamic Model for ZrO2(am) Solubility at 25 °C in the Ca2+–Na+–H+–Cl−–OH−–H2O System: A Critical Review," *J Solution Chem*, vol. 47, no. 5, pp. 855–891, 2018, doi: 10.1007/s10953-018-0766-4.

[50] P. L. Brown and C. Ekberg, *Hydrolysis of Metal Ions*. Weinheim, Germany: Wiley-VCH Verlag GmbH & Co. KGaA, 2016.

[51] S. Verdier, S. Delalande, N. van der Laak, J. Metson, and F. Dalard, "Monochromatized x-ray photoelectron spectroscopy of the AM60 magnesium alloy surface after treatments in fluoride-based Ti and Zr solutions," *Surface and Interface Analysis*, vol. 37, no. 5, pp. 509–516, May 2005, doi: https://doi.org/10.1002/sia.2042.

[52] G. Šekularac, J. Kovač, and I. Milošev, "Comparison of the Electrochemical Behaviour and Self-sealing of Zirconium Conversion Coatings Applied on Aluminium Alloys of series 1xxx to 7xxx," *J Electrochem Soc*, vol. 167, no. 11, p. 111506, 2020.

[53] A. Kraš and I. Milošev, "The Aqueous Chemistry of Zirconium as a Basis for Better Understanding the Formation of Zirconium Conversion Coatings: Updated Thermodynamic Data," *J Electrochem Soc*, vol. 170, no. 2, p. 21508, 2023, doi: 10.1149/1945-7111/acb9c2.

[54] C. Gabrielli, M. Keddam, F. Minouflet-Laurent, K. Ogle, and H. Perrot, "Investigation of zinc chromatation. I - Application of QCM-ICP coupling," *Electrochim Acta*, vol. 48, no. 8, pp. 965–976, Apr. 2003, doi: 10.1016/S0013-4686(02)00809-5.

[55] B. Vuillemin, R. Oltra, H. Perrot, C. Sauvage, and O. Néel, "Study of the Chemical Conversion of Aluminum Alloys by Coupling CFDE and EQCM," *J Electrochem Soc*, vol. 151, pp. C229–C235, 2004, doi: 10.1149/1.1649755.

[56] A. Kosari *et al.*, "Nanoscopic and in-situ cross-sectional observations of Li-based conversion coating formation using liquid-phase TEM," *Npj Mater Degrad*, vol. 5, no. 1, p. 40, 2021, doi: 10.1038/s41529-021-00189-y.

[57] H. S. Isaacs, K. Sasaki, C. S. Jeffcoate, V. Laget, and R. Buchheit, "Formation of Chromate Conversion Coatings on Aluminum and Its Alloys: An In Situ XANES Study," *J Electrochem Soc*, vol. 152, no. 11, p. B441, 2005, doi: 10.1149/1.2041027.

[58] B. Díaz, L. Freire, M. Mojío, and X. R. Nóvoa, "Optimization of conversion coatings based on zinc phosphate on high strength steels, with enhanced barrier properties," *Journal of Electroanalytical Chemistry*, vol. 737, pp. 174–183, Jan. 2015, doi: 10.1016/j.jelechem.2014.06.035.

[59] P. Campestrini, S. Böhm, T. Schram, H. Terryn, and J. H. W. de Wit, "Study of the formation of chromate conversion coatings on Alclad 2024 aluminum alloy using spectroscopic ellipsometry," *Thin Solid Films*, vol. 410, no. 1–2, pp. 76–85, May 2002, doi: 10.1016/S0040-6090(02)00253-5.

[60] C. G. da Silva, I. C. P. Margarit-Mattos, O. R. Mattos, H. Perrot, B. Tribollet, and V. Vivier, "The molybdate-zinc conversion process," *Corros Sci*, vol. 51, no. 1, pp. 151–158, Jan. 2009, doi: 10.1016/j.corsci.2008.10.019.

[61] L. Li, J. Lei, S. Yu, D. He, W. Qu, and F. Pan, "In situ ellipsometric studies of formation kinetics of rare earth metal conversion coatings on magnesium alloy," *Physica Status Solidi (C) Current Topics in Solid State Physics*, vol. 5, no. 5, pp. 1308–1311, May 2008, doi: 10.1002/pssc.200777890.

[62] J. Feng, Y. Wang, X. Lin, M. Bian, and Y. Wei, "SECM in situ investigation of corrosion and self-healing behavior of trivalent chromium conversion coating on the zinc," *Surf Coat Technol*, vol. 459, p. 129411, Apr. 2023, doi: 10.1016/j.surfcoat.2023.129411.

[63] J. Cerezo *et al.*, "Influence of surface hydroxyls on the formation of Zr-based conversion coatings on AA6014 aluminum alloy," *Surf Coat Technol*, vol. 254, pp. 277–283, 2014, doi: 10.1016/j.surfcoat.2014.06.030.

[64] X. Liu *et al.*, "Environmentally Friendly Zr-Based Conversion Nanocoatings for Corrosion Inhibition of Metal Surfaces Evaluated by Multimodal X-ray Analysis," *ACS Appl Nano Mater*, vol. 2, no. 4, pp. 1920–1929, 2019, doi: 10.1021/acsanm.8b02309.

[65] A. C. Bastos, M. C. Quevedo, O. V. Karavai, and M. G. S. Ferreira, "Review—On the application of the scanning vibrating electrode technique (SVET) to corrosion research," *J Electrochem Soc*, vol. 164, no. 14, pp. C973–C990, 2017, doi: 10.1149/2.0431714jes.

[66] S. Rossi, M. Fedel, F. Deflorian, and M. del Carmen Vadillo, "Localized electrochemical techniques: Theory and practical examples in corrosion studies," *Comptes Rendus Chimie*, vol. 11, no. 9, 2008, doi: 10.1016/j.crci.2008.06.011.

[67] G. Frankel, "Fundamentals of Corrosion Kinetics," A. E. Hughes, J. M. C. Mol, M. L. Zheludkevich, and R. G. Buchheit, Eds., Dordrecht: Springer Netherlands, 2016, pp. 17–32. doi: 10.1007/978-94-017-7540-3_2.

[68] G. E. P. Box, "Science and Statistics," *J Am Stat Assoc*, vol. 71, no. 356, pp. 791–799, Dec. 1976, doi: 10.1080/01621459.1976.10480949.

[69] G. Šekularac, J. Kovač, and I. Milošev, "Prolonged protection, by zirconium conversion coatings, of AlSi7Mg0.3 aluminium alloy in chloride solution," *Corros Sci*, vol. 169, p. 108615, Jun. 2020, doi: 10.1016/j.corsci.2020.108615.

[70] D. Kramar, "Process modelling using design of experiments," in *Metal Cutting-theory and applications*, G. Globočki-Lakić, D. Kramar, and J. Kopać, Eds., Banja Luka and Ljubljana: Faculty of Mechanical Engineering, University of Banja Luka and Faculty of Mechanical Engineering, University of Ljubljana, 2014.

[71] M. Nabizadeh *et al.*, "Investigation of hybrid Zr-aminosilane treatment formation on zinc substrate and comparison to advanced high strength stainless steel," *Appl Surf Sci*, vol. 610, p. 155554, 2023, doi: https://doi.org/10.1016/j.apsusc.2022.155554.

[72] H. Eivaz Mohammadloo and A. A. Sarabi, "Ti-based conversion coatings on cold-rolled steel substrate: The effect of practical parameters and Ti source on surface and electrochemical properties," *Corrosion*, vol. 72, no. 6, pp. 791–804, 2016, doi: 10.5006/1936.

[73] K. Ogle and R. G. Buchheit, "Conversion Coatings," in *Encyclopedia of Electrochemistry*, A. J. Bard and M. Stratmann, Eds., in Vol. 4, Corrosion and Oxide Films. , Weinheim: Wiley-VCH, 2003. doi: 10.1002/9783527610426.bard040503.

[74] K. Ogle and M. Wolpers, "Phosphate Conversion Coatings," in *Corrosion: Fundamentals, Testing, and Protection*, S. D. Cramer and B. S. Covino, Eds., ASM International, 2003, pp. 712–719. doi: 10.31399/asm.hb.v13a.a0003678.

[75] K. Li, J. Liu, T. Lei, and T. Xiao, "Optimization of process factors for self-healing vanadium-based conversion coating on AZ31 magnesium alloy," *Appl Surf Sci*, vol. 353, pp. 811–819, Oct. 2015, doi: 10.1016/j.apsusc.2015.07.052.

[76] P. Santa Coloma, U. Izagirre, Y. Belaustegi, J. B. Jorcin, F. J. Cano, and N. Lapeña, "Chromium-free conversion coatings based on inorganic salts (Zr/Ti/Mn/Mo) for aluminum alloys used in aircraft applications," *Appl Surf Sci*, vol. 345, pp. 24–35, Aug. 2015, doi: 10.1016/j.apsusc.2015.02.179.

[77] S. Wery, M. De Petris-Wery, M. Feki, and H. F. Ayedi, "Application of a factorial design to study a chromate-conversion process," *J Coat Technol Res*, vol. 7, no. 1, pp. 39–47, Jan. 2010, doi: 10.1007/s11998-008-9150-4.

[78] P. Puomi, H. M. Fagerholm, J. B. Rosenholm, and R. Sipilä, "Optimization of commercial zirconic acid based pretreatment on hot-dip galvanized and Galfan coated steel," *Surf Coat Technol*, vol. 115, no. 1, pp. 79–86, 1999, doi: 10.1016/S0257-8972(99)00171-1.

[79] J. Reck, Y.-M. Wang, and H.-H. H. Kuo, "Development of Zirconium-based Conversion Coatings for the Pretreatment of AZ91D Magnesium Alloy Prior to Electrocoating," in *Magnesium Technology 2011*, Cham: Springer International Publishing, 2011, pp. 523–529. doi: 10.1007/978-3-319-48223-1_97.

[80] Y. Huang and F. Mansfeld, "Evaluation of the Effects of Different Process Parameters on the Corrosion Protection Provided by Cerium-Based Coatings on Galvanized Steels," *CORROSION*, vol. 65, no. 8, pp. 507–510, Aug. 2009, doi: 10.5006/1.3319154.

[81] S. El Hajjaji, A. Lgamri, E. Puech-Costes, A. Guenbour, A. Ben Bachir, and L. Aries, "Optimization of conversion coatings: study of the influence of parameters with experimental designs," *Appl Surf Sci*, vol. 165, no. 2–3, pp. 184–192, Sep. 2000, doi: 10.1016/S0169-4332(00)00444-X.

[82] G. S. Frankel and M. Rohwerder, "Electrochemical Techniques for Corrosion," in *Encyclopedia of Electrochemistry*, vol. 4, M. Stratmann and G. Frankel, Eds., Weinheim: Wiley, 2003. doi: 10.1002/9783527610426.bard040007.

[83] D. Ho, N. Brack, J. Scully, T. Markley, M. Forsyth, and B. Hinton, "Cerium Dibutylphosphate as a Corrosion Inhibitor for AA2024-T3 Aluminum Alloys," *J Electrochem Soc*, vol. 153, no. 9, p. B392, 2006, doi: 10.1149/1.2217260.

[84] P. Rodič, I. Milošev, and G. S. Frankel, "Corrosion of Synthetic Intermetallic Compounds and AA7075-T6 in Dilute Harrison's Solution and Inhibition by Cerium(III) Salts," *J Electrochem Soc*, vol. 170, no. 3, p. 031503, Mar. 2023, doi: 10.1149/1945-7111/acc0a3.

[85] F. D. Timmins, "Avoiding paint failures by prohesion," *J. Oil. Col. Chem. Assoc.*, vol. 62, no. 4, pp. 131–135, 1979.

[86] J. B. Harrison and T. C. K. Tickle, "New aspects of the atmospheric corrosion of steel and their implications," *Journal of the Oil and Colour Chemists' Association*, vol. 45, no. 8, p. 571, 1962.

[87] R. L. Howard, S. B. Lyon, and J. D. Scantlebury, "Accelerated tests for the prediction of cut-edge corrosion of coil-coated architectural cladding," *Prog Org Coat*, vol. 37, no. 1–2, pp. 91–98, Nov. 1999, doi: 10.1016/S0300-9440(99)00060-0.

[88] J. B. Harrison, "Prediction of Performance of Primers and its Relationship to the Performance of a Full Paint System in Practice," *British Corrosion Journal*, vol. 4, no. 2, pp. 58–65, Mar. 1969, doi: 10.1179/000705969798325596.

[89] G. Gusmano *et al.*, "Zirconia primers for corrosion resistant coatings," *Surf Coat Technol*, vol. 201, no. 12, pp. 5822–5828, Mar. 2007, doi: 10.1016/J.SURFCOAT.2006.10.036.

[90] S. Wang, J. Zhang, O. Gharbi, V. Vivier, M. Gao, and M. E. Orazem, "Electrochemical impedance spectroscopy," *Nature Reviews Methods Primers*, vol. 1, no. 1, p. 41, Jun. 2021, doi: 10.1038/s43586-021-00039-w.

[91] F. L. Floyd *et al.*, "Using electrochemical impedance spectroscopy to predict the corrosion resistance of unexposed coated metal panels," *Prog Org Coat*, vol. 66, no. 1, pp. 8–34, Sep. 2009, doi: 10.1016/j.porgcoat.2009.04.009.

[92] F. L. Floyd, S. Tatti, and T. Provder, "Using DC electrochemical techniques to assess the relative corrosiveness of water-based coatings and their ingredients," *J Coat Technol Res*, vol. 4, no. 2, pp. 111–129, Jun. 2007, doi: 10.1007/s11998-007-9012-5.

[93] R. Srinivasan and F. Fasmin, *An Introduction to Electrochemical Impedance Spectroscopy*, 1st ed. Boca Raton: CRC Press, 2021. doi: 10.1201/9781003127932.

[94] A. Cox and S. B. Lyon, "An electrochemical study of the atmospheric corrosion of mild steel-I. Experimental method," *Corros Sci*, vol. 36, no. 7, pp. 1167–1176, 1994, doi: 10.1016/0010-938X(94)90141-4.

[95] F. Mansfeld, "Electrochemical impedance spectroscopy (EIS) as a new tool for investigating methods of corrosion protection," *Electrochim Acta*, vol. 35, no. 10, pp. 1533–1544, Oct. 1990, doi: 10.1016/0013-4686(90)80007-B.

[96] "ГОСТ 9.302-88. Edinaya sistema zashchity ot korrozii i stareniya. Pokrytiya metallicheskie i nemetallicheskie neorganicheskie, Metodykontrolya," Izd. Standardov, Moscow, 1990.

[97] S. Mancini, "Conversion Coatings: Phosphate vs. Zirconium | Products Finishing." Accessed: Oct. 18, 2023. [Online]. Available: https://www.pfonline.com/articles/conversion-coatings-phosphate-vs-zirconium-

[98] ASTM International, "ASTM F22-21, Standard Test Method for Hydrophobic Surface Films by the Water-Break Test." ASTM International, West Conshohocken, Dec. 10, 2021. doi: 10.1520/F0022-21.

[99] R. G. Kelly, J. R. Scully, D. Shoesmith, and R. G. Buchheit, *Electrochemical Techniques in Corrosion Science and Engineering*. CRC Press, 2002. doi: 10.1201/9780203909133.

[100] ASTM International, "ASTM G59-97(2020), Standard Test Method for Conducting Potentiodynamic Polarization Resistance Measurements." ASTM International, West Conshohocken, Jun. 14, 2023. doi: 10.1520/G0059-97R20.

[101] L. Wang *et al.*, "Insight into physical interpretation of high frequency time constant in electrochemical impedance spectra of Mg," *Corros Sci*, vol. 187, p. 109501, Jul. 2021, doi: 10.1016/j.corsci.2021.109501.

[102] I. Thompson and D. Campbell, "Interpreting Nyquist responses from defective coatings on steel substrates," *Corros Sci*, vol. 36, no. 1, pp. 187–198, Jan. 1994, doi: 10.1016/0010-938X(94)90119-8.

[103] M. E. Orazem and B. Tribollet, *Electrochemical Impedance Spectroscopy*. Wiley, 2008. doi: 10.1002/9780470381588.

[104] D. H. van der Weijde, E. P. M. van Westing, and J. H. W. de Wit, "Electrochemical techniques for delamination studies," *Corros Sci*, vol. 36, no. 4, pp. 643–652, Apr. 1994, doi: 10.1016/0010-938X(94)90070-1.

[105] E. Barsoukov and J. R. Macdonald, *Impedance Spectroscopy*. Wiley, 2005. doi: 10.1002/0471716243.

[106] C. C. Herrmann, G. G. Perrault, and A. A. Pilla, "Dual reference electrode for electrochemical pulse studies," *Anal Chem*, vol. 40, no. 7, pp. 1173–1174, Jun. 1968, doi: 10.1021/ac60263a011.

[107] F. Mansfeld, S. Lin, Y. C. Chen, and H. Shih, "Minimization of High-Frequency Phase Shifts in Impedance Measurements," *J Electrochem Soc*, vol. 135, no. 4, pp. 906–907, Apr. 1988, doi: 10.1149/1.2095825.

[108] A. Ghanbari and M. M. Attar, "Corrosion Behavior of Zirconium Treated Mild Steel with and Without Organic Coating: a Comparative Study," *Surface Review and Letters*, vol. 21, no. 06, p. 1450088, Dec. 2014, doi: 10.1142/S0218625X14500887.

[109] A. Lasia, *Electrochemical Impedance Spectroscopy and its Applications*. New York, NY: Springer New York, 2014. doi: 10.1007/978-1-4614-8933-7.

[110] A. Niaz, "Complementary use of electrochemical testing techniques to study corrosion processes of HVOF Inconel 625, CoNiCrAlY and WCCoCr coatings," University of Nottingham, 2013.

[111] P. Campestrini, E. P. M. van Westing, and J. H. W. de Wit, "Influence of surface preparation on performance of chromate conversion coatings on Alclad 2024 aluminium alloy: Part II: EIS investigation," *Electrochim Acta*, vol. 46, no. 17, pp. 2631–2647, May 2001, doi: 10.1016/S0013-4686(01)00476-5.

[112] H. Otmacic Curkovic, E. Stupnisek-Lisac, and H. Takenouti, "Electrochemical quartz crystal microbalance and electrochemical impedance spectroscopy study of copper corrosion inhibition by imidazoles," *Corros Sci*, vol. 51, no. 10, pp. 2342–2348, Oct. 2009, doi: 10.1016/j.corsci.2009.06.018.

[113] C. M. Abreu, M. J. Cristóbal, R. Losada, X. R. Nóvoa, G. Pena, and M. C. Pérez, "High frequency impedance spectroscopy study of passive films formed on AISI 316 stainless steel in alkaline medium," *Journal of Electroanalytical Chemistry*, vol. 572, no. 2, pp. 335–345, Nov. 2004, doi: 10.1016/j.jelechem.2004.01.015.

[114] C. Andrade, M. Keddam, X. R. Nóvoa, M. C. Pérez, C. M. Rangel, and H. Takenouti, "Electrochemical behaviour of steel rebars in concrete: influence of environmental factors and cement chemistry," *Electrochim Acta*, vol. 46, no. 24–25, pp. 3905–3912, Aug. 2001, doi: 10.1016/S0013-4686(01)00678-8.

[115] M. Özcan, İ. Dehri, and M. Erbil, "EIS study of the effect of high levels of SO2 on the corrosion of polyester-coated galvanised steel at different relative humidities," *Prog Org Coat*, vol. 44, no. 4, pp. 279–285, Aug. 2002, doi: 10.1016/S0300-9440(02)00060-7.

[116] Q. JIANG *et al.*, "Electrochemical corrosion behavior of arc sprayed Al–Zn–Si–RE coatings on mild steel in 3.5 % NaCl solution," *Transactions of Nonferrous Metals Society of China*, vol. 24, no. 8, pp. 2713–2722, Aug. 2014, doi: 10.1016/S1003-6326(14)63402-6.

[117] A. Collazo, X. R. Nóvoa, C. Pérez, and B. Puga, "EIS study of the rust converter effectiveness under different conditions," *Electrochim Acta*, vol. 53, no. 25, pp. 7565–7574, Oct. 2008, doi: 10.1016/j.electacta.2007.11.078.

[118] N. B. Pilling and R. E. Bedworth, "The oxidation of metals at high temperature," *J. Inst. Met.*, vol. 29, pp. 529–582, 1923.

[119] J. R. Scully, "Polarization Resistance Method for Determination of Instantaneous Corrosion Rates," *CORROSION*, vol. 56, no. 2, pp. 199–218, Feb. 2000, doi: 10.5006/1.3280536.

[120] I. Frateur, C. Deslouis, M. E. Orazem, and B. Tribollet, "Modeling of the cast iron/drinking water system by electrochemical impedance spectroscopy," *Electrochim Acta*, vol. 44, no. 24, pp. 4345–4356, Jul. 1999, doi: 10.1016/S0013-4686(99)00150-4.

[121] A. Lasia, "Impedance of porous electrodes," *Journal of Electroanalytical Chemistry*, vol. 397, no. 1–2, pp. 27–33, Nov. 1995, doi: 10.1016/0022-0728(95)04177-5.

[122] R. de Levie, "On porous electrodes in electrolyte solutions," *Electrochim Acta*, vol. 8, no. 10, pp. 751–780, Oct. 1963, doi: 10.1016/0013-4686(63)80042-0.

[123] J. M. Hu, J. Q. Zhang, and C. N. Cao, "Determination of water uptake and diffusion of Cl— ion in epoxy primer on aluminum alloys in NaCl solution by electrochemical impedance spectroscopy," *Prog Org Coat*, vol. 46, no. 4, pp. 273–279, Jun. 2003, doi: 10.1016/S0300-9440(03)00010-9.

[124] I. Milošev, T. K. Mikić, and M. Gaberšček, "The effect of Cu-rich sub-layer on the increased corrosion resistance of Cu–xZn alloys in chloride containing borate buffer," *Electrochim Acta*, vol. 52, no. 2, pp. 415–426, Oct. 2006, doi: 10.1016/j.electacta.2006.05.024.

[125] T. Kosec, D. K. Merl, and I. Milošev, "Impedance and XPS study of benzotriazole films formed on copper, copper–zinc alloys and zinc in chloride solution," *Corros Sci*, vol. 50, no. 7, pp. 1987–1997, Jul. 2008, doi: 10.1016/j.corsci.2008.04.016.

[126] C. Montella, "Voigt circuit representation model for electrochemical impedances under finite-length diffusion conditions," *Journal of Electroanalytical Chemistry*, vol. 879, p. 114785, Dec. 2020, doi: 10.1016/j.jelechem.2020.114785.

[127] P. Leuaa, D. Priyadarshani, A. K. Tripathi, and M. Neergat, "Internal and External Transport of Redox Species across the Porous Thin-Film Electrode/Electrolyte Interface," *The Journal of Physical Chemistry C*, vol. 123, no. 35, pp. 21440–21447, Sep. 2019, doi: 10.1021/acs.jpcc.9b02795.

[128] M. Schönleber and E. Ivers-Tiffée, "Approximability of impedance spectra by RC elements and implications for impedance analysis," *Electrochem commun*, vol. 58, pp. 15–19, Sep. 2015, doi: 10.1016/j.elecom.2015.05.018.

[129] P. Agarwal, M. E. Orazem, and L. H. Garcia-Rubio, "Measurement Models for Electrochemical Impedance Spectroscopy: I. Demonstration of Applicability," *J Electrochem Soc*, vol. 139, no. 7, pp. 1917–1927, Jul. 1992, doi: 10.1149/1.2069522.

[130] Y.-K. Song and F. Mansfeld, "Evaluation of the corrosion resistance of different galvanized steels treated in a cerium salt solution," *Materials and Corrosion*, vol. 56, no. 4, pp. 229–236, Apr. 2005, doi: 10.1002/maco.200403830.

[131] D. D. Macdonald and M. Urquidi-Macdonald, "Theory of Steady-State Passive Films," *J Electrochem Soc*, vol. 137, no. 8, pp. 2395–2402, Aug. 1990, doi: 10.1149/1.2086949.

[132] R. G. Buchheit, M. Cunningham, H. Jensen, M. W. Kendig, and M. A. Martinez, "A Correlation Between Salt Spray and Electrochemical Impedance Spectroscopy Test Results for Conversion-Coated Aluminum Alloys," *CORROSION*, vol. 54, no. 1, pp. 61–72, Jan. 1998, doi: 10.5006/1.3284829.

[133] D. Peng, J. Wu, X. Yan, X. Du, Y. Yan, and X. Li, "The formation and corrosion behavior of a zirconium-based conversion coating on the aluminum alloy AA6061," *J Coat Technol Res*, vol. 13, no. 5, pp. 837–850, Sep. 2016, doi: 10.1007/s11998-016-9789-1.

[134] G. E. P. Box, W. G. Hunter, and S. J. Hunter, *Statistics for Experimenters: Design, Innovation, and Discovery*, vol. 559. New York: Wiley, 2005.

[135] R. Yang, P. Y. Xu, Y. Jing, and G. Xin, "Evaluating the anti-corrosion behavior of hybrid zirconium-polyethyleneimine layer by mean of electrochemical method," *J Phys Conf Ser*, vol. 1605, no. 1, p. 012159, Aug. 2020, doi: 10.1088/1742-6596/1605/1/012159.

[136] H. R. P. Cardoso, C. Rapacki, and J. Z. Ferreira, "Monitoring of a Zr-based conversion coating on galvanised steel and its performance against corrosion," *Corrosion Engineering, Science and Technology*, vol. 54, no. 8, pp. 726–730, Nov. 2019, doi: 10.1080/1478422X.2019.1657703.

[137] J. A. Grandle and S. R. Taylor, "Electrochemical Impedance Spectroscopy of Coated Aluminum Beverage Containers: Part 1 — Determination of an Optimal Parameter for Large Sample Evaluation," *CORROSION*, vol. 50, no. 10, pp. 792–803, Oct. 1994, doi: 10.5006/1.3293469.

[138] J. Konopka, "Examination of the Fluorine K Line and Iron L Line Overlap by EDS and WDS, Application Note 52455," Madison, WI, USA, 2013. [Online]. Available: www.thermoscientific.com

[139] J. I. Goldstein, D. E. Newbury, J. R. Michael, N. W. M. Ritchie, J. H. J. Scott, and D. C. Joy, *Scanning Electron Microscopy and X-Ray Microanalysis*. New York, NY: Springer New York, 2018. doi: 10.1007/978-1-4939-6676-9.

[140] R. K. Mishra, A. K. Zachariah, and S. Thomas, "Energy-Dispersive X-ray Spectroscopy Techniques for Nanomaterial," in *Microscopy Methods in Nanomaterials Characterization*, Elsevier, 2017, pp. 383–405. doi: 10.1016/B978-0-323-46141-2.00012-2.

[141] M. Pourbaix, *Atlas of Electrochemical Equilibria in Aqueous Solutions*, 2nd ed. Texas: National Association of Corrosion Engineers, 1974.

[142] Y. Zhai, Z. Zhao, G. S. Frankel, J. Zimmerman, T. Bryden, and W. Fristad, "A Replacement for Phosphate Conversion Coating Based on Hexafluorozirconic Acid," Apr. 2008. doi: 10.4271/2008-01-1158.

[143] H. Eivaz Mohammadloo, A. A. Sarabi, R. Mohammad Hosseini, M. Sarayloo, H. Sameie, and R. Salimi, "A comprehensive study of the green hexafluorozirconic acid-based conversion coating," *Prog Org Coat*, vol. 77, no. 2, pp. 322–330, 2014, doi: 10.1016/j.porgcoat.2013.10.006.

[144] P. Cao, X. Zhou, L. Ran, J. Tang, and J. Yang, "The 3D nano-trench interface to manipulate the stripping/plating behavior for stable Zn anode," *J Power Sources*, vol. 528, p. 231215, Apr. 2022, doi: 10.1016/j.jpowsour.2022.231215.

[145] S. Thomas, N. Birbilis, M. S. Venkatraman, and I. S. Cole, "Corrosion of Zinc as a Function of pH," *CORROSION*, vol. 68, no. 1, pp. 015009-1-015009–9, Jan. 2012, doi: 10.5006/1.3676630.

[146] C. G. da Silva, I. C. P. Margarit-Mattos, O. R. Mattos, H. Perrot, B. Tribollet, and V. Vivier, "The molybdate-zinc conversion process," *Corros Sci*, vol. 51, no. 1, pp. 151–158, Jan. 2009, doi: 10.1016/j.corsci.2008.10.019.

[147] A. Afseth, J. H. Nordlien, G. M. Scamans, and K. Nisancioglu, "Effect of heat treatment on electrochemical behaviour of aluminium alloy AA3005," *Corros Sci*, vol. 44, no. 1, pp. 145–162, Jan. 2002, doi: 10.1016/S0010-938X(01)00024-5.

[148] O. Engler, K. Kuhnke, and J. Hasenclever, "Development of intermetallic particles during solidification and homogenization of two AA 5xxx series Al-Mg alloys with different Mg contents," *J Alloys Compd*, vol. 728, pp. 669–681, Dec. 2017, doi: 10.1016/j.jallcom.2017.09.060.

[149] Z. Jin, C. Cai, Y. Yuan, D. Kang, J. Hunter, and X. Zhou, "The behaviour of AA5754 and AA5052 aluminium alloys in alkaline etching solution: Similarity and difference," *Mater Charact*, vol. 171, p. 110768, Jan. 2021, doi: 10.1016/j.matchar.2020.110768.

[150] Z. Jin *et al.*, "The behaviour of iron-containing intermetallic particles in aluminium alloys in alkaline solution," *Corros Sci*, vol. 179, p. 109134, Feb. 2021, doi: 10.1016/j.corsci.2020.109134.

[151] N. Birbilis and R. G. Buchheit, "Investigation and Discussion of Characteristics for Intermetallic Phases Common to Aluminum Alloys as a Function of Solution pH," *J Electrochem Soc*, vol. 155, no. 3, p. C117, 2008, doi: 10.1149/1.2829897.

[152] P. Campestrini, E. P. M. van Westing, H. W. van Rooijen, and J. H. W. de Wit, "Relation between microstructural aspects of AA2024 and its corrosion behaviour investigated using AFM scanning potential technique," *Corros Sci*, vol. 42, no. 11, pp. 1853–1861, Nov. 2000, doi: 10.1016/S0010-938X(00)00002-0.

[153] L. F. Mondolfo, *Aluminum Alloys: Structure and Properties*. Butterworths, 1976.

[154] I. Milošev, B. Kapun, and P. Rodič, "The Relation Between the Microstructure of Aluminum Alloy 7075-T6 and the Type of Cerium Salt in the Formation of the Cerium Conversion Layer," *J Electrochem Soc*, vol. 169, no. 9, p. 091501, Sep. 2022, doi: 10.1149/1945-7111/ac8d35.

[155] P. Campestrini, E. P. M. van Westing, and J. H. W. de Wit, "Influence of surface preparation on performance of chromate conversion coatings on Alclad 2024 aluminium alloy: Part I: Nucleation and growth," *Electrochim Acta*, vol. 46, no. 16, pp. 2553–2571, May 2001, doi: 10.1016/S0013-4686(01)00475-3.

[156] P. Campestrini, H. Terryn, J. Vereecken, and J. H. W. de Wit, "Chromate Conversion Coating on Aluminum Alloys: II: Effect of the Microstructure," *J Electrochem Soc*, vol. 151, no. 6, p. B359, 2004, doi: 10.1149/1.1736682.

[157] C. J. Brinker and G. W. Scherer, *Sol-Gel Science: The Physics and Chemistry of Sol-Gel Processing*, 1st ed. Boston: Academic Press, 1990.

[158] P. Campestrini, G. Goeminne, H. Terryn, J. Vereecken, and J. H. W. de Wit, "Chromate Conversion Coating on Aluminum Alloys: I. Formation Mechanism," *J Electrochem Soc*, vol. 151, no. 2, p. B59, 2004, doi: 10.1149/1.1637355.

[159] W. Zhang, B. Hurley, and R. G. Buchheit, "Characterization of Chromate Conversion Coating Formation and Breakdown Using Electrode Arrays," *J Electrochem Soc*, vol. 149, no. 8, p. B357, 2002, doi: 10.1149/1.1485774.

[160] S. Díaz, "ZnFe anomalous electrodeposition: stationaries and local pH measurements," *Electrochim Acta*, vol. 47, no. 25, pp. 4091–4100, Sep. 2002, doi: 10.1016/S0013-4686(02)00416-4.

[161] S. Thomas, I. S. Cole, M. Sridhar, and N. Birbilis, "Revisiting zinc passivation in alkaline solutions," *Electrochim Acta*, vol. 97, pp. 192–201, May 2013, doi: 10.1016/j.electacta.2013.03.008.

[162] M. S. Venkatraman, I. S. Cole, and B. Emmanuel, "Corrosion under a porous layer: A porous electrode model and its implications for self-repair," *Electrochim Acta*, vol. 56, no. 24, pp. 8192–8203, Oct. 2011, doi: 10.1016/j.electacta.2011.06.020.

[163] G. Cao and Y. Wang, *Nanostructures and Nanomaterials*, vol. 2. in World Scientific Series in Nanoscience and Nanotechnology, vol. 2. World Scientific, 2011. doi: 10.1142/7885.

[164] P. Campestrini, E. P. M. van Westing, and J. H. W. de Wit, "Influence of surface preparation on performance of chromate conversion coatings on Alclad 2024 aluminium alloy - Part I: Nucleation and growth," *Electrochim Acta*, vol. 46, no. 17, pp. 2631–2647, 2001, doi: 10.1016/S0013-4686(01)00476-5.

[165] V. Bonamigo Moreira, A. Puiggalí-Jou, E. Jiménez-Piqué, C. Alemán, A. Meneguzzi, and E. Armelin, "Green Nanocoatings Based on the Deposition of Zirconium Oxide: The Role of the Substrate," *Materials*, vol. 14, no. 4, p. 1043, Feb. 2021, doi: 10.3390/ma14041043.

[166] T. G. Harvey, "Cerium-based conversion coatings on aluminium alloys: a process review," *Corrosion Engineering, Science and Technology*, vol. 48, no. 4, pp. 248–269, Jun. 2013, doi: 10.1179/1743278213Y.0000000089.

[167] J. H. Osborne, "Observations on chromate conversion coatings from a sol–gel perspective," *Prog Org Coat*, vol. 41, no. 4, pp. 280–286, May 2001, doi: 10.1016/S0300-9440(01)00143-6.

[168] F. A. Cotton, S. L. S. C. S. M. Bochmann, C. A. Murillo, G. Wilkinson, R. N. Grimes, and M. Bochmann, *Advanced Inorganic Chemistry*, 6th ed. in A Wiley-Interscience Publication. Wiley, 1999.

[169] R. J. H. Clark, D. C. Bradley, and P. Thornton, "The Chemistry of Titanium, Zirconium and Hafnium," in *Comprehensive Inorganic Chemistry*, 1st ed., in Pergamon Texts in Inorganic Chemistry. , Pergamon Press, 1973, pp. 419–490.

[170] G. D. Considine, Ed., *Van Nostrand's Encyclopedia of Chemistry*, 5th ed. New Jersey: Wiley, 2005.

[171] J.-P. Jolivet, *Metal oxide nanostructures chemistry: synthesis from aqueous solutions*, 2nd ed. New York: Oxford University Press, 2019. doi: 10.1093/oso/9780190928117.001.0001.

[172] T. E. Macdermott, "The structural chemistry of zirconium compounds," *Coord Chem Rev*, vol. 11, no. 1, pp. 1–20, 1973, doi: https://doi.org/10.1016/S0010-8545(00)82017-2.

[173] N. Rao, M. N. Holerca, and V. Pophristic, "Computational Study of the Small Zr(IV) Polynuclear Species," *J Chem Theory Comput*, vol. 4, no. 1, pp. 145–155, Jan. 2008, doi: 10.1021/ct7001094.

[174] N. Ingri, W. Kakolowicz, L. G. Sillén, and B. Warnqvist, "High-speed computers as a supplement to graphical methods—V1Haltafall, a general program for calculating the composition of equilibrium mixtures," *Talanta*, vol. 14, no. 11, pp. 1261–1286, Nov. 1967, doi: 10.1016/0039-9140(67)80203-0.

[175] I. Puigdomènech, E. Colàs, M. Grivé, I. Campos, and D. García, "A tool to draw chemical equilibrium diagrams using SIT: Applications to geochemical systems and radionuclide solubility," *MRS Online Proceedings Library*, vol. 1665, no. 1, pp. 111–116, 2014, doi: 10.1557/opl.2014.635.

[176] I. Puigdomènech, "Spana." [Online]. Available: https://sites.google.com/site/chemdiagr/home/java-versions

[177] W. Hummel, "Ionic strength corrections and estimation of SIT ion interaction coefficients," Villigen, 2009.

[178] L. Gmachowski, "Fractal Aggregates and Polymer Coils: Dynamic Properties," in *Encyclopedia of Surface and Colloid Science*, 3rd ed., P. Somasundaran, Ed., CRC Press, 2015, pp. 2863–2872. doi: 10.1081/E-ESCS3-120012631.

[179] F. J. Mompeán and H. Wanner, "The OECD Nuclear Energy Agency Thermochemical Database Project," *Radiochim Acta*, vol. 91, no. 11, pp. 617–622, 2003, doi: doi:10.1524/ract.91.11.617.23468.

[180] OECD Nuclear Energy Agency, *Modelling in aquatic chemistry*. Paris: OECD Publications, 1997.

[181] I. Puigdomènech, "Spana." KTH Royal Institute of Technology, Stockholm, 2020.

[182] H. S. Yu, X. He, S. L. Li, and D. G. Truhlar, "MN15: A Kohn–Sham global-hybrid exchange–correlation density functional with broad accuracy for multi-reference and single-reference systems and noncovalent interactions," *Chem Sci*, vol. 7, no. 8, pp. 5032–5051, 2016, doi: 10.1039/C6SC00705H.

[183] M. J. Frisch *et al.*, "Gaussian 16 Revision A.03." Gaussian, Inc., Wallingford, 2016.

[184] F. Weigend and R. Ahlrichs, "Balanced basis sets of split valence, triple zeta valence and quadruple zeta valence quality for H to Rn: Design and assessment of accuracy," *Physical Chemistry Chemical Physics*, vol. 7, no. 18, pp. 3297–3305, 2005, doi: 10.1039/B508541A.

[185] A. Kokalj, "XCrySDen-a new program for displaying crystalline structures and electron densities," *J Mol Graph Model*, vol. 17, no. 3–4, pp. 176–179, 1999, doi: 10.1016/S1093-3263(99)00028-5.

[186] R. G. Bates and A. K. Vijh, *Determination of pH: theory and practice*, 2nd ed. New York: Wiley, 1973.

[187] K. F. Lim, "Negative pH Does Exist," *J Chem Educ*, vol. 83, no. 10, p. 1465, Oct. 2006, doi: 10.1021/ed083p1465.

[188] D. K. Kozlica and I. Milošev, "Technical Note: Does Cr6+ Really Exist? Difference Between Charge and Oxidation State and How to Record Them," *Corrosion*, vol. 77, no. 7, pp. 696–699, Apr. 2021, doi: 10.5006/3840.

[189] C. Walther, J. Rothe, M. Fuss, S. Büchner, S. Koltsov, and T. Bergmann, "Investigation of polynuclear Zr(IV) hydroxide complexes by nanoelectrospray mass-spectrometry combined with XAFS," *Analytical and Bioanalytical Chemistry*, vol. 388, no. 2. pp. 409–431, 2007. doi: 10.1007/s00216-007-1223-1.

[190] R. E. Connick and W. H. McVey, "The Aqueous Chemistry of Zirconium," *J Am Chem Soc*, vol. 71, no. 9, pp. 3182–3191, Sep. 1949, doi: 10.1021/ja01177a070.

[191] T. Sasaki, O. Nakaoka, R. Arakawa, T. Kobayashi, I. Takagi, and H. Moriyama, "Detection of polynuclear zirconium hydroxide species in aqueous solution by desktop ESI-MS," *Journal of Nuclear Science and Technology*, vol. 47, no. 12. pp. 1211–1218, 2010. doi: 10.3327/jnst.47.1211.

[192] A. Clearfield, "The mechanism of hydrolytic polymerization of zirconyl solutions," *J Mater Res*, vol. 5, no. 1, pp. 161–162, 1990, doi: DOI: 10.1557/JMR.1990.0161.

[193] R. E. Connick and W. H. Reas, "The Hydrolysis and Polymerization of Zirconium in Perchloric Acid Solution1," *J Am Chem Soc*, vol. 73, no. 3, pp. 1171–1176, Mar. 1951, doi: 10.1021/ja01147a087.

[194] T. Kobayashi, S. Nakajima, R. Motokawa, D. Matsumura, T. Saito, and T. Sasaki, "Structural Approach to Understanding the Solubility of Metal Hydroxides," *Langmuir*, vol. 35, no. 24, pp. 7995–8006, Jun. 2019, doi: 10.1021/acs.langmuir.9b01132.

[195] P. D. Southon, J. R. Bartlett, J. L. Woolfrey, and B. Ben-Nissan, "Formation and Characterization of an Aqueous Zirconium Hydroxide Colloid," *Chemistry of Materials*, vol. 14, no. 10, pp. 4313–4319, Oct. 2002, doi: 10.1021/cm0211913.

[196] N. Rao, M. N. Holerca, M. L. Klein, and V. Pophristic, "Computational study of the Zr 4+ tetranuclear polymer, [Zr 4(OH) 8(H 2O) 16] 8+," *Journal of Physical Chemistry A*, vol. 111, no. 45. pp. 11395–11399, 2007. doi: 10.1021/jp0734880.

[197] C. Ekberg, G. Källvenius, Y. Albinsson, and P. L. Brown, "Studies on the hydrolytic behavior of zirconium(IV)," *J Solution Chem*, vol. 33, no. 1, pp. 47–79, 2004, doi: 10.1023/B:JOSL.0000026645.41309.d3.

[198] D. A. Zyuzin, E. M. Moroz, A. S. Ivanova, and A. N. Shmakov, "Structure characteristics of disordered zirconium hydroxoxides," *Crystallography Reports*, vol. 48, no. 3, pp. 413–415, 2003, doi: 10.1134/1.1578124.

[199] A. Clearfield, G. P. D. Serrette, and A. H. Khazi-Syed, "Nature of hydrous zirconia and sulfated hydrous zirconia," *Catal Today*, vol. 20, no. 2, pp. 295–312, 1994, doi: https://doi.org/10.1016/0920-5861(94)80008-1.

[200] M. M. Kasprzak, A. Erxleben, and J. Ochocki, "Properties and applications of flavonoid metal complexes," *RSC Adv*, vol. 5, no. 57, pp. 45853–45877, 2015, doi: 10.1039/c5ra05069c.

[201] T. Sasaki, T. Kobayashi, I. Takagi, and H. Moriyama, "Hydrolysis Constant and Coordination Geometry of Zirconium(IV)," *J Nucl Sci Technol*, vol. 45, no. 8, pp. 735–739, Aug. 2008, doi: 10.1080/18811248.2008.9711474.

[202] T. Kobayashi, D. Bach, M. Altmaier, T. Sasaki, and H. Moriyama, "Effect of temperature on the solubility and solid phase stability of zirconium hydroxide," *Radiochim Acta*, vol. 101, no. 10, pp. 645–651, 2013, doi: 10.1524/ract.2013.2074.

[203] M. Altmaier, V. Neck, and T. Fanghänel, "Solubility of Zr(IV), Th(IV) and Pu(IV) hydrous oxides in CaCl2 solutions and the formation of ternary Ca-M(IV)-OH complexes," *Radiochim Acta*, vol. 96, no. 9–11, pp. 541–550, 2008, doi: doi:10.1524/ract.2008.1535.

[204] Y.-J. Hu, K. E. Knope, S. Skanthakumar, M. G. Kanatzidis, J. F. Mitchell, and L. Soderholm, "Understanding the Role of Aqueous Solution Speciation and Its Application to the Directed Syntheses of Complex Oxidic Zr Chlorides and Sulfates," *J Am Chem Soc*, vol. 135, no. 38, pp. 14240–14248, Sep. 2013, doi: 10.1021/ja405555h.

[205] C. Hagfeldt, V. Kessler, and I. Persson, "Structure of the hydrated, hydrolysed and solvated zirconium(iv) and hafnium(iv) ions in water and aprotic oxygen donor solvents. A crystallographic, EXAFS spectroscopic and large angle X-ray scattering study," *Dalton Transactions*, vol. 14, pp. 2142–2151, 2004, doi: 10.1039/B402804J.

[206] Section of Analytical Chemistry of the International Union of Pure and Applied Chemistry, *Solubility constants of metal oxides, metal hydroxides and metal hydroxide salts in aqueous solution*, vol. 6, no. 2. in Pure and Applied Chemistry, vol. 6. London: Butterworths, 1963. doi: doi:10.1351/pac196306020125.

[207] M. Pourbaix, *Atlas of Electrochemical Equilibria in Aqueous Solutions*, 2nd ed. Texas: National Association of Corrosion Engineers, 1974.

[208] H.-R. Cho *et al.*, "Combined LIBD and XAFS investigation of the formation and structure of Zr(IV) colloids," *Anal Bioanal Chem*, vol. 383, no. 1, p. 28, 2005, doi: 10.1007/s00216-005-3354-6.

[209] A. Clearfield, "Structural aspects of zirconium chemistry," *Rev. pure appl. Chem.*, vol. 14, p. 91, 1964.

[210] A. Clearfield and P. A. Vaughan, "The crystal structure of zirconyl chloride octahydrate and zirconyl bromide octahydrate," *Acta Crystallogr*, vol. 9, no. 7, pp. 555–558, Jul. 1956, doi: https://doi.org/10.1107/S0365110X56001558.

[211] G. M. Muha and P. A. Vaughan, "Structure of the Complex Ion in Aqueous Solutions of Zirconyl and Hafnyl Oxyhalides," *Journal of Chemical Physics*, vol. 33, pp. 194–199, 1960.

[212] M. J. D. Rushton, I. Ipatova, L. J. Evitts, W. E. Lee, and S. C. Middleburgh, "Stoichiometry deviation in amorphous zirconium dioxide," *RSC Adv*, vol. 9, no. 29, pp. 16320–16327, 2019, doi: 10.1039/C9RA01865D.

[213] D. Vanderbilt, X. Zhao, and D. Ceresoli, "Structural and dielectric properties of crystalline and amorphous ZrO2," *Thin Solid Films*, vol. 486, no. 1, pp. 125–128, 2005, doi: https://doi.org/10.1016/j.tsf.2004.11.232.

[214] M. Durandurdu, "Amorphous zirconia: ab initio molecular dynamics simulations," *Philosophical Magazine*, vol. 97, no. 16, pp. 1334–1345, Jun. 2017, doi: 10.1080/14786435.2017.1296201.

[215] M. Henry, J.-P. Jolivet, and J. Livage, "Aqueous chemistry of metal cations: Hydrolysis, condensation and complexation," in *Chemistry, Spectroscopy and Applications of Sol-Gel Glasses. Structure and Bonding, vol. 77.*, 1st ed., R. Reisfeld and C. K. JJørgensen, Eds., Berlin: Springer Berlin, Heidelberg, 1992, pp. 153–206. doi: 10.1007/BFb0036968.

[216] J. Livage, K. Doi, and C. Mazieres, "Nature and Thermal Evolution of Amorphous Hydrated Zirconium Oxide," *Journal of the American Ceramic Society*, vol. 51, no. 6, pp. 349–353, Jun. 1968, doi: https://doi.org/10.1111/j.1151-2916.1968.tb15952.x.

[217] A. S. Solovkin and Z. N. Tsvetkova, "The chemistry of aqueous solutions of zirconium salts (Does the zirconyl ion exist?)," *Russian Chemical Reviews*, vol. 31, no. 11, p. 655, 1962, doi: 10.1070/RC1962v031n11ABEH001326.

[218] P. D. Deck and D. W. Reichgott, "Characterization of chromium-free no-rinse prepaint coatings on aluminum and galvanized steel," *Metal Finishing*, vol. 90, no. 9. pp. 29–35, 1992.

[219] N. W. Khun and G. S. Frankel, "Effect of Hexafluorozirconic Acid Pretreatment on Cathodic Delamination of Epoxy Coatings from Steel Substrates," *Corrosion*, vol. 71, pp. 277–284, 2015.

[220] R. Mohammad Hosseini, A. A. Sarabi, H. Eivaz Mohammadloo, and M. Sarayloo, "The performance improvement of Zr conversion coating through Mn incorporation: With and without organic coating," *Surf Coat Technol*, vol. 258, pp. 437–446, 2014, doi: 10.1016/j.surfcoat.2014.08.056.

[221] R. G. Pearson, "Hard and Soft Acids and Bases," *J Am Chem Soc*, vol. 85, no. 22, pp. 3533–3539, Nov. 1963, doi: 10.1021/ja00905a001.

[222] A. K. Babko, "The relationship between the stability of fluorocomplexes and the position of the central atom in the periodic system," *Russ. J. Inorg. Chem.*, vol. 4, pp. 485–486, 1959.

[223] G. Goldstein, "Equilibrium Distribution of Metal-Fluoride Complexes," *Anal Chem*, vol. 36, pp. 243–244, 1964.

[224] R. M. Sawant, U. K. Thakur, and K. L. Ramakumar, "Potentiometric Investigation of Fluoride Complexes of Zirconium(IV) and Hafnium(IV) in 1 M (H,Na)ClO4 Medium Using a Fluoride Ion Selective Electrode," *J Solution Chem*, vol. 34, no. 2, pp. 113–135, 2005, doi: 10.1007/s10953-005-2693-4.

[225] C. E. Tomlinson, "Conversion coatings for metal surfaces," US5380374A, Jan. 10, 1995

[226] B. Dunham, "Zirconium pretreatments: Not just for early adopters anymore," *Metal Finishing*, vol. 110, no. 6. pp. 18–21, 2012. doi: 10.1016/S0026-0576(13)70215-0.

[227] S. Verdier, N. van der Laak, F. Dalard, J. Metson, and S. Delalande, "An electrochemical and SEM study of the mechanism of formation, morphology, and composition of titanium or zirconium fluoride-based coatings," *Surf Coat Technol*, vol. 200, no. 9, pp. 2955–2964, 2006, doi: https://doi.org/10.1016/j.surfcoat.2004.10.139.

[228] I. Milošev and G. S. Frankel, "Review—Conversion Coatings Based on Zirconium and/or Titanium," *J Electrochem Soc*, vol. 165, no. 3, pp. C127–C144, Feb. 2018, doi: 10.1149/2.0371803jes.

[229] Y. Guan, J.-G. G. Liu, and C.-W. wei Yan, "Novel Ti/Zr Based Non-Chromium Chemical Conversion Coating for the Corrosion Protection of Electrogalvanized Steel," *Int J Electrochem Sci*, vol. 6, no. 10, pp. 4853–4867, Oct. 2011.

[230] H. Eivaz Mohammadloo, A. A. Sarabi, R. Mohammad Hosseini, M. Sarayloo, H. Sameie, and R. Salimi, "A comprehensive study of the green hexafluorozirconic acid-based conversion coating," *Prog Org Coat*, vol. 77, no. 2, pp. 322–330, 2014, doi: 10.1016/j.porgcoat.2013.10.006.

[231] H. Eivaz Mohammadloo and A. A. Sarabi, "Titanium composite conversion coating formation on CRS In the presence of Mo and Ni ions: Electrochemical and microstructure characterizations," *Appl Surf Sci*, vol. 387, pp. 252–259, Nov. 2016, doi: 10.1016/j.apsusc.2016.06.095.

[232] L. Zhu, F. Yang, and N. Ding, "Corrosion resistance of the electro-galvanized steel treated in a titanium conversion solution," *Surf Coat Technol*, vol. 201, no. 18, pp. 7829–7834, 2007, doi: 10.1016/j.surfcoat.2007.03.024.

[233] L. Kolditz and A. Feltz, "Über fluorhaltige Komplexe. I Die Papierchromatographie und -elektrophorese der Fluorozirkonate," *Z Anorg Allg Chem*, vol. 310, no. 4–6, pp. 195–203, Jul. 1961, doi: https://doi.org/10.1002/zaac.19613100403.

[234] M. A. Fedotov and A. V Belyaev, "A study of the hydrolysis of ZrF62−and the structure of intermediate hydrolysis products by 19F and 91Zr NMR in the 9.4 T field," *Journal of Structural Chemistry*, vol. 52, no. 1, pp. 69–74, 2011, doi: 10.1134/S0022476611010094.

[235] V. P. Tolstoi and B. Altangerel, "Hydrolysis of ZrF62−anions in solutions of copper(II) ammine and synthesis of CuxZr(OH)yFz nanolayers by the ionic layering method," *Russ J Gen Chem*, vol. 76, no. 11, pp. 1716–1718, 2006, doi: 10.1134/S1070363206110065.

[236] J. E. Huheey, E. A. Keiter, R. L. Keiter, and O. K. Medhi, *Inorganic Chemistry: Principles of Structure and Reactivity*, 4th ed. Pearson Education, 2000.

[237] C. J. Brinker and G. W. Scherer, *Sol-Gel Science: The Physics and Chemistry of Sol-Gel Processing*, 1st ed. Boston: Academic Press, 1990.

[238] N. M. Laptash, E. V Kovaleva, A. A. Mashkovskii, A. Yu. Beloliptsev, and L. A. Zemnukhova, "Hydrolysis of antimony(III) fluoride complexes," *Journal of Structural Chemistry*, vol. 48, no. 5, pp. 848–854, 2007, doi: 10.1007/s10947-007-0126-5.

[239] C. E. Roberson and R. B. Barnes, "Stability of fluoride complex with silica and its distribution in natural water systems," *Chem Geol*, vol. 21, no. 3, pp. 239–256, 1978, doi: https://doi.org/10.1016/0009-2541(78)90047-5.

[240] C. E. Tomlinson, "Conversion coatings for metals using group IV-A metals in the presence of little or no fluoride and little or no chromium," US5952049A, Sep. 14, 1999 [Online]. Available: https://patents.google.com/patent/US5952049A/en

[241] C. F. Baes and R. E. Mesmer, *The Hydrolysis of Cations*. New York: John Wiley & Sons, 1977.

[242] A. Clearfield, "Structural aspects of zirconium chemistry," *Rev. pure appl. Chem.*, vol. 14, p. 91, 1964.

[243] N. V. Nikolenko, V. G. Vereshchak, A. D. Grabchuk, and O. S. Ostrovskaya Dnepropetrovsk, "Olation and oxolation kinetics of zirconium(4) hydroxide; Kinetika olyatsii i oksolyatsii gidroksida tsirkoniya," *Zhurnal Fizicheskoj Khimii*, vol. 69, no. 5, pp. 822–826, 1995.

[244] S. K. Tiwari, M. Tripathi, and R. Singh, "Electrochemical behavior of zirconia based coatings on mild steel prepared by sol–gel method," *Corros Sci*, vol. 63, pp. 334–341, 2012, doi: https://doi.org/10.1016/j.corsci.2012.06.026.

[245] I. Milošev, B. Kapun, P. Rodič, and J. Iskra, "Hybrid sol–gel coating agents based on zirconium(IV) propoxide and epoxysilane," *J Solgel Sci Technol*, vol. 74, no. 2, pp. 447–459, 2015, doi: 10.1007/s10971-015-3620-9.

[246] X. F. Yang, D. E. Tallman, V. J. Gelling, G. P. Bierwagen, L. S. Kasten, and J. Berg, "Use of a sol–gel conversion coating for aluminum corrosion protection," *Surf Coat Technol*, vol. 140, no. 1, pp. 44–50, 2001, doi: https://doi.org/10.1016/S0257-8972(01)01002-7.

[247] P. Rodič, S. Zanna, I. Milošev, and P. Marcus, "Degradation of Sol-Gel Acrylic Coatings Based on Si and Zr Investigated Using Electrochemical Impedance, Infrared and X-Ray Photoelectron Spectroscopies," *Front Mater*, vol. 8, p. 756447, Nov. 2021, doi: 10.3389/fmats.2021.756447.

[248] Yu. A. Bushlaev, Yu. E. Gorbunova, and M. P. Gustyakova, "The oxyfluorides of zirconium and hafnium," *Bulletin of the Academy of Sciences of the USSR, Division of chemical science*, vol. 11, no. 2, pp. 177–183, 1962, doi: 10.1007/BF00908014.

[249] L. Kolditz and A. Feltz, "Über fluorhaltige Komplexe. II. Über die Hydrolyse von Fluorozirkonaten und die Kondensation der Hydrolysenprodukte," *Z Anorg Allg Chem*, vol. 310, pp. 204–216, 1961.

[250] L. Kolditz and A. Feltz, "Über fluorhaltige Komplexe. III. Über Zirkontetrafluoridhydrate, Zirkonhydroxofluoride und ihre Kondensationsprodukte," *Z Anorg Allg Chem*, vol. 310, no. 4–6, pp. 217–224, Jul. 1961, doi: https://doi.org/10.1002/zaac.19613100405.

[251] P. Campestrini, G. Goeminne, H. Terryn, J. Vereecken, and J. H. W. de Wit, "Chromate Conversion Coating on Aluminum Alloys," *J Electrochem Soc*, vol. 151, no. 2, p. B59, 2004, doi: 10.1149/1.1637355.

[252] H. Eivaz Mohammadloo, A. A. Sarabi, A. A. Sabbagh Alvani, H. Sameie, and R. Salimi, "Nano-ceramic hexafluorozirconic acid based conversion thin film: Surface characterization and electrochemical study," *Surf Coat Technol*, vol. 206, no. 19–20, pp. 4132–4139, 2012, doi: 10.1016/j.surfcoat.2012.04.009.

[253] T. Lostak *et al.*, "Formation and characterization of Fe3+-/Cu2+-modified zirconium oxide conversion layers on zinc alloy coated steel sheets," *Electrochim Acta*, vol. 112, pp. 14–23, 2013, doi: https://doi.org/10.1016/j.electacta.2013.08.161.

[254] P. Campestrini, E. P. M. van Westing, and J. H. W. de Wit, "Influence of surface preparation on performance of chromate conversion coatings on Alclad 2024 aluminium alloy - Part I: Nucleation and growth," *Electrochim Acta*, vol. 46, no. 17, pp. 2631–2647, 2001, doi: 10.1016/S0013-4686(01)00476-5.

[255] N. V. Mandich, "Chemistry and Theory of Chromium Deposition. Part 1. Chemistry," *Plating and Surface Finishing*, vol. 84, no. 5, pp. 108–115, 1997.

[256] W. Zhang, B. Hurley, and R. G. Buchheit, "Characterization of Chromate Conversion Coating Formation and Breakdown Using Electrode Arrays," *J Electrochem Soc*, vol. 149, no. 8, p. B357, 2002, doi: 10.1149/1.1485774.

[257] C. E. Tomlinson, "Conversion coatings for metals using group IV-A metals in the presence of little or no fluoride and little or no chromium," US5952049A, Sep. 14, 1999

[258] E. Ramanathan and S. Balasubramanian, "Comparative study on polyester epoxy powder coat and amide cured epoxy liquid paint over nano-zirconia treated mild steel," *Prog Org Coat*, vol. 93, pp. 68–76, 2016, doi: https://doi.org/10.1016/j.porgcoat.2016.01.007.

[259] M. Matsukawa, K. Makino, and T. Shimakura, "Chemical conversion coating agent and surface-treated metal," US20040187967A1, 2004

[260] S. Le Manchet, D. Verchère, and J. Landoulsi, "Effects of organic and inorganic treatment agents on the formation of conversion layer on hot-dip galvanized steel: An X-ray photoelectron spectroscopy study," *Thin Solid Films*, vol. 520, no. 6, pp. 2009–2016, Jan. 2012, doi: 10.1016/j.tsf.2011.09.064.

[261] H. Ohtaki and T. Radnai, "Structure and dynamics of hydrated ions," *Chem Rev*, vol. 93, pp. 1157–1204, 1993.

[262] A. Gossard, G. Toquer, S. Grandjean, and A. Grandjean, "Coupling between SAXS and Raman spectroscopy applied to the gelation of colloidal zirconium oxy-hydroxide systems," *J Solgel Sci Technol*, vol. 71, no. 3, pp. 571–579, 2014, doi: 10.1007/s10971-014-3409-2.

[263] M. Savastano, C. Bazzicalupi, G. Ferraro, E. Fratini, P. Gratteri, and A. Bianchi, "Tales of the Unexpected: The Case of Zirconium(IV) Complexes with Desferrioxamine," *Molecules*, vol. 24, no. 11, p. 2098, Jun. 2019, doi: 10.3390/molecules24112098.

[264] P. D. Southon, J. R. Bartlett, J. L. Woolfrey, and B. Ben-Nissan, "Formation and Characterization of an Aqueous Zirconium Hydroxide Colloid," *Chemistry of Materials*, vol. 14, no. 10, pp. 4313–4319, Oct. 2002, doi: 10.1021/cm0211913.

[265] N. Rao, M. N. Holerca, and V. Pophristic, "Computational Study of the Small Zr(IV) Polynuclear Species," *J Chem Theory Comput*, vol. 4, no. 1, pp. 145–155, Jan. 2008, doi: 10.1021/ct7001094.

[266] C. Hagfeldt, V. Kessler, and I. Persson, "Structure of the hydrated, hydrolysed and solvated zirconium(iv) and hafnium(iv) ions in water and aprotic oxygen donor solvents. A crystallographic, EXAFS spectroscopic and large angle X-ray scattering study," *Dalton Transactions*, vol. 14, pp. 2142–2151, 2004, doi: 10.1039/B402804J.

[267] C. Walther, J. Rothe, M. Fuss, S. Büchner, S. Koltsov, and T. Bergmann, "Investigation of polynuclear Zr(IV) hydroxide complexes by nanoelectrospray mass-spectrometry combined with XAFS," *Analytical and Bioanalytical Chemistry*, vol. 388, no. 2. pp. 409–431, 2007. doi: 10.1007/s00216-007-1223-1.

[268] H.-R. Cho *et al.*, "Combined LIBD and XAFS investigation of the formation and structure of Zr(IV) colloids," *Anal Bioanal Chem*, vol. 383, no. 1, p. 28, 2005, doi: 10.1007/s00216-005-3354-6.

[269] N. Rao, M. N. Holerca, M. L. Klein, and V. Pophristic, "Computational study of the Zr 4+ tetranuclear polymer, [Zr 4(OH) 8(H 2O) 16] 8+," *Journal of Physical Chemistry A*, vol. 111, no. 45. pp. 11395–11399, 2007. doi: 10.1021/jp0734880.

[270] A. Gossard, G. Toquer, S. Grandjean, and A. Grandjean, "Coupling between SAXS and Raman spectroscopy applied to the gelation of colloidal zirconium oxy-hydroxide systems," *J Solgel Sci Technol*, vol. 71, no. 3, pp. 571–579, 2014, doi: 10.1007/s10971-014-3409-2.

[271] M. Ely, J. Światowska, A. Seyeux, S. Zanna, and P. Marcus, "Role of Post-Treatment in Improved Corrosion Behavior of Trivalent Chromium Protection (TCP) Coating Deposited on Aluminum Alloy 2024-T3," *J Electrochem Soc*, vol. 164, no. 6, pp. C276–C284, Mar. 2017, doi: 10.1149/2.0431706jes.

[272] C. Trinidad *et al.*, "Effect of surface preparation treatments on copper enrichment on 2024 aluminium alloy surface," *Appl Surf Sci*, vol. 560, p. 149991, Sep. 2021, doi: 10.1016/j.apsusc.2021.149991.

[273] R. Viroulaud, J. Światowska, A. Seyeux, S. Zanna, J. Tardelli, and P. Marcus, "Influence of surface pretreatments on the quality of trivalent chromium process coatings on aluminum alloy," *Appl Surf Sci*, vol. 423, pp. 927–938, Nov. 2017, doi: 10.1016/j.apsusc.2017.06.246.

[274] A. Benninghoven, E. Niehuis, D. Greifendorf, D. van Leyen, and W. Lange, "Analytical Application of a High Performance TOF-SIMS," 1986, pp. 497–499. doi: 10.1007/978-3-642-82724-2_131.

[275] K. Wien, "TOF-SIMS analysis of polymers," *Nucl Instrum Methods Phys Res B*, vol. 131, no. 1–4, pp. 38–54, Aug. 1997, doi: 10.1016/S0168-583X(97)00147-X.

[276] V. Cristaudo *et al.*, "A combined XPS/ToF-SIMS approach for the 3D compositional characterization of Zr-based conversion of galvanized steel," *Appl Surf Sci*, vol. 562, p. 150166, Oct. 2021, doi: 10.1016/j.apsusc.2021.150166.

[277] S. Verdier, S. Delalande, N. van der Laak, J. Metson, and F. Dalard, "Monochromatized x-ray photoelectron spectroscopy of the AM60 magnesium alloy surface after treatments in fluoride-based Ti and Zr solutions," *Surface and Interface Analysis*, vol. 37, no. 5, pp. 509–516, May 2005, doi: 10.1002/sia.2042.

[278] H.-H. Strehblow, B. Titze, and B. P. Loechel, "The breakdown of passivity of iron and nickel by fluoride," *Corros Sci*, vol. 19, no. 7, pp. 1047–1057, Jan. 1979, doi: 10.1016/S0010-938X(79)80094-3.

[279] H.-H. Strehblow, "Mechanisms of Pitting Corrosion," in *Corrosion Mechanisms in Theory and Practice*, 2nd ed., P. Marcus, Ed., Boca Raton: CRC Press, 2002, p. 44.

[280] B. Löchel and H.-H. Strehblow, "Breakdown of passivity of iron by fluoride," *Electrochim Acta*, vol. 28, no. 4, pp. 565–571, Apr. 1983, doi: 10.1016/0013-4686(83)85043-9.

[281] K. E. Heusler and L. Fischer, "Kinetics of Pit Initiation at Passive Iron," *Materials and Corrosion*, vol. 27, no. 8, pp. 551–556, Aug. 1976, doi: 10.1002/maco.19760270802.

[282] K. F. Lorking and J. E. O. Mayne, "The corrosion of aluminium in solutions of sodium fluoride and sodium chloride," *British Corrosion Journal*, vol. 1, no. 5, pp. 181–182, Mar. 1966, doi: 10.1179/000705966798327795.

[283] A. F. Beck, M. A. Heine, D. S. Keir, D. van Rooyen, and M. J. Pryor, "Further studies of the electrical characteristics of oxide films on aluminium," *Corros Sci*, vol. 2, no. 2, pp. 133–145, Jan. 1962, doi: 10.1016/0010-938X(62)90005-7.

[284] T. Xue, W. C. Cooper, R. Pascual, and S. Saimoto, "Effect of fluoride ions on the corrosion of aluminium in sulphuric acid and zinc electrolyte," *J Appl Electrochem*, vol. 21, no. 3, pp. 238–246, Mar. 1991, doi: 10.1007/BF01052577.

[285] M. F. Abd Rabbo, J. A. Richardson, and G. C. Wood, "A study of conversion coating development on aluminium in chromate/fluoride solutions using secondary ion mass spectrometry," *Corros Sci*, vol. 18, no. 2, pp. 117–123, Jan. 1978, doi: 10.1016/S0010-938X(78)80082-1.

[286] P. M. Natishan and W. E. O'Grady, "Chloride Ion Interactions with Oxide-Covered Aluminum Leading to Pitting Corrosion: A Review," *J Electrochem Soc*, vol. 161, no. 9, pp. C421–C432, Jun. 2014, doi: 10.1149/2.1011409jes.

[287] J. A. Richardson and G. C. Wood, "The Interpretation of Impedance Changes on Oxide-Coated Aluminum Produced by Immersion in Inhibitive and Corrosive Aqueous Media," *J Electrochem Soc*, vol. 120, no. 2, p. 193, 1973, doi: 10.1149/1.2403419.

[288] W. M. Carroll, M. Murphy, and C. B. Breslin, "The corrosion/dissolution behaviour of aluminium in solutions containing both chloride and fluoride ions," *Corros Sci*, vol. 34, no. 9, pp. 1495–1507, Sep. 1993, doi: 10.1016/0010-938X(93)90244-B.

[289] P. Guo *et al.*, "Direct observation of pitting corrosion evolutions on carbon steel surfaces at the nano-to-micro- scales," *Sci Rep*, vol. 8, no. 1, p. 7990, May 2018, doi: 10.1038/s41598-018-26340-5.

[290] J. L. Trompette, L. Arurault, S. Fontorbes, and L. Massot, "Influence of the anion specificity on the electrochemical corrosion of anodized aluminum substrates," *Electrochim Acta*, vol. 55, no. 8, pp. 2901–2910, Mar. 2010, doi: 10.1016/j.electacta.2009.12.063.

[291] J. L. Trompette, "Implications of the kosmotrope/chaotrope nature of the anions on the breakdown of passivity of iron by halides," *Corros Sci*, vol. 82, pp. 108–114, May 2014, doi: 10.1016/j.corsci.2014.01.005.

[292] S. Verdier, N. van der Laak, F. Dalard, J. Metson, and S. Delalande, "An electrochemical and SEM study of the mechanism of formation, morphology, and composition of titanium or zirconium fluoride-based coatings," *Surf Coat Technol*, vol. 200, no. 9, pp. 2955–2964, Feb. 2006, doi: 10.1016/j.surfcoat.2004.10.139.

[293] T. Rodney, "Fluorinated acid compounds, compositions and methods of use," WO2018104796A1, Jun. 14, 2017

[294] B. Szczygieł, J. Winiarski, and W. Tylus, "Effect of deposition time on morphology, corrosion resistance and mechanical properties of Ti-containing conversion coatings on zinc," *Mater Chem Phys*, vol. 129, no. 3, pp. 1126–1131, Oct. 2011, doi: 10.1016/j.matchemphys.2011.05.074.

[295] Y.-T. Tsai, K.-H. Hou, C.-Y. Bai, J.-L. Lee, and M.-D. Ger, "The influence on immersion time of titanium conversion coatings on electrogalvanized steel," *Thin Solid Films*, vol. 518, no. 24, pp. 7541–7544, Oct. 2010, doi: 10.1016/j.tsf.2010.05.042.

[296] L. Zhu, F. Yang, and N. Ding, "Corrosion resistance of the electro-galvanized steel treated in a titanium conversion solution," *Surf Coat Technol*, vol. 201, no. 18, pp. 7829–7834, Jun. 2007, doi: 10.1016/j.surfcoat.2007.03.024.

[297] H. Eivaz Mohammadloo and A. A. Sarabi, "Titanium composite conversion coating formation on CRS In the presence of Mo and Ni ions: Electrochemical and microstructure characterizations," *Appl Surf Sci*, vol. 387, pp. 252–259, Nov. 2016, doi: 10.1016/j.apsusc.2016.06.095.

[298] J. E. Huheey, E. A. Keiter, R. L. Keiter, and O. K. Medhi, *Inorganic Chemistry: Principles of Structure and Reactivity*, 4th ed. New York: HarperCollins College Publishers, 1993.

[299] MAVOM Chemie BV, "Safety Data Sheet for MAVOMcoat 160." MAVOM Chemie BV, Jun. 23, 2015.

[300] MAVOM Chemie BV, "Safety Data Sheet for MAVOMcoat 1700." MAVOM Chemie BV, Nov. 17, 2017.

[301] Henkel Corporation, "Safety Data Sheet for BONDERITE M-NT 1." Sep. 2018.

[302] Henkel Corporation, "Technical Data Sheet for BONDERITE M-NT 1." Henkel Corporation, Aug. 2016.

[303] SurTec International GmbH, "Safety Data Sheet for SurTec® 650 chromitAL TCP." SurTec International GmbH, Mar. 27, 2021.

[304] SurTec International GmbH, "Technical Data Sheet for SurTec® 650 chromitAL TCP." SurTec International GmbH, Mar. 27, 2021.

[305] Ralph. H. Petrucci, W. S. Harwood, and F. G. Herring, *General Chemistry: Principles and Modern Applications*, 8th ed. New Jersey: Prentice Hall, 2002.

[306] B. Beverskog and I. Puigdomenech, "Revised pourbaix diagrams for iron at 25–300 °C," *Corros Sci*, vol. 38, no. 12, pp. 2121–2135, Dec. 1996, doi: 10.1016/S0010-938X(96)00067-4.

[307] B. Beverskog and I. Puigdomenech, "Revised pourbaix diagrams for zinc at 25–300 °C," *Corros Sci*, vol. 39, no. 1, pp. 107–114, Jan. 1997, doi: 10.1016/S0010-938X(97)89246-3.

[308] Nuclear Energy Agency (NEA), *Chemical Thermodynamics of Iron, Part 1*, vol. 13a. Paris: OECD Publishing, 2013.

[309] Lemire R. J., U. Berner, C. Musikas, D. A. Palmer, P. Taylor, and O. Tochiyama, *Chemical Thermodynamics of Iron. Part 2*, vol. 13b. Paris: OECD Publishing, 2020.

[310] R. M. Smith and A. E. Martell, "NIST Critically Selected Stability Constants of Metal Complexes Database." National Institute of Standards and Technology, Gaithersburg, MD, 2004.

[311] D. K. Nordstrom and H. M. May, "Aqueous Equilibrium Data for Mononuclear Aluminum Species," in *The Environmental Chemistry of Aluminum*, G. Sposito, Ed., Boca Raton, Florida: CRC Press, 1996, pp. 39–80. doi: 10.1201/9780138736781-2.

[312] P. Bénézeth, D. A. Palmer, and D. J. Wesolowski, "Aqueous high-temperature solubility studies. II. The solubility of boehmite at 0.03 m ionic strength as a function of

temperature and pH as determined by in situ measurements," *Geochim Cosmochim Acta*, vol. 65, no. 13, pp. 2097–2111, Jul. 2001, doi: 10.1016/S0016-7037(01)00585-3.

[313] Y. Zhang and M. Muhammed, "Critical evaluation of thermodynamics of complex formation of metal ions in aqueous solutions," *Hydrometallurgy*, vol. 60, no. 3, pp. 215–236, May 2001, doi: 10.1016/S0304-386X(01)00148-7.

[314] F. J. Mompeán and H. Wanner, "The OECD Nuclear Energy Agency Thermochemical Database Project," *Radiochim Acta*, vol. 91, no. 11, pp. 617–622, Nov. 2003, doi: 10.1524/ract.91.11.617.23468.

[315] W. Hummel, "Ionic strength corrections and estimation of SIT ion interaction coefficients," Villigen, 2009.

[316] Henkel Corporation, "Metal Pre-treatment Paves the Way for Greater Sustainability in Automotive Industry." Accessed: Mar. 02, 2024. [Online]. Available: https://www.henkel-northamerica.com/spotlight/2022-13-12-metal-pre-treatment-paves-the-way-for-greater-sustainability-in-automotive-industry-1788088

[317] C. Vargel, "Galvanic Corrosion," in *Corrosion of Aluminium*, Elsevier, 2004, pp. 149–164. doi: 10.1016/B978-008044495-6/50013-6.

[318] B. MacDougall, J. Bardwell, and M. J. Graham, "A Comparison of the passivation of Fe and Ni in borate and sulfate solution," in *Proceedings of an international symposium honoring Doctor Norman Hackerman on his seventy-fifth birthday*, E. MacCafferty and R. J. Broad, Eds., Pennington, NJ: The Electrochemical Society, 1986, pp. 254–266.

[319] R. G. Pearson, "Hard and Soft Acids and Bases," *J Am Chem Soc*, vol. 85, no. 22, pp. 3533–3539, Nov. 1963, doi: 10.1021/ja00905a001.

[320] J. A. Paula, D. Majuste, N. H. J. Freire, E. M. Mazzer, V. F. C. Lins, and V. S. T. Ciminelli, "Effect of fluoride complexation by aluminium ions on the corrosion behaviour of aluminium cathodes used in zinc electrowinning," *Journal of Materials Research and Technology*, vol. 22, pp. 2062–2077, Jan. 2023, doi: 10.1016/j.jmrt.2022.12.037.

[321] T. H. Nguyen and R. T. Foley, "On the Mechanism of Pitting of Aluminum," *J Electrochem Soc*, vol. 126, no. 11, pp. 1855–1860, Nov. 1979, doi: 10.1149/1.2128815.

[322] V. P. Tolstoi and B. Altangerel, "Hydrolysis of ZrF62—anions in solutions of copper(II) ammine and synthesis of CuxZr(OH)yFz nanolayers by the ionic layering method," *Russ J Gen Chem*, vol. 76, no. 11, pp. 1716–1718, 2006, doi: 10.1134/S1070363206110065.

[323] G. M. Muha and P. A. Vaughan, "Structure of the Complex Ion in Aqueous Solutions of Zirconyl and Hafnyl Oxyhalides," *J Chem Phys*, vol. 33, no. 1, pp. 194–199, Jul. 1960, doi: 10.1063/1.1731077.

[324] M. G. Taryba, M. F. Montemor, and S. V. Lamaka, "Quasi-simultaneous Mapping of Local Current Density, pH and Dissolved O_2," *Electroanalysis*, vol. 27, no. 12, pp. 2725–2730, Dec. 2015, doi: 10.1002/elan.201500286.

[325] E. McCafferty, *Introduction to Corrosion Science*. New York, NY: Springer New York, 2010. doi: 10.1007/978-1-4419-0455-3.

[326] C. Wang *et al.*, "Local pH and oxygen concentration at the interface of Zn alloys in Tris-HCl or HEPES buffered Hanks' balanced salt solution," *Corros Sci*, vol. 197, p. 110061, Apr. 2022, doi: 10.1016/j.corsci.2021.110061.

[327] C. Tonna, C. Wang, D. Mei, S. V. Lamaka, M. L. Zheludkevich, and J. Buhagiar, "Biodegradation behaviour of Fe-based alloys in Hanks' Balanced Salt Solutions: Part I.

material characterisation and corrosion testing," *Bioact Mater*, vol. 7, pp. 426–440, Jan. 2022, doi: 10.1016/j.bioactmat.2021.05.048.

[328] C. Wang, C. Tonna, D. Mei, J. Buhagiar, M. L. Zheludkevich, and S. V. Lamaka, "Biodegradation behaviour of Fe-based alloys in Hanks' Balanced Salt Solutions: Part II. The evolution of local pH and dissolved oxygen concentration at metal interface," *Bioact Mater*, vol. 7, pp. 412–425, Jan. 2022, doi: 10.1016/j.bioactmat.2021.05.014.

[329] P.-E. Tegehall, "The mechanism of chemical activation with titanium phosphate colloids in the formation of zinc phosphate conversion coatings," *Colloids and Surfaces*, vol. 49, pp. 373–383, 1990, doi: 10.1016/0166-6622(90)80118-N.

[330] N. Takaomi, Y. Nagashima, and K. Shimoda, "Conditioning metal surfaces prior to phosphate conversion coating," EP0977908A1, Feb. 09, 2000 [Online]. Available: https://patents.google.com/patent/EP0977908A1/en

[331] B. P. Nikol'skii, V. I. Andreev, R. I. Lyubtsev, and M. S. Polyakov, "O vzaimodejstvii tsirkoniya s polikremnevymi kislotami v vodnykh rastvorakh," *Radiokhimiya*, vol. 16, no. 1, pp. 92–99, 1974, [Online]. Available: http://inis.iaea.org/search/search.aspx?orig_q=RN:05126726

[332] T. Uchiyama, E. Isoyama, H. Takenaka, and M. Kaji, "Surface treatment process for imparting hydrophilic properties to aluminum articles," US4462842A, Jul. 31, 1984 Accessed: Mar. 25, 2024. [Online]. Available: https://patents.google.com/patent/US4462842

[333] C. E. Tomlinson, "Chromate-free conversion coatings for metals," US5759244A, Jun. 02, 1998 Accessed: Mar. 25, 2024. [Online]. Available: https://patents.google.com/patent/US5759244A/en

[334] P. Rodič, S. Zanna, I. Milošev, and P. Marcus, "Degradation of Sol-Gel Acrylic Coatings Based on Si and Zr Investigated Using Electrochemical Impedance, Infrared and X-Ray Photoelectron Spectroscopies," *Front Mater*, vol. 8, Nov. 2021, doi: 10.3389/fmats.2021.756447.

[335] R. K. Iler, *The Chemistry of Silica: Solubility, Polymerization, Colloid and Surface Properties and Biochemistry*. New York: John Wiley & Sons, 1979. [Online]. Available: https://api.semanticscholar.org/CorpusID:94670558

[336] A. Clearfield, "The mechanism of hydrolytic polymerization of zirconyl solutions," *J Mater Res*, vol. 5, no. 1, pp. 161–162, Jan. 1990, doi: 10.1557/JMR.1990.0161.

[337] A. Clearfield, G. P. D. Serrette, and A. H. Khazi-Syed, "Nature of hydrous zirconia and sulfated hydrous zirconia," *Catal Today*, vol. 20, no. 2, pp. 295–312, Jun. 1994, doi: 10.1016/0920-5861(94)80008-1.

[338] M. S. Dargusch *et al.*, "Exploring the Role of Manganese on the Microstructure, Mechanical Properties, Biodegradability, and Biocompatibility of Porous Iron-Based Scaffolds," *ACS Biomater Sci Eng*, vol. 5, no. 4, pp. 1686–1702, Apr. 2019, doi: 10.1021/acsbiomaterials.8b01497.

[339] M. J. Brusco, D. Steinley, and J. D. Cradit, "An Exact Algorithm for Hierarchically Well-Formulated Subsets in Second-Order Polynomial Regression," *Technometrics*, vol. 51, no. 3, pp. 306–315, Aug. 2009, doi: 10.1198/tech.2009.08022.

[340] M. Gotić and S. Musić, "Mössbauer, FT-IR and FE SEM investigation of iron oxides precipitated from FeSO4 solutions," *J Mol Struct*, vol. 834–836, pp. 445–453, May 2007, doi: 10.1016/j.molstruc.2006.10.059.

[341] P. J. Larkin, *Infrared and Raman Spectroscopy*, 2nd ed. Amsterdam: Elsevier, 2018. doi: 10.1016/C2015-0-00806-1.

[342] M. Veneranda, J. Aramendia, L. Bellot-Gurlet, P. Colomban, K. Castro, and J. M. Madariaga, "FTIR spectroscopic semi-quantification of iron phases: A new method to evaluate the protection ability index (PAI) of archaeological artefacts corrosion systems," *Corros Sci*, vol. 133, pp. 68–77, Apr. 2018, doi: 10.1016/j.corsci.2018.01.016.

Bibliography

Publications Related to the Thesis

Journal Articles

A. Kraš and I. Milošev, "The aqueous chemistry of zirconium as a basis for better understanding the formation of zirconium conversion coatings: updated thermodynamic data," *J. Electrochem. Soc.*, vol. 170, no. 2, p. 021508, Feb. 2023, doi: 10.1149/1945-7111/acb9c2.

A. Kraš, I. Milošev, A. Seyeux, and P. Marcus, "Investigating the presence of polymerised forms in the zirconium conversion coatings on cold-rolled steel: proof of concept," *Npj Mater. Degrad.*, accepted.

A. Kraš and I. Milošev, "Comparative Electrochemical and Thermodynamic Study of Cold-rolled Steel, Al alloy AA5754, and Zn Corrosion in Fluoride and Chloride Solutions," *Electrochim. Acta*, submitted.

A. Kraš, D. Kramar, and I. Milošev, "Characterisation of the deposition and protection performance of Zr conversion coatings on steel and zinc substrates using the response surface methodology," to be submitted.

A. Kraš, D. Kramar, and I. Milošev, "Experimental approach and assessment of Zr conversion coatings on Al alloy using response surface methodology," to be submitted.

Conference Paper

Kraš, A. and Milošev, I. Optimisation of Zr-based conversion coatings on different substrates via response surface methodology, EUROCORR 2022, European Corrosion Congress, Corrosion in a Changing World - Energy, Mobility and Digitalization, 28 August - 1 September 2022, Berlin, Germany. [COBISS.SI–ID 30582823]

Biography

Ana Kraš was born on September 17, 1995, in Zagreb, Croatia. She earned her master's degree in applied chemistry in 2019 from the Faculty of Chemical Engineering and Technology at the University of Zagreb, Croatia, under the supervision of Prof. Sanja Martinez. In October 2019, she began her PhD studies as a Young Researcher under the guidance of Prof. Ingrid Milošev at the Jožef Stefan International Postgraduate School. Ana Kraš has authored or co-authored four scientific papers, two of which are related to her doctoral research. Her scientific interests encompass the broad field of electrochemistry, with a specific focus on corrosion science. She is interested in advancing the use of more sophisticated electrochemical methods, such as the electrochemical quartz crystal microbalance, rotating (ring) disc electrode, and electrochemical impedance spectroscopy, and on incorporating thermodynamic and statistical analysis to enhance mechanistic corrosion studies.